UNIVERSITY OF OKLAHOMA

GRADUATE COLLEGE

DEVELOPMENT OF A CONDUCTIVE BIOINK HYDROGEL FOR TRANSLATIONAL SPINAL CORD REGENERATION

A DISSERTATION

SUBMITTED TO THE GRADUATE FACULTY

in partial fulfillment of the requirements for the

Degree of

DOCTOR OF PHILOSOPHY

By

EMI A. KIYOTAKE
Norman, Oklahoma
2020

DEVELOPMENT OF A CONDUCTIVE BIOINK HYDROGEL FOR TRANSLATIONAL SPINAL CORD REGENERATION

A DISSERTATION APPROVED FOR THE
STEPHENSON SCHOOL OF BIOMEDICAL ENGINEERING

BY THE COMMITTEE CONSISTING OF

Dr. Michael Detamore, Chair

Dr. Ari Berkowitz

Dr. Han Yuan

Dr. Handan Acar

Dr. Michael Martin

Acknowledgments

There are so many individuals I would like to share my gratitude with for helping me survive the adventures of my Ph.D. For making a last-minute decision to go to graduate school, I certainly was not prepared for all the personal and intellectual challenges that I was about to face. I relish the adventure of rock climbing outside and hiking 14,000+ ft mountains, but I would not have survived this mountain called graduate school, had it not been for the help and support from my lab family, mentors, family, and friends. I would like to thank all the wonderful people in my life who have cheered me on and supported me in different ways.

First and foremost, I would like to thank my advisor, Dr. Michael Detamore, for the continuous mentorship, support, and opportunity to pursue all my goals in my personal and professional life. He was an amazing mentor and I could not have asked for a better one. Thank you for convincing me to follow you to the University of Oklahoma, where I have had more opportunities to grow that I could have ever imagined. Despite all the challenges of taking on a new field for both of us, I appreciate the constant cheering through all the failures and successes.

I would like to thank my committee members, Dr. Ari Berkowitz, Dr. Han Yuan, Dr. Handan Acar, and Dr. Michael Martin for their support and guidance throughout my graduate studies at OU. Not only did each committee member provide thoughtful perspectives that expanded and strengthened my dissertation research, they individually mentored me and helped me grow on a personal level.

I would like to additionally thank Dr. Stefan Wilhelm for his direct guidance on all things gold nanoparticles. He was an unexpected, but wonderful mentor that enabled and fully supported my gold nanorod investigations.

I would like to thank all the co-authors of the presented work: Hannah Homburg for all her help with animal care and taking care of all of my needs at OUHSC during the COVID-19 pandemic, and Camille Milton and Dr. Adam Smitherman for help with the animal surgeries. I would like to thank Nathan Donahue for his learned and developed expertise in Inductively Coupled Plasma-Mass Spectrometry (ICP-MS) and help with the constant troubleshooting of gold nanorods. I would like to thank all our collaborators for their assistance in various aspects of the research: Dr. Susan Nimmo for her expertise in Nuclear Magnetic Resonance (NMR) Spectroscopy and kindness to teach me advanced 2D NMR techniques, Dr. Preston Larson for his expertise and help in obtaining Transmission Electron Microscopy (TEM) images, Dr. Tingting Gu for help with confocal imaging, Dr. Yingtao Liu for help with conductivity testing, Dr. Kar-Ming Fung for his pathology expertise, the Stephenson Cancer Pathology Core at OUHSC for generously providing histology and staining services, and Boushra Ajeeb for her discovery of the literature paper that enabled the gold nanorod synthesis to finally work.

Research reported in the dissertation was supported by the Translational Regenerative Medicine Lab. I would like to thank Peggy and Charles Stephenson for their generosity and kindness in starting the Stephenson School of Biomedical

Engineering and the graduate fellowship I was awarded, both of which made my Ph.D. project possible. I would like to thank other mentors, Dr. Kim Wolfinbarger for teaching me how to develop my leadership skills through the Holmes Leadership Program and Dr. Anne Engemann for the leadership and career mentorship.

I would like to thank all the undergraduate researchers that have helped in the completion of the research, including Emily Thomas for her immense dedication to research for the last 3 years and continued help throughout the COVID-19 pandemic, and Alexander Douglas for his quick learning, willingness to always help, and collection of rheological data. Both students taught me a great deal about mentorship, and they will both make fantastic doctors (Ph.D. and M.D.) one day.

I would like to thank all the alum and current members of the Translational Regenerative Medicine Lab at OU/ Tissue Engineering Lab at KU: Dr. Jakob Townsend for teaching me how to science, how not to take on appealing side-projects, having writing parties, and for always being there for me as a friend. I would like to thank Drs. Emily Beck, Vineet Gupta, A.J. Mellott, and Salma Mahzoon for teaching me all the essential lab techniques and advice in navigating graduate school. I would like to thank Peggy Keefe for being an amazing and supportive lab manager and keeping me fed with baked goods. I will always volunteer to be a guinea pig for her baking.

I would like to thank my boyfriend, Larson Sewell, for always taking care of me through my ups and downs and listening to me when I needed it the most. I would like to thank my friend Nicole Wen for all the support, keeping me fed with homecooked lunches, and always motivating me to do my best. I would like to thank my fellow grad students, from KU and OU, and climbing friends for being amazing friends and relieving all the stress of graduate school. I never expected to have made so many supportive friendships in so little time.

Finally, I would like to thank my parents, brother, and rest of my family for making me who I am today and their continuous love and support throughout every new adventure I take. I appreciate all the care packages sent to the lab that would always make everyone jealous!

Table of Contents

List of Figures

Chapter 1

No figures

Chapter 2

Chapter 3

Chapter 4

Chapter 5

List of Tables

Chapter 1

No Tables

Chapter 2

Chapter 3

Chapter 4

Chapter 5

Chapter 6

No Tables

Abstract

Spinal cord injury (SCI) patients rarely recover full functionality with current clinical treatments. There are two approaches for developing treatments for SCI: 1) rehabilitation strategies and 2) regenerative medicine strategies. Individually, each strategy has not been able to facilitate full functional recovery after severe SCI. Rehabilitation strategies have shown better functional recovery compared to regenerative medicine approaches, especially when motor training was combined with electrical stimulation (ES) for patients with incomplete SCIs. However, patients with more severe injuries may not recover full functionality from only rehabilitation approaches. As discussed in the SCI literature, there is a need to combine the fields of rehabilitation and regenerative medicine to maximize functional recovery, but there are not many methods to synergistically combine the fields. Conductive biomaterials may be the missing link that enables synergistic combination of regenerative medicine with the rehabilitation approach of ES. Unfortunately, there are a paucity of *in vivo* studies using conductive biomaterials for SCI. One problem is that most conductive biomaterials are preformed scaffolds that are risky and challenging to implant in an SCI, which does not have defined borders. However, an injectable biomaterial may be easier to deliver into the most common contusion SCI than a preformed scaffold and thus, may be more translational. Given that the bioprinting field focuses on several of the same parameters used in developing injectable biomaterials, that field may offer insight in designing injectable materials. In the current dissertation,

an existing fast-crosslinking pentenoate-functionalized hyaluronic acid (PHA) hydrogel precursor was first developed into a bioink and the rheology of the bioink was characterized to predict printability. The PHA bioink was then developed to be adhesive for rat neural stem cells (rNSCs) through the incorporation of a newly developed pentenoate-functionalized gelatin (PGel) based on the same chemistry employed for PHA. The rheology of the adhesive formulations of the PHA/PGel bioink were characterized to determine the printable formulations. Finally, a conductive and injectable/bioprintable hydrogel was developed by incorporating gold nanorods (GNRs) into PHA/PGel, and was subsequently applied to a thoracic level (T8) lateral hemi-section rat spinal cord injury (SCI) model. While no significant differences in functional recovery or axon regeneration were found across any of the tested material groups, the feasibility of the injectable/paste-like GNR hydrogel precursors and the long-term safety of the crosslinked hydrogels were demonstrated. No previous studies have applied a GNR-based conductive hydrogel to SCI, therefore, the significance of the current dissertation was the development of a conductive biomaterial that was a bioprintable/translational platform for contusion SCIs. The GNR hydrogel may be further refined with the addition of other regenerative medicine approaches to promote axon regeneration and synergistically combined with rehabilitative approaches, such as ES, to facilitate full functional recovery after SCI.

Chapter 1 : Introduction

The long-term goal of this dissertation is the development of a conductive and injectable biomaterial for bioprinting and application to treat spinal cord injury (SCI). SCI causes permanent damage to the spinal cord and full functional recovery is uncommon with current clinical treatments. While motor training alone does not typically promote full functional recovery, combinations of rehabilitation strategies (e.g., motor training with electrical stimulation (ES)) have been the most effective treatment in promoting over ground independent stepping in humans thus far. Rehabilitation strategies aim to promote neural plasticity in any remaining, undamaged axonal pathways and/or activate intrinsic spinal cord neural circuits, known as central pattern generators (CPGs), that produce rhythmic activation of muscles, such as for walking, and are intact and exist below the injury. However, the most severely injured SCI patients have not benefited as much from motor training with ES compared to patients with incomplete injuries, possibly due to patients with severe injuries having little to no remaining spared pathways. For more severely injured patients, locomotion may be possible from task-specific ES combined with motor training to activate CPGs related to locomotion. While rats and cats have long been able to recover locomotion after complete transections via ES-enabled CPG activation, translation to humans has been slower, but there have been recent successes of over-ground independent stepping in a few patients. Determination of the requisite ES parameters to activate CPGs and identification of other spinal networks and/or CPGs in humans

remains a challenge and for full functional recovery beyond locomotion, the axonal pathways may need to be regenerated and retrained. Several regenerative medicine approaches aim to regenerate the axonal pathways; however, regenerative medicine approaches alone so far have not yet been successful in promoting full functional recovery either.

The SCI literature has indicated the need to combine rehabilitation strategies with regenerative medicine strategies to maximize the functional outcomes, which embodies the principles of regenerative rehabilitation. In regenerative rehabilitation for SCI, regenerative medicine approaches are needed to regenerate the spinal cord tissue and rehabilitation approaches are needed to enhance neural plasticity to form new neural pathways. Currently, there are few methods that synergistically combine regenerative medicine approaches with rehabilitation approaches; however, conductive biomaterials may be the linchpin that synergistically combines the two fields. Currently, there are a paucity of *in vivo* studies with conductive biomaterials. One challenge with conductive biomaterials is that many scaffolds are preformed and unable to conform to the irregular borders of typical contusion SCIs, and implantation risks further damage. However, an injectable material able to conform to the injury may have better translation for SCIs. The bioprinting field focuses on several of the same parameters that apply to the development of injectable biomaterials and therefore, may offer insight in designing injectable materials. Fortunately, the bioprinting field focuses on the development of injectable biomaterials for

biomedical applications. There is a need for additional injectable conductive biomaterials for SCI and bioinks have relevant rheology that enable easier translation.

In the current dissertation, a conductive and bioprintable hydrogel was developed, refined for neural tissue engineering, and applied to a rat SCI model in the following three aims. The first aim was to develop and characterize the rheology of a bioprintable pentenoate-functionalized hyaluronic acid (PHA) hydrogel precursor. The second aim was to promote neural stem cell adhesion and viability by developing a pentenoate-functionalized gelatin (PGel) hydrogel and fabricating a printable PHA/PGel hydrogel. The final third aim was to establish a conductive and injectable PHA/PGel hydrogel through the incorporation of gold nanorods (GNRs), and to apply and evaluate the feasibility and long-term safety of the GNR hydrogel in a rat SCI model. The following chapters are the chronological organization of the content of the current dissertation:

Chapter 2 is a review of SCI, including the current regenerative medicine approaches in clinical trials and the rehabilitation approaches for SCI, with discussion of the translational limitations of each approach. I further discussed the potential for conductive biomaterials to synergistically link the two fields and leverage the principles of regenerative rehabilitation to maximize functional recovery after SCI. Finally, the main categories of conductive composites (e.g., conductive polymers, carbon-based materials, metallic nanoparticle-based

materials) were reviewed and the translational potential of each approach was discussed. I concluded that several of the current conductive biomaterials were preformed scaffolds, which may be difficult to translate to contusion SCIs; however, injectable composites with blended conductive fillers may be more translational for SCI and able to synergistically combine regenerative medicine and rehabilitation approaches (e.g., ES).

Chapter 3 addresses **Aim 1**, which developed an existing biomaterial, PHA, as a bioink. The rheology and bioprinted shape fidelity of different molecular weights and concentrations of PHA precursors were evaluated. We aimed to universalize the bioprinting field by selecting and promoting three standard rheological tests (i.e., viscosity, yield stress, and storage modulus recovery) to characterize the rheology of bioinks and correlate it to the printability.

Chapter 4 addresses **Aim 2**, which developed the PHA bioink to support rat neural stem cell (rNSC) adhesion and viability for nerve tissue engineering. The same functionalization chemistry was used to develop a PGel hydrogel. Varying formulations of PGel hydrogels were evaluated with rNSCs to evaluate adhesion, but the PGel hydrogels degraded quickly. Therefore, the adhesive PGel formulations were incorporated into PHA to make PHA/PGel hydrogels adhesive for rNSCs with long-term stability in culture. Finally, the rheology and printability of the adhesive formulations of PHA/PGel hydrogel precursors were evaluated to select a PHA/PGel hydrogel formulation that supported rNSCs and had a bioprintable/translational precursor.

Chapter 5 addresses **Aim 3**, which developed the PHA/PGel bioink that was adhesive for rNSCs into a conductive bioink through the incorporation of GNRs. High aspect ratio GNRs were synthesized and various concentrations of GNRs were tested in PHA/PGel hydrogels to develop conductive GNR hydrogels. The cytotoxicity and printability of the GNR hydrogels were evaluated with rNSCs *in vitro* and to select a formulation for further evaluation *in vivo*. The feasibility of injecting the selected GNR hydrogel and the long-term safety of the hydrogel was evaluated *in vivo* in a thoracic level (T8) lateral hemi-section SCI model in rats.

Chapter 6 is the conclusion to the dissertation, where the major findings of all three aims, limitations of the studies, and recommendations for future research are discussed.

Chapter 2 : Regenerative Rehabilitation with Conductive Biomaterials for Spinal Cord Injury[1]

Abstract

The individual approaches of regenerative medicine efforts alone and rehabilitation efforts alone are insufficient to fully restore function after severe spinal cord injury (SCI). Regenerative rehabilitation may harness the power of these two disparate fields by combining them to maximize recovery. For SCI, regenerative medicine approaches may be leveraged to promote regeneration of the spinal cord tissue, and rehabilitation approaches may be able to promote reorganization of the regenerated neural pathways and intact spinal circuits. Conductive biomaterials could be a linchpin than empowers the synergy between regenerative medicine and rehabilitation approaches, as electrical stimulation applied to the spinal cord could facilitate neural reorganization. In this review, we discussed current regenerative medicine approaches in clinical trials and the rehabilitation, or neuromodulation, approaches for SCI, along with their respective translational limitations. Furthermore, we reviewed the translational potential of conductive composites (e.g., conductive polymers, carbon-based materials, metallic nanoparticle-based materials) as they pertain to SCI. We

[1]In preparation for submission to *Acta Biomaterialia* as: Kiyotake EA, Martin MD, Detamore MS. Regenerative Rehabilitation with Conductive Biomaterials for Spinal Cord Injury.

concluded that pre-formed scaffolds may be difficult to translate to contusion SCIs; however, injectable composites that contain blended conductive components and that can form a scaffold within the injury may be more translational. Injectable, conductive biomaterials thereby may enable regenerative medicine to become a translational tool to enhance the outcomes associated with the latest rehabilitation treatments. There are currently no *in vivo* SCI studies that evaluated conductive materials combined with rehabilitation approaches. The use of conductive biomaterials creates a synergistic opportunity to merge the fields of regenerative medicine and rehabilitation and redefine what regenerative rehabilitation means for the spinal cord.

Introduction

There are two separate approaches discussed individually in recent reviews of the most translational approaches for promoting functional recovery after spinal cord injury (SCI) (see **Table 2.1** for a list of acronyms): regenerative medicine and rehabilitation (see **Fig. 2.1**). Regenerative medicine approaches(1) are methods using cells, drugs, biologics, and/or materials; for example, for the purposes of replenishment of lost cell populations, promotion of axon sprouting, growth, or synapse formation, intrinsic enhancement of cell survival, and/or neutralization of the extrinsic axon-inhibiting environment. By manipulating the intrinsic and/or extrinsic environment, regenerative medicine approaches for SCI typically aim to promote regeneration of the axons and restore the spinal cord to the same functional level prior to injury. Regenerative medicine approaches for

SCI have been described with other terminologies in other reviews, such as microscopic approaches/cellular-molecular interventions,(2) biological approaches,(3) or Hutson and Giovanni(4) used specific subdivisions of neuronal intrinsic signaling, neuronal extrinsic environment, and neural stem cell grafts.

In contrast to regenerative medicine, rehabilitation methods for SCI include motor training and external stimuli such as electrical stimulation (ES) to drive the reorganization of remaining axons in the spared tissue or intact spinal circuits. Additionally, the definition of rehabilitation approaches for SCI can be expanded to include neurochemical stimulation (e.g., serotonergic and dopaminergic receptor agonists), as these stimulation methods have been applied to SCI to achieve outcomes similar to using other rehabilitation methods. Rehabilitation approaches have been referred to in other reviews as neuromodulation,(4) technological approaches,(3) and macroscopic/systems-circuitry level approaches.(2)

For SCI, regenerative medicine approaches and rehabilitation approaches individually have not yet resulted in full functional recovery. Combinations of rehabilitation approaches, specifically motor training paired with ES, have shown the greatest recovery of walking after SCI in small clinical studies compared to individual regenerative medicine therapies and individual rehabilitation approaches. Even so, patients with more severe injuries and little to no spared tissue may need regenerative medicine approaches to regenerate the damaged pathways, as these patients may not benefit much from rehabilitation alone. The

synergistic combination of regenerative medicine approaches and rehabilitation approaches is known as regenerative rehabilitation.(5-7)

The underlying principle of regenerative rehabilitation is to apply rehabilitation protocols with regenerative medicine to optimize functional recovery through tissue regeneration. For SCI, given the better functional outcomes of the rehabilitation protocols, there is a need to develop regenerative medicine therapies that are not only combined with rehabilitation approaches, but further augment the effects and maximize functional recovery. Regenerative rehabilitation principles have been applied in areas such as skeletal muscle, cardiac tissue, brain plasticity, and bone.(1) Even though the specific terminology of “regenerative rehabilitation” has only been used in few SCI studies,(8) several clinical, *in vivo*, and *in vitro* SCI studies have already utilized the principles (e.g., cells + motor training,(9) conductive biomaterials + ES,(10-16) scaffold + cells + ES(17)). The limited reviews of “regenerative rehabilitation” with mention of SCI have broadly focused on neural pathologies(18) or specifically focused on neural stem cells and physical rehabilitation.(19) While not specifically using the “regenerative rehabilitation” terminology, concepts akin to regenerative rehabilitation principles for SCI have been discussed within several excellent reviews.(2-4, 20) Each review discussed the need to combine approaches in the future, but there remains a need for a review about the synergistic development of regenerative medicine approaches within the framework of rehabilitation

approaches, and moreover about how to improve the clinical translatability of combined approaches.

To further build upon and universalize the principles of regenerative rehabilitation for SCI, we cover current regenerative medicine approaches and rehabilitation approaches for SCI and further discuss the emerging field of conductive biomaterials, which falls at the intersection of regenerative medicine and rehabilitation for SCI (see **Fig. 2.1**). Conductive biomaterials could provide a medium for ES to be delivered directly to cells to enhance neural plasticity and thereby promote a regenerative biological response. Several reviews have discussed the application of conductive biomaterials for biomedical applications(21) and tissue engineering,(22, 23) but the most recent review of conductive biomaterials for nerve tissue engineering was in 2011.(24) These reviews of conductive biomaterials have been broad in scope and only mentioned SCI as one example application. Therefore, an updated review of conductive biomaterials for SCI is needed. In this review, we additionally cover the conductive biomaterials that have been developed to date and their advantages and disadvantages for translation to application in SCI.

Spinal Cord Injury

Clinical significance

Traumatic spinal cord injury (SCI) causes permanent damage to the spinal cord and there are currently no clinical treatments that promote full recovery of motor and sensory function. While there has been a substantial amount of SCI

research, new clinical treatments are not surfacing as rapidly. In the United States, SCI currently affects approximately 294,000 people with approximately 17,800 new cases of SCI each year.(25) The majority of civilian SCIs result from motor accidents, falls, and gunshot wounds. SCIs in the military were found to be typically from blast injuries as opposed to penetrating injuries, and compared to civilian injuries, military SCIs were more severe and typically involved multiple spinal levels.(26) SCI usually entails a traumatic impact to the spine that shifts or crushes one or more vertebrae, causing compression of the spinal cord and disruption of motor and/or sensory axon tracts. Depending on the level (i.e., cervical, thoracic, lumbar) and on the extent of damage across the cord (i.e., complete, incomplete), varying amounts of paralysis may occur below the level of the injury.

Patients are typically assessed for neurological recovery using the American Spinal Injury Association (ASIA) Impairment Scale (AIS), which is an internationally standardized system,(27) and which provides scores for motor and sensory loss. Completeness of SCIs according to ASIA protocols range from grade A to E, where grade A is complete motor and sensory loss below the level of injury, grade B is complete motor loss with incomplete sensory loss, grade C and D are incomplete motor and sensory loss (where grade C patients have less than half of key muscle functions and grade D patients have at least half of key muscle functions below the injury), and grade E is normal.

Current treatments can include early decompression surgery, to alleviate pressure of a malaligned or broken spinal column and prevent further damages the spinal cord, and/or rehabilitation, which attempts to leverage the intrinsic plasticity of the nervous system to re-train remaining uninjured pathways. Other current treatments include mean arterial pressure (MAP) therapy, steroids, and moderate hypothermia. MAP therapy aims to avoid systemic hypotension and to improve spinal cord perfusion.(28) Delivery of the steroid methylprednisolone sodium succinate (MPSS) was historically used for neuroprotection, but the clinical use of MPSS has rapidly decreased following three large randomized trials from the National Acute Spinal Cord Injury Studies that showed no difference in neurological recovery.(29) Moderate hypothermia (33°C) introduced by intravascular cooling strategies aims to protect against ischemia and neural cell death.(30) While MAP therapy, steroids, and hypothermia treatments may result in some neurological recovery, they aim to help prevent the damaging cascade of events (i.e., secondary injury) after the initial injury and typically do not result in full functional recovery.

Even though spontaneous recoveries of motor, sensory, and/or autonomic functions within the first year after the injury can occur, the recovery usually plateaus 12 to 18 months post-injury and patients do not typically recover additional functions. The extent of spontaneous recovery is typically limited and was found to be dependent on the severity, where improvement of at least 1 grade was reported in one meta-analysis of 114 studies with ~20,000 patients for

19% of AIS A, 74% of AIS B, 87% of AIS C, and 47% of AIS D patients.(31) Additionally, and not surprisingly, full recovery was reportedly more common in less severely injured patients than more severely injured patients (i.e., 47% of AIS D patients fully recovered but only 9% of AIS C patients, 0.3% AIS B, and 0% of AIS A patients recovered). The National Spinal Cord Injury Statistics Center 2019 Annual Statistical Report of SCI patients from 1972 to 2019, showed that at the time of initial injury the largest group of patients was the most severe, where 43% were AIS A, 29% were AIS D, 12% were AIS C, 11% were AIS B, <1% were recovered and AIS E, and <5% were unknown.(32)

In the last few decades, overall neurological recovery has not significantly improved,(31) and an effective treatment is still needed, particular for the most severe AIS A patients.

Pathophysiology creates challenges in determining when to deliver treatments

Developing treatments for SCI is challenging as the pathophysiology of SCI is complex with physical, cellular, and molecular variations over time depending on the severity (i.e., complete, incomplete) and type of injury (e.g., contusion, penetrating).(33-36) In addition to the type of treatment, the timing of treatment delivery and how it gets delivered are important considerations. SCI consists of a primary and secondary injury, where the primary injury is the initial mechanical insult that causes direct damage to neural and glial cells and may include vascular injury. After the primary injury, there is a degenerative response

known as the secondary injury, where there is hemorrhage, apoptosis, swelling, inflammation, excitotoxicity, ionic imbalance, and an overall unstable environment. The secondary injury is typically described as the acute (i.e., hours to a few days post-injury), subacute (i.e., weeks to months post-injury), and chronic injury (i.e., more than 1-year post-injury). To treat the acute injury in the short timeframe immediately after injury (i.e., within the first 1 to 2 days), injectable drugs or biologics are easier to deliver than complex treatments such as autologous cell therapies because it is not possible to do 1 to 2 weeks of cell expansion in 1 to 2 days. Implantation of biomaterial therapies in the early stages risk compromising spontaneous recovery, especially if spinal cord tissue must be removed to make a scaffold fit. Additionally, the exact size and shape of an injury is difficult to discern, and therefore challenging for a surgeon to trim a scaffold to fit into the injury. Injectable therapies still have risk, but they are less invasive and may not be as risky as biomaterial implantation.

Subsequently, in the following days to weeks, the subacute stage encompasses additional cell death, ischemia, hypoxia, inflammation, free radical production, and edema. Within the first day after injury, spinal cord ependymal cells from the lining of the central canal, which are normally dormant, rapidly proliferate.(37) Within 3 days, these ependymal cells migrate from the central canal to the injury, and differentiate into astrocytes that surround the injury core of stromal cells.(37) The injury becomes inhibitory toward axon regeneration due to the presence of chondroitin sulfate proteoglycans (CSPGs) and myelin-

associated inhibitors (MAIs). CSPGs and MAIs activate Nogo receptors (NgRs), several of which inhibit neurite growth. CSPGs are astrocyte-secreted proteoglycans (e.g., aggrecan, neurocan, phosphacan, versican) that activate NgRs and subsequent signaling pathways known to inhibit axon growth, and prevent protein tyrosine phosphatase sigma (PTPΩ; a transmembrane protein) from activating axon-growth-promoting signaling pathways,(38) among other mechanisms covered by other excellent reviews.(39) MAIs are transmembrane proteins normally present in myelin that are thought to be released from disrupted myelin after injury.(40) In the later subacute stage, astrocytes secrete fibrous-like scar tissue that develops into a stable glial scar in the chronic stage, which creates a physical barrier that prevents axon regeneration. The inhibitory environment and glial scar never resolve, creating a permanent physical and chemical barrier to axon regeneration, resulting in permanent functional deficits.

As nerve regeneration is typically a slow process over months to years, injectable drugs, biologics, and more complex treatments delivered in the subacute and chronic stages, would most likely need a sustained delivery platform or multiple dosages to maintain a therapeutic effect for an extended period. Treatments delivered in the subacute stage may face similar challenges to acute treatments where it is more difficult to differentiate the efficacy of the treatment versus normal spontaneous recovery. In clinical trials, larger numbers of patients will be required to demonstrate the efficacy of acute and subacute treatments compared to chronic treatments, where the chance of neurological

improvement is lower. Delivery of treatments, including implantation of biomaterials, in the chronic stage after spontaneous recovery plateaus, may be less risky than the subacute or acute stages because spontaneous recovery will not be compromised.

In summary, in the early stages after SCI, cell therapies may not be feasible to deliver and they risk compromising spontaneous recovery. Injectable drugs and biologics might be easier to deliver shortly after injury and in the acute stage to reduce the secondary injury compared to cell or biomaterial therapies; however, discriminating between spontaneous recovery and the effect of the treatment will be difficult and will require large sample sizes. During the later subacute and chronic stages, sustained release of drugs from biomaterials might be more translatable than repeated dosages of drugs or biologics by themselves. Cell and biomaterial therapies may be less likely to compromise spontaneous recovery in the chronic stage. Furthermore, injectable biomaterials are less invasive and less risky than preformed scaffold implantation, and therefore, more translational for SCI.

Current therapeutic approaches: Regenerative medicine

The principles of regenerative rehabilitation are based on combining rehabilitation approaches and regenerative medicine treatments to maximize the functional outcomes; therefore, regenerative medicine approaches must be developed with clinical translation and synergism with rehabilitation approaches in mind. In this section, we discuss the current application of cells, drugs,

biologics, and biomaterials in clinical trials and further discuss the current clinical limitations of each approach. Different regenerative medicine approaches share the same overarching goal, which is typically to repair the damaged tissues. However, there are two distinct mechanisms separating regenerative medicine approaches. Specifically, cellular therapies are typically used to replace the lost neural cell population and/or create a regenerative environment, whereas biomaterials are typically intended to aid or facilitate regeneration via the existing cell population.

Cell-based therapies

Cell-based therapies for spinal cord repair have been reviewed extensively and encompass the use of neural stem cells (NSCs),(41, 42) pluripotent stem cells (i.e., embryonic stem cells (ESCs) or induced pluripotent stem cells (iPSCs)) (43), mesenchymal stem cells (MSCs),(34, 44, 45) olfactory ensheathing cells (OECs),(46) and/or Schwann cells (SCs).(47) There are 17 cell-based U.S. clinical trials for SCI, not including cells with biomaterials, that are recruiting, not yet recruiting, active not recruiting, or enrolling by invitation on ClinicalTrials.gov as of July 2020 (see **Table 2.2**). The majority of current cell-based therapies for SCI utilize MSCs or other bone-marrow derived stem cells. Fewer SCI studies involve NSCs or OECs, and there no current trials using iPSCs or SCs. Neural progenitor cell types (e.g., NSCs and iPSCs) that can differentiate into neurons have been investigated for SCI treatments for the purpose of directly replenishing the neural populations. In contrast, the non-neural cell types (e.g., MSCs, OECs,

SCs) are hypothesized to support functional recovery through a variety of mechanisms such as regulating inflammation, secreting growth factors to support cell survival, and remyelinating axons.(48) While many cell therapies with varying types of neural and non-neural cells have shown functional improvement after transplantation in animal SCI models, the efficacy in humans has yet to be proven. Many small clinical studies have not resulted in sufficient functional improvement or have had limitations in the experimental design (e.g., lack of appropriate controls and showing increased efficacy compared to normal spontaneous recovery).(34)

There are several translational disadvantages that will need to be overcome for cell-based therapies to succeed: 1) limited cell sources, 2) costly and time-consuming *in vitro* culture, and 3) low cell survival after implantation. Adult NSCs are only found in the brain and spinal cord,(37) which are difficult and perhaps impractical to harvest for autologous use, but could be harvested from allogeneic donor tissue. ESCs and fetal-derived NSCs have ethical hurdles, but these hurdles may perhaps be mitigated by relying on immortalized cell lines such as the NSCs derived from fetal spinal cords used in clinical trials by Neuralstem Inc. (ClinicalTrials.gov Identifier: NCT01772810). Additionally, NSCs differentiated from iPSCs that were derived from autologous somatic cells are easily accessible and a more practical source than autologous brain or spinal cord derived NSCs. Other non-neural autologous cell sources are more surgically accessible than true NSCs and easier to isolate than autologous NSCs. Through

routine procedures, autologous MSCs can be obtained from bone marrow or adipose tissue, and either autologous (if available) or allogeneic Wharton's jelly mesenchymal cells can be obtained from umbilical cords. OECs can be harvested from the olfactory bulb or the olfactory mucosa, and SCs can be harvested from the sural nerve. The downside of harvesting autologous tissues is that patients must undergo and recover from a second surgery (with autologous umbilical cord cells being an exception). Allogeneic cells from donor tissues can be a feasible source, but patients may need to take immunosuppressive drugs and donor cells may be limited.

Regardless of cell source, a limitation of most cell therapies is the need for *in vitro* cell expansion because of the low number of cells obtained from biopsies or grafts. Given that the survival rate of transplanted cells is low, a therapeutic effect is only achieved with large numbers of cells. Note for example that current clinical trials implant up to 100 million cells (ClinicalTrials.gov, see supplemental **Table 2.2**). Harvested cells typically require 4-5 weeks of *in vitro* expansion in addition to the time needed for isolation and differentiation (e.g., of progenitor cells). Furthermore, isolated cells, such as progenitor cells or from tissues that include multiple types of cells (i.e., olfactory bulb/mucosa), need standardized testing to verify the purity of final implanted cells to prevent unwanted side effects or tumorigenicity.(41) Cell expansion is time consuming, expensive, and requires current good manufacturing practice (GMP) for regulatory approval. There are additional challenges to consider after *in vitro* culture such as determination of

cell density to avoid clotting, when to deliver cells for the maximum therapeutic effect, and the route of administration, which are discussed in more detail by Tang *et al.*(41)

In summary, before cell therapies can become a widespread realistic treatment option, there are current translational limitations that need to be addressed such as the limited efficacies shown so far and low cell survival after implantation. Other inherent challenges of cell therapies that will be more difficult to address are the time-consuming *in vitro* cell culture and the need for GMP facilities. Despite the latter challenges that will likely remain, the future of cell-based therapies is thought to require combinations with other strategies to reduce some of the former limitations,(34, 48, 49) such as using biomaterials and/or biologics to improve cell viability. Promising combinations of cells with other regenerative medicine approaches are further discussed in later sections.

Drugs & Biologics

Given the translational issues of cell-based treatments, several small molecule drugs and biologics are in clinical trials that promote some degree of functional recovery after SCI by 1) neutralizing/degrading the extrinsic inhibitory components that prevent axon growth, and/or 2) intrinsically preventing apoptosis to promote neuron survival. For a few excellent reviews, we refer readers to Vecino and Kwok(39) and Badhiwala *et al.*(50) There are several antibodies and proteins in clinical trials (ClinicalTrials.gov, see **Table 2.3**) that bind to the inhibitory components in the glial scar. Therapeutics that bind inhibitors (e.g.,

neurite outgrowth inhibitor (Nogo-A), MAIs, Repulsive Guidance Molecule A (RGMa)) are designed to prevent receptor binding to either deactivate downstream axon-inhibitory signaling pathways and/or enable axon-growth signaling pathways. Aside from targeting extrinsic factors, there are small molecule drugs and biologics in clinical trials for intrinsically preventing apoptosis and supporting cell survival (ClinicalTrials.gov, see **Table 2.3**). Some small molecule drugs (e.g., cation channel blockers) aim to reduce excitotoxicity and the ionic imbalance causing apoptosis, and some biologics (e.g., growth factors) aim to upregulate cell survival pathways, reduce inflammation, or promote angiogenesis.

Several drugs and biologics have had success in improving functional recovery in animal models that target extrinsic inhibitory components, intrinsic cell survival pathways, and inflammation. An enzyme (i.e., chondroitinase ABC (ChABC)) and a peptide (i.e., intracellular sigma peptide (ISP)) have been particularly successful in promoting some functional recovery by degrading or preventing the binding of chondroitin sulfate proteoglycans (CSPGs), respectively. Promising preclinical drugs that upregulate survival/anti-apoptotic pathways to promote survival of damaged neurons and upregulate axon growth pathways include purine nucleoside and inosine.(2) Several growth factors have been investigated for neural differentiation, neuroprotection, and promoting axon growth (e.g., brain-derived growth factor (BDNF), nerve growth factor (NGF), neurotrophin-3 (NT-3), and glial-derived neurotrophic factor (GDNF)).(51, 52)

Finally, there are promising preclinical drugs and biologics that have been investigated to reduce inflammation (e.g., minocycline, interleukin 4 (IL-4), and CD95),(53) reduce secondary damage initially after SCI, and/or polarize macrophages toward an M2-like regenerative phenotype. Inflammation is complex and may be beneficial in the early stages post-injury for aiding debris removal and limiting tissue damage, but inhibitory in the later stages as the inflammation persists and prevents regeneration.(2, 35) We recommend three excellent reviews for further reading on inflammation after SCI.(54-56)

The main translational challenges of using drugs and biologics to treat SCI are targeted delivery and delivery of a therapeutic dose. Systemic delivery of drugs and biologics is difficult due to the low permeability of the blood-spinal cord barrier (BSCB), which only allows compounds less than 400 Da to cross.(53) The low diffusion of molecules across the BSCB necessitates high doses to be delivered to achieve therapeutic effects at the site of injury, which can result in systemic cytotoxicity and off-target effects.(33) To bypass the BSCB, therapeutics can be delivered locally, but injection into the intrathecal space around the spinal cord is hindered by the rapid clearance by the cerebral spinal fluid (CSF).(33) Furthermore, biologics such as growth factors are susceptible to enzymatic cleavage and have short circulation times(44) (e.g., NT-3 has a half-life of 30 minutes after systemic injection,(57) ChABC loses enzymatic activity in 3-5 days(58)). Injection of biologics can be further limited in clinical translation because of limited supply, occasional safety and immunogenicity concerns of

donor human or bacterial origins, and potentially high cost of isolation and purification from tissues. Overall, the local delivery of drugs and biologics both typically require repeated injections or continuous delivery by infusion to achieve the desired therapeutic effects,(44, 58) which is inconvenient and/or painful for patients and costly to produce.

In summary, drugs and biologics have been developed to neutralize extrinsic factors and/or be neuroprotective, which may lead to less long-term damage; however, by only reducing the secondary injury and not promoting regeneration, there may be limited functional recovery. Nevertheless, modulating the inhibitory environment with neuroprotective/neutralizing drugs to create a permissive environment for axon growth in a combination strategy may improve the efficacy of regenerative approaches. Drugs and biologics will need to overcome the translational limitations of delivering a therapeutic dose and targeted delivery to the injury. However, in the future, drugs and biologics may have the advantage of oral or intravenous administration for earlier treatment (e.g., in the acute stage) than a cellular or material-based therapy that requires transport to a hospital and surgery. Combining acutely delivered drugs/biologics to create a permissive environment combined with regenerative approaches delivered in the later stages could leverage the advantages of both approaches for better functional recovery.

Biomaterials

The development of biomaterials typically aims to provide a physical and permissive environment that enables or promotes axon growth. There are two main areas of focus: 1) delivering and enhancing cell therapies, drugs, and biologics, and 2) controlling scaffold architectures to guide neurite outgrowth. Several types of scaffolds (e.g., extracellular matrix-based polymers, non-mammalian natural polymers, synthetic polymers) have been developed and investigated *in vitro* and *in vivo* (we refer readers to two reviews(59, 60) for more comprehensive reviews of biomaterials for SCI), with few clinical studies or trials. Of the eight current (i.e., active, recruiting, not yet recruiting) clinical trials with biomaterials for SCI (as of July 2020, clinicaltrils.gov, see **Table 2.4**), most focus on combining biomaterials with cells. Only two of the eight current clinical trials that we identified are investigating a material alone, and are both investigating a poly(lactic-co-glycolic acid) (PLGA) scaffold called “Neuro-Spinal Scaffold” (ClinicalTrials.gov Identifiers: NCT02138110, NCT03762655)), which has shown moderate improvements in the first enrolled patient.(61)

To overcome the translational limitations of cell therapies, drugs, and biologics, biomaterials have been widely employed in the literature to deliver these therapeutics. Five of the eight current clinical trials that use biomaterials focus on using scaffolds to deliver cells because the materials can protect cells from the shear stresses of being injected through a needle and protect cells from the inhibitory injury environment, thus improving the survival of implanted cells

and functional recovery in animal models. There are two different scaffold approaches that have been presented in combination with cells. The first is a collagen scaffold with a sural nerve graft to deliver autologous OECs (ClinicalTrials.gov Identifier: NCT03933072). The other is a linearly ordered collagen scaffold from decellularized bovine aponeurosis (NeuroRegen Scaffold), which delivers umbilical cord-derived MSCs (UC-MSCs), mononuclear cells (ClinicalTrials.gov Identifiers: NCT02352077, NCT02510365, NCT02688062), or NSCs (ClinicalTrials.gov Identifier: NCT02688049). While improvements were moderate in eight chronic patients treated with the NeuroRegen Scaffold with UC-MSCs (e.g., no change in ASIA classification, but some improved autonomic functions and motor evoked potentials),(62) two acute patients had significant functional voluntary motor improvements after 12 months.(63) Increased numbers of patients in the trial and proper controls in later phases are needed to confirm these promising initial results. Finally, the last trial is investigating the same collagen scaffold combined with ES (ClinicalTrials.gov Identifiers: NCT03966794).

Outside of clinical trials, several other combinations of biomaterials with cells and/or with drugs/biologics have been investigated, and are covered in several reviews, of which we particularly recommend those by Katoh *et al,*(64) Wang *et al*,(60) and Ham and Leipzig.(65) For example, genetically modified cells, nano-sized, and micro-sized biomaterials have all been utilized for extended release of a conjugated drug or biologic. However, even with extended

release, nanocarriers (e.g., carbon nanotubes (CNTs), polymeric nanoparticles) still have translational limitations similar to delivering drugs and biologics alone in terms of needing further characterization of clearance, getting past the BSCB, the large initial release of drugs on or near the surface, and/or attaining high payloads within the nanocarriers. Therefore, combinations of encapsulating drug-loaded nanocarriers within macro-scale biomaterials (e.g., particles or fibers in hydrogels or electrospun scaffolds) have been investigated to achieve local delivery, sustained release, and mitigation of the burst effect, as reviewed by Song *et al.*(53)

In addition to acting as a carrier for cells, drugs, and biologics, some biomaterials have a 3D structure that has been engineered for guided axon growth *in vitro* and *in vivo* (e.g., aligned nanofibers, hollow channels, patterned nanotubes). Specifically, aligned nanofibers have been shown to increase *in vitro* neurite outgrowth and orientation in the direction of nanofibers more than randomly aligned fibers.(53) Additionally, aligned nanofibers have been fabricated into 3D tubular shapes by rolling electrospun films into multi-layered tubes,(66) or dispersing aligned fibers in hydrogels(67) or made into composite guidance channels(68) for *in vivo* studies. Besides architectures, incorporating CNTs into hydrogels (e.g., Matrigel®, chitosan, polyethylene glycol-diacrylate (PEG-DA)) has shown greater *in vitro* neural cell adhesion and neurite outgrowth than the material alone and aligned CNTs have shown greater *in vitro* cell alignment than randomly orientated CNTs.(53)

Although several of the translational limitations that are associated with cell therapies, drugs, biologics, and biomaterials have been overcome, there are still additional translational limitations that need to be addressed before widespread utilization in clinical studies can be expected. Preformed conduits and fibers may be easy to trim and surgically implant into a gap created by the transected or hemi-section SCI model; however, surgically implanting a preformed scaffold into human SCIs, most of which are contusion or compression-type injuries is more challenging. Preformed scaffolds would need to be trimmed and shaped to fit within the cyst-like injury in the operating room, or need to be fabricated in the shape of the defect, which may not be able to be determined at a sufficient resolution via current imaging techniques. Alternatively, glial scar tissue in the spinal cord would need to be removed to create a gap (although occasionally a transection-type injury and gap may exist)(69). As we mentioned earlier, removal of spinal cord tissue to implant preformed biomaterials during the acute stage has a higher risk that may compromise spontaneous recovery. In contrast, implanting preformed biomaterials during the chronic stage, after spontaneous recovery plateaus, is less risky because spontaneous recovery is not compromised, although introducing additional damage to the cord by removing tissue still has inherent risks. Injectable biomaterials are less invasive and less risky, which may be more translational for contusion SCIs. Any preformed scaffold would need to be highly deformable to be injectable (e.g.,

shape memory polymers,(70) cryogels(71)), but hydrogel precursors could be injected into an injury prior to gelation.

Several reviews(33, 72-75) and other original research(76-79) have discussed the need for hydrogel precursors to be injectable for better clinical translation. To be injectable, precursor solutions would ideally be low-viscosity and/or shear-thinning. For other characterizations of precursor rheology, see our recent review in Townsend *et al.*(80) Although liquid hydrogel precursors may be capable of conforming and forming *in situ* inside the injury cavity, these liquids may be difficult to surgically place in a bleeding, fluid-filled environment. To overcome the placement and fitting challenges, a shear-thinning viscous or paste-like hydrogel precursor would be able to be surgically placed while still conforming to an injury of any shape. As we have previously investigated with hyaluronic acid-based(81, 82) and cartilage matrix-based hydrogels,(83) shear thinning paste-like precursors can be injected and enable easy surgical placement in irregularly-shaped defects.(80) While a paste-like hydrogel precursor may be easier to surgically deliver for cartilage defects where a surgeon could inject the paste-like biomaterial into the defect and press-fit the material to conform into the defect, an injured spinal cord in the late subacute/chronic stage in contrast may be more of an enclosed fluid-filled cyst rather than an open cavity, and injection of a viscous precursor to fill the space without leaking away may be more appropriate.

In summary, biomaterials have been developed for delivering cell therapies, drugs, and biologics to overcome translational limitations of each, and the added benefits of the tunable 3D architecture has been further engineered to guide neurite outgrowth. While preformed scaffolds may be more difficult to apply to the most common contusion SCIs due to necessary shaping in the operating room, injectable and viscous biomaterials that could fill and conform to the shape of a contusion SCI may be less invasive and more clinically translatable.

Current therapeutic approaches: rehabilitation

Given that even the most severely injured patients usually retain some axonal pathways and sensorimotor circuits in the spinal cord below the injury, most will go through activity-based rehabilitation therapies to promote reorganization of neural pathways, but motor training alone typically does not enable patients to produce movements voluntarily. To augment motor training, clinical research has investigated two methods to increase the excitability of spared axons and/or intact spinal circuits: 1) ES and 2) pharmacological stimulation. One of the proposed mechanisms of stimulation is that the increased excitability makes it easier for motor and sensory inputs to reach the action potential threshold of neurons, resulting in subsequent firing and continuation of the signal. Repetitive usage of a neural pathway encourages synaptic formation and maintenance, and thus re-organization through spared tracts, interneurons, motor neurons, and neural circuits which can improve voluntary function. The use of ES for SCI is a vast field, which is summarized in an excellent recent review

by Shah and Lavrov.(84) For an overview of other stimulation techniques in a broader review of SCI, we refer readers to Hutson and Di Giovanni.(4)

Electrical stimulation

ES can be delivered at various locations to stimulate different parts of the spinal cord. Electrical epidural stimulation (EES) is investigated the most, and typically uses surgically implanted electrode patches on the spinal dura to directly deliver ES to the dorsal spinal cord right below the injury. However, non-invasive stimulation techniques are being developed as alternatives. These include transcutaneous stimulation, where electrodes are placed over the skin and injury site, and transcranial magnetic stimulation, which uses an electric current in a coil to generate a magnetic field that stimulates the brain and descending tracts to the SCI. Given the extensive field of ES for SCI, we briefly discuss ES in rats and cats, the challenges of translation to humans, and provide a few illustrative and recent clinical studies that have achieved encouraging clinical functional recovery to date.

Rehabilitation approaches in rats and cats with incomplete SCIs can induce stepping that is most likely due to promoting neural plasticity/reorganization in spared tissue and/or activating intact spinal locomotor circuits. However, in transected rats and cats with no spared tissue, it is thought the stepping motions that can be elicited by rehabilitation approaches are due to activation of the intact spinal circuits. In cats with complete spinal transections (no brain input), it is well known that locomotor training, ES, pharmacological

stimulation, or various combinations can produce step-like motions.(85) Similarly, rats with complete spinal transections can achieve step-like motions with ES and/or pharmacological stimulation but stimulation without motor training resulted in stepping that was not full-weight bearing, and rats tended to drag their feet and produced uncoordinated, inconsistent stepping. With ES, pharmacological stimulation, and locomotor training, full weight-bearing locomotion and stepping motions indistinguishable from voluntary stepping have been achieved in rats.(86) While rodents may not need the motor cortex for locomotion, humans may have a higher dependence on supraspinal input during locomotion, such as for balance, and translation of such rehabilitation approaches has been slower to humans. EES alone has enabled human patients with complete injuries (i.e., AIS grade A) to produce volitional movement, but not independent stepping so far.(87) As reviewed by Shah *et al,*(84) there are several EES parameters being investigated to improve recovery of a stepping motion. These parameters include multisite vs. single-site stimulation with electrode arrays, locations of stimulation (lumbosacral), frequencies, pulse intervals, and relative timing of stimulation pulses in different segments.

Similar to rats, combining motor training and ES has had encouraging functional recovery in terms of enabling over-ground independent stepping (with assistive devices). In one study, patients were treated with intensive motor training at the same time as task-specific spatiotemporally-controlled EES programs, which stimulated different areas of an electrode array in different

sequences at specific intervals.(88) The results were that the use of specific spatiotemporal activation patterns enabled over-ground walking with assistive devices ~15-85 weeks after electrode implantation in two patients with incomplete injuries (i.e., AIS grade B).(88) However, for two other patients with complete injuries (i.e., AIS grade A), over-ground walking was not achieved, and instead only stepping with body-weight support on a treadmill was achieved.(88) None of the four participants could step at all without the EES turned on.

Another more recent study employed spatiotemporally-controlled EES with motor training for three patients. Two patients had incomplete injuries, and they experienced improved over-ground walking with EES turned on after only a week of training, and then had neurological recovery after only a few months of training to the point where they had improved over-ground walking with assistive devices without the EES on.(89) For the patient with the complete injury, over-ground walking with a walker was achieved only when the EES was on. While the patient with the complete injury could not walk with the EES off, they could fully extend their legs against gravity, which they were not able to do prior to starting the treatment. A third study with a patient with a complete injury yielded similar task-specific EES-enabled independent over-ground stepping (with assistance) after 43 weeks of the EES combined with motor training.(90)

Although these clinical studies offer promising results, the authors noted a limited number of patients were treated to determine feasibility, and larger studies and controls will be needed to demonstrate efficacy. Several clinical studies

involving EES with or without motor training are ongoing, but there are additional considerations (i.e., the timing and sequence of interventions, determining the subsets of patients that benefit the most) that are discussed further in a review of rehabilitation and ES for SCI and traumatic brain injury (TBI) by Hofer and Schwab.(91) The promising outcomes in complete patients are thought to be due to the activation of intact spinal networks for locomotion, and these methods may be a short-term approach to recover locomotion; however, tissue regeneration may still be necessary for full recovery of functions beyond locomotion until the spinal networks in humans are better understood and able to be leveraged for enhanced recovery.

While EES is the most widely studied method of ES, there are disadvantages and limitations, such as the invasive electrode implantation into the spinal dura. Given that implanted electrodes can cause tissue damage and gliosis around the electrode, and can therefore reduce the ability of the electrode to stimulate the tissue,(4) non-invasive stimulation has been investigated. Two types of non-invasive stimulation are transcutaneous and transcranial stimulation. Transcutaneous stimulation involves electrodes placed on the skin over the spine at the level of the injury, instead of surgical implantation on the spinal dura with EES. Benefits of transcutaneous stimulation include that it is noninvasive, inexpensive, and readily available, and therefore very low risk. However, transcutaneous stimulation does not offer the precise control over location and timing of stimulation of specific muscle groups available with EES.

The efficacy of transcutaneous stimulation is inconclusive and still needs to be demonstrated in larger clinical trials,(92) and indeed there are several ongoing clinical trials.

Another noninvasive approach is brain stimulation via transcranial direct current stimulation or magnetic stimulation, which can induce a current and stimulate spared descending pathways using an electric current in an external handheld coil that generates a magnetic field. With repetitive task training, transcranial stimulation has been shown in small case studies to facilitate activity-dependent voluntary motor function, particularly with fine motor hand function.(4, 20) In other studies, however, effects of transcranial stimulation have been found to be small or inconclusive.(93, 94) Several clinical trials attempting to demonstrate clear treatment benefits are ongoing.

The field of ES treatments used for SCI is vast, and recent clinical advancements in the use of spatiotemporally controlled EES simultaneously with motor training has shown significant promise to promote functional recovery of independent stepping with assistive devices. Larger studies are needed to confirm efficacy, and the parameter space must be fine-tuned in clinical studies to further enhance efficacy. Rehabilitation approaches may primarily promote reorganization through spared tissue in incomplete patients and activation of intact spinal circuits below the lesion in complete patients to enable locomotion. However, activation and control of spinal networks with sensory input to generate locomotion may be a more immediate approach to recover locomotion, but tissue

regeneration may still be necessary for full recovery. In addition, limitations with the implanted electrodes will need to be addressed in the future for EES. While noninvasive methods exist, such as transcutaneous stimulation and transcranial stimulation, they have less direct control over the site of stimulation and the efficacy shown so far has been limited.

Pharmacological stimulation

Stimulation can be achieved through pharmacological approaches as an alternative or in addition to electrical stimulation. Several pharmacological stimulants are FDA approved and have been widely employed to treat various neurological disorders, which enables easier translation to SCI. Neurotransmission is critical for controlling neural signaling in the spinal cord, and the use of pharmacological stimulation with EES aims to promote long-distance re-growth of axons in clinical trials for SCI. Pharmacological stimulation studies are limited to delivering monoaminergic molecules, and further limited to only those molecules that modulate neurotransmitters. For example, 5-hydroxytryptophan (5-HTP) is the precursor to serotonin, which is known to stimulate serotonergic receptors, and has resulted in increased hindlimb activity in rat contusion models of SCI.(95, 96) As such, a phase II/III clinical trial for 5-HTP (along with levodopa (L-DOPA), the precursor to dopamine) is ongoing (ClinicalTrials.gov Identifier: NCT04000919). Pharmacological stimulation with monoaminergic drugs has been explored in combination with EES. For example, a few rodent studies have demonstrated better stepping quality with the

combination of pharmacological stimulation and EES compared to animals treated with only one modality.(84, 97) The improved performance associated with combined EES and pharmacological stimulation justifies the ongoing clinical trials that are investigating pharmacological drugs paired with gait training. For example, a serotonin re-uptake blocker, Lexapro (escitalopram), and a serotonin agonist, buspirone (ClinicalTrials.gov Identifiers: NCT01753882, NCT04105114) are being investigated with gait training. Given the wide use of pharmacological stimulation in other neural diseases, the translation to SCI may be easier than other more complex methods of delivery for regenerative medicine approaches; however, systemic delivery of monoaminergic drugs may have potential off-target effects. Furthermore, the efficacy thus far has been limited and future investigations are needed to demonstrate the safety and efficacy of pharmacological stimulation with gait training.

In current clinical trials, pharmacological stimulation has been applied in combination with gait training, and could similarly be combined with regenerative medicine approaches for SCI. As a form of stimulation that could enhance neuroplasticity, delivery of monoaminergic drugs could be a less invasive method than EES, which may translate better or combine well with regenerative medicine approaches in the future. However, outcomes of current clinical trials and future human trials will be needed to demonstrate the safety and efficacy.

Conductive biomaterials: linking regenerative medicine and rehabilitation approaches

Individually, regenerative medicine and rehabilitation approaches have yet to effectively promote locomotor recovery for SCI patients. The most successful examples of locomotor recovery in human clinical studies have arguably been from combinations of motor training with EES, which are both rehabilitation approaches; however, larger clinical trials are needed to confirm the extent of efficacy. Despite the encouraging clinical results, patients with more severe injuries have not yet benefitted as much as patients with incomplete injuries from rehabilitation approaches alone. As others have noted,(2-4) functional recovery from SCI may be improved by combining regenerative medicine and rehabilitation. Regenerative medicine approaches aim to modulate the inhibitory environment and promote axonal regeneration, and rehabilitation approaches aim to stimulate regenerated tissues and promote reorganization of neural pathways. There are only a few ongoing clinical trials for combined therapeutic approaches: a collagen scaffold with EES, and umbilical cord blood-mononuclear cells with lithium carbonate and locomotor training (ClinicalTrials.gov Identifiers: NCT03966794, NCT03979742). Similarly, there are few *in vivo* studies combining rehabilitation approaches and regenerative medicine approaches. One study by Lin *et al.*(8) demonstrated better *in vivo* motor recovery in rats when treated with a combination of an NT-3 loaded poly(ε-caprolactone-co-ethyl ethylene

phosphate) (PCLEEP) scaffold with rehabilitation, compared to rats treated with only the scaffold (no rehabilitation).

The overarching problem of rehabilitation approaches, including ES, is the reliance on spared connections that patients with more severe injuries may lack, and therefore severely injured patients benefit less from rehabilitation. Regenerative medicine may be able to facilitate regeneration of neural pathways for rehabilitation approaches to elicit their effects on. In translation of combined regenerative rehabilitation treatments, several rehabilitation approaches are already in clinical trials.

The pragmatic problem now is translating the regenerative medicine approaches of cells, drugs, biologics, and biomaterials for clinical use that complement rehabilitation approaches. Conductive biomaterials can link rehabilitation and regenerative medicine approaches by providing a medium for ES delivery to cells in addition to providing a platform for delivery of regenerative medicine approaches (e.g., cells, drugs, biologics) and/or pharmacological stimulants (see **Fig. 2.1**). The intrinsic structure of a neuron is designed to pass electrochemical signals, so it is not surprising that neurons and neural progenitors respond to ES in terms of proliferation, differentiation, and migration.(98) Conductive biomaterials have been thought to benefit SCI as a scaffold to bridge the lesion and provide immediate connectivity; however, there are variable *in vitro* results of the effects of conductive biomaterials alone.(10-12, 14) The synergy between conductive biomaterials coupled with ES has clearly been established

in vitro through improved neurite growth beyond what each approach can do alone.

Given that many cell types respond to ES (e.g., fibroblasts, myoblasts, osteoblasts),(23) several types of conductive materials have been developed and investigated for a variety of applications, including nerve regeneration in general, spinal cord regeneration in particular, and additionally biosensors, drug delivery, and tissue engineering of cardiac and muscle tissues. There are three categories of conductive biomaterials: 1) conductive polymers, 2) carbon-based materials, and 3) metallic particle-based materials, and additionally there are combinations of each. In the following sub-sections, we discuss the fabrication methods used for each category of conductive biomaterial along with the associated translational advantages and disadvantages in the context of treating spinal cord injury.

Methods for fabricating conductive composites

As others have reviewed, the most commonly discussed methods of fabricating of conductive composites are 1) coating,(22) 2) *in situ* processes,(22, 23, 99, 100) and most commonly, 3) blending.(22, 23, 99, 100) Coating methods usually involve coating the surface of a preformed non-conductive scaffold with the conductive component (e.g., covalent attachment, immersion/drying, spin-coating). In the specific case of composites with conductive polymers, the polymer can be coated on a non-conductive scaffold through polymerization of the monomer directly onto the surface of the scaffold through electrochemical

deposition.(101) Electrochemical deposition typically involves application of an electric potential to oxidize a bulk solution of monomer and electrolyte, which results in polymerization onto the electrode in a thin film; however, the deposition can alternatively be onto the surface of a material.

In situ processes are methods of forming conductive components (e.g., metal particle formation, polymerization to form conductive polymers) within other non-conductive scaffolds. For conductive polymers, *in situ* polymerization utilizes methods that are similar to chemical synthesis methods for conductive polymers, where a strong oxidizing or reducing agent is added to a bulk solution of a monomer to cause polymerization. *In situ* polymerization is typically a two-step process. First, a preformed non-conductive scaffold is saturated with the monomer of the conductive polymer. Second, an oxidizing or reducing agent is then added to initiate polymerization of the conductive polymer within the preformed scaffold. Similar to the two-step process of *in situ* polymerization, *in situ* formation of metal nanoparticles involves saturation of a preformed non-conductive scaffold, except with metal ions, followed by addition of a reducing agent to form nanoparticles within the scaffold.(102) Another two-step *in situ* formation method is to reduce the metal ions with a non-conductive polymer followed by scaffold formation of the non-conductive polymer.(103, 104) Less commonly, *in situ* polymerization has been accomplished via polymerization of the monomer to surround other nanoparticles.(99, 105) More recently, one-step processes for *in situ* polymerization have been developed, whereby the monomer

of the conductive polymer was polymerized at the same time as non-covalent gelation of another polymer (i.e., semi-interpenetrating network (IPN)),(106) or whereby the conductive monomer was used to crosslink monomer-functionalized polymers (i.e., covalent semi-IPN).(107)

The blending method is the most utilized of the three methods, and involves mixing of preformed conductive components (i.e., macro-, micro-, nano-sized particles) with precursors of other non-conductive materials, followed by fabrication of the blended precursor through conventional methods (e.g., electrospinning, freeze-dried casting, hydrogel crosslinking). All three types of conductive materials (i.e., polymers, carbon-based, and metal-based) have been used with the blending method to make conductive composites. The conductivity of composites with conductive particles and an insulating polymer matrix are well described by percolation theory,(21) where at a critical volume of conductive filler (i.e., the percolation threshold) the conductivity increases by several orders of magnitude. Below the threshold, the electrical properties of the composite are dominated by the insulating matrix because electron paths are not formed, and above the threshold there is little effect on the conductivity with increasing concentration of the conductive component.

Given that the addition of filler usually makes polymers stiffer and more brittle, different materials, sizes, and shapes of filler have been investigated to decrease the percolation threshold and reduce the amount of filler needed to attain a conductive network. Smaller particles (e.g., nanoparticles) have lower

thresholds than larger particles (e.g., microparticles), and therefore several types of nanoparticles have been developed to make conductive composites for a wide variety of applications that include tissue engineering and regenerative medicine. Furthermore, particles with higher aspect ratios have lower percolation thresholds than spherical particles, leading to several composites being made with nanotubes or nanowires. Spherical particles require shorter interparticle distances and thus higher concentrations to maintain a conductive network, but high-aspect ratio particles can maintain contact with greater interparticle distances to form a conductive network with lower concentrations.

Each fabrication method has advantages and disadvantages. First, coating processes are simple and effective to impart conductivity to a non-conductive scaffold. However, as noted in the review on conductive hydrogels by Min *et al,*(22) the independent layers of the conductive coating and scaffold could lead to cracking and delamination if there is not sufficient interaction and bonding between the layers. Second, those authors further discussed that *in situ* processes resulted in homogeneous distributions of the conductive component throughout the scaffold, which could improve conductivity and mechanical performance. The discussed disadvantage was that these *in situ* methods could be more complex than the other fabrication methods, in part by consisting of multiple steps. Third, the blending method is a simple and widely adaptable process that can be used with various conductive fillers (e.g., conductive polymer particles, carbon-based particles, metal particles). A homogeneous distribution of

the conductive material is important for creating a conductive network without compromising mechanical performance, but homogenous distributions of nanoparticles can be difficult to achieve, as nanoparticles can aggregate quickly and irreversibly. Additionally, from the small size of nanoparticles, the blending method requires high concentrations of nanoparticles to reach the critical volumes of filler to form conductive networks.

Given that the coating method takes place after the formation of a non-conductive scaffold, conductive composites fabricated via this method are therefore not conducive to injectable delivery systems and by definition must be in a preformed solid form for implantation. The same is true for *in situ* polymerization methods that follow a conventional two-step process, which necessitate the creation of a preformed scaffold. The problem is that preformed scaffolds may not conform to the shape of contusion or cyst-like SCIs, and the scaffold may require trimming to fit within the injury or the spinal cord tissue may need to be surgically removed to enable the scaffold to fit. Overall, preformed scaffolds are less translational than composites that could be injected and form within the injury. For application in SCI, the most translational methods of forming composites are the one-step *in situ* processes or the blending method of high aspect ratio nanomaterials with a material capable of conforming to the shape and size of the injury.

Conductive polymers

Conductive polymers have traditionally been used in a wide range of applications in society including capacitors, flexible electronics, and organic light emitting diodes (OLEDs), but the lack of solubility in water, rigid mechanical performance, and poor processability after polymerization have limited the uses for biomedical applications. As such, conductive polymer composites have been developed to overcome some of these limitations by improving solubility and degradation, and thereby forming 3D scaffolds for biosensors, drug release systems, neural interfaces, and tissue engineering (e.g., bone, cardiac, nerve, muscle). For more comprehensive reviews on conductive polymers, there are multiple outstanding reviews that we recommend.(21-24, 100, 108-110) Conductive polymers typically have alternating single and double bonds that result in overlapping π-orbitals, or a conjugated π-system, which then allows electrons to be mobile along the polymer chain. However, these conductive polymers by themselves are not highly conductive relative to the broader materials spectrum (see **Fig. 2.2**), with conductivities in a range similar to insulators to semiconductors.(108, 111) Therefore, to improve conductivity, doping such polymers through oxidation (p-doping) or reduction (n-doping) with counterions provides charge carriers and can increase polymer conductivities into a range more on the order of semiconductors to metals. The most commonly known conductive polymers in order from the most common to the least common for biomedical applications are polypyrrole (PPy), polyaniline (PANI),

polythiophene (PT), a derivative of PT called poly(3,4-ethylenedioxythiophene) (PEDOT), and poly(p-phenylene vinylene) (PPV). The composites of each conductive polymer that have been investigated for biomedical applications, and specifically on nerve regeneration, are shown in **Table 2.5**.

PPy is the most commonly investigated conductive polymer for SCI because of the high conductivity (up to 10^3 S/cm,(100) see **Fig. 2.2**), ease of synthesis, and ease of biomolecule incorporation.(21, 111) PPy composites have been formed by *in situ* polymerization,(112-116) coating,(101, 117) and blended polymer nanoparticles into films(118-120) or scaffolds.(121, 122) Only a few studies have used PPy in SCI animal models. For example, a few studies synthesized electrospun films made of blends of PPy particles with PLA, rolled up the films into tubes, and implanted them in rat transection SCI models.(118, 119) Another study used a PPy hydrogel patch that was crosslinked with tannic acid and then implanted into a rat hemi-section SCI model.(123) While motor functional recovery in rats was better with PPy materials than sham controls, rats did not fully recover complete motor function.

Conductive polymer films that are rolled into tube shapes are useful for peripheral nerve regeneration and perhaps for the niche group of patients with transection SCIs; however, the pre-defined shape may be a limiting factor in translating to the treatment of contusion SCIs. Tube-shaped scaffolds may not be able to conform well to the injury borders or may require resection of some spinal cord tissue and fixation to the cord (e.g., suturing), where the latter would

be highly invasive and might only be feasible for patients with chronic injuries. Development of PPy hydrogel blends that consist of PPy crosslinked with other molecules,(123) or are non-conductive polymers conjugated to pyrrole and crosslinked via pyrrole polymerization,(107, 124) have been more promising in terms of clinical translation. However, these formulations still require prefabrication because crosslinking conditions are not biocompatible (e.g., use of oxidative initiator such as iron(III) chloride, which is toxic). A one-step self-assembly between polymers (i.e., polypyrrole and sodium alginate)(106) has more clinical translatability, but these have yet to be used for SCI either *in vitro* or *in vivo*.

After PPy, PANI is the second most investigated conducting polymer and is a polymer of aniline that exists in three oxidation states (i.e., fully oxidized pernigraniline base, half-oxidized emeraldine base, and fully reduced leucoemeraldine base).(100) PANI in the emeraldine form has good conductivity (up to $2x10^2$ S/cm,(100) see **Fig. 2.2**), low cost, good stability, ability to switch between the conductive and resistive state, and potential antimicrobial and antioxidant activity.(99, 100) PANI by itself is non-toxic; however, the biocompatibility of different PANI composites depends on the composition, size and shape of nanoparticles, dopants, and preparation. The biocompatibility is decreased by low molecular weight compounds from the reaction byproducts and acids that form the PANI salts.(99) Similar to PPy, the poor processability and biodegradability have limited the biological applications. The majority of PANI

composites have been made into films using *in situ* polymerization(125-127) or blending PANI nanoparticles into film precursors.(128, 129) PANI films have been used for *in vitro* studies or for peripheral nerve regeneration *in vivo*, but not yet for SCI *in vivo*. 3D scaffolds are needed for SCI and recent *in vitro* studies made strides in developing composite PANI hydrogels that formed a 3D network with a variety of methods. For example, PANI hydrogels were made by crosslinking PANI with phytic acid,(105) or by blending PANI nanofibers and chitosan.(130) PANI oligomers have been grafted to natural polymers that were subsequently crosslinked into scaffolds,(131-133) or aniline was blended with a synthetic polymer followed by *in situ* polymerization and formation of a sponge-like cryogel.(127) Given that several of the three-dimensional scaffolds of PANI composites have non-biocompatible synthesis conditions, the scaffolds require prefabrication before implantation, such as the scaffold that have been coated with PANI.(134, 135) However, blends of PANI materials or grafted PANI oligomers with scaffolds that form under biocompatible conditions (e.g., gelatin)(131) and/or are injectable could be a promising approach to impart conductivity in established non-conductive biomaterials to create more clinically translatable options.

Aside from the most commonly investigated PPy and PANI, newer conducting polymers, such as PT and PT derivatives, have been explored because of their similar electrical properties to PPy. PT films have been developed and used for biosensors and flexible electronics,(136) but are not

widely used in regenerative medicine. On the other hand, PEDOT, a derivative of PT, has high conductivity (up to 400 S/cm(100) or 1000 S/cm,(137) see **Fig. 2.2**), better chemical stability than PT, and is transparent. PEDOT has gained considerable attention in biomedical engineering because the monomer is soluble in water, which makes blending with different materials in aqueous conditions easier. PEDOT is commonly doped with poly(4-styrenesulfonate) (PSS) and the resulting PEDOT:PSS combination is commercially available as a colloidal suspension; however, the downside is the need for additives (e.g., ethylene glycol) or post-processing (e.g., thermal annealing) to improve conductivity and stability in water for biomedical applications.(138) There are efforts to improve the solubility and conductivity of PEDOT without the need for additives by synthesizing monomer derivatives that self-dope.(137)

Films of PEDOT have been synthesized via *in situ* polymerization,(139, 140) but to form a 3D scaffold and treat a transection SCI in rats, one study coated carbon microfibers with PEDOT:PSS-co-maleic acid, and then rolled up 30 of these coated microfibers in an alginate membrane.(141) Functional recovery was not assessed, but the functionalized PEDOT scaffold resulted in enhanced blood vessel formation and axonal regeneration, no increase in inflammation, and reduced scarring. Most PEDOT composites that have been employed *in vitro* for application to nerve regeneration have been fabricated via the blending process.(141-145) PPy and PANI have water-insoluble monomers and polymers, therefore, the aqueous colloidal suspension of PEDOT:PSS is

easier to blend with other materials in aqueous conditions in comparison to PPy and PANI.

Another method to fabricate PEDOT composites for *in vitro* studies was a method similar to two-step *in situ* polymerization, except the PEDOT scaffold was synthesized first via copper ion gelation, followed by swelling in of the non-conductive polymer and polymerization to form an IPN.(146) Regardless of whether PEDOT:PSS composites were fabricated via an IPN, the coating method,(11, 147) or blending, in each case these methods required the scaffolds to be preformed, which has limited translatability to contusion SCIs. Despite the use of preformed PEDOT:PSS composites, the most significant advantage of PEDOT:PSS over other conductive polymers is the improved solubility. The improved solubility of PEDOT:PSS has resulted in the bioprinting community developing composites of PEDOT:PSS together with other materials that have biocompatible gelation processes for extrusion (e.g., methacrylated gelatin (GelMA)),(143) ink-jet,(138) and stereolithography (SLA) bioprinting (e.g., PEG-DA).(148, 149) In the future, the regenerative medicine field in general, and for SCI in particular, may benefit from applying some of the bioprintable PEDOT:PSS composites that could be more clinically translatable.

Similar to PEDOT:PSS, PPV is a newer polymer with water-soluble monomers; however, without doping, it is considered an insulator. There have been older studies investigating different dopants to improve the conductivity of PPV (up to 10 S/cm with AsF_5 and 100 S/cm with H_2SO_4)(150) and more recent

studies with aloin and $FeCl_3$ (up to 10^{-4} S/cm, see **Fig. 2.2**).(12) There is a paucity of PPV studies for tissue engineering applications and nerve regeneration thus far. In one *in vitro* study, poly[2-methoxy-5-(2-ethyl-hexyloxy)1,4-phenylene vinylene] (MEH-PPV) and polycaprolactone (PCL) were blended and electrospun into films that supported neural cell viability the same as tissue culture plastic.(12) The MEH-PPV:PCL meshes were electrically stimulated and neural cells had enhanced neurite formation compared to non-stimulated controls. In another study, a PPV composite hydrogel was developed with polyacrylamide for controlled drug release.(151) While the PPV hydrogel was not specifically for nerve regeneration, the methods of grinding a PPV film into a powder for blending could be applied and incorporated into other polymers with biocompatible formation conditions for application to SCI. PPV has been minimally applied to regenerative medicine and has not been applied to SCI yet, but one of the limiting factors of all conductive polymers is the low conductivity when blended (see **Fig. 2.2)**. To improve the conductivity, other conductive polymers have been combined with carbon-based materials,(152-156) or metallic particles.(157, 158) If the low conductivity can be improved, the water-soluble polymer may enable future development of blends with PPV into more clinically translational materials for SCI.

In summary, several conductive polymers have been developed and tested *in vitro* with promising neurite outgrowth, especially when coupled with ES; however, only a handful of *in vivo* SCI studies with conductive polymers exist. Of

the few *in vivo* studies with conductive polymers, the functional recovery of rats treated with conductive polymers has been better than shams but has not yet resulted in full functional recovery. For translation of conductive polymers for SCI in the future, the most promising fabrication method is the blending method to incorporate the conductive polymers into injectable materials that can form within the injury. The bioprinting field has developed several 'bioink' formulations of biomaterial precursors containing PEDOT:PSS, which are injectable and form after printing under biocompatible conditions. The formulations that can serve as bioinks for extrusion-based bioprinting can additionally serve as injectable materials for regenerative medicine applications.(80) In the future, it may be beneficial for the regenerative medicine and SCI field to adapt bioprintable materials for contusion SCIs. Using the blending method, several of the conductive polymers could be integrated with injectable materials that can form in the injury, but the most promising conductive polymers that have been developed and tested *in vitro* are polymer-grafted PANI oligomers and the water soluble, PEDOT:PSS polymer, both of which could be enable future development of conductive polymer blends for application to SCI.

Carbon-based materials

Carbon-based materials include graphene, graphene oxide (GO), and CNTs and have been explored for nerve regeneration because they are highly conductive (10^3 to 10^4 S/cm, see **Fig. 2.2**) and have large surface areas for functionalizing biomolecules and modulating cell responses. We refer readers to

several reviews for additional information about graphene-based composites for biomedical applications,(159) stem cells,(160) in SCI,(161) and about biofunctionalized CNTs(162) and CNTs in the central nervous system (CNS).(163) In this section, we cover GO, CNTs, and the blends of each that have been used to fabricate conductive biomaterials for nerve repair, along with their translational advantages and disadvantages (see **Table 2.6**).

Graphene is a single 2D sheet of sp^2-hybridized graphite, and graphene-based materials come as a colloidal suspension of sheets (0.5 to 5 nm thick, 10 nm to 5 μm lateral size).(159) Graphene has been shown to be biocompatible as an immobilized surface for neural cell growth(164) and able to promote greater differentiation when coated in laminin compared to control surfaces.(165) Even so, the hydrophobicity and aggregation of graphene have limited the biological applications, and therefore pristine graphene is rarely used. On the other hand, the oxidized state of graphene, GO, contains several hydroxyl groups that increase the hydrophilicity, decrease aggregation, and increase the ability to adsorb biomolecules, but unfortunately decrease the conductivity. Reduction of GO via thermal, chemical, or electrical treatments produces reduced GO (rGO), with fewer hydroxyl groups, thereby achieving conductivities closer to pristine graphene.

To make 3D scaffolds to treat SCI *in vivo*, rGO-only scaffolds have been formed via freeze-drying,(166, 167) thermal crosslinking,(168) or both with additional exposure to chemical vapors.(169) All the implanted scaffolds were

preformed, as opposed to injectable delivery with *in situ* polymerization, due to the scaffold formation conditions being non-biocompatible. Functional recovery was not evaluated in any of these SCI studies to date, but these studies did report positive outcomes such as new microvasculature, evidence of myelination, reduced gliosis, and reduced inflammation. Blends of other materials with GO and rGO have been fabricated to improve mechanical performance and for easier functionalization during *in vitro* and *in vivo* SCI studies. During a few *in vitro* studies, the coating method was used to coat GO on electrospun polymers and evaluated with neural cells(170) or oligodendrocytes,(171) but the formed 2D scaffolds may be less translational for SCI.

3D scaffolds for *in vivo* studies have been made, but similar to *in vivo* studies with graphene, the non-biocompatible formation conditions made prefabrication necessary for all scaffolds implanted in rat SCI models. In one example, blended PLGA/GO nanofiber mats were electrospun and functionalized with growth factors before being implanted in a rat SCI model. This approach resulted in better functional recovery, reduced cavity formation, and more neurons compared to PLGA alone.(172) In another study, scaffolds were preformed by embedding rGO microfibers in gelatin and crosslinking in paraformaldehyde for 7 days before implantation in a rat SCI model. The rGO/gelatin scaffold resulted in new microvasculature and decreased gliosis, but there was no evaluation of functional recovery.(173) Further *in vivo* studies are needed to evaluate functional recovery associated with rGO-based scaffolds. In

terms of clinical translation, all preformed scaffolds were implanted because the crosslinking methods for GO and rGO scaffolds are not biologically compatible, but future methods that are more translational could involve blending GO or rGO into materials that can undergo gelation in the injury and conform to the size and shape of the injury.

In contrast to graphene and GO, CNTs are sheets of graphite rolled into a cylinder as single-walled (SWCNTs) or multi-walled CNTs (MWCNTs) with enormous aspect ratios. These high aspect ratios are due to CNTs being hundreds of nanometers to microns in length and only 1-3 nm or 10-200 nm in diameter for SW- and MWCNTs, respectively. CNTs have been used in biomedical applications because of the high aspect ratio, high conductivity (up to 10^5 S/cm),(22) ease of functionalization to deliver therapeutics, and improved mechanical performance when combined in composites. The biggest disadvantages of CNTs are the insolubility in water and the aggregation, which causes cytotoxicity. In the CNS, CNTs can cause inflammation, reactive oxygen species overproduction, and mitochondrial dysfunction.(163)

Despite the cytotoxicity, CNTs are still widely used in biomedical and neural applications because the large surface area can easily be functionalized to 1) deliver high loads of biomolecules compared to other nanoparticle delivery systems and 2) improve hydrophilicity, dispersion, biocompatibility, and the ability to form composite materials. CNTs have been employed *in vitro* with some degree of success. In one example, functionalized CNTs were evaluated as a

surface coating to improve neuronal adhesion,(174) and in another example, CNTs were delivered to cells as a suspension, which resulted in better delivery of NGF that promoted cell differentiation and growth.(175) However, delivery of CNT suspensions *in vivo* resulted in modest functional recovery in a rat SCI model.(176)

3D scaffolds of CNTs and CNT composites have been developed mostly for peripheral nerve applications but have non-biocompatible synthesis conditions, which require prefabrication and limit translation for treating SCI. For example, methods that are often non-biocompatible include chemical vapor deposition,(177) coating methods,(178, 179) electrospinning,(15, 180-182) oven drying,(183) UV crosslinking for extended amounts of time,(16) coagulation in ethanol,(184) freeze drying,(185-187) electrodeposition,(188) and Matrigel®.(13) For application to SCI, CNT composites formed via the blending method with biocompatible formation conditions may be more translational. Examples of CNT composites with biocompatible formation conditions include UV-crosslinked polyacrylamide/thiolated PEG (PEG-SH) hydrogel,(14) crosslinkable PEG-DA hydrogel,(189) UV-crosslinked GelMA hydrogel.(190) CNT composites that can form under biological conditions may have improved translation for contusion SCI and should be further investigated *in vivo*.

In summary, there have been some pioneering *in vivo* SCI studies involving graphene-based scaffolds and composites that have established feasibility and safety, but not yet efficacy. In the future, more *in vivo* studies are

needed to establish the efficacy and functional recovery after SCI with graphene-based conductive composites. Furthermore, composites of graphene with other materials that can form under biological conditions will need to be developed for translation to contusion SCIs. While functionalized CNTs can overcome hydrophilicity, aggregation, and cytotoxicity problems, the preformed scaffolds will limit translation to SCI. Additional CNT composites that can form under safe biological conditions are needed for translation to contusion SCIs.

Metallic particle-based materials

Metal nanoparticles have been highly attractive to fabricate conductive composites for a variety of applications because of the tremendous conductivities of metals. Conductive composites using gold, silver, platinum, and/or metal oxides (e.g., iron oxide) have been fabricated and investigated for biomedical applications such as hydrogels with gold nanoparticles (AuNPs) or iron oxide nanoparticles (IONPs). However, there are limited studies applied to neural tissue engineering *in vitro* and even fewer applied to treat SCI *in vivo*. Among the metal particles, AuNP composites are the most widely developed for tissue engineering and have been applied in cardiac, muscle, and peripheral nerve applications.

Silver nanoparticles (AgNPs) are advantageous for their antibacterial, optical, and photo-thermal properties, but were shown to disrupt the neural cytoskeleton and reduce neurite length and differentiation in cultured NSCs *in vitro.*(191) Furthermore, in one *in vivo* rat study, AgNPs exacerbated neuronal injury and increased BSCB leakage and edema when delivered after SCI.(192)

In a review on the inflammatory response to silver in the CNS by Wu *et al,*(193) AgNPs were implicated in stimulating reactive oxygen species and nitric oxide production, thereby causing neuroinflammation.

In terms of other metals, platinum nanoparticles are another available option, but these have mostly been used for catalysts and biosensors,(194) and not yet for nerve regeneration. As another metal example, IONPs have been used for SCI, but mostly to leverage their magnetic and optical properties and not to form conductive composites. The use of conductive composites has been limited for SCI, so in the remainder of this section, we now return our focus to composites made with AuNPs for cardiac and skeletal muscle applications, and then later will address IONPs that have been used for SCI (see **Table 2.7**).

AuNPs are attractive because they are highly conductive (up to 10^5 S/cm, see **Fig. 2.2**), easy to scale up, easy to functionalize, and can be made into a variety of shapes, including nanorods and nanowires. Gold is usually considered to be non-toxic and several studies using larger particles (30-100 nm) did not find acute side effects from systemic delivery. However, there could be size-dependent long-term toxicity of small AuNPs (<1.4 nm), which are thought to aggregate inside cells and be cytotoxic, and there are varying cytotoxicity results for medium-size AuNPs (8-37 nm).

The easy functionalization of AuNPs has been leveraged to fabricate several composite materials for drug delivery, particularly for delivering cancer therapeutics via photothermal triggered release,(195, 196) and novel tissue

engineering scaffold studies using AuNPs to crosslink polymer scaffolds.(195, 197, 198) There are a precious few AuNP composites that have been tested *in vivo* for SCI. In one example, AuNPs were employed for fibroblast growth factor (FGF) delivery with a scaffold composed of agarose and poly(N-isopropylacrylamide) (PNIPAM) with bone marrow-derived MSCs.(199) The composite scaffold resulted in better functional recovery than sham controls after 6 weeks, but the AuNPs were intended for FGF delivery, not conductivity.

Aside from composites using AuNPs for drug delivery, most conductive gold composites have been fabricated for cardiac and skeletal muscle tissue engineering, not neural regeneration. Several of the AuNP composites were preformed and synthesized by methods that are not biologically compatible, which included *in situ* formation of AuNPs,(102) coating,(200, 201) freeze-drying,(199, 202, 203) and electrospinning.(204) The blending method has been used to fabricate AuNP conductive composite scaffolds that form under biocompatible conditions. There are three examples: gelation via laponite nanoparticle interactions,(205) GelMA photopolymerization,(206, 207) and Schiff base-mediated collagen/cellulose crosslinking.(208) Additionally, *in situ* processes have been used to fabricate composite scaffolds with biologically compatible conditions where $HAuCl_4$ was reduced in chitosan to form chitosan-stabilized AuNPs, followed by scaffold formation via thermogelation at 37°C by varying mechanisms (i.e., chitosan/β-glycerophosphate,(104) blending with PNIPAM).(103)

Another advantage of AuNPs is the ability to control the shape of the nanoparticle during synthesis. As discussed earlier, spherical nanoparticles in conductive composites have higher percolation thresholds than high aspect ratio nanoparticles, which means higher concentrations of spherical nanoparticles are needed to attain the critical volume fraction for conductivity. High enough concentrations of nanoparticles can be challenging to obtain. Therefore, high aspect ratio nanoparticles (e.g., nanorods, nanowires) have been investigated to make composites because they have lower percolation thresholds and lower concentrations can be used. A disadvantage of gold nanorods (GNRs) and gold nanowires is that a toxic surfactant, hexadecyltrimethylammonium bromide (CTAB), is required for shape-controlled synthesis and further stabilization. The cytotoxicity is linked to the CTAB, but has been mitigated by coating the CTAB bilayer on the surface of the AuNP with non-toxic biomolecules (e.g., GelMA).(203) Complete replacement of the CTAB is difficult with normal ligand-exchange methods because of the high affinity of CTAB to gold. However, indirect ligand exchanges on different AuNP sizes and shapes through deposition and etching of a silver layer have been successful in completely removing CTAB and replacing it with a non-toxic citrate coating, making the GNR more suitable for biomedical applications.(209)

GNRs(203, 206, 207, 210) and nanowires(202) have been incorporated into composites via the blending method for *in vitro* cardiac tissue engineering or for photothermally triggered drug delivery,(211) but there are only a select few

composites with GNRs for peripheral nerve tissue engineering. One example for peripheral nerve tissue engineering was a blended GNR and silk fibroin composite that promoted better neural adhesion and proliferation than silk fibroin controls *in vitro.*(212) For SCI, GNR composites have not yet been investigated to the best of our knowledge, but GNRs alone have been delivered *in vitro* to neural cells. For example, GNRs delivered to neural cells with laser stimulation resulted in longer neurite growth than laser stimulation alone,(213) and in a follow-up study, GNRs induced intracellular calcium transients.(214) GNRs have additionally been used to improve the stability of ChABC for future application to SCI.(215) While there are few studies with conductive GNR composites for nerve regeneration, the composites used in cardiac tissue engineering that form under biological conditions could be adapted and highly translational for SCI. Several AuNP or GNR composites have been developed to be injectable(103, 104, 205, 208) or bioprintable,(197, 203) enhancing their translatability.

While AuNPs have been used to fabricate conductive composites, IONPs have been applied in SCI for their magnetic properties and not for conductivity. Additionally, IONPs have low cytotoxicity, are a magnetic resonance imaging (MRI) contrast agent that can label cells, and fabricate minimally invasive, aligned scaffolds. For example, IONPs have been used to label and track cells via MRI after *in vivo* delivery of cell suspensions,(216) or within a hydrogel *in vitro.*(217) In addition, functionalized IONPs have been used for imaging cells and releasing ChABC for SCI *in vivo.*(218) To leverage the magnetic properties, IONPs were

blended into hydrogels, implanted in a SCI rat model, and subjected to electromagnetic fields to facilitate axonal regeneration via mechanical stretching of neuronal membranes and attenuation of oxidative damage.(219) There was no detectable functional recovery, but there was less demyelination and more sprouting from neurons than sham controls.

For aligned topographies, IONPs have been blended and fabricated into microparticles, aligned in a magnetic field before hydrogel crosslinking, and finally dissolved to make aligned tubular microstructures to guide axon regeneration for peripheral nerve regeneration.(220) In addition to a templating technique, injectable hydrogels with aligned topographies have been made by magnetically aligning rod-shaped microgels made from PEG/IONPs(221) or macro-sized tubular fiber conduits made from electrospun IONPs with poly (L-lactic acid) (PLLA)(222) or PLGA(223) in hydrogel precursors (i.e., fibrin, fibrin/Matrigel®, collagen/Matrigel®). For all studies, the aligned tubular structures promoted *in vitro* guided neurite outgrowth within the hydrogels. In the future, the developed injectable hydrogels could be injected into a contusion SCI as a minimally invasive approach.

In summary, composites utilizing metal particles are not widely used for spinal cord injury, but gold and iron oxide may be the most promising metals for SCI. From cardiac tissue engineering studies, several AuNP or GNR conductive composites have been developed that are injectable and can form under biological conditions. Additionally, high-aspect-ratio nanoparticles (e.g., GNRs,

gold nanowires) have advantages of needing lower concentrations than spherical nanoparticles to obtain a conductive scaffold. Finally, non-conductive IONP-based composites are promising because of the magnetic properties and ability to non-invasively align IONP nanoparticles or micro-sized rod-shaped scaffolds or fibers in an injectable natural polymer for guided axon growth.

Discussion

The integration of regenerative medicine and rehabilitation approaches, or regenerative rehabilitation, may be necessary for full functional recovery in patients with complete injuries. Rehabilitation approaches have showed clinical promise in achieving better functional recovery than current treatments, but full functional recovery has not yet been achieved. The key limitation of rehabilitation approaches is the reliance on spared tissue that patients with a severe SCI; however, regenerative medicine may be able to overcome this problem by promoting regeneration of the spinal cord tissue. Combined together, rehabilitation approaches may facilitate reorganization of the regenerated neural pathways for meaningful functional improvements.

Despite the wide variety of regenerative medicine approaches for SCI (e.g., cells, drugs, biologics, scaffolds), the field has been limited by translational challenges to the clinic. With one *in vivo* SCI study(8) using the “regenerative rehabilitation” terminology and several additional studies and reviews utilizing the principles, the SCI field has been combining these fields to improve functional outcomes. However, when combining regenerative medicine and rehabilitation

approaches, the compatibility of the approaches must be considered, as one approach could negatively affect the other. There is a need for regenerative medicine approaches that are designed specifically to synergize with rehabilitation approaches. Conductive biomaterials are strategically poised to integrate regenerative medicine and rehabilitation through use of the conductive biomaterial to deliver regenerative medicine approaches for regenerating the spinal cord tissue while facilitating transfer of ES through the injury to promote neural plasticity.

Common to all categories of conductive composites, the most translational method was blending to mix conductive particles/materials into scaffold precursors that can subsequently form in an injury (e.g., via photocrosslinking, self-assembly, thermogelation). Furthermore, conductive composites developed for bioprinting are injectable and could be highly translational for SCI. One consideration of conductive composites that contain non-conductive materials is that the conductivity is lower than the pristine conductive component. Attaining sufficient concentrations of conductive particles can be difficult because of high percolation thresholds for spherical shapes. Fortunately, high aspect ratio particles such as gold nanorods or nanowires decrease the percolation threshold and can be used to achieve conductivity at lower concentrations. Another avenue that has been used to enhance the conductivity of composites was to combine two or more conductive components, and most of the combinations have included at least one carbon-based material and a conductive polymer. Inclusion of

multiple conductive fillers may be another avenue for future development of highly conductive composites.

In application to SCI, there are currently no *in vivo* studies using conductive biomaterials with ES or with ES/motor training. Additionally, there are limited numbers of *in vivo* SCI studies using only conductive biomaterials. However, for decades, *in vitro* studies have drawn on the fundamental principles underlying both regenerative medicine and rehabilitation by using conductive biomaterials with ES to deliver ES to neural cells, resulting in increased neurite outgrowth, neural differentiation, and proliferation. Complex combinations can be cumbersome for regulatory approval and hinder translation; therefore, proper controls are warranted to evaluate each component alone to identify the most influential component(s) to simplify translation or demonstrate a compounded and synergistic effect. While the combined effect of conductive materials with ES has been well characterized *in vitro*, the independent effect of conductive materials on neural cells is variable. Some conductive materials alone enhance neurite growth, but some materials have the same neurite growth compared to non-conductive materials. Unfortunately, non-conductive controls are not often included and conductive biomaterials with ES are compared to the same material without ES, which does not elucidate the effects of conductive materials. Future *in vitro* and *in vivo* investigations will be needed to elucidate the effects of conductive biomaterials by themselves and determine whether the effects of ES combined with conductive biomaterials compound and are truly synergistic.

Evidence exists that rehabilitation approaches may be most effective when combining two separate neuromodulation approaches: ES and motor training, but the dependence of rehabilitation techniques on spared tissues may not be sufficient for severely injured SCI patients. By developing regenerative medicine strategies to overcome the limitation of rehabilitation approaches and linking the two fields, conductive biomaterials with ES and motor training may be a promising new direction for regenerative rehabilitation to improve functional outcomes for SCI patients.

Chapter 3 : Development and Quantitative Characterization of the Precursor Rheology of Hyaluronic acid Hydrogels for Bioprinting[2]

Abstract

Bioprinting technologies have tremendous potential for advancing regenerative medicine due to the precise spatial control over depositing a printable biomaterial, or bioink. Despite the growing interest in bioprinting, the field is challenged with developing biomaterials for extrusion-based bioprinting. The paradigm of contemporary bioink studies relies on trial-and-error methods for discovering printable biomaterials, which has little practical use for others who endeavor to develop bioinks. There is pressing need to follow the precedent set by a few pioneering studies that have attempted to standardized bioink characterizations for determining the properties that define printability. Here, we developed a pentenoate-functionalized hyaluronic acid hydrogel (PHA) into a printable bioink and used three recommended, quantitative rheological assessments to characterize the printability: 1) yield stress, 2) viscosity, and 3) storage modulus recovery. The most important characteristic is the yield stress; we found a yield stress upper limit of ~1000 Pa for PHA. Measuring the viscosity

---

[2]Published as: Kiyotake EA, Douglas AW, Thomas EE, Nimmo SL, Detamore MS. Development and Quantitative Characterization of the Precursor Rheology of Hyaluronic acid Hydrogels for Bioprinting. *Acta Biomaterialia.* 2019;95:176-187. doi:10.1016/j.actbio.2019.01.041

was advantageous for determining shear-thinning behavior, which aided in extruding highly viscous PHA through a nozzle. Post-printing recovery is required to maintain shape fidelity and we found storage modulus recoveries above ~85% were sufficient for PHA. Two formulations had superior printability (i.e.,1.5 MDa PHA - 4 wt%, and 1 MDa PHA - 8 wt%), and increasing cell concentrations in PHA up to 9 x 10^6 cells/mL had minimal effects on the printability. Even so, other factors such as sterilization and peptide modifications to enhance bioactivity may influence printability, highlighting the need for investigators to consider such factors when developing new bioinks.(1)

Introduction

Bioprinting is a revolutionary technology that has empowered tissue engineers to recapitulate the native structure of tissues by allowing for spatial control over the deposition of printable materials, or bioinks, in addition to controlling cell distribution and the location of bioactive molecules within printed materials.(224-228) Conventional regenerative medicine research has investigated biomaterials containing homogeneous distributions of cells and biomolecules; however, native tissues are complex shapes with hierarchical structures from the macroscale down to the nanoscale, and homogeneous biomaterials that lack structured cues may not be capable of fully regenerating complex tissues. Bioprinting greatly increases the number of possibilities for physical arrangements of different biomaterials, cells, and biomolecules to mimic native tissues and enhance regeneration.(229)

While there are a growing number of bioprinters commercially available, the bottleneck for research is the lack of printable bioinks.(227, 230, 231) Bioinks must satisfy traditional criteria for biomaterials in regenerative medicine such as promoting cell functions (e.g., migration, proliferation, differentiation), but must additionally ensure cell survival throughout the printing process and any post-modifications (e.g., hydrogel crosslinking). Along with the biological requirements, bioinks are challenging to develop because of their physical requirements.(231, 232) Hydrogels are a commonly used platform for regenerative medicine because hydrogels facilitate cell survival and fulfill the biological requirements of a bioink; however, many hydrogel precursors are non-viscous liquids that are incapable of being deposited as a 3D structure without a mold, thus rendering them useless for extrusion-based bioprinting.(233) Fortunately, the development of new printable bioinks has emerged as a promising subdiscipline within the bioprinting community, but less fortunately, much of the research depends on trial-and-error of different material formulations to determine printability, with limited characterization of the material's physical properties or correlation of the characterization to the printability.(234-239) Currently, there are no standardized methods to characterize a material's printability,(231, 233) and the development of new bioinks is limited by time-consuming trial-and-error methods. Standardized characterization would stand to benefit from focusing on defining 'printability windows' for the properties that pertain to the requirements of the bioprinting process. For successful bioprinting,

bioinks must 1) flow through a needle or nozzle as a stable filament, 2) ‘instantly’ retain its 3D shape after deposition on a platform, and 3) support the weight of additional deposited material without collapsing. A few of the rheological properties that relate to the process of bioprinting are the viscosity, yield stress, and storage modulus recovery, but only a handful of reviews and studies have attempted to standardize the characterization,(240-246) and few new bioink papers have characterized their bioink with any of the suggested standardized methods, which include viscosity/shear thinning,(233, 244, 247) yield stress,(233, 241, 242) recovery,(244, 247) and storage/loss modulus.(243) Between the limited number of characterization studies, the viscosity has been well-characterized in a few ways to define quantitative ‘printable windows’ for the loss tangent or predicting printing parameters; however, the printability windows for yield stress and storage modulus recovery have not been quantitatively defined for universal comparison. Reproducible methodology is a key step toward developing protocols that can accelerate the development of new bioinks globally, and facilitate comparisons among groups, thus, there is a need for a continued effort to follow the precedent set by the aforementioned pioneering studies that began using uniform characterizations for bioinks.(243, 244)

Several types of bioinks are currently being investigated for extrusion-based bioprinting, such as hydrogels, cell aggregates, and decellularized extracellular matrix.(226, 233, 248) Hydrogels are advantageous because of their high-water content and biocompatibility, and there are several synthetic polymers

(e.g., Pluronic®, poly(ethylene glycol) (PEG)) and natural polymers (e.g., collagen, gelatin, hyaluronic acid (HA), chitosan, alginate, agarose) that have been bioprinted. Furthermore, there are chemically modified versions of both natural and synthetic hydrogels (e.g., methacrylated or diacrylated polymers) and blends of different types of hydrogels (e.g., gelatin/chitosan or PEG-diacrylate/alginate). HA is advantageous because it leverages benefits of both natural and synthetic hydrogels.(249) Similar to other natural polymers, HA is an extracellular matrix polymer found in several tissues (e.g., cartilage, epithelium, nerve) and is non-immunogenic. Similar to synthetic materials, HA is commercially available from microbial fermentation and can be easily chemically modified. The high viscosity of HA and chemical tunability for crosslinking capabilities enabled us to previously develop HA into a paste-like precursor for cartilage and bone regeneration,(82, 250-252) which had translational advantages for surgical placement. Our initial focus on surgical placement organically dovetailed into repurposing hydrogel precursor rheological characterization for identifying necessary physical properties for bioprinting.(253) In our previous work, we used a methacrylated HA hydrogel, but our work has evolved to using a pentenoate-functionalized HA (PHA) because of the rapid photocrosslinking of the thiol-ene click chemistry compared to the methacrylate chemistry.(254)

The purpose of the current study was to demonstrate the utility of standard protocols that can aid new bioink development, and we demonstrated the

characterizations by developing PHA, a known biomaterial,(254) into a bioink as an example. The current study examined the yield stress, viscosity, and storage modulus recovery as standard, quantifiable characterizations that can be compared between groups. Furthermore, we compared the parameters of the printable PHA formulations to the non-printable formulations in effort to define a window of printability for each parameter. Given that bioinks are commonly used to bioprint cells, we evaluated the rheological effects of different concentrations of rat bone marrow-derived mesenchymal stem cells (rBMSCs) within PHA, in addition to evaluating the cell viability of two cell types, rBMSCs and rat neural stem cells (rNSCs), after bioprinting. The goals of the experiments presented here were to develop a hyaluronic acid-based hydrogel precursor as a bioink and to characterize three vital rheological parameters to continue defining printability parameters to ultimately aid the development of new bioinks.

Materials and Methods

Materials

Unless otherwise stated, all materials were purchased from Sigma-Aldrich (St. Louis, MO).

Synthesis of pentenoate-functionalized hyaluronic acid

PHA was synthesized from two different molecular weights of hyaluronic acid, 1.5 MDa and 1 MDa (actual MW: 1.55 MDa and 823 kDa; Lifecore Biomedical, Chaska, MN). PHA was synthesized as we described previously(251) except with the modification of the addition of a catalyst. Briefly,

HA was dissolved in deionized water (DI) at a concentration of 0.5% (w/v) at room temperature before N,N-Dimethylformamide (DMF) was added at a 3:2 water to DMF ratio. In an additional step beyond our previous work, we added a catalyst, 4-(dimethylamino)pyridine, for the purpose of increasing the reaction efficiency of conjugating the pentenoate groups to the hydroxyls on the HA. Specifically, the catalyst was added to the HA in the water and DMF solution at a ratio of 0.25 g per g of HA and allowed to dissolve. 4-pentenoic anhydride was added in a 5-fold molar excess to HA and the pH was maintained between 8 and 9 with 1M sodium hydroxide for approximately 1 hour. After reacting overnight at room temperature, sodium chloride was added to achieve a final concentration of 0.5 M. Four times the reaction volume of acetone was added to precipitate the PHA and the solution was centrifuged at 7000 *x g* to separate the PHA from the acetone. The centrifuged PHA pellets were collected and dissolved in DI water before being transferred to dialysis tubing (MWCO: 6-8 kDa, VWR, Radnor, PA) to remove impurities. PHA was dialyzed in DI water for 48 hours with water exchanges every 12 hours before the solution was brought to a physiological pH of 7.4, frozen, and lyophilized. Dry PHA was stored at -20°C.

Characterization of PHA

The degree of substitution, or percent of repeating disaccharide units in PHA that were functionalized with a pentenoate group, was quantified using a Varian VNMRS-500 MHz NMR Spectrometer equipped with a 5 mm indirect detection room temperature probe (Varian, Palo Alto, CA). A PHA sample at 10

mM (i.e., concentration of the repeat unit) was prepared in deuterium oxide (D_2O; Cambridge Isotope Laboratories, Inc., Andover, MA) as a solvent. For all batches of PHA, a proton was collected at 80°C with 16 scans, a recycle delay of 35 seconds, a 90-degree pulse width, and a 60-second pre-acquisition delay. NMR was performed at 80ºC to compare to the reported 1H-NMR spectrum of PHA, which was collected at 80ºC.(254) Furthermore, the higher temperature of 80ºC shifted the D2O peak to 4.163 ppm,(255) which limited overlap with the majority of the proton peaks of PHA, and after performing NMR on 1.5 MDa PHA at different temperatures (i.e., 25, 50, and 80ºC), proton peaks were more resolved at 80ºC than at 25 or 50ºC and provided more accurate integrations. The percent functionalization was determined by integration of the alkene peaks (2.46 and 2.29 ppm) on the pentenoate group, normalized to the acetyl methyl group (1.91 ppm) of the disaccharide repeat unit. 24-33% of the repeating disaccharide units of HA were functionalized with a pentenoate group for all the 1 MDa and 1.5 MDa batches of PHA synthesized and used in the current study.

Cell culture

All cell culture supplies were purchased from Thermo Fisher Scientific (Waltham, MA) unless otherwise stated. The rNSCs were purchased (Thermo Fisher Scientific; originally isolated from the cortex of Sprague Dawley rats at day 14 of gestation) and were cultured according to manufacturer protocols. Tissue culture flasks were coated with 1% CTS™ CELLstart™ Substrate in Dulbecco's phosphate-buffered saline with calcium and magnesium (DPBS) for 1 hour in a

37°C, 5% CO_2 incubator. The rNSCs were cultured on coated flasks and in KnockOut DMEM/F-12 Basal Medium supplemented with StemPro Neural Stem Cell Serum Free Medium (NSC SFM) Supplement (2%), recombinant human basic fibroblast growth factor (bFGF; 20 ng/mL), recombinant human epidermal growth factor (EGF; 20 ng/mL), GlutaMAX™-I supplement (2 mM), and penicillin-streptomycin (Pen/Strep; 1%). The rNSCs medium was changed every 2-3 days and cells were passaged at 80% confluency using StemPro™ Accutase™ Cell Dissociation Reagent.

The rBMSCs were purchased (ScienCell, Carlsbad, CA; originally isolated from the bone marrow from adult Charles River Sprague Dawley rats) and cultured in DMEM (low glucose, pyruvate) supplemented with fetal bovine serum (FBS; certified, US Origin; 10%) and Pen/Strep (1%). The rBMSCs medium was changed every 2-3 days and were passaged at 80% confluency using Trypsin-EDTA (0.25%) phenol red.

Hydrogel precursor preparation

Different PHA precursor formulations of each molecular weight of PHA were prepared for rheological testing by varying the concentration of PHA (i.e., 6-9 weight percent (wt%) for 1 MDa PHA and 3-6 wt% for 1.5 MDa PHA). Additionally, precursor formulations with 1.5 MDa PHA (4 wt%) with varying concentrations of cells were prepared for rheological testing and cell viability testing. For all precursors, PHA was dissolved overnight at a 2X concentration in phosphate buffered saline (PBS), before being mixed with 0.05% (w/v) Irgacure

2959 (I2959) for a photoinitiator, dithiothreitol (DTT) at a 1:1 thiol:ene molar ratio for a crosslinker, and the remaining volume of PBS or PBS with cells. PHA precursors were left for 15-30 minutes in the dark to fully incorporate the added liquids. Due to the paste-like consistency of PHA precursors, letting the precursor mix completely was vital to achieve a homogeneous paste. PHA precursors were mixed once more and loaded into UV-shielding cartridges and centrifuged with a short-spin cycle for 30 seconds to eliminate air bubbles.

Rheological testing

The viscosity (n = 5), yield stress (n = 3), and storage modulus recovery (n = 3) of the PHA precursors without cells and the viscosity (n = 5) and yield stress (n = 5 for 7 x 10^6 cells/mL and n = 3 for all other groups) of PHA precursors with rBMSCs (passage 9-12, 10^6 to 9 x 10^6 cells/mL) were evaluated on a Discovery Hybrid Rheometer-2 (TA Instruments, New Castle, DE) equipped with parallel 20-mm crosshatched plates. Cellink® Start (Cellink®, Gothenburg, Sweden) is a commercially-available, bioprintable support material and was used as a control group in rheological studies because of its optimized printability. Additionally, Colgate Total® toothpaste (Colgate-Palmolive, New York City, NY) was used as a comparator group to put the results into a more understandable context. All tests were conducted at 25°C and with a gap of 500 μm. Viscosity curves were determined by a logarithmic shear rate sweep from a shear rate of 0.1 s^{-1} to 100 s^{-1} with 3 points per decade. The yield stress was determined by an oscillatory shear stress sweep from 1 to 5000 Pa, and the yield stress was

defined as the shear stress at the crossover point of the storage (G') and loss (G") moduli, as we have done previously.(83, 251, 252, 256) The storage modulus recovery was determined by three phases of oscillatory shearing at a frequency of 1 Hz after a 5-minute soak time where no stresses were applied, similar to what has been done previously in our group.(82) Materials underwent 5 minutes of a constant shear stress of 10 Pa to determine an initial storage modulus, 30 seconds of high shear stress of 3000 Pa (i.e., above the material's yield stress to mimic extrusion and flow through a bioprinter nozzle), and another 5 minutes of a constant shear stress of 10 Pa. The initial storage modulus was defined by the average storage modulus of the initial 5 minutes of the material being exposed to 10 Pa of shear stress. The recovered storage modulus was defined by the storage modulus 5 seconds after the shear stress transitioned from 3000 Pa back to 10 Pa. The percent recovery was defined as the recovered storage modulus divided by the initial storage modulus and multiplied by 100%.

Printability assessment

The g-code for a grid structure was generated from a 10 x 10 x 1.2 mm (LxWxH) rectangular prism using Repetier-Host software (Hot-World GmbH & Co. KG, Willich, Germany). The object was sliced in Repetier-Host into three 0.4 mm layers, with 43% rectilinear pattern infill to create 6 parallel lines, no perimeter or shells, and a printhead speed of 10 mm/s to generate a distinct path and structure for assessing the printed materials. PHA precursors in bioprinter cartridges were loaded into a pneumatic, extrusion-based Inkredible+ bioprinter

(Cellink®) and the 3-layer grid structure was bioprinted through a sterile 27G (i.e., 0.21 mm diameter) polypropylene conical nozzle (Cellink®) onto a glass microscope slide (24 mm x 76 mm, L x W). The pressure used (40-180 kPa) to extrude the material was adjusted for each material to achieve a consistent flow and the best print possible. Images of printed materials were captured on a DSLR camera (Nikon D5500, B&H Photo Video, New York City, NY) with a macro lens (Nikon AF-S Micro-NIKKOR 60mm f/2.8G ED Lens, B&H Photo Video).

The printability of each PHA precursor was qualitatively assessed by evaluating the shape fidelity of the printed grid within 1 minute after printing prior to any crosslinking and scoring it on a scale of 0 to 3, based on a review presented by Malda *et al*.(233) where 0 was no shape fidelity, 1 was poor shape fidelity with low undefined structure, 2 was medium shape fidelity with intermediate irregular patterns, and 3 was high shape fidelity with well-defined building potential. Factors that affected shape fidelity were the edge shape of the individual printed strands (e.g., no edges, soft/undefined edges, clean/stable edges, fragmented/irregular edges), and overall stability of the printed structure shortly after it was printed (e.g., retainment of the grid structure after printing, or relaxation of the material into a puddle after printing). ImageJ was used to measure the strut size of bioprinted grid structures and the particle analysis feature in ImageJ was used to measure the pore areas, similar to Wilson *et al*.(245)

Cell viability analysis

To determine the cell viability after bioprinting, 1.5 MDa PHA was sterilized by ethylene oxide gas (AN74i, Anderson Anprolene, Haw River, NC) before a 4 wt% solution was prepared with 10^6 cells/mL of rBMSCs (passage 5; n = 3) or rNSCs (passage 3, n = 3) using the methods previously described. Hydrogel precursors of each cell type were bioprinted into rectangular prisms (8 x 6 x 0.3 mm, LxWxH), not the same grid structure as was used for the shape fidelity assessment, onto microscope slides (**Fig. 3.1A**). Each slide of hydrogels was crosslinked under a 312 nm handheld UV light at 9 mW/cm^2 (EB-160C, Spectroline, Westbury, NY) for 2 minutes (**Fig. 3.1B**). While 365 nm light is perceived to be safer than 312 nm light for cells, we used 312 nm light because the photoinitiator used (I2959) has an absorbance peak around 311 nm, which increased the crosslinking efficiency compared to 365 nm light. With 312 nm light, the amount of time needed for crosslinking PHA was only 2 minutes, which limited the amount of time cells were exposed to UV and did not have detrimental effects in previous studies.(82, 83, 250, 257) An 8-well removable silicon chamber (Ibidi, Martinsried, Germany) was sealed on top of the printed and crosslinked hydrogels and each cell's respective medium was added to each well (**Fig. 3.1C**). Cells were cultured for 7 days with medium changes every other day. 2 hours after bioprinting, and after 7 days of culture, hydrogels were stained with the LIVE/DEAD Viability/Cytotoxicity Kit for mammalian cells for 20 minutes using 2 mM calcein AM and 2 mM ethidium homodimer-1 (Thermo Fisher Scientific).

Representative images of each group were taken on a Leica TCS SP8 confocal microscope (Leica Microsystems, Wetzlar, Germany) by taking a z-stack of 501 slices throughout the entire hydrogel. An approximate cell viability was determined from the images by comparing live and dead cell counts obtained with the Analyze Particle feature in ImageJ. We noted the cell densities between rBMSCs and rNSCs appeared to be slightly different in the confocal images taken. Based on the printability assessments of PHA with cells showing minor effects on printing from the addition of varying concentrations of cells, we did not anticipate a slight variation in cell density to significantly affect the viability. Therefore, the cell viability data still provided a reasonable representation of the effect of bioprinting on cell viability for both cell types.

Statistical methods

GraphPad Prism (Graphpad Software Inc, La Jolla, CA) was used to perform all statistical analyses. All groups were analyzed with a one-way analysis of variance (ANOVA), followed by Tukey's *post-hoc* test. Results were considered significant at a level of $p < 0.05$. All results were reported as mean $\pm$ standard deviation.

Results

Printability assessment

All hydrogel precursors were printed into a 3-layer grid (**Fig. 3.2A**), given a shape fidelity score (**Fig. 3.2B**), and imaged from above (**Fig. 3.2C**). Images were analyzed in ImageJ for pore area and strut size (corresponding

measurements below each image in **Fig. 3.2C**). Cellink® Start was used as a control group because of its optimized printability and good shape fidelity (shape fidelity score = 3) after printing (**Fig 3.2A**). Cellink® Start printed with clean edges, was well-matched to the original grid file, and retained its shape after being printed. Toothpaste was included as a comparator group (**Fig. 3.2A**) to provide a more understandable context but failed to extrude through a 27G nozzle. Even with a larger 22G nozzle, toothpaste only printed with medium shape fidelity (score = 2). While the printed structure matched the model decently, it had soft edges (i.e., curved turns instead of 90 degree turns) and relaxed over time into a less defined structure. The pore area and strut size of Cellink® Start were 0.13 mm^2 and 1.07 mm, respectively, while toothpaste had a pore area of 0.32 mm^2 and a strut size of 0.92 mm.

For the 1 MDa PHA groups (**Fig. 3.2C**, top row), the 5 wt% had no shape fidelity and immediately lost its shape after being deposited, resulting in a puddle (score = 0). The 6 wt% performed better than the 5 wt%, where the original structure of the 6 wt% was still visible after printing; however, the edges were soft, and the shape fidelity was still poor (score = 1). The 7 and 8 wt% groups both printed with clean and defined edges similar to the Cellink® Start but given that the 7 wt% relaxed within a few minutes into an undefined shape, the 7 wt% had medium shape fidelity (score = 2) while the 8 wt% had good shape fidelity (score = 3). While the 9 and 10 wt% groups had structures that imitated the original model, both groups had sharper and fractured edges with printed lines

that were irregular, which resulted in a medium shape fidelity (score = 2) for the 9 wt% group and a poor shape fidelity (score = 1) for the 10 wt% group. For pore area there generally appeared to be a trend of increased pore area with increased PHA concentration, ranging from 0.05 mm^2 (7 wt% PHA) to 0.71 mm^2 (10 wt% PHA), with the exception of the 6 wt% PHA (0.22 mm^2). For strut size, there generally appeared to be a trend of decreased strut size with increased PHA concentration, ranging from 1.48 mm (6 wt% PHA) to 0.45 mm (10 wt% PHA). For context, the inner diameter of the nozzle used to bioprint the formulations was 0.21 mm and therefore, we anticipated the minimum strut size would be 0.21 mm. Out of the 1 MDa PHA groups, the 8 wt% appeared to have the closest pore area and strut size to Cellink® Start.

For 1.5 MDa PHA groups (**Fig. 3.2C**, bottom row), the 3 wt% group was similar to the 1 MDa - 6 wt% group with no shape fidelity (score = 0) because of the immediate loss of structure upon deposition. The 4 wt% group was most similar to the 1 MDa - 8 wt%, with well-defined edges and good shape fidelity (score = 3). The 5 and 6 wt% groups were akin to the 1 MDa - 9 and 10 wt% groups, respectively, with medium (score = 2) and poor (score = 1) shape fidelity from the fractured edges and irregularity of the printed lines. Similar to the 1 MDa PHA, there appeared to be the same general trends of increased pore area and decreased strut size with increased PHA concentration for the 1.5 MDa PHA. The pore areas ranged from 0.14 mm^2 (4 wt% PHA) to 0.59 mm^2 (6 wt% PHA) and the strut sizes ranged from 1.04 mm (4 wt% PHA) to 0.51 mm (6 wt% PHA). Out

of the 1.5 MDa PHA groups, the 4 wt% appeared to have the closest pore area and strut size to Cellink® Start.

Shape fidelity scores were plotted against the PHA concentration for the 1 and 1.5 MDa PHA groups (**Fig. 3.2B**). For both molecular weights, as the concentration of PHA increased, the shape fidelity increased, reached a peak, and decreased. The groups that printed with medium, poor, or no shape fidelity had two distinct sets of characteristics, depending on if the PHA concentration was greater than or less than the previously mentioned ideal concentrations. The precursors that had a lower PHA concentration either had soft edges or relaxed into a puddle after printing. On the other hand, the precursors with a higher concentration had sharper or fractured edges that printed more irregularly. Overall, the concentration for each molecular weight of PHA that printed with best shape fidelity were 1 MDa - 8 wt% and 1.5 MDa - 4 wt% (**Fig. 3.2B-C**, red boxes).

Rheological testing

Viscosity evaluation

All of the materials displayed decreasing viscosities with increasing shear rates from 0.1 to 100 s^{-1} (i.e., shear thinning) (**Fig. 3.3A-B**), with viscosities ranging from 410 to 11,600 Pa-s at 0.1 s^{-1} and from 1 to 18 Pa-s at 100 s^{-1}. The Cellink® Start appeared to have a linear decrease in viscosity from 1510 Pa-s at 0.1 s^{-1} to 5 Pa-s at 100 s^{-1} on the log-log plot of viscosity versus shear rate, but the toothpaste viscosity, which ranged from 570 at 0.1 s^{-1} to 13 Pa-s at 100 s^{-1}, appeared to be more similar to the PHA groups with a gradual decrease at lower

shear rates and a sharper decrease at higher shear rates. Overall, increasing the PHA concentration generally appeared to have increased the viscosity behavior but at the highest shear rate, all materials had viscosities under 18 Pa-s. Toothpaste had viscosity behavior similar to the PHA groups, but the toothpaste shear thinning behavior appeared to not decrease as quickly as the PHA groups.

Yield stress evaluation

None of the 1 MDa PHA groups had a yield stress, but all the 1.5 MDa PHA groups did have a yield stress (**Fig. 3.3C**). For reference, toothpaste had a yield stress of 105 ± 6 Pa. For the 1.5 MDa PHA, there was a trend of increased yield stress with increased PHA concentration. Specifically, the yield stresses of the 3 and 4 wt% groups were 320 ± 90 Pa and 380 ± 17 Pa, respectively, and were not significantly different from Cellink® Start, which had a yield stress of 217 ± 5 Pa. The 5 wt% group had a yield stress of 1140 ± 150 Pa that was approximately 5.3 times greater than Cellink® Start and 3.5 times greater than the 3 wt% group ($p < 0.005$). the yield stress of the 6 wt% group was 2010 ± 360 Pa, which was greater than all other groups ($p < 0.005$).

Storage modulus recovery evaluation

Because the 1 MDa PHA groups did not have a yield stress and the loss modulus, G', was higher than the storage modulus, G", at all shear rates, there would be no loss or recovery of the storage modulus after shearing and the recovery was not evaluated. All references to PHA here refer specifically to the

1.5 MDa groups. Cellink® Start and PHA 3 wt% and 4 wt% all had recovered storage moduli that were not significantly different from their initial storage moduli (**Fig. 3.3D**). Specifically, Cellink® Start had an 87 ± 1% storage modulus recovery, 3 wt% had an 89 ± 2% recovery, and 4 wt% had an 85 ± 6% recovery. Toothpaste and the 5 wt% and 6 wt% had decreased recovered storage moduli from their initial storage moduli ($p < 0.0001$), where the percent recoveries of the storage modulus were 32 ± 2%, 76 ± 5%, and 68 ± 5%, respectively.

Printability and rheological assessments of PHA with encapsulated cells

The 1.5 MDa - 4 wt% PHA precursor with varying cell concentrations (i.e., 10^6, 3 x 10^6, 5 x 10^6, 7 x 10^6, and 9 x 10^6 cells/mL) was evaluated for shape fidelity after bioprinting (**Fig. 3.4A**), yield stress (**Fig. 3.4B**), and viscosity (**Fig. 3.4C**). The bioprinted 3-layer grid of all PHA groups with cells, despite the increasing cell concentrations, printed with high shape fidelity (i.e., score = 3) with clean and defined edges that maintained their structure after printing. The pore areas and strut sizes of the PHA with varying cell concentrations were similar to PHA without cells and fell within the range of 0.09 to 0.22 mm^2 for pore area and 0.94 to 1.14 mm for strut size (listed under each respective image in **Fig. 3.4A**). The yield stress of the PHA with 10^6 cells/mL (580 ± 15 Pa) was approximately 1.5 times greater than PHA with no cells (380 ± 17 Pa), 1.4 times greater than the PHA with 5 x 10^6 cells/mL (410 ± 20 Pa), and 1.75 times greater than the PHA with 9 x 10^6 cells/mL (330 ± 60 Pa). The yield stresses of the PHA with 3, 5, 7 and 9 x 10^6 cells/mL were 430 ± 50, 410 ± 20, 310 ± 70, and 330 ± 60 Pa,

respectively, and were not different from the yield stress of PHA without cells (380 ± 17 Pa). The viscosities of all the PHA with cells groups at shear rates ranging from 0.1 to 100 s^{-1} generally appeared to show similar shear thinning behavior to PHA without cells. Overall, the PHA groups with cells displayed similar shear thinning behavior compared to the PHA alone.

Viability assessment

1.5 MDa - 4 wt% PHA was separately bioprinted into the rectangular scaffolds (8 x 6 x 0.3 mm) with 100% infill, not the grids previously used for shape fidelity assessments, and were crosslinked with encapsulated rBMSCs or rNSCs (**Fig. 3.1**). Live/Dead staining showed live cells in green and dead cells in red on the day hydrogels were bioprinted (day 0) and after 7 days of culture (**Fig. 3.5**). From the cell counts of the representative image of each group, the rBMSCs had a viability around 100% after the bioprinting and hydrogel crosslinking process. After 7 days of culture, the viability only decreased to 83%. On the other hand, the rNSCs had a viability of about 87% after the bioprinting and crosslinking processes. After 7 days of culture, the viability dropped to approximately 55%. We noted that the size of the rNSCs at day 7 appeared larger than they were at day 0, and we speculate the increased cell size could be due to a small amount of cell spreading or spontaneous differentiation.

Discussion

We have established a quantitative range of printability, or printability window, of the yield stress and storage modulus recovery, using a PHA bioink as

an example. In the experiments performed here, we have not only developed a known crosslinkable hyaluronic acid hydrogel into a printable material, but we quantified three rheological assessments that are universally comparable (i.e., yield stress, storage modulus recovery, and viscosity) and determined two printability windows of yield stress and storage modulus recovery for PHA. While the ranges of printability determined from the experiments presented here are specific for PHA, the application of the methods are standard rheological experiments that can be employed by any group to define the printability of other materials and develop new bioinks. Toothpaste and a commercially available bioink, Cellink® Start, were tested alongside the PHA here to further demonstrate the applicability of the rheological experiments, but one limitation of the studies here was that other potentially printable biomaterials were not tested. Even so, the data provided here provides a quantitative point of comparison or starting point for the development of new bioinks, especially for other HA-based materials or similar natural polymers.

To provide a link between the qualitative trial-and-error methods and the quantitative rheological measures of viscosity, yield stress, and storage modulus recovery, a shape fidelity assessment was employed to determine the printability of different PHA formulations. From previous work, we found that lower molecular weight (i.e., 60 kDa) PHA precursor solutions had a low viscosity, even at higher concentrations (i.e., 10 wt%); therefore, we investigated higher molecular weights of PHA as potential bioinks (i.e., 1 and 1.5 MDa). From the qualitative shape

fidelity assessments, the formulations that printed with good shape fidelity were the 1 MDa - 8 wt% PHA and the 1.5 MDa - 4 wt%. Comparing the two groups that printed with good shape fidelity, the 1.5 MDa - 4 wt% contained half the concentration of PHA compared to the 1 MDa - 8 wt%, which made the higher molecular weight PHA a more practical material source for a bioink because the lower concentration uses less material. In the current study, we used a simple qualitative scale for evaluating shape fidelity. There are other methods of quantifying the shape fidelity, such as using image analysis software to measure pore area, circularity of pores,(258) strut size,(245) printed area,(237) or filament fusion/filament collapse.(242) As Ribeiro *et al.* (242) emphasized, there is a need for a universal testing method of bioink shape fidelity, or correlation of shape fidelity with another quantitative measure (e.g., yield stress) to compare between different bioinks.

The viscosity of a bioink is an important parameter to characterize because it determines how much pressure is necessary to keep the material extruding at a desired flow rate. Higher viscosity materials or materials with a yield stress maintain their shape after printing better than low viscosity materials or materials without a yield stress; however, a material experiences high shear forces when flowing through a needle, and viscous bioinks necessitate shear thinning behavior, or having lower viscosities at high shear rates, to be able to flow through a needle.(245) The relevant shear rates for needles have been estimated to be 100-500 s^{-1} all along the length of the needle, whereas tapered

nozzles had higher estimated shear rates around 200-3000 s^{-1} localized to just the nozzle tip.(244, 259) In the current study, PHA failed to extrude through a 22G blunt-tip needle (i.e., 0.413 mm diameter), but was extrudable through a 27G nozzle tip (i.e., 0.21 mm diameter), making nozzles a more practical choice for extrusion of materials with high viscosity.

As others have found,(233, 241-244, 247) the viscosity measurement alone is insufficient for determining printability. In these studies, we found that the PHA formulations that printed the best did not have a distinct viscosity behavior that differentiated them from the groups that did not print well. Comparing the viscosity curve of the Cellink® Start to the printable 1.5 MDa - 4 wt% group, both groups had shear thinning behavior and converged to viscosities below 18 Pa-s at a shear rate of 100 s^{-1}, which is in the neighborhood of the relevant shear rates through a nozzle; however, the Cellink® Start followed a different, more linear decrease with increasing shear rates when compared to the PHA groups. Therefore, there was not a “printable” viscosity range and the viscosity alone could not be used to determine printability. The most important information the viscosity data provided was determining whether the material was shear thinning, which was vital for the extrusion of viscous materials through a nozzle. Others, such as Paxton *et al.*(244) found similar results and demonstrated additional uses for viscosity data in predicting other printing parameters. Specifically, they used the viscosity data to determine the shear thinning coefficients from a Power Law regression and predicted the printing parameters ranges for the printing pressure

and nozzle geometry. They found that the higher viscosity materials would require higher pressures and larger diameter nozzles for successful extrusion.

The yield stress is the most important parameter to characterize because a yield stress is required for a material to hold its shape after bioprinting and support the weight of added layers. Comparing the yield stresses of the PHA formulations that had good shape fidelity to the formulations that did not, printable materials had yield stresses below a maximum threshold value of around 1000 Pa, where PHA with a yield stress above the threshold printed with fractured and irregular lines. The upper limit of the yield stress determined from our results specifically applies to extrusion of PHA through a 27G (i.e., 0.21 mm) nozzle at the pressures used here, and the yield stress limits for different size nozzles or materials may deviate from that value (see **Table 3.1**). For example, Paxton *et al*.(244) found that the printable formulation of poloxamer 407 through a 0.25 mm nozzle had a yield stress of 227 Pa, but the formulation with a 348 Pa yield stress was not printable, indicating a yield stress limit around 300 Pa. While there may be different yield stress limits for different materials to print with good shape fidelity, a material with high viscosity may be sufficient for printing with good shape fidelity under the right conditions. Among these conditions for good shape fidelity for high viscosity materials, the most important is time, and specifically the time elapsed from printing from the nozzle to crosslinking for a given layer. Given enough time, even the highest viscosity bioink in theory can flow (i.e., change shape) if it does not possess a sufficient yield stress.

In the current study, none of the 1 MDa PHA groups had yield stresses, but the 1 MDa - 8 wt% printed with good shape fidelity. The 8 wt% group had a high enough viscosity (i.e., 4 times greater than the 1.5 MDa - 4 wt%) to compensate for the lack of a yield stress within the time period given for crosslinking. Similarly, Paxton *et al*.(244) found a printable formulation of alginate-gelatin that did not have a yield stress, but was still able to be printed with good shape fidelity, which was accomplished by lowering the print bed temperature to increase the viscosity of the material upon deposition. While a high viscosity is not a substitute for a yield stress, we found that a material with a high viscosity may delay the movement of the material after printing, and aid in shape retainment, especially if a crosslinking mechanism is employed directly or soon after printing. Overall, the existence of a yield stress is the most important parameter to characterize for evaluating whether the material can retain a printed shape and the yield stress limit for a particular material and nozzle size can be used to determine printable formulations.

Given that the yield stress does not account for a material's exposure to high shear stresses during the extrusion process, the storage modulus recovery is necessary to characterize to determine how well the yield stress and original properties are recovered after printing. In the current study, we demonstrated that PHA formulations that printed with good shape fidelity and the Cellink® Start material had storage modulus recoveries above 85%, similar to others.(240, 260) We propose a minimum threshold for storage modulus recovery of 85% for

printable PHA formulations. While the recovery data may not be entirely relevant for other polymer systems, we believe the 85% target is a reasonable starting point and guideline for novel bioinks entering the literature. We additionally found that higher viscosities could mitigate the impact on the shape fidelity of materials with low recovery. Even though the 1.5 MDa - 3 wt% and 4 wt% PHA had similar recoveries of their storage modulus, it is possible that because the 3 wt% was less viscous, the shape fidelity started out with soft edges and deteriorated to no edges, where the 4 wt% printed with rigid edges and relaxed to normal defined edges. Crosslinkable hydrogels can additionally overcome low recoveries by initiating crosslinking throughout the printing process to conserve the printed structure immediately upon deposition.(261) The PHA hydrogels used here are advantageous for overcoming low recoveries because of the quick crosslinking time (~2 min) compared to other previously used methacrylated HA chemistries with longer crosslinking times (~5-30 min).(82, 250) Overall, for the PHA formulations, groups with good shape fidelity had storage modulus recoveries above 85%.

Given that many bioinks are used to bioprint cells in constructs that mimic native tissues or even print multiple cell types in different locations on the same structure, it is important to investigate the effects that cells have on the printability of bioinks and how well cells survive the printing and post-printing processes (e.g., UV crosslinking). To illustrate and quantify this point, we demonstrated that the increasing cell concentration in 1.5 MDa - 4 wt% PHA with 1 x 10^6 cells/mL

increased the yield stress but otherwise had minimal effects at higher cell concentrations up to 9 x 10^6 cells/mL on the printed shape fidelity, yield stress and viscosity when compared to PHA with no cells. Other studies found opposite trends of decreasing bioink viscosity when 2.5 x 10^6 cells/mL or less were encapsulated.(258, 259) Given the discrepancy, for development of future bioinks, it will be important to take into account the effects of encapsulated cells on the printability of the bioinks and characterize bioinks accordingly. Given that the tested cell concentrations did not diminish printability, cell viability studies were conducted with 10^6 cells/mL. Even though exposure to UV light may be harmful to cells, we have previously shown high viability of cells after hydrogel encapsulation and exposure to 312 nm light.(82, 250, 257) PHA has a fast thiol-ene crosslinking chemistry and only requires a short duration of UV exposure (i.e., 2 minutes) and a low concentration of photoinitiator I2959 (i.e., 0.05% w/v) for sufficient crosslinking, thus, we did not anticipate the UV exposure to significantly increase cell death. In support of our hypothesis, there was good viability of rBMSCs and rNSCs (i.e., greater than 87%) after exposure to UV light and additionally being extruded through a nozzle. Altogether, the high cell viabilities indicated that the 1.5 MDa - 4 wt% PHA precursor met the minimum biological requirement of keeping cells alive throughout the bioprinting process. The rBMSCs maintained a good viability after 7 days of culture; however, the rNSCs began to lose viability. Even though rNSCs initially survived the stresses of bioprinting, the rNSCs may not be as robust as the rBMSCs and experienced

negative long-term effects from the bioprinting process. Several studies showed that cell viability after printing decreases as the viscosity of the material increases and as the nozzle diameter decreases because of the high shear stresses.(262, 263) The rNSCs may have been more susceptible to damage from the high shear stresses compared to the rBMSCs. Low pressures and larger nozzles are favorable for printing cells, (262, 263) but larger nozzles reduce the resolution of the print. Low-viscosity crosslinkable materials may be able to overcome the limitations by simultaneously depositing and crosslinking the material to form stable structures.(261)

Another consideration that may affect printability is the effect of different sterilization techniques on material composition and mechanical performance. Ethylene oxide was used as a sterilization technique for PHA to be used in cell viability studies and because ethylene oxide can participate in addition reactions with amines, carboxylic acids, hydroxyls, and sulfhydryl groups,(264) preliminary studies with NMR showed there was most likely residual ethylene oxide in the sample, which could be eliminated by sample aeration after sterilization. Further, we found there was most likely an addition reaction of the ethylene oxide onto the carboxylic acids or hydroxyls present on the PHA backbone. Other studies found similar addition reactions occurring on materials with carboxylic acids.(264, 265) In terms of rheological performance, preliminary studies with sterilized PHA showed that the ethylene oxide sterilization could have affected the yield stress and viscosity, but further verification will need to be performed in future studies.

A few other studies found effects on other scaffolds after ethylene oxide sterilization in terms of yield strength, swelling, pore morphology, and molecular weight, but the effects were not the same among all the materials tested,(264, 266, 267) which highlights the need for each material to be characterized individually, as the effects vary. Overall, we emphasize the need to characterize the effects on compositional and mechanical performance from the sterilization technique used because of the potential influences on the printability.

We have developed the printability of the PHA material in these studies; however, HA materials lack motifs for cell attachment, reducing the applicability for regenerative medicine. In preliminary studies, we found that rNSCs do not adhere or spread well when encapsulated or are seeded on PHA hydrogels. The same challenges arise with other inert synthetic polymers, but polymer modifications with adhesive peptides are used to overcome this challenge. Similar to synthetic polymers, PHA can be modified with thiolated bioactive factors, such as adhesive peptides, which can enhance the bioactivity for better regeneration of tissues. While the overall bioactivity may be enhanced, such modifications could influence or alter the printability. Preliminary studies involving bioprinted PHA modified with laminin-based adhesive peptides for enhancing rNSC adhesion resulted in similar printability, but the specific rheological effects need to be further investigated. We speculate the rheological performance could be dependent on peptide concentration, size, and interactions. At lower concentrations, the rheology could be dominated by the long polymer chains of

PHA and similar to that of PHA alone; however, the conjugation of a high concentration or longer peptides may cause more peptide “branches” on PHA and thus, more physical entanglements and a potentially higher yield stress. On the other hand, the ability of peptides to interact with other peptides or the polymer via charge or hydrogen bonding may influence the interactions with neighboring peptides, causing aggregations or repulsions, and further influencing the bulk rheological properties and printability. From the immense variety of peptides that can be synthesized, the influence of peptide modifications to polymers on printability is another topic in need of further investigation by the bioprinting field.

Conclusions

There are several physical properties, printing parameters, and biological requirements that all influence the printability of a material from an extrusion-based bioprinter. In terms of physical properties, we assessed the printability of varying formulations of a hyaluronic acid-based hydrogel precursor, PHA, and characterized the formulations with three rheological tests: viscosity, yield stress, and storage modulus recovery. We found that the viscosity alone did not determine printability, but the viscosity behavior was valuable in determining if PHA had shear thinning behavior and would be extrudable through a nozzle during bioprinting. Further, possession of a yield stress was a critical characteristic for maintaining a printed shape; however, the yield stress upper limit for PHA through a 27G (i.e., 0.21 mm diameter) nozzle was 1000 Pa, where

PHA formulations with yield stresses beyond 1000 Pa printed with irregular lines. While the yield stress could be a direct indicator of printability, a material could print with high shape fidelity if the viscosity was high enough to delay the material relaxation and a crosslinking mechanism was employed directly or soon after printing to retain the printed shape. Similarly, good storage modulus recovery after shearing was necessary for preventing material relaxation and maintaining the printed shape fidelity after being extruded, but materials with high viscosity could reduce the relaxation effect of PHA formulations that had low recovery through use of a quick UV crosslinking mechanism. Bioprinting has significant advantages for controlling the spatial location of different cell types to mimic the native hierarchy of tissues, but bioprinting cells comes with additional challenges. We found minimal effects of cell concentration on the printability of PHA, but others have found that it decreased viscosities. Additionally, we found that the carboxylic acid and hydroxyl-containing PHA may be susceptible to compositional changes from ethylene oxide sterilization, which may in turn influence the printability. Another parameter that may influence printability is the use of peptide modifications on PHA or other inert polymers to overcome the lack of motifs for cell attachment. Overall, cell concentration, sterilization methods, and peptide modifications are important considerations to account for during future bioink development. To demonstrate the feasibility of using PHA as a bioink, we found that two stem cell types each had good viabilities after printing. Overall, in these studies we developed a hyaluronic acid-based hydrogel into a

bioink, characterized different formulations with three quantifiable rheological assessments, and determined printability windows for the yield stress and storage modulus recovery of PHA. We hope to accelerate future bioink development by recommending the rheological evaluation of the viscosity, yield stress, and storage modulus recovery to promote the use of standardized characterizations for more efficient, quantitative, and reliable methods to develop new printable bioinks.

Chapter 4 : Injectable Hyaluronic Acid/Gelatin Hydrogel for Application to Spinal Cord Injury[3]

Abstract

The combination of regenerative medicine and rehabilitation approaches, known as regenerative rehabilitation, may be necessary for functional recovery after contusion spinal cord injury (SCI). Regenerative medicine approaches are needed to regenerate axonal pathways and work synergistically with rehabilitation approaches. The bottleneck for developing regenerative medicine approaches to treat SCIs in the context of rehabilitation is that biomaterials for SCI treatments tend to be pre-formed solids. Implantation of preformed solids into a spinal cord may cause serious risk for a rehabilitating patient and is thus undesirable. This inherent risk may be overcome by the use of hydrogel bioinks for injectable delivery and retention in contusion SCIs. The bioprinting field is a fertile ground for injectable biomaterials, as fluid mechanics (i.e., rheology) and cytocompatibility are paramount to success. In the current studies, a new pentenoate-functionalized gelatin (PGel) hydrogel was developed, and 2D nuclear magnetic resonance (NMR) spectroscopy on PGel was used to confirm and quantify the degree of functionalization. Rat neural stem cells lacked

[3]In preparation to *Tissue Engineering* as: Kiyotake EA, Thomas EE, Nimmo SL, Townsend JM, Detamore MS. Injectable Hyaluronic Acid/Gelatin Hydrogel for Application to Spinal Cord Injury.

adhesion to a previously developed fast-crosslinking, pentenoate-functionalized hyaluronic acid (PHA) bioink, and in the current studies, some PGel formulations degraded within 14 days. Therefore, the PGel and PHA were combined to solve the problem of the other, where the PGel improved rNSC adhesion and PHA improved the precursor printability and long-term stability of the post-crosslinked hydrogels. The 4%/5% and 3%/10% PHA/PGel formulations were adhesive for rNSCs and had improved long-term stability. Finally, the 4%/5% PHA/PGel hydrogel precursor (i.e., before UV-crosslinking) had more desirable rheological properties for bioprinting/translation to SCI compared to the 3%/10% formulation. While both formulations were injectable (i.e., shear thinning), the 4%/5% formulation had better shape retention after extrusion (i.e., higher yield stress and storage modulus recovery), which may translate to better material retention in a SCI, until the rapid formation of the hydrogel (2 minutes). The injectability, paste-like rheology, and fast UV-crosslinking (2 minutes), and of the 4%/5% PHA/PGel bioink may be leveraged as a translational platform for future application to SCI.

Introduction

Spinal cord injury (SCI) affects 17,800 people in the United States every year, with 294,000 current patients.(25) Current clinical treatments (e.g., rehabilitation) have not yet been able to promote full functional recovery, but recent human studies have made significant progress in achieving independent stepping (with assistive devices) when coupling motor training with electrical stimulation by leveraging the remaining spared pathways and promoting

neuroplasticity.(88, 90) However, the majority of SCI patients that have severe injuries with minimal spared pathways may experience little benefit from rehabilitation-based therapies alone. Regenerative medicine approaches are needed to help regenerate the damaged spinal cord tissue and form new axonal pathways. The combination of regenerative medicine and rehabilitation approaches, termed regenerative rehabilitation,(5-7) may be the most promising approach to regenerate the spinal cord tissue and promote plasticity to maximize functional outcomes.

There are far fewer regenerative medicine approaches that have made it to clinical trials for SCI than rehabilitation approaches. Of the regenerative medicine approaches that are in clinical trials for SCI, most are cell-based therapies, which have key translational limitations (e.g., limited proven efficacy, low cell survival, the need for good manufacturing practice facilities). Biomaterials have been used to overcome some of the limitations that cell therapies face, but biomaterials themselves have different translational limitations when applied to SCI. For example, most biomaterials have non-biocompatible formation conditions, requiring the pre-fabrication and fitting of the material into the injury. While prefabricated materials may be appropriate for transection-type SCIs, they may be challenging to apply to the most common type of SCI, which is a cyst-like, contusion injury. Most preformed materials would require trimming to fit within the injury or removal of spinal cord tissue to make space for the material, which risks causing further functional damage. Biomaterials that are injectable

and that can form within the injury may be better suited to augment rehabilitation approaches, and may therefore be more translatable than preformed scaffolds for SCI.

A fertile ground for exploring injectable materials is the bioprinting field, where fluid mechanics (i.e., rheology) and cytocompatibility are paramount to success. Several bioinks developed for extrusion-based bioprinting are injectable and form under biologically compatible conditions for cell encapsulation. The development of bioprintable materials, or bioinks, typically involves developing the rheology (e.g., viscosity, yield stress, storage modulus recovery) of biomaterials to be injectable, retain their shape after extrusion, and form under biocompatible conditions. The inherent rheology of bioinks and other paste-like materials are advantageous for surgical delivery and retainment of biomaterials in several areas of regenerative medicine,(80, 82, 83, 251) and could more specifically be advantageous for treating SCI. Other studies have utilized the high viscosity of hyaluronic acid (HA) to make HA-based bioink formulations or injectable hydrogels.(197, 268) We previously adapted a pentenoate-functionalized hyaluronic acid (PHA) hydrogel as a bioink;(81) however, our preliminary *in vitro* studies with rat neural stem cells (rNSCs) showed that PHA did not support rNSC adhesion, similar to what others have found with fibroblasts or oligodendrocyte progenitors on HA-based hydrogels.(197, 268) Those studies incorporated gelatin to promote cellular adhesion (e.g., via the RGD sequences); however, the hydrogels had long curing times (i.e., 2-3 days or 30-60 min), which

may not be sufficiently retained if injected into a hemorrhaging SCI with constant cerebral spinal fluid flow around the cord, and thus unrealistic for translation. Therefore, there is an unmet need for injectable hydrogels with faster gelation times for better retention within the injury. The purpose of this study was to adapt the fast-crosslinking PHA bioink to support neural stem cell growth through the inclusion of the newly developed pentenoate functionalized-gelatin (PGel), while maintaining the paste-like and injectable rheology for bioprinting and translation for application to SCI.

Materials and Methods

Materials

All chemicals were purchased from Sigma-Aldrich unless otherwise stated.

Pentenoate-functionalized hyaluronic acid (PHA) and gelatin (PGel) synthesis

PHA was synthesized from 1.5 MDa hyaluronic acid (HA, actual MW: 1.56 MDa; Lifecore Biomedical, Chaska, MN) as we previously described.(81) PGel was synthesized using a similar protocol using gelatin from porcine skin (Type A, ~300 g Bloom). Briefly, HA or gelatin were fully dissolved in deionized (DI) water (HA: 2 g into 150 mL (0.5 w/v%) at 25°C, gelatin: 5 g in 100 mL at 37°C (5 w/v%)). A catalyst, 4-(dimethylamino)pyridine (HA: 500 mg, gelatin: 250 mg) was then added. Once dissolved, N,N-Dimethylformamide (DMF) (HA: 200 mL (3:1 water:DMF ratio), gelatin: 50 mL (2:1 water:DMF ratio)) was added and allowed

to mix. 4-pentenoic anhydride (12 mL) was added slowly and the pH was maintained between 8.5-9 with dropwise addition of sodium hydroxide (1 M) for 1 hour, until the pH remained constant. The PHA reaction was left to react overnight before dry sodium chloride was added (10 g, 0.5 M). In contrast, the PGel solution (5 mL) was immediately precipitated. Both PHA and PGel were precipitated in acetone with four- or eight times the reaction volume, respectively (40 mL). While PHA was precipitated directly in the glass beaker and then transferred to 50-mL plastic tubes, the PGel (5 mL) was transferred to 50-mL plastic tubes and then precipitated with acetone to prevent adherence to glass upon precipitation. PHA or PGel were centrifuged (6000 x *g*, 3 min) on a Centrifuge 5430R (Eppendorf®, Hamburg, Germany) to pellet the precipitate. The acetone was decanted PHA pellets were collected in a glass beaker with a stir bar and dissolved in DI water (400 mL) overnight. For PGel, DI water was added to each tube with a pellet (20 mL per tube) and placed on a tube rocker (~1 h) until dissolved. PHA or PGel were then dialyzed in DI water (MWCO: 6–8 kDa, VWR) for 48 hours with water exchanges every 12 hours to remove impurities. After dialysis, PHA (at room temperature) or PGel (heated to 37°C on a stirring hot plate) solutions were adjusted to a physiological pH of 7.4 with dropwise addition of sodium hydroxide (1 M), frozen at –20°C, and lyophilized. Dry PGel was stored at –20°C.

1D and 2D NMR of PHA and PGel

The functionalization of PHA was determined using NMR Spectroscopy on a Varian VNMRS-500 MHz NMR Spectrometer equipped with a 5 mm indirect detection room temperature probe (Varian, Palo Alto, CA), as we previously described.(81) NMR samples were prepared by dissolving 2-3 mg of PHA or PGel in 0.7 mL of deuterium oxide (D_2O; Cambridge Isotope Laboratories, Inc., Andover, MA). The PGel sample was dissolved with an internal standard, 3-(Trimethylsilyl)propionic-2,2,3,3-d4 acid sodium salt (TMSP) at 1 mg/mL. To ensure accuracy in the integration, a long recycle and pre-acquisition delay were employed to allow for full relaxation of the protons. Therefore, the integrated proton spectrum of PHA was collected at 80°C (16 scans, 35 s recycle delay, 90-degree pulse width, 60-s pre-acquisition delay). The integrated proton of PGel was collected at 25°C with identical parameters. The percent functionalization of PHA was determined through integration of an alkene peak corresponding to one proton of the pentenoate group (5.82 ppm) and normalization to the acetyl methyl group (1.91 ppm) on the repeating disaccharide. The molar concentration of pentenoate functionalization of PGel was determined through integration of the alkene peak corresponding to one proton of the pentenoate group (5.84 ppm) and quantified using an internal standard (TMSP, 0 ppm), as has been done previously for methacrylated gelatin.(269)

The ^1H resonances for the HA, gelatin, PHA, and PGel were assigned by 2D NMR methods to confirm pentenoate functionalization. The following 2D

experiments were run on gelatin and PGel at 25°C and HA and PHA at 80°C: ^{1}H-^{1}H Total Correlation Spectroscopy (TOCSY), ^{1}H-^{1}H homonuclear correlation spectroscopy (COSY), ^{1}H{^{13}C} heteronuclear single quantum coherence spectroscopy (HSQC), phase edited to distinguish CH_2 and CH_3 signals, and ^{1}H{^{13}C} heteronuclear multiple bond correlation spectroscopy (HMBC). MestReNova software v.12.0.1 (Mestrelab Research, Santiago de Compostela, Spain) was used to process all 1D spectra with a baseline correction, phase correction, and a 1 Hz exponential weighting function. The 2D spectra were collected with 1024 points in f2, 128 points in f1, and a three second recycle delay. Non-uniform sampling was used to reduce data collection time by 50%. The data were then processed with a cosine squared and a gaussian function in the f2 dimension, and a cosine function in the f1 dimension. Zero filling and linear progression were also applied in the f1 dimension to increase the processed data size to 2048 points in f1.

Hydrogel formation

For *in vitro* studies, ethylene oxide gas was used to sterilize dry PHA and PGel (AN74i, Anderson Anprolene, Haw River, NC). Hydrogels made for characterization and *in vitro* studies and were formed as follows. PGel hydrogels were dissolved at 2X in phosphate buffered saline (PBS) at 37°C for 5-10 minutes. PHA/PGel hydrogels were formed by first dissolving PGel in PBS at 2X (37°C for 5-10 min), before adding to PHA to dissolve (4°C, overnight). PGel or PHA/PGel were mixed with photoinitiator, Irgacure 2959 (I2959, 0.05 w/v% final

concentration in the hydrogel) and crosslinker, DL-Dithiothreitol (DTT, ≥98%). Final concentrations of PGel, PHA, and DTT were varied for the *in vitro* and characterization studies and are defined in the subsequent Experimental Design sub-section. The PGel hydrogel precursors were mixed via pipetting. A metal spatula was used to mix PHA/PGel hydrogel precursors and were left for 15–30 min in the dark to fully incorporate the added liquids. Air bubbles were eliminated by centrifugation with a short-spin cycle (30 s).

PHA/PGel hydrogels for all characterization and *in vitro* studies were formed by depositing precursor solutions into a rectangular rubber mold (1 mm thickness) between 2 glass slides followed by crosslinking with a handheld UV light (312 nm, 9 mW/cm^2; EB-160C, Spectroline, Westbury, NY) for 2 minutes. Hydrogels were swollen in PBS overnight at 37°C and cylindrical hydrogels were punched out of the swollen hydrogel with a 6-mm biopsy punch. For *in vitro* studies, all materials aside from PHA and PGel were sterilized via autoclaving or ethylene oxide prior to use and hydrogels were prepared under sterile conditions.

PGel hydrogels for mechanical characterization were formed with the same methods as PHA/PGel hydrogels, except the glass slides were coated with a siliconizing reagent (Sigmacote®) prior to hydrogel formation to prevent the adherence of PGel hydrogels to the glass. PGel hydrogels for *in vitro* studies were fabricated directly in sterile flat-bottomed 96-well or 48-well plates where 33 µL or 100 µL, respectively, of hydrogel precursor was pipetted into each well to coat the bottom and crosslinked with UV light (2 min) under sterile conditions.

Hydrogels were swollen in sterile PBS overnight at 37°C with 2 PBS exchanges (1 and 12 hours after fabrication) to swell out excess DTT.

Experimental Designs

For PGel *in vitro* studies (n = 6-8), mechanical testing (n = 5-6), and swelling/absorption characterization (n = 6), PGel hydrogels were fabricated with varied PGel concentrations (i.e., 5, 10, 15 wt%) and DTT concentrations (i.e., 0.25, 0.5 x_{DTT}, where x_{DTT} is the mmol of DTT per g of PGel). The mass concentrations of DTT for each group were as follows: 5 wt% PGel-0.25 x_{DTT} (1.93 mg/mL), 5 wt%-0.5 x_{DTT} (3.86 mg/mL), 10 wt%-0.25 x_{DTT} (3.86 mg/mL), 10 wt%-0.5 x_{DTT} (7.71 mg/mL), 15 wt%-0.25 x_{DTT} (5.78 mg/mL), and 15 wt%-0.5 x_{DTT} (11.57 mg/mL).

For PHA/PGel *in vitro* studies (n = 5-7), mechanical testing (n = 5-6), and swelling/absorption characterization (n = 6), PHA/PGel hydrogels were fabricated with varied PHA (i.e., 3, 4, 5 wt%) and PGel concentrations (i.e., 5, 10 wt%). The amount of DTT was determined by the summation of the amount needed to crosslink 10% of the repeat units on PHA (given that 34% of the repeat units had pentenoate groups, determined via NMR) and the amount needed for the 0.25 x_{DTT} condition for the PGel. DTT concentrations for each group were as follows: 3%/5% (PHA wt%/PGel wt%) (2.52 mg/mL), 3%/10% (4.45 mg/mL), 4%/5% (2.72 mg/mL), 4%/10% (4.65 mg/mL), 5%/5% (2.92 mg/mL), and 5%/10% (4.85 mg/mL).

For rheological studies, the viscosity (n = 3), yield stress (n = 3 or 5), and storage modulus recovery (n = 3) were characterized of PHA/PGel precursors (i.e., 3%/10%, 4%/5% (PHA wt%/PGel wt%)). For bioprinting and the shape fidelity assessment, the 4%/5% precursor was tested (n = 4).

Mechanical testing and swelling characterization

The compressive elastic modulus of the hydrogels was determined on a Discovery Hybrid Rheometer-2 (DHR-2; TA Instruments, New Castle, DE) using 8-mm parallel plates to compress samples at a 5 µm/s rate (~0.25% strain/second) until 20% strain at 25°C under dry conditions, as previously described.(270) A micrometer was used to measure hydrogel diameters prior to testing and used to calculate the cross-sectional area. A 0.01 N tare load was used to ensure the parallel plates were in contact with the hydrogel before compression and determine the hydrogel height. A custom MATLAB® script was used to calculate the stress by dividing the force by the initial cross-sectional area and to then calculate the slope of the linear portion of the stress-strain curve (i.e., 5-15% strain) to determine the compressive modulus.

For absorption and swelling measurements, hydrogels were immediately punched after gelation into cylindrical hydrogels to measure the fabricated mass. After swelling in PBS (24 h, 37°C), the swollen mass was measured, and then after freezing (–20°C) and lyophilization, the dry mass was measured. The swelling ratio was calculated as the swollen mass divided by the dry mass. The absorption was calculated as the swollen mass divided by the fabricated mass.

Rheological testing

The rheology of PHA/PGel precursors was measured on a DHR-2 rheometer with parallel 20-mm crosshatched plates (25°C, 500 µm gap), as we previously described.(81) Viscosity curves were obtained by a logarithmic shear rate sweep from 0.1 s^{-1} to 100 s^{-1} (3 points per decade). The storage (G') and loss (G") moduli were measured over an oscillatory shear stress sweep from 1 to 1000 Pa, and the yield stress was determined by the crossover point of these storage and loss moduli. After a 5-minute soak time, the storage modulus recovery was measured during three phases of oscillatory shearing at a 1 Hz frequency (i.e., 5 min of 10 Pa shear stress, 30 s of 1000 Pa shear stress, 5 min of 10 Pa shear stress). The initial storage modulus was calculated from the average storage modulus of the initial phase, and the recovered storage modulus was the first recorded storage modulus in the third phase (5 s after the transition from 1000 Pa to 10 Pa). The storage modulus recovery was the recovered storage modulus divided by the initial storage modulus, multiplied by 100%.

The printability was assessed by bioprinting PHA/PGel precursors on an Inkredible+ bioprinter (Cellink®, Gothenburg, Sweden) as we previously described.(81) Briefly, the g-code was generated for a 10 x 10 x 1.2 mm rectangular prism in Repetier-Host (Hot-World GmbH & Co. KG, Willich, Germany) with three layers, 43% rectilinear infill, 10 mm/s printhead speed, and no perimeter. The precursors were back-loaded into a bioprinter cartridge, centrifuged for ~25-30 s on a short spin cycle, and bioprinted through a sterile

polypropylene conical nozzle (27G) (Cellink®) using pressures of 60-80 kPa to reach a consistent flow and print. Images were taken on a Nikon D5500 camera (Nikon, Tokyo, Japan) with a macro lens (Nikon AF-S Micro-NIKKOR 60 mm f/2.8G ED Lens, Nikon). The printability was assessed using a qualitative shape fidelity score as previously described (scale of 0 to 3, where 0 is no shape fidelity and 3 is high shape fidelity with well-defined building potential.(81) ImageJ (National Institutes of Health, Bethesda, MD) was used to analyze the strut size and pore area of the bioprinted precursors. The strut size was determined from several measured widths of horizontal and vertical struts from each sample, and the pore area was determined using the Analyze Particle feature to measure several pores per sample.

Cytotoxicity *in vitro* studies

Unless otherwise stated, all cell culture supplies were purchased from Thermo Fisher Scientific (Waltham, MA). Rat neural stem cells (rNSCs) (Thermo Fisher Scientific) were cultured on tissue culture flasks coated with CTS™ CELLstart™ Substrate (1% diluted in Dulbecco's phosphate-buffered saline with calcium and magnesium (DPBS)) for 1 hour in a 37°C incubator. Cells were cultured with KnockOut DMEM/F-12 Basal Medium supplemented with StemPro Neural Stem Cell Serum Free Medium (NSC SFM) Supplement (2%), recombinant human basic fibroblast growth factor (bFGF; 20 ng/mL), recombinant human epidermal growth factor (EGF; 20 ng/mL), GlutaMAX™-I supplement (2 mM), and penicillin-streptomycin (Pen/Strep; 1%). The medium

was changed every 2-3 days and cells were dissociated with StemPro™ Accutase™ Cell Dissociation Reagent for passaging once they reached 80% confluency. For all *in vitro* studies, rNSCs were seeded on hydrogels at 50,000 cells/cm^2 (passage 3) and cultured for 7 days with medium changes on day 1 and every other day afterwards.

PGel hydrogels were formed in 96-well plates for assays and 48-well plates for imaging. PHA/PGel hydrogels were formed and punched out as described in the previous Hydrogel Formation sub-section and were placed at the bottom of 96-well plates using a sterile metal spatula for both assays and imaging. Additional hydrogels for each group were fabricated without seeded cells to serve as material controls (n = 2 for the PGel study, n = 3 for the PHA/PGel study). Additional wells were coated with CTS™ CELLstart™ as described above and seeded with the same density of cells for a comparator group of normal plated cells (n = 8 for the PGel study, n = 7 for the PHA/PGel study).

The metabolic activity of rNSCs on day 1 and day 7 was measured using the alamarBlue Cell Viability Reagent (Thermo Fisher Scientific), according to manufacturer's instructions. Briefly, after the removal of medium from each well, the alamarBlue reagent (10X) was diluted in pre-warmed medium (1X solution) and 150 µL was added to each well and incubated (6 hours). A BioTek Cytation™ 5 plate reader (BioTek, Winooski, VT) was used to measure the fluorescence (excitation: 540 nm, emission: 590 nm). The fluorescence was normalized to the average fluorescence of the plated cells group for each day. After the alamarBlue

assay, the total DNA content of the same samples was quantified. The alamarBlue/medium was removed from each well and the cells were digested in 150 µL of papain solution (125 µg/mL papain from papaya latex, 5 mM N-acetyl cysteine, and 5 mM (ethylenedinitrilotetraacetic acid disodium salt dihydrate (EDTA) in PBS) overnight at 60°C, as previously described.(257) Samples were stored in tubes in the freezer at –20°C. To prepare samples, tubes were thawed, vortexed, and centrifuged to pellet the polymer (10,000 rpm or 9391 x *g*, 5 min). The total DNA content in the supernatant of each sample was quantified using the Quant-iT PicoGreen dsDNA Assay Kit (Thermo Fisher Scientific), according to manufacturer's instructions. A BioTek Cytation™ 5 plate reader (excitation: 485 nm, emission: 528 nm) was used to measure the fluorescence and the total DNA was determined with a DNA standard curve. To determine the metabolic activity normalized to the total DNA content, the alamarBlue fluorescence of each sample was divided by the total DNA content, with further normalization to the average of the plated cells group or to the 3%/5% (PHA wt%/PGel wt%) group for the PHA/PGel study.

On day 1 and 7, rNSCs on PGel hydrogels in the 48-well plate were stained with the LIVE/DEAD Viability/Cytotoxicity Kit for mammalian cells (calcein AM (2 µM), ethidium homodimer-1 (4 µM) in PBS; Thermo Fisher Scientific) for 20 minutes before replacing the solution with PBS. Images of each hydrogel were taken on a Keyence BZ-X800 Automated Fluorescence Microscope (KEYENCE Corporation of America, Itasca, IL) with z-stacks and were stacked in the

microscope software. Given the aggregations of the cells and the limitations of the LIVE/DEAD stain (i.e., the dead stain intercalating with the DNA without distinct separation between aggregated cells), direct quantification of the viability from counting live and dead cells may be an inaccurate estimate of viability and was not performed.

On day 1 and 7, rNSCs on PHA/PGel hydrogels in 96-well plates were fixed with 10% neutral buffered formalin (VWR) and stored in PBS at –4°C until imaged. Scanning electron microscopy (SEM) images were taken on a Hitachi TM3000 Tabletop SEM (Hitachi, Schaumburg, IL).

Statistical methods

GraphPad Prism (GraphPad Software Inc., La Jolla, CA) was used to perform all statistical analyses. A two-way analysis of variance (ANOVA) was used to analyze results from hydrogel mechanical, swelling, and absorption testing, metabolic activity, DNA content, metabolic activity normalized to DNA content, followed by Tukey's *post-hoc* test. A two-tailed t-test was used to analyze yield stress and storage modulus recovery tests. A two-way ANOVA with repeated measures was used to analyze viscosity curves with Bonferroni's *post-hoc* test to determine the simple effects between the viscosities for each material for each shear rate. $p < 0.05$ was considered significant. Results were reported as the mean ± standard deviation.

Results

Confirmation and quantification of pentenoate functionalization on PHA and PGel

The proton spectra of HA, PHA, gelatin, and PGel were fully assigned (**Fig. 4.1**, **Tables 4.1-4**) by 2D NMR methods, using the ^{1}H-^{1}H 2D TOCSY, COSY, HSQC, and HMBC correlations. The ^{1}H-^{1}H 2D TOCSY separates amino acid residues by correlating protons within a single spin system. The COSY experiments identified the ^{1}H resonances on adjacent carbon atoms within a spin system for sequential assignment (data not shown). The phase edited HSQC experiments correlated the ^{1}H resonance to the ^{13}C resonance of the attached carbon and distinguished CH and CH_3 signals from CH_2 signals (data not shown). The HMBC experiments correlated the ^{1}H resonances with ^{13}C resonances that were separated by 2-3 bonds, effectively placing the amino acid residues within the compound (data not shown).

Each sugar ring of HA is a distinct spin system allowing the ^{1}H-^{1}H 2D TOCSY spectra (**Fig. 4.1A**) to distinguish between the unique sugar ring resonances (**Table 4.1**). The ^{1}H-^{1}H 2D TOCSY peaks of the N-acetyl-D-glucosamine spin system (highlighted in red) showed correlation of the proton signals of the 2, 3, 4, and 5 ring protons (refer to the HA structure in **Fig. 4.1A** for numbering scheme) to the proton signal of ring position 6, correlations to each other and to the ring's anomeric proton at 4.47 ppm. Additionally, weaker correlations from the methyl on the acetyl group (1.9 ppm) to the ring protons

were observed. The of D-glucuronic acid spin system (highlighted in light blue) showed the proton signals (4 to 5 ppm) of the 2', 3', 4', and 5' ring carbons correlated to each other and to the anomeric 1' carbon signal (4.33 ppm). Each amino acid of the gelatin sample is a distinct spin system, and therefore, readily observed in the ^{1}H-^{1}H 2D TOCSY spectra (**Fig. 4.1B**). The proton signals of the following amino acids that were greater than 3 wt%(269) were assigned (**Table 4.3)** and highlighted in **Fig. 4.1B**: arginine (green), lysine (dark blue), proline (orange), hydroxyproline (yellow), alanine (pink), glycine (red), glutamic acid (gray), aspartic acid (dark purple), and serine (light purple).

Pentenoate conjugation occurred at hydroxyl groups in HA. When compared to the HA ^{1}H-^{1}H 2D TOCSY (**Fig. 4.2A**), the PHA ^{1}H-^{1}H 2D TOCSY (**Fig. 4.2B**) showed a new spin system that consisted of four new peaks: two alkenes and two alkanes of the pentenoate group (highlighted in red at 5.82, 5.0, 2.46, 2.29 ppm). The assigned PHA proton signals (**Table 4.2**) from the sugar rings were similar to the signals in HA.

Pentenoate conjugation occurred at hydroxyl and amine groups in gelatin. When compared to gelatin (**Fig. 4.2C**), the PGel spectra showed a new spin system that consisted of four new peaks (**Fig. 4.2D**, highlighted in red at 2.33, 2.51, 5.04, 5.84 ppm) of the pentenoate group. The proton resonances of PGel were assigned (**Table 4.4**) and the pentenoate group in PGel had similar resonances as the pentenoate group of PHA. While two of the amino acid spin systems (i.e., lysine, serine) were not detected in the PGel ^{1}H-^{1}H 2D TOCSY, the

shifted signals from the functionalized lysine were detected (called modified lysine in **Table 4.4**).

Quantification of the pentenoate functionalization of PHA (**Fig. 4.2E**), revealed that 38% of the repeat units were functionalized with a pentenoate group, which was ~0.108 millimoles of pentenoate per gram (mmol/g) of PHA. The quantification of the pentenoate functionalization of PGel (**Fig. 4.2F**), revealed that there was ~0.025 mmol/g of PGel.

PGel mechanical testing and swelling characterization

The compressive moduli of PGel ranged from 4 ± 2 kPa up to 153 ± 18 kPa, where the moduli increased with increased PGel concentration and DTT concentration (**Fig. 4.3A**). The modulus of the hydrogel with the highest PGel and DTT concentrations (i.e.,15%/0.5, PGel wt%/x_{DTT}) was 1.5, 2.9,7.6, 25.9, and 39.7 times greater ($p < 0.0001$) than the 15%-0.25, 10%/0.5, 10%/0.25, 5%/0.5, and 5%/0.25 hydrogels, respectively. The modulus of the 15%/0.25 hydrogel was 1.9, 4.9, 17, and 26 times greater ($p < 0.0001$) than 10%/0.5, 10%/0.25, 5%/0.5, and 5%/0.25 hydrogels, respectively. The modulus of the 10%/0.5 hydrogel was 2.6 greater ($p < 0.001$) than the 10%/0.25 hydrogels, and 8.9 and 13.7 times greater ($p < 0.001$) than 5 wt% PGel hydrogels with 0.5 and 0.25 x_{DTT}, respectively.

The absorption of all PGel hydrogels ranged from 0.80 ± 0.07 to 0.97 ± 0.03, which are all less than 1 and indicated that the hydrogels contracted and lost water after fabrication (**Fig. 4.3B**). The absorption of the hydrogels with the

highest PGel concentration and lowest DTT concentration (i.e.,15%/0.25) were about 12-21% greater than the hydrogels with the same PGel concentration and highest DTT concentration, 15%/0.5 ($p < 0.01$), and the hydrogels with the lowest PGel concentrations, 5%/0.5 ($p < 0.0001$) and 5%/0.25 ($p < 0.001$). The absorption of the middle PGel concentrations, 10%/0.25 and 10%/0.5 hydrogels, were 14-15% greater than that of the 5%/0.5 hydrogels ($p < 0.001$).

The swelling ratio decreased from 15.4 ± 0.5 to 4.4 ± 0.4 as the PGel concentration increased, with a smaller effect from the DTT concentration (**Fig. 4.3C**). The swelling ratio of hydrogels with the lowest PGel concentrations, 5%/0.25 and 5%/0.5, were 1.9-3.4 times higher ($p < 0.0001$) than all the hydrogels with 10 and 15 wt% PGel. The swelling ratio of the 10%/0.25 hydrogel was 21, 39, and 78% greater than the 10%/0.25 ($p < 0.01$), 15%/0.25 ($p < 0.0001$), and 15%/0.5 ($p < 0.0001$) hydrogels, respectively. The swelling ratio of the 10%/0.5 and 15%/0.25 hydrogels were each 47% ($p < 0.0001$) and 28% ($p < 0.01$) greater than the 15%/0.5 hydrogel, respectively.

PHA/PGel mechanical testing, swelling, and rheological characterization

The compressive moduli of the PHA/PGel hydrogels ranged from 63 ± 4 kPa to 172 ± 20 kPa (**Fig. 4.3D**). The hydrogel with the highest PHA and PGel content (i.e., 5%/10%, PHA wt%/PGel wt%) had the highest compressive modulus, which was 1.6-2.7 times greater than all the other tested hydrogels ($p < 0.0001$). Hydrogels with higher PGel content (i.e., 4%/10% and 3%/10%) were

37-70% greater than the hydrogels with the lowest PHA and PGel content, 4%/5% ($p < 0.05$) and 3%/5% ($p < 0.01$).

The absorption of PHA/PGel hydrogels ranged from 1.31 ± 0.03 to 1.51 ± 0.03 (**Fig. 4.3E**). Absorption was higher with greater PHA concentrations, where the 4%/5%, 5%/5%, and 5%/10% hydrogels were 10-16% greater than the 3%/5%, 3%/10%, and 4%/10% hydrogels ($p < 0.0001$).

As seen in **Fig. 4.3F**, the swelling ratios ranged from 10.3 ± 0.2 to 14.7 ± 0.2. Hydrogels with the lower PGel concentration (i.e., 5 wt%) had swelling ratios that were 16-42% higher ($p < 0.0001$) than those of the hydrogels with the higher PGel concentration (i.e., 10 wt%). PHA concentration had less of an effect on the swelling ratio, except the swelling ratio of 3%/10% hydrogels were 15% greater than the 5%/10% hydrogels ($p < 0.01$).

The rheology the 4%/5% and 3%/10% PHA/PGel hydrogel precursors was characterized in **Fig. 4.4**. Both formulations had similar shear thinning viscosity curves (**Fig. 4.4A**) and the viscosities of the 4%/5% and 3%/10% precursors were 4.3 ± 1.2 and 0.9 ± 0.1 Pa-s at the highest tested shear rate of 100 s^{-1}, respectively. The viscosities were not significantly different. At lower shear rates (i.e., 0.10, 0.22, 0.46 s^{-1}), the 4%/5% hydrogel precursor (lighter blue line, circle markers) was 2.4-3.0 times more viscous (1,260 ± 150, 1,100 ±160, 650 ± 110 Pa-s, $p < 0.0001$) than the 3%/10% hydrogel precursor (darker black line, square markers) (520 ± 200, 380 ± 170, 210 ± 130 Pa-s). The yield stress (**Fig. 4.4B**) of the 4%/5% hydrogel precursor (210 ± 20 Pa) was 2.2 times greater ($p < 0.001$)

than the 3%/10% hydrogel precursor (93 ± 20 Pa). The storage modulus recovery (**Fig. 4.4C**) of the 4%/5% hydrogel precursor (79 ± 2%) was 95% greater ($p < 0.001$) than the 3%/10% hydrogel precursor (41 ± 5%). After bioprinting (**Fig. 4.4D**), the 4%/5% hydrogel precursor had good shape fidelity (score = 3) with a strut size of 1.07 ± 0.08 mm and pore area of 0.24 ± 0.03 mm^2. The 3%/10% precursor had poor shape fidelity and did not hold the bioprinted shape (strut size and pore area not able to be measured). Overall, the 4%/5% formulation precursor printed with better shape fidelity and had a higher yield stress and storage modulus recovery than the 3%/10% formulation.

PGel hydrogels promoted rNSC adhesion at lower PGel concentrations

The metabolic activity of the rNSCs seeded on PGel hydrogels for 7 days and normalized to seeded cells is shown in **Fig. 4.5A**. On day 1 the normalized metabolic activity ranged from 0.13 ± 0.05 to 0.19 ± 0.11, which was less than 20% of the metabolic activity of the plated cell control. Cells on the 15%/0.25, 10%/0.25, and 5%/0.5 hydrogels had 2.6 ($p < 0.01$), 2.3 ($p < 0.05$), and 2.3 ($p < 0.05$) times greater metabolic activity than cells on the 15%/0.5 hydrogels. After 7 days, the metabolic activity of cells on all PGel groups ranged from 0.01 ± 0.01 to 0.64 ± 0.07, which was less than 70% of the metabolic activity of the plated cell control, but the cells on the 5%/0.5 hydrogels had 2.3 ($p < 0.0001$), 1.7 ($p < 0.0001$), 1.3 ($p < 0.01$), 4.4 ($p < 0.0001$), and 53.4 ($p < 0.0001$) times higher metabolic activity than cells on all other hydrogels: 5%/0.25, 10%/0.25, 10%/0.5, 15%/0.25, and 15%/0.5, respectively. The cells on the 10%/0.5 hydrogels had

the second highest metabolic activity that was 1.7, 1.3, 3.4, and 40.8 times greater than the metabolic activity of cells on the 5%/0.25 ($p < 0.0001$), 10%/0.25 ($p < 0.05$), 15%/0.25 ($p < 0.0001$), and 15%/0.5 ($p < 0.0001$) hydrogels. The third highest metabolic activity belonged to the cells on the 5%/0.25 and 10%/0.25 hydrogels, which were not significantly different from each other, but were ~2.2 and ~25 times higher than cells on the 15%/0.25 and 15%/0.5 hydrogels ($p < 0.0001$), respectively. Finally, the metabolic activity of the cells on the 15%/0.25 hydrogels was 12.1 times greater than for the 15%/0.5 hydrogels ($p < 0.05$). The greatest to least metabolic activity of cells on PGel hydrogels on Day 7 was 5%/0.5 > 10%/0.5 > 5%/0.25, 10%/0.25 > 15%/0.25 > 15%/0.5 and is denoted by A-E on the right panel of **Fig 4.5A**, where each letter denotes statistical significance of that group relative to groups with all other letters.

The DNA contents of the seeded rNSCs ranged from 53 ± 50 ng to 147 ± 30 ng and are shown in **Fig. 4.5B**. On day 1, four of the hydrogel groups had 2.1-2.8 times greater DNA content than the 5%/0.25 hydrogels: 5%/0.5 ($p < 0.0001$), 10%/0.25 ($p < 0.0001$), 10%/0.5 ($p < 0.001$), and 15%/0.5 ($p < 0.01$). Additionally, the 10%/0.25 hydrogels had 62% more DNA than the 15%/0.25 hydrogels. After 7 days, the DNA content ranged from 97 ± 8 ng to 146 ± 13 ng. The 5%/0.5 hydrogels had the greatest DNA content, which was ~41% greater than the 5%/0.25 ($p < 0.05$), 10%/0.25 ($p < 0.05$), 15%/0.25 ($p < 0.05$), and 15%/0.5 ($p < 0.01$) hydrogels.

To evaluate the metabolic activity on a per cell (i.e., per ng of DNA content) basis, the metabolic activity was normalized to the DNA content. For context to normal plated cells and to allow comparisons between the *in vitro* studies presented here, the data was further normalized to the plated cells group (where 1.0 represents the metabolic activity of the plated cells). The normalized metabolic activity of rNSCs on a per cell basis on PGel hydrogels is shown in **Fig. 4.5C** and ranged from 0.06 ± 0.06 to 0.20 ± 0.14. On day 1, the normalized metabolic activity for all groups was below 20% of the plated cell controls, but the cells on the 15%/0.5 hydrogels had 3.3 times the metabolic activity of the cells on the 15%/0.25 hydrogels ($p < 0.01$). After 7 days, the normalized metabolic activity ranged from 0.03 ± 0.02 to 1.12 ± 0.16 and the cells on the 5%/0.5 and 10%/0.5 hydrogels exceeded the plated cell controls (i.e., normalized metabolic activity > 1.0). Cell on hydrogels with the 5 and 10 wt% PGel had higher metabolic activity than the cells on the 15 wt% PGel hydrogels. Specifically, the hydrogels with the higher DTT concentration, 5%/0.5 and 10%/0.5, had 3.5 times greater normalized metabolic activity than the 15%/0.25 hydrogels ($p < 0.001$), and 33-35 times greater activity than the 15%/0.5 ($p < 0.0001$) hydrogels. On the other hand, the lower DTT concentrations, 5%/0.25 and 10%/0.25, had less of an effect with 2.7 times greater normalized metabolic activity than the cells on the 15%/0.25 hydrogels ($p < 0.05$), and 26 times greater activity than the cells on the 15%/0.5 hydrogels ($p < 0.0001$).

The LIVE and DEAD stains of rNSCs seeded on PGel hydrogels are shown in **Fig. 4.6**, along with plated cell controls (right column). There was qualitatively similar cell adhesion to all hydrogels after 1 day (~12 h) with the presence of live and dead cells (**Fig. 4.6A**). A magnified image of the white inset box is shown to the right of the wider field-of-view image and qualitatively showed that the cells on hydrogels had rounded morphologies. In comparison, plated cell controls qualitatively had more cells with elongated morphologies. After 7 days (**Fig. 4.6B**), several of the 5%/0.5 hydrogels were too soft to handle and were often aspirated into the pipette tips during gentle medium and staining solution exchanges. Few images were able to be obtained, but the visible cells had formed into neurospheres instead of adhering to the hydrogel. In all other groups on day 7, qualitatively similar densities of cells and cell spreading were seen in all hydrogel groups and in the plated cell control. There appeared to be more dead cells on the 15 wt% PGel hydrogels than the 5 or 10 wt% PGel hydrogels.

PHA/PGel hydrogels with less PHA promoted better rNSC adhesion

The metabolic activity of rNSCs seeded onto PHA/PGel hydrogels for 7 days was evaluated and normalized to the plated cells control group (**Fig. 4.7A**). On day 1, the metabolic activities ranged from 0.36 ± 0.01 to 0.83 ± 0.42. While the main effect of the PHA was significant ($p < 0.01$), none of the groups were different from one another other from the Tukey's *post-hoc* test. On day 7, the metabolic activities ranged from 0.65 ± 0.41 to 1.30 ± 0.32. The cells on the 3%/10% hydrogels had the highest metabolic activity and had 2.0, 1.6, and 1.7

times greater metabolic activity than the cells on the 3%/5% ($p < 0.001$), 5%/5% ($p < 0.05$), and 5%/10% ($p < 0.01$) hydrogels, respectively.

The total DNA content of seeded rNSCs on day 1 (**Fig. 4.7B**) were not significantly different among hydrogel groups and ranged from 186 ± 12 ng to 201 ± 9 ng. On day 7, the DNA contents of the seeded cells ranged from 110 ± 29 ng to 220 ± 25 ng. All groups at day 7 had greater DNA contents than the 3%/5% group, where the 3%/10% group had 49% greater ($p < 0.05$) DNA content and all the 4% and 5% PHA containing groups had 1.8-2 times greater DNA content ($p < 0.0001$). Additionally, the 5%/5% hydrogels had 35% greater DNA content than the 3%/10% hydrogels ($p < 0.05$).

The metabolic activity was normalized to the DNA content and further normalized to the 3%/5% hydrogels in **Fig. 4.7C**. On day 1, the main effect of the PHA was significant ($p < 0.01$); however, there were not any individual differences among groups from the Tukey's *post-hoc* test. The range of normalized metabolic activity on day 1 was 0.44 ± 0.02 to 1.04 ± 0.52. After 7 days, the normalized metabolic activity ranged between 0.53 ± 0.10 to 1.16 ± 0.25 and the cells on the 3%/10% hydrogels had the greatest normalized metabolic activity. Cells on the 3%/10% hydrogels had 50-55% greater ($p < 0.01$) and 2.1-2.2 times greater ($p < 0.0001$) normalized metabolic activity than the 4% and 5% PHA containing groups, respectively. Additionally, the cells on the 3%/5% hydrogel had 83-87% greater normalized metabolic activity than both groups containing 5% PHA ($p < 0.01$).

Given the opaque nature of the PHA/PGel hydrogels, SEM images were taken of the seeded cells on day 1 and 7 (**Fig. 4.8**). On day 1 (**Fig. 4.8A**), rNSCs were adhered to all PHA/PGel hydrogels at similar densities, qualitatively. After 7 days (**Fig. 4.8B**), there were qualitatively fewer visible cells on the 3%/5% hydrogels, and the cells did not have spread morphologies. On all other PHA/PGel hydrogels, cells appeared to have spread morphologies and covered a greater portion of the hydrogel than on day 1.

Discussion

We developed and characterized a hyaluronic acid- and gelatin-based hydrogel bioink that supported the adhesion and proliferation of rNSCs. The rheology of the PHA/PGel bioink precursor (i.e., prior to crosslinking) establishes the injectability and paste-like handling properties, which may enable easy surgical placement and retainment within a cyst-like contusion SCI. The pre-crosslinking rheology combined with the fast-crosslinking (~2 min) and post-crosslinking compatibility with rNSCs make the developed PHA/PGel hydrogel a suitable candidate biomaterial for future application for nerve regeneration, specifically for treatment of SCI.

In the current study, we found that PGel hydrogels promoted rNSC adhesion but lacked a printable precursor and degraded quickly *in vitro*. On the other hand, PHA hydrogels had a printable precursor and the hydrogels did not visibly degrade but were not adhesive for rNSCs. Combining PHA and PGel solved the problem of the other to produce a printable precursor that promoted

rNSC adhesion with better long-term stability. The PHA hydrogels had previously been evaluated with seeded rNSCs in preliminary studies and most cells failed to adhere to the PHA and instead formed neurospheres that washed off over the course of the experiment (data not shown). Other studies have similarly shown lack of fibroblast and oligodendrocyte progenitor cell adhesion to HA-based hydrogels, and improved cell adhesion with the inclusion of gelatin.(197, 268) However, the HA/gelatin hydrogels had long gelation times (2-3 days or 30-60 min) which may not be able to be retained in a SCI before gelation. The pentenoate chemistry applied to HA and gelatin in the current study enabled fast UV-crosslinking of all hydrogels.

From the lack of adhesion to PHA, rNSC adhesion was initially evaluated on PGel-only hydrogels with various concentrations of PGel (i.e., 5, 10, 15 wt%) and crosslinker, DTT (i.e., 0.25, 0.5 x_{DTT}) to narrow down potential PHA/PGel formulations. All the PGel formulations supported rNSC adhesion after 1 day, except the softest formulation of the 5% PGel/0.25 x_{DTT}, which were difficult to handle, and by day 7, those hydrogels were easily aspirated or destroyed. After 7 days, the 5 and 10% PGel groups supported better rNSC viability than the 15 wt% PGel groups and were similar to plated cell controls. The PGel hydrogels had similar compressive moduli to rat (7-8 kPa(271)) and human spinal cord (40 kPa(272)), but the metabolic activity of rNSCs was not correlated with stiffness. There was similar metabolic activity per ng of DNA for all the 5% PGel and 10% groups, which all had different compressive moduli (i.e., 4-5 kPa for 5% PGel,

20-53 kPa for 10% PGel). For the rheology, the PGel precursor was injectable, but the watery precursor did not have a yield stress and was not printable via an extrusion bioprinter. Despite the better cell response of rNSCs on 5% and 10% PGel hydrogels than PHA hydrogels, the PGel hydrogels ultimately lacked a printable precursor and showed signs of visible degradation after 7 days.

To improve the integrity of the hydrogel, and to decrease the rate of degradation and improve precursor rheology, PHA was incorporated into PGel hydrogels. Given the better rNSC adhesion and survival on the 5 and 10% PGel hydrogels, different PHA concentrations (i.e., 3, 4, 5 wt%) were incorporated into 5 or 10% PGel hydrogels and evaluated for rNSC adhesion and viability. The PHA/PGel hydrogels showed minimal degradation over 7 days in the current study, and in preliminary studies, did not visibly degrade after 14 days (data not shown). In addition to improved stability, rNSCs had better adhesion to PHA/PGel hydrogels after 1 day (i.e., ~36 to 83%) compared to PGel only hydrogels (i.e., ~13 to 19%), where each study was relative to plated cell controls. There was less rNSC adhesion and lower metabolic activity on the hydrogel with the lowest PHA and PGel concentrations (i.e., 3% PHA/5% PGel), but otherwise there was a trend that as the PHA concentration increased, the metabolic activity decreased. The addition of PHA to PGel hydrogels increased the compressive modulus because of the higher total mass content of polymer. Additionally, the compressive modulus of PHA/PGel hydrogels may have increased compared to PGel hydrogels because PHA/PGel hydrogels formed a single network as a semi-

IPN given that PHA and PGel can crosslink to each other in addition to themselves. However, similar to PGel, the normalized rNSC metabolic activity did not seem to be correlated with stiffness, as the metabolic activity for each PHA concentration was the same, irrespective of the PGel concentration and different stiffnesses. Given that PHA hydrogels alone did not support rNSC adhesion, the decreased adhesion with higher PHA concentrations on PHA/PGel hydrogels was most likely due to the lack of cell adhesion to PHA. The highest rNSC metabolic activity and cell adhesion was on the 3%/10% PHA/PGel formulation, followed by the 4%/5%, and 4%/10% formulations.

Of the crosslinked PHA/PGel formulations that promoted the best rNSC adhesion, the rheological properties of 3%/10% and 4%/5% pre-crosslinked (precursor solutions) were tested to determine their printability as bioinks and thus their potential for injectable placement. While the 4%/10% formulation showed the same metabolic activity per DNA content as the 4%/5%, the hydrogel precursor was not tested because of the high PGel concentrations, which were twice the amount needed for the 4%/5% formulation. Previously, we demonstrated three rheological tests to quantify the printability for an extrusion-based bioprinter: yield stress, viscosity, and storage modulus recovery.(81) From the viscosity curves, both formulations in the current study were shear-thinning and could be extruded through a tapered nozzle. Both formulations had a yield stress, which theoretically enables shape retention. The 4%/5% had a higher yield stress than the 3%/10% and required slightly higher pressures on a

pneumatic bioprinter to extrude, but both used moderate pressures within the capabilities of the bioprinter.

The most significant rheological difference between the two PHA/PGel formulations was the storage modulus recovery. After experiencing high shear stresses, similar to the high shear stresses of being bioprinted through a nozzle, the 4%/5% had good recovery of the storage modulus (i.e., ~80%); however, the 3%/10% formulation had poor recovery (i.e., ~40%). While both formulations had a yield stress and theoretically could retain a shape, the poor storage modulus recovery resulted in the printed shape relaxing immediately after extrusion through a nozzle, or poor post-printing shape retention. For surgical placement, poor post-extrusion shape retention corresponds to potential leakage from the defect site after injection. Overall, the 4%/5% PHA/PGel hydrogel precursor printed successfully and retained high shape fidelity and the 3%/10% hydrogel precursor printed without retaining any shape fidelity. These results are consistent with the results from our previous study where 4% PHA hydrogel precursors printed with high shape fidelity and 3% PHA hydrogel precursor printed and immediately relaxed into a puddle with no retained shape.(81) In the current study, the high molecular weight of the HA (i.e., 1.5 MDa) may have influenced the printability of PHA/PGel more than the lower molecular weight gelatin (i.e., 50-100 kDa), as even the addition of 10 wt% gelatin did not improve the printability of the 3 wt% PHA.

In addition to the development of the 4%/5% PHA/PGel hydrogel as a printable bioink, the ability of the hydrogel precursor to be injectable has translational potential for application to SCI and in regenerative medicine in general. The injectability (i.e., shear thinning) of the PHA/PGel may enable injection of the material into a contusion type SCI, which may be easier for surgeons to use and less invasive compared to implantation of a preformed scaffold (although shape memory polymers in highly deformable hydrogels are one of the few examples of an injectable preformed scaffold(70)). In contrast to other less viscous and injectable HA or gelatin hydrogel precursors used for SCI,(70, 76, 78) the PHA/PGel hydrogels were paste-like to enable better retention in the injury. Besides paste-like materials, HA/gelatin hydrogels developed for bioprinting were pre-crosslinked to enable post-printing shape retention,(197, 253) which may translate to material retention within an SCI. A comprehensive review by Macaya and Spector(75) discussed other injectable scaffolds that can undergo gelation within an injury and that have been applied to SCI (e.g., agarose, collagen, fibrin/fibrinogen, hyaluronic acid/methylcellulose). While there were several injectable material precursors, there were other intrinsic disadvantages of several materials such as the limited degradation of agarose (> 6 weeks *in vivo*) or too fast of degradation of fibrin (< 7 days *in situ*). As an additional example, these authors observed in several studies that collagen materials delivered as liquid precursors required a ‘clean’ hemi- or transection injury, as any hemorrhage impeded gelation or resulted in uneven gelation.

More homogeneous gelation may be achieved from immediate gelation (e.g., modified self-assembling peptides, peptide amphiphiles), or alternatively from more viscous or paste-like material precursors that can be retained in the injury until gelation. For a more comprehensive review of the necessary precursor rheology for material placement in surgical applications and bioprinting in a broader context outside of SCI, we refer readers to our recent review.(80) However, there are limited studies involving paste-like biomaterial precursors for SCI,(69) and the rheological characterizations of the material have not typically been performed. The significance of the PHA/PGel developed in the current study is the paste-like precursor rheology (i.e., possession of a yield stress) and good shape retention after extrusion (i.e., high storage modulus recovery). The rheological parameters not only enabled the precursor to be bioprinted with good shape fidelity, but may additionally enable translation for better material precursor retention after injection into a contusion SCI until gelation, which is rapid for PHA/PGel (2 minutes) with exposure to UV light.

In addition to evaluating the rheology and cell adhesion, we demonstrated the utility of 2D NMR techniques in confirming and quantifying the functionalization of PHA and the newly synthesized PGel. Several polymers, including PHA and PGel, typically have several overlapping signals in the ^{1}H spectra, which make characterization with conventional 1D NMR challenging. For PGel, the assignment of all the proton signals was more complex than PHA because gelatin is composed of several amino acids in varying amounts and

sequences, whereas hyaluronic acid is a repeating disaccharide unit. While 1D NMR methods have been commonly used to confirm functionalization of a variety of biomaterials, fewer studies have utilized 2D NMR characterizations of HA and gelatin.(269, 273) For more complex spectra of polymers, 2D NMR methods may be necessary to distinguish new signals of a functional group from shifted original polymer signals. Specifically for HA and gelatin, the assigned $^{1}H\{^{13}C\}$ 2D HSQC spectra have been used to show polymer functionalization.(269, 273) In the current study, we used an HSQC and other experiments (i.e., COSY, HMBC, TOCSY) to fully assign the signals in the HA and gelatin spectra, which had chemical shifts that were similar to those in the limited studies in the literature that reported the resonances. Furthermore, instead of showing the assigned HSQC experiment, we demonstrated the utility of a ^{1}H-^{1}H 2D TOCSY to confirm the functionalization by visualizing the distinct spin system of the pentenoate group in PHA and PGel and distinguishing the new signals from shifted original polymer signals.

Quantification of gelatin functionalization can be challenging due to the inherent variable amino acid composition of gelatin. In studies using methacrylated gelatin, methacrylation occurs mostly at amines, and the most common methods to determine the degree of methacrylation are by measuring the corresponding decrease in amines/lysines. Measuring the decrease has been done qualitatively/quantitively with NMR (by observing the lysine methylene signals at 2.8–2.95 ppm) and/or by a quantitative measure of free amines (e.g.,

the Habeeb method/2,4,6-Trinitrobenzene Sulfonic Acid (TNBS) assay).(274-277) However, in the current study, there were two problems with measuring decreased lysine signals for determining the degree of functionalization of PGel. First, the assumption that functionalization only occurs on the free amine of lysines may not be valid for PGel, where both amines and hydroxyls on several amino acids (e.g., lysine, hydroxyproline, serine) could be functionalized by pentenoate groups. Second, lysine was not detected in the NMR spectra of PGel. Even though shifted signals from functionalized lysine was present, the modified lysine signals overlapped with arginine signals on the 2D spectra, which did not allow for an integration calculation of the functionalized lysine peak. Another more direct measure of the degree of functionalization that has been used is the integration of the methacrylate double bond normalized to the phenylalanine signal,(278) but this method requires the amino acid composition to be known. Finally, a simpler and more robust method by Claaßen *et al.*,(269) directly quantified the amount of methacrylate by normalizing the integrated signals of the methacrylate group to a new internal standard (i.e., TMSP), which was included in the sample at a known concentration. The method using TMSP as an internal standard was performed in the current study for determination of functionalization with the pentenoate group on gelatin (see Methods). The PHA was more functionalized per gram than PGel, which may be because PHA has more pentenoate modifiable groups (i.e., multiple hydroxyls per repeat unit) per unit mass than PGel (i.e., not all of the amino acids can be functionalized). In the

context of the study that developed the TMSP method, which had several methacrylated gelatins with the functionalization ranging from 0.34 to 0.96 mmol/g, the PGel developed in the current study had a lower pentenoate functionalization of 0.025 mmol/g. There is room for improvement to fabricate higher functionalized PGel for hydrogels with improved mechanical performance; however, in the current study we demonstrated that by adjusting the PGel concentration (i.e., 5 to 15 wt%) and crosslinker concentration (i.e., 0.25 or 0.5 x_{DTT}), the PGel hydrogels could achieve a wide range of compressive elastic moduli from 4 to 153 kPa. Overall, the 2D NMR enabled confirmation and quantification of the functionalization with the pentenoate group on PHA and newly developed PGel.

Conclusions

The previously developed PHA bioink had limited rNSC adhesion, thus, in the current study, a new functionalized gelatin, PGel, was developed, characterized with 2D NMR, and was found to promote cell adhesion. However, the PGel-only hydrogels lacked printability and degraded quickly *in vitro*. In the combination of PHA and PGel, each solved the problem of the other to formulate a printable hydrogel precursor before crosslinking and a post-crosslinked hydrogel that was adhesive for cells and stable over time. The shear thinning property of the precursor was important for extrusion of the paste-like PHA/PGel precursor for printing, and may additionally enable injection to a SCI. Furthermore, the possession of a yield stress and recovery of the storage

modulus was important for shape retention of the precursor after printing, which may translate to better material retention after injection in a SCI, until the rapid formation (2 minutes) of the PHA/PGel hydrogels. The 4%/5% PHA/PGel hydrogel was identified to meet our criteria of rNSCs adhesion and bioprintability. The significance of the current study was the development of the injectable and paste-like PHA/PGel rheology to overcome the typical challenges of a liquid hydrogel precursor and enable material retention in a future SCI application. We identified a platform with two common materials (i.e., HA and gelatin) that were combined, and determined the final formulation specifically for future application to SCI based on both the precursor rheology (pre-crosslinking) and the cell adhesion of the crosslinked hydrogel. Other investigators may apply the rheological characterizations in the current study to a variety of biomaterials for future development of new bioinks or injectable materials for other biomedical engineering applications.

Chapter 5 : Conductive and Injectable Hyaluronic Acid/Gelatin Hydrogels for Treating Rat Spinal Cord Injury [4]

Abstract

In patients with spinal cord injury (SCI), full functional recovery is uncommon with current clinical treatments. Rehabilitation strategies have resulted in better functional recovery when motor training was combined with electrical stimulation (ES); however, patients with more severe injuries that do not benefit as much from rehabilitation strategies alone may require the incorporation of tissue regeneration for full functional recovery. There is growing evidence in the SCI literature indicating the need to combine the fields of rehabilitation and regenerative medicine to maximize functional recovery. Unfortunately, there are limited methods to synergistically combine rehabilitation and regenerative medicine, but conductive biomaterials could be the missing link that enables synergistic combination with ES. There are limited studies with conductive biomaterials for SCI. One problem is that many conductive biomaterials are pre-formed scaffolds, which may hinder clinical translation to a contusion-type SCI. Alternatively, an injectable biomaterial, such as those from the bioprinting field, may be more translational for contusion SCIs. In the current

[4]In preparation to *Acta Biomaterialia* as: Kiyotake EA, Thomas EE, Homburg HB, Milton CK, Smitherman AD, Donahue ND, Fung KM, Wilhelm S, Martin MD Detamore MS. Conductive and Injectable Hyaluronic Acid/Gelatin Hydrogels for Treating Rat Spinal Cord Injury.

work, a conductive and injectable/bioprintable hydrogel was developed by incorporating gold nanorods (GNRs) into a previously developed fast crosslinking, bioprintable pentenoate-functionalized hyaluronic acid (PHA) and pentenoate-functionalized gelatin (PGel) hydrogel. High aspect ratio GNRs were synthesized and the toxic CTAB coating was exchanged with non-toxic citrate. The GNR hydrogels were conductive and supported the adhesion and viability of seeded rat neural stem cells (rNSCs). Finally, the GNR, PHA/PGel, PHA, or PGel hydrogels were applied to a T8 lateral hemi-section rat spinal cord injury (SCI) model. While no significant differences in functional recovery or regeneration were found between any of the tested material groups, the feasibility and long-term safety of implanting the GNR hydrogel was established. With no previous studies evaluating a GNR-based conductive hydrogel for application to SCI, this study filled that gap and, in the future, may provide a tunable translational platform for application to the more clinically relevant model of contusion SCIs with applied ES.

Introduction

Spinal cord injury (SCI) affects 294,000 people in the United States currently, with 17,800 new patients every year.(25) Functional recovery is uncommon after SCI with current clinical treatments. There are two main approaches to promote functional recovery after SCI: 1) rehabilitation approaches and 2) regenerative medicine approaches. Rehabilitation approaches include motor training, electrical stimulation (ES), and/or

neurochemical stimulation to promote the plasticity and reorganization of the remaining axonal pathways. Regenerative medicine approaches include cells, drugs, biologics, and/or scaffolds to repair and regenerate axonal pathways. For SCI, rehabilitative and regenerative medicine approaches individually have not yet resulted in full functional recovery in humans, and each has limitations.

Significant functional recovery, although not full functional recovery, has been made using rehabilitation approaches. For example, epidural ES (EES) is ES delivered through a surgically implanted electrode patch on the spinal dura at the injury site. In rats and cats, locomotor training and/or pharmacological stimulation have been able to produce a stepping response after incomplete SCIs by activating spinal locomotor circuits (also known as central pattern generators (CPGs)) and/or promoting neural plasticity and reorganization in spared tissue (covered in detail in a few excellent reviews by Shah *et al.*(84) and Rossignol *et al*.(85)). In rats with a complete transection and no spared tissue, a stepping motion can still be elicited and controlled through sensory feedback that activates the CPGs.(86) While rodents may not need the motor cortex to produce locomotion, the development of a stepping response in humans has been more difficult to achieve than in rats thus far. Activation of and control of CPGs with sensory input to generate locomotion in humans may be a more immediate approach to recover locomotion, but tissue regeneration may still be necessary for full recovery.

Motor training alone does not typically result in full functional recovery in humans with complete injuries, but EES combined with motor training has been widely investigated *in vivo* and in clinical trials (clinicaltrials.gov) with promising results. In a few recent small clinical studies, electrode arrays were developed that delivered ES via spatially controlled patterns of activation in specific intervals for stepping motions (spatiotemporal control). Spatiotemporal ES with motor training together enabled independent stepping (with assistive devices) in patients with incomplete injuries (AIS grade B).(88-90) More recently, EES alone has been able to demonstrate volitional muscle control, but not yet stepping, while EES was active in the first seven patients with complete injuries in the Epidural Stimulation After Neurologic Damage (ESTAND) clinical trial.(87)

Despite the promising results of rehabilitation approaches, patients with more severe injuries that do not benefit as much from rehabilitation approaches may need regenerative medicine strategies to first regenerate the tissue and axonal pathways for full functional recovery. However, there has been limited functional recovery seen with regenerative medicine approaches so far and there have been fewer regenerative medicine approaches in clinical trials compared to rehabilitation approaches. Therefore, the combination of regenerative medicine and rehabilitation, known as regeneration rehabilitation,(7, 19) may be needed for full functional recovery. Several *in vivo* studies(8, 279) and a few clinical trials for SCI have already applied regenerative rehabilitation principles (e.g., cells + motor training, scaffold + EES). From the better outcomes that have been

achieved with rehabilitation approaches for SCI thus far, there is a need for regenerative medicine approaches to be translated for use in the clinic and to be developed to complement and enhance the rehabilitation approaches. One regenerative medicine solution may be to use conductive biomaterials to synergistically integrate regenerative medicine approaches and rehabilitation approaches.

Conductive biomaterials combined with ES and motor training could better deliver ES directly to neurons, to simultaneously promote tissue regeneration and neural plasticity for enhanced functional recovery. We refer readers to three excellent reviews that cover conductive biomaterials with electrical stimulation.(21, 24, 44) *In vitro* studies with conductive materials and ES have improved differentiation and neurite growth,(98) and may be able to regenerate axons. Furthermore, clinical ES may facilitate reorganization of intact spinal networks with the regenerated axons and promote better functional recovery. The development of additional conductive biomaterials that can incorporate regenerative medicine approaches and possibly be synergistic with ES are needed.

Given that most biomaterials are insulators, higher conductivities (i.e., semi-conductor range) have been achieved by creating composites by combining biomaterials with conductive components (e.g., carbon-based structures, conductive polymers, metallic-based particles). Composites with conductive polymers tend to have lower conductivities than composites with carbon-based

materials or metallic particles. Carbon-based composites typically have cytotoxicity concerns.(22, 24, 161) However, metal nanoparticles, such as gold nanoparticles, impart high conductivities to composites and are known to be inert and biocompatible.(280) Gold nanoparticle-based composites have been widely investigated for tissue engineering purposes, particularly in cardiac, muscle, and peripheral nerve applications. However, the use of gold nanoparticles in hydrogels to treat SCI has been limited to using gold nanoparticles for growth factor delivery,(199) not to fabricate a conductive composite. To create a conductive composite by blending conductive nanoparticles, high concentrations are typically needed. In that context, the advantage of higher aspect ratio nanoparticles (e.g., nanorods, nanotubes, nanowires) is that the required threshold concentration to achieve conductivity is decreased.(21) A few studies by Navaei *et al.*(203, 206, 207, 210) fabricated conductive gold nanorod (GNR) hydrogels for cardiac and skeletal muscle applications. GNR biomaterials may be a promising approach for developing a conductive biomaterial for SCI; however, many biomaterials are preformed scaffolds that may be more challenging to implant into a human contusion SCI with ill-defined borders than into an animal model with a well-defined surgical defect.(10-16) There is a need for the development of biomaterials that are not only conductive, but also translational for SCI. While preformed scaffolds may be challenging to implant into a contusion SCI, injectable hydrogel precursors (i.e., before crosslinking) that can form a hydrogel (i.e., crosslinked) under biological conditions within the injury

may be well-suited for translation to SCI. Furthermore, a common clinical limitation of typically less viscous hydrogel precursors is leakage out of the injury before crosslinking, and a more viscous or paste-like rheology of the precursor is needed, such as bioinks from the extrusion bioprinting field.

The purpose of the current study was to fabricate a translational biomaterial platform for SCI by developing a conductive hydrogel that had 1) an injectable and paste-like precursor, 2) biocompatible crosslinking conditions, and 3) was conductive once crosslinked. Given that several conductive biomaterials have non-biocompatible crosslinking conditions and hydrogel precursors are typically less viscous, conductive, injectable, and paste-like hydrogel precursors are needed for minimally invasive delivery and enhanced material retainment in the injury. In the current study, we synthesized high aspect ratio, citrate capped-GNRs (citrate-GNRs) and incorporated into a previously developed bioprintable hydrogel formulation comprised of pentenoate-functionalized hyaluronic acid (PHA) and pentenoate-functionalized gelatin (PGel). We evaluated the conductivity and ability of the GNR hydrogels to support adhesion and the viability of rat neural stem cells (rNSCs). We characterized the rheology of the GNR hydrogel precursor for evaluating the injectability and paste-like consistency for both, translatability and printability. Finally, we evaluated the feasibility, long-term safety, axon regeneration, and functional recovery after delivering a GNR hydrogel to an acute, lateral thoracic level (T8) hemi-section in a rat SCI model. The goals of the current study were to develop and demonstrate the feasibility of

a conductive GNR hydrogel as a translational platform that can be synergistically combined with ES in a regenerative rehabilitation approach to maximize functional recovery after SCI.

Materials and Methods

Materials

Gold(III) chloride trihydrate ($HAuCl_4$, ≥99.9%), hexadecyltrimethylammonium bromide (CTAB) (≥99%), hydrochloric acid (HCl, 37%), hydroquinone (≥99.0%), nitric acid (HNO_3, 70%), polyvinylpyrrolidone (PVP, M_W: 55,000), silver nitrate ($AgNO_3$, ≥99%), sodium borohydride ($NaBH_4$, 99%), sodium hydroxide (NaOH, ≥98%), hydrogen peroxide (H_2O_2, 30%), L-ascorbic acid (AA, ≥98%), sodium citrate tribasic dihydrate (≥99%) and all other chemicals were purchased from Sigma-Aldrich (St. Louis, MO) unless otherwise noted. Acetone (≥99.5%) was purchased from VWR (Radnor, PA). All reagents for gold nanorod synthesis were prepared with nanopure water from a Purist Pro UV Ultrapure Water System (RephiLe Bioscience, Ltd., Boston, MA) and prepared fresh daily except for $HAuCl_4$ and NaOH. All glassware and Teflon-coated stir bars were cleaned with aqua regia (3:1 HCl:HNO_3) and rinsed 15 times with nanopure water before each synthesis.

GNR Synthesis

High aspect ratio CTAB-capped GNRs (CTAB-GNRs) were synthesized using a seed mediated growth method that used hydroquinone, instead of

ascorbic acid, to achieve high yields (~100%), high aspect ratios (~6-8), and minimal sphere contamination, according to a protocol established by Vigderman and Zubarev(281) (see graphic in **Fig. 5.1A**). The seed-mediated method involved a growth solution of CTAB, $HAuCl_4$, $AgNO_3$, and hydroquinone, where the latter is a weak reducing agent that reduced Au^{3+} to Au^{+}. Subsequent addition of small gold seeds (1-2 nm in diameter) to the growth solution catalyzed the reduction of Au^{+} onto the surface of the seeds. The CTAB surfactant and silver block growth by preferentially adhering to the {110} facets of gold (i.e., the sides of the rods) and thus, encourage growth on the {001} plane (i.e., the ends of the rods), resulting in an anisotropic nanorod shape.

For the seed solution, reagents were prepared as described here: $NaBH_4$ (0.01 M) was prepared in NaOH (0.01 M) and was placed at –20°C for 20 minutes, and CTAB (0.1 M) was fully dissolved in nanopure water on a stirring hotplate set to 30°C. The seed solution was made in a 20-mL scintillation vial with a cleaned stir bar (5/8” x 5/16”) under vigorous stirring (setting 3) on a 30°C, C-MAG HS 7 hotplate (IKA Works, Inc., Wilmington, NC). The CTAB (5 mL, 0.1 M) solution was added to the vial followed by the addition of $HAuCl_4$ stock (50 µL, 50 mM), which led to a color change from clear to orange. The ice-cold (liquid, not solid) $NaBH_4$ (230 µL, 0.01 M) was taken from the –20°C freezer after 20 minutes and added rapidly in one shot to the $HAuCl_4$/CTAB solution, which was followed by an immediate color change to light brown. The solution was stirred for 15-20 minutes to make 1-2 nm gold seeds, which was verified by Ultraviolet-

Visible-Near infra-red (UV-Vis-NIR) spectroscopy on an Agilent Cary 5000 UV-Vis-NIR spectrophotometer (Agilent, Santa Clara, CA) (described below) and Dynamic Light Scattering (DLS) on a Malvern ZetaSizer (Malvern Instruments, Worcestershire, UK) (described below).

GNRs were synthesized in cleaned glass bottles (250 mL bottles, ~100 mL batches) with a cleaned stir bar (1 ½" x 3/8") under heavy stirring (setting 2) at 30°C on a hotplate. The additional reagents were prepared as follows: $AgNO_3$ (0.1 M) and hydroquinone (0.1 M) were dissolved in nanopure water and wrapped in aluminum foil to protect from light. A growth solution in each bottle was prepared as follows: to 100 mL of CTAB (0.1 M), $HAuCl_4$ stock (1 mL, 50 mM) was added, which led to a color change from clear to orange. $AgNO_3$ (700 µL, 0.1 M) was added, then hydroquinone (5 mL, 0.1 M) was slowly but continuously added, resulting in a color change from orange to clear. The growth solution was stirred for 5-10 minutes on the 30°C hotplate before the seed solution (160 µL) was added. The growth solution with the seed solution was kept stirring for 15-20 minutes on the 30°C hotplate, and the solution started turning cloudy within the first 2-5 minutes. After the 15-20 minutes, the stir bars were removed and the bottles were transferred to a 30°C water bath for 12 hours, where the solution gradually turned dark brown as GNRs formed. GNR formation was confirmed via UV-Vis-NIR, as described below.

To purify the GNRs, the reaction solution from each bottle was centrifuged on a Centrifuge 5910R (Eppendorf®, Hamburg, Germany) at 13,500 x *g* for 20

minutes in 50-mL tubes and carefully decanted. Each 50 mL tube was washed with 30 mL of PVP (112 mM, using the molecular weight of the repeat unit) as a steric stabilizer to prevent aggregation. GNRs were centrifuged a second time to remove most of the PVP, decanted, and each tube was washed in 50 mL of nanopure water. GNRs were centrifuged a third time to concentrate in ~3-5 mL of nanopure water.

Citrate-GNRs via Indirect Ligand Exchange

The cytotoxic CTAB on CTAB-capped GNRs was replaced with non-toxic trisodium citrate through an indirect ligand exchange protocol (see graphic in **Fig. 5.1B**), as previously described.(209) The process involved coating GNRs with a thin (~4 nm) layer of silver to displace the CTAB, followed by the use of a hydrogen peroxide in a sodium citrate solution to etch away the silver and leave a clean GNR surface stabilized by citrate. The original protocol was adapted for longer and higher aspect ratio GNRs with the following minor modifications: initial GNR concentration (0.38 mg/mL) and the Ag:Au ratio (0.158:1).

Briefly, the reagents were prepared as follows: PVP (112 mM) was diluted to 47 mM in nanopure water, sodium citrate (10 mM), and H_2O_2 (3%) were each prepared in nanopure water, AA (40 mM) was prepared in nanopure water and wrapped in aluminum foil to protect from light, and $AgNO_3$ (10 mM) was prepared in nanopure water and diluted to 0.3 mM and protected from light with aluminum foil. The concentrated CTAB-GNRs (30 mL, 0.38 mg/mL) were diluted in nanopure water. To coat CTAB-GNRs with silver, in a 1000 mL bottle, the PVP

(144 mL, 47 mM), CTAB-GNRs (30 mL, 0.38 mg/mL), and AA (3 mL, 40 mM) were mixed for ~2 minutes on a stir plate (setting 1.5-2). In one rapid addition, the $AgNO_3$ (30 mL, 0.3 mM) was then added and the solution was stirred for 10 minutes at room temperature. Acetone (414 mL) was added at a 2:1 ratio of acetone:solution volume and was mixed well (~3 min), followed by centrifugation (13,500 x *g*, 10 min) in 50-mL tubes. Acetone was decanted and the loose GNR pellets in the remaining acetone were sonicated (1 min) using a Branson 3800 Ultrasonic Cleaner (Cleanosonic, Richmond, VA). Then the pellets were pipetted and combined into one 50-mL tube that was centrifuged (13,500 x *g*, 10 min), re-dispersed in sodium citrate (6 mL, 10 mM), and transferred to a 100-mL glass bottle. To etch away the silver and CTAB and leave a clean surface on the GNRs, 3% H_2O_2 (27 mL) was added to the sodium citrate solution and left for 3 hours at room temperature. The solution was then centrifuged (13,500 x *g*, 15 min) in a 50-mL tube and re-dispersed in sodium citrate (3 mL, 10 mM) for 12 hours at room temperature to complete the ligand exchange. The solution was centrifuged (13,500 x *g*, 20 min), re-dispersed in nanopure water (30 mL), and sonicated (3 min). Citrate-capping of GNRs (citrate-GNRs) was confirmed with zeta potential measurements and gel electrophoresis, as described below, to distinguish between the positive charge of CTAB and the negative charge of citrate.

For *in vitro* and *in vivo* studies, citrate-GNRs were diluted to 100 mL before being sterile-filtered using a Steriflip® PLUS membrane (MilliporeSigma, Burlington, MA), centrifuged (13,500 x *g*, 20 min) and re-suspended in nanopure

water (6 mL). The sterile citrate-GNRs were confirmed via UV-Vis-NIR and TEM, and concentration/mass distribution were determined via ICP-MS.

GNR Characterization

UV-VIS-NIR

UV-Vis-NIR samples were prepared by diluting centrifuged GNRs in nanopure water (~1:10 ratio GNRs to water) to bring samples into the concentration range of the instrument. UV-Vis-NIR spectra were collected in quartz cuvettes and scanned from 300-1300 nm on an Agilent Cary 5000 UV-Vis-NIR spectrophotometer (Agilent, Santa Clara, CA) after collecting a baseline using nanopure water.

Zeta Potential

Surface charge of GNRs (pH 6.0-6.5) was determined with zeta potential measurements with a Malvern ZetaSizer (Malvern Instruments, Worcestershire, UK) in a disposable zeta potential cuvette. Samples for zeta potential of CTAB-GNRs were taken directly after the second centrifugation from the 200 mL batch of GNRs that were resuspended in 100 mL of nanopure water (no dilution necessary). Samples of citrate-GNRs were taken after the final centrifugation of the indirect ligand exchange (no dilution necessary).

Gel Electrophoresis

Surface charge of GNRs was further confirmed with gel electrophoresis using a VWR® Gel Electrophoresis System (VWR). Agarose gels were prepared

as follows: agarose (0.5 w/v%) was mixed in 0.5X Tris-Borate-EDTA (TBE) buffer (Fisher, Waltham, MA) in a 250 mL Erlenmeyer flask, heated in a microwave (2 min total with swirling every 30 s) until dissolved, cooled until just warm, and poured into a gel tray with a comb in a casting apparatus. The agarose was set at room temperature for 1 hour. The gel was run in a gel box filled with TBE buffer (0.5X) at 50V for 1 hour. Samples of CTAB-GNRs or citrate-GNRs (10 µL) were mixed with 2 µL Ficoll 400 to keep the samples in the wells, and 10 µL of sample was loaded into each well.

Transmission Electron Microscopy

TEM samples were prepared by drying 2 µL of GNRs onto copper grids (Carbon Type-B 300 mesh Copper; Ted Pella Inc., Redding, CA) that were plasma-coated. TEM images were taken by a 200-kV field emission JEOL2010F analytical TEM (JEOL-USA, Peabody, MA) equipped with a Direct Electron DE-12 camera. ImageJ software was used to determine the length and width from ~250 GNRs from the collected TEM images. The aspect ratio was calculated from these images by dividing the length by the width of each rod.

Inductively Coupled Plasma-Mass Spectrometry

Elemental analysis measurements for total gold content and nanorod mass quantification were performed using a NexION2000 ICP-MS (Perkin Elmer, Waltham, MA) fitted with a High Efficiency Sample Introduction System, as previously described.(282, 283) Batch ICP-MS samples were prepared by

dissolving 10 µL of GNRs (from the 200 mL batch resuspended in 3 mL of nanopure water) into 1 mL of aqua regia for 5 minutes. The GNRs in aqua regia were further diluted in nanopure water to obtain a concentration in range of the instrument and prepared standard curves. Final dilutions for batch ICP-MS ranged from $5x10^4$ to $2.5x10^6$-fold dilutions of the original GNR concentration (from a 200 mL batch resuspended in 3 mL). Single-particle ICP-MS samples were prepared using a $5x10^6$-fold dilution into nanopure water.

To determine the total dissolved gold in the digested nanorod samples, a prepFAST IC sample introduction system (Elemental Scientific Inc., Omaha, NE) was used and a dissolved gold calibration curve was made. The instrument was operated in standard peak hopping mode. Au195 signal was grouped to the signal from the internal standard-Ir193. 5 replicates were collected to ensure accuracy of the measurements. Synthesis yield was determined based on the mass concentration of Au measured by ICP-MS compared to the theoretical maximum amount of Au in a 200 mL batch of GNRs (19.7 mg). Yield from the indirect ligand exchange was determined by dividing the mass concentration of Au measured after the exchange by the amount of Au measured before.

To determine the mass of intact individual nanorods, single particle ICP-MS was employed.(284) The instrument was used in single-particle mode and the parameters/conditions are listed in **Table 5.1**. The introduction system consisted of a 2.0-mm quartz injector (PerkinElmer), an Asperon Spray Chamber (PerkinElmer), and a high efficiency concentric glass nebulizer (HEN Meinhard).

Samples were delivered to the nebulizer at a flow rate of 10 µL min^{-1} using a Single Cell Micro DX Autosampler (Elemental Scientific Inc.). To maximize analyte signal and reduce interferences the ICP-MS was tuned with the NexION setup solution (PerkinElmer, N8145051). Fast sequential measurements of ion signals from atomized nanoparticles were obtained by sending nanoparticles through an argon plasma. All data were acquired and processed in Syngistix single-cell/single-particle Application Module Software V.1.5 (PerkinElmer). The SP-ICP-MS particle transport efficiency was determined using commercially available polystyrene microparticles (~3 µm in diameter) doped with Lu175 (Fluidigm, South San Francisco, CA) according to a previously published procedure.(285) The transport efficiency was 58.5 ± 3.9%. The mass detector was configured to only analyze Au197 signal and the ICP-MS was calibrated with dissolved gold ion standards made from serially diluting a stock solution of 1000 µg/mL (Au) ICP Single-Component Standard in 2% HCl (High Purity Standards 100021-2-100, North Charleston, SC). With the dissolved Au calibration curve and the measured pulse intensity from a nanorod ion plume, the nanorod mass was back-calculated as described by Pace *et al.*(284) The Syngistix software was used to apply a threshold to all samples and enhance the signal to noise ratio via collection of signal at three standard deviations (3σ) above the continuous background.(286)

Pentenoate-functionalized hyaluronic acid (PHA) and gelatin (PGel) synthesis

PHA was synthesized from hyaluronic acid (HA, actual MW: 1.56 MDa; Lifecore Biomedical, Chaska, MN) as we previously described.(81) PGel was synthesized using an adapted PHA synthesis protocol. PGel was made from gelatin from porcine skin (Type A, ~300 g Bloom, Sigma Aldrich). Briefly, HA (2 g) or gelatin (5 g) were dissolved in deionized (DI) water (HA: 0.5 w/v%, 150 mL, gelatin: 5 w/v%, 100 mL, 37°C), and then a catalyst, 4-(dimethylamino)pyridine (Sigma Aldrich) (HA: 500 mg, gelatin: 250 mg), was added. N,N-Dimethylformamide (DMF, Sigma Aldrich) was added (PHA: 3:1 water:DMF, 200 mL, PGel: 2:1 water:DMF, 50 mL) and mixed before 4-pentenoic anhydride (Sigma Aldrich) (PHA: 2.4 mL per g of HA or gelatin) was slowly added. A pH of 8.5-9 was maintained using dropwise addition of sodium hydroxide (1 M) for 30 minutes to 1 hour. The PHA reaction was left to react overnight before sodium chloride was added (final concentration 0.5 M, 10 g). In contrast, the PGel was immediately precipitated. PHA or PGel were precipitated in acetone at a volume that was four- or eight times the reaction volume, respectively. PHA was precipitated directly in the glass beaker and PGel was precipitated in plastic 50-mL tubes to prevent adherence to glass. PHA or PGel were centrifuged (6000 x *g*, 3 min) on a centrifuge 5430R (Eppendorf®) and the acetone was decanted. PHA pellets were transferred to a glass beaker before dissolving in DI water (400 mL). PGel pellets were dissolved in DI water (20 mL per tube) in each tube. PHA

or PGel were then dialyzed in DI water (MWCO: 6–8 kDa, VWR) with water exchanges every 12 hours for a total of 48 hours. PHA or PGel were adjusted to a physiological pH of 7.4 using dropwise addition of sodium hydroxide (1 M) (PGel was additionally heated to 37°C). PHA or PGel were frozen at –20°C and lyophilized. Dry PHA and PGel were stored at –20°C.

PHA and PGel characterization

PHA and PGel functionalization were determined using Nuclear Magnetic Resonance (NMR) Spectroscopy using a Varian VNMRS-500 MHz NMR Spectrometer equipped with a 5 mm indirect detection room temperature probe (Varian, Palo Alto, CA), as we previously described.(81) Briefly, to prepare NMR samples, PHA (2-3 mg) or PGel (10 mg) were dissolved in 0.7 mL of deuterium oxide (D_2O; Cambridge Isotope Laboratories, Inc., Andover, MA). PGel samples were additionally dissolved with 3-(Trimethylsilyl)propionic-2,2,3,3-d_4 acid sodium salt (TMSP, 1 mg/mL, Sigma Aldrich) as an internal standard. The proton spectra of PHA and PGel were collected at 80°C and 25°C, respectively, with 16 scans, a 35 s recycle delay, 90-degree pulse width, and a 60 s pre-acquisition delay to ensure accuracy in the integration and allow for full relaxation of the protons. The spectra were processed/analyzed in MestReNova software v.12.0.1 (Mestrelab Research, Santiago de Compostela, Spain). The degree of functionalization of PHA was determined through peak integration of the alkene proton from the pentenoate group (5.82 ppm) and normalization to the acetyl methyl group (1.91 ppm). 34% of the repeat units of the PHA used in the current

study were functionalized with pentenoate groups, which was a molar concentration of 0.097 mM. The molar concentration of PGel was determined via integration of the alkene proton peak from the pentenoate group (5.84 ppm) compared to the internal standard, TMSP (0 ppm). PGel had 0.025 mM of pentenoate groups.

Crosslinking to form hydrogels

Four types of hydrogels were used in the current study for *in vitro* and *in vivo* studies: 1) PGel, 2) PHA, 3) PHA/PGel, 4) PHA/PGel/GNRs. The specific groups and concentrations that were investigated are specified in the corresponding sections below. Dry PHA and PGel were sterilized using ethylene oxide gas (AN74i, Anderson Anprolene, Haw River, NC) for *in vitro* and *in vivo* studies. PHA/PGel hydrogels made for all characterization, *in vitro* studies, and *in vivo* studies consisted of PHA (4 wt%, 40 mg/mL), PGel (5 wt%, 50 mg/mL), the photoinitiator Irgacure 2959 (I2959, 0.05 w/v%), the crosslinker dithiothreitol (DTT, 2.72 mg/mL), GNRs (varying concentrations, indicated in each methods section), and nanopure water. Hydrogels were formed as follows: PGel (61.8 mg/mL) was dissolved in the sterile citrate-GNR suspensions or in nanopure water for 5-10 minutes. The PGel solution was used to dissolve the PHA (49.4 mg/mL), which was further dissolved overnight at 4°C. The next day, I2959 stock (5 mg/mL) was dissolved in nanopure water in a 60°C bead bath for 20 minutes, and a DTT stock (30 mg/mL) was dissolved in nanopure water at room temperature. The dissolved PHA/PGel solution was mixed with I2959 (100 µL of

5 mg/mL stock added per mL of total hydrogel) and DTT (90.8 µL of 30 mg/mL stock added per mL of total hydrogel) at room temperature with a metal spatula. PHA/PGel precursors were left for 15–30 min in the dark to fully incorporate the added liquids. PHA/PGel precursors were mixed once more and centrifuged with a short-spin cycle (30 s) to eliminate air bubbles.

Hydrogels for all characterization and *in vitro* studies (see graphic in **Fig. 5.2**) were formed by placing precursor solutions into a rectangular cutout in a rubber mold (1 mm thickness) between 2 glass slides and were UV-crosslinked with a handheld 312 nm light at 9 mW/cm^2 (EB-160C, Spectroline, Westbury, NY) for 2 minutes on each side. Hydrogels were swollen overnight at 37°C in nanopure water. A 6-mm biopsy punch was used to punch out cylindrical hydrogels.

Hydrogel characterization

Conductivity testing

For electrical conductivity testing, different concentrations of citrate-GNRs (i.e., 0, 0.4, 0.6, 0.8, 1.0, 1.2 mg/mL) were incorporated into PHA/PGel hydrogels (n = 5 or 6). Nanopure water was used to fabricate the hydrogels, as opposed to PBS, to minimize the ionic conductivity and to measure the direct electrical conductivity of the hydrogel. While PBS better mimics the *in vitro* and *in vivo* environments, the ionic conductivity of free ions in solution does not have the same cellular effects as electrical conductivity.(23) Given the sodium counterion on the PHA, PHA/PGel hydrogels with no gold were ionically conductive and were

included as baseline controls. Hydrogel resistance was measured using the two-probe method with a 34401A Agilent Multimeter (Agilent, Santa Clara, CA) as adapted from previous methods.(287) Briefly, two wires from the multimeter were attached to copper tape on the top and bottom of paper-covered parallel plates on an Instron 5969 uniaxial tester (Instron, Norwood, MA). Excess surface moisture was removed from the hydrogels with a Kimwipe™ (but the hydrogel itself was still hydrated), the hydrogel was set on the copper tape, and the top plate was lowered until there was complete contact with the hydrogel. The resistance measurements were logged for 1-2 min (~400 data points) and the resistance of each sample was determined as the average of the stable data points (20^{th} data point to the last data point). Prior to testing, the heights and diameters of the hydrogels were measured with a micrometer and the latter was used to calculate the circular cross-sectional area of each sample. The conductivity was calculated as the inverse of the resistivity, which was the cross-sectional area multiplied by the resistance and divided by the length (i.e., height of the gel).

Mechanical testing

PHA/PGel hydrogels with (0.8 mg/mL) and without citrate-GNRs were tested for solid mechanics (n = 5 or 6), as previously described.(270) The compressive elastic moduli of the hydrogels were determined by compression at a strain rate of 5 μm/s (~0.25% strain/second) with 8-mm parallel plates until 20% strain at 25°C (under dry conditions) on a Discovery Hybrid Rheometer-2 (TA

Instruments, New Castle, DE). Prior to testing, a 0.1 N tare load was applied to hydrogels to ensure the geometry was in contact with the hydrogel surface and determine the hydrogel height. Hydrogel diameters were measured on a micrometer prior to testing to calculate the cross-sectional area. The compressive elastic modulus was calculated in a custom MATLAB® script as the slope of the linear portion of the stress-strain curve (i.e., 5-15% strain), where stress was calculated as the force divided by the initial cross-sectional area.

Absorption and swelling characterization

For absorption and swelling measurements, PHA/PGel hydrogels with (0.8 mg/mL) and without citrate-GNRs were tested (n = 6). Hydrogels were formed and immediately punched into cylindrical hydrogels to measure the fabricated mass. The swollen mass was measured after swelling in nanopure water (24 h, 37°C), and the dry mass was measured after freezing at –20°C and lyophilization overnight. The swelling ratio was calculated as the ratio of the swollen mass to the dry mass. The absorption was calculated as the ratio of the swollen mass to the fabricated mass.

Rheology and shape fidelity of the hydrogel precursor

For rheological characterization, the viscosity (n = 3), yield stress (n = 3), and storage modulus recovery (n = 3) were measured on a DHR-2 rheometer equipped with parallel 20-mm crosshatched plates, as we previously described.(81) All rheology was performed at 25°C with a 500 μm gap. Briefly,

viscosity curves were evaluated using a logarithmic shear rate sweep (0.1 s^{-1} to 100 s^{-1}). The yield stress was determined from the crossover point of the storage (G') and loss (G") moduli, which were evaluated using an oscillatory shear stress sweep (1 to 1000 Pa). The storage modulus recovery was evaluated with a series of three phases of oscillatory shearing (1 Hz) after a 5-minute soak time: 5 min of 10 Pa shear stress (initial storage modulus), 30 s of 1000 Pa shear stress, and 5 min of 10 Pa shear stress (recovered storage modulus). The storage modulus recovery was calculated as the recovered storage modulus divided by the initial storage modulus and multiplied by 100%.

The printability of the PHA/PGel/GNR hydrogel precursor was assessed (n = 3) by bioprinting with an Inkredible+ bioprinter (Cellink®, Gothenburg, Sweden) as we previously described.(81) The hydrogel precursor were backloaded into a printing cartridge printed with a 27 G tapered nozzle (Cellink) into a 3-layer, 10 mm x 10 mm grid with 43% infill and no perimeter. PHA/PGel/GNRs required ~100-105 kPa of pressure for proper extrusion. A Nikon D5500 camera (Nikon, Tokyo, Japan) with a macro lens (Nikon AF-S Micro-NIKKOR 60 mm f/2.8G ED Lens, Nikon) was used to image the printed constructs. The strut sizes and pore areas of the bioprinted precursor constructs were analyzed in ImageJ (National Institutes of Health, Bethesda, MD). The average strut size from each print was determined from several measured widths of horizontal and vertical struts, which were then averaged across the samples. The average pore area was calculated using the Analyze Particle feature to

measure several pores from each sample, which were then averaged across the samples.

Cytotoxicity *in vitro* studies

For *in vitro* studies, PHA/PGel hydrogels with different concentrations of sterile citrate-GNRs (i.e., 0, 0.4, 0.6, 0.8 mg/mL) were formed and seeded with cells (n = 4 or 5) or were used as acellular material controls (n = 3). Hydrogels were formed as mentioned earlier, except under sterile conditions, and were placed into the bottom of a sterile 96-well flat-bottomed plate.

All cell culture supplies were purchased from Thermo Fisher Scientific (Waltham, MA) unless otherwise stated. Rat neural stem cells (rNSCs) were purchased from Thermo Fisher Scientific. The rNSCs were cultured in tissue culture flasks that had been coated (1 h in a 37°C incubator) with CTS™ CELLstart™ Substrate (1% diluted in Dulbecco's phosphate-buffered saline with calcium and magnesium (DPBS)). The medium was changed every 2-3 days with KnockOut DMEM/F-12 Basal Medium supplemented with StemPro Neural Stem Cell Serum Free Medium (NSC SFM) Supplement (2%), recombinant human basic fibroblast growth factor (bFGF; 20 ng/mL), recombinant human epidermal growth factor (EGF; 20 ng/mL), GlutaMAX™-I supplement (2 mM), and penicillin-streptomycin (Pen/Strep; 1%). StemPro™ Accutase™ Cell Dissociation Reagent was used to dissociate cells for passaging once they reached 80% confluency. For the *in vitro* study, cells were seeded at 50,000 cells/cm^2 (passage 2, 16,000 cells/gel) and cultured for 7 days with medium changes on days 1, 3, 5, and 7.

The media from the cell-seeded hydrogels with 0.8 mg/mL GNRs and no GNRs were collected for quantification of released gold by ICP-MS (n = 3). Media samples were taken on day 1, 3, 5, and 7. Media samples (50 µL) were digested in aqua regia (10-fold dilution) for 1 hour in a 60°C water bath before 50 µL was diluted in nanopure water (100-fold dilution) and analyzed by batch ICP-MS according to the GNR Characterization methods section. The background from a media-alone sample was subtracted from all the other samples. The theoretical maximum gold content per GNR hydrogel was estimated to be 22.6 µg based on the GNR concentration and volume of the hydrogel. The gold content in the media samples was divided by the theoretical maximum gold content to estimate the amount of released gold as a percentage of the total gold in a hydrogel.

To evaluate cell adhesion and viability on day 1 and day 7, the alamarBlue Cell Viability Reagent (Thermo Fisher Scientific) was used to measure the metabolic activity of rNSCs, according to manufacturer's instructions. The medium from each well was removed, and the alamarBlue reagent (10X) was added to pre-warmed complete medium to obtain a 1X solution, which was added to each well and incubated for 6.5 hours. The fluorescence (excitation: 540 nm, emission: 590 nm) was measured on a BioTek Cytation™ 5 plate reader (BioTek, Winooski, VT). The fluorescence was normalized to the average fluorescence of the 0 mg/mL GNR hydrogel group for each day. After the alamarBlue assay, the same samples were used to measure the total DNA content. The alamarBlue/medium was removed from each well and the cells were digested

overnight at 60°C in 150 µL of papain solution (125 µg/mL papain from papaya latex, 5 mM N-acetyl cysteine, and 5 mM ethylenedinitrilotetraacetic acid disodium salt dihydrate (EDTA) in PBS), as previously described.(257) Samples were stored at –20°C until further testing. For testing, samples were thawed, vortexed, and centrifuged (10,000 rpm or 9391 x *g* for 5 min) to pellet any polymer. The DNA content in the supernatant was quantified with the Quant-iT PicoGreen dsDNA Assay Kit (Thermo Fisher Scientific), according to manufacturer's instructions, and the fluorescence was measured on a BioTek Cytation™ 5 plate reader (excitation: 485 nm, emission: 528 nm). The metabolic activity of each sample was normalized to the DNA content by dividing the raw alamarBlue fluorescence by the total DNA content (ng), with further normalization to the average of the 0 mg/mL GNR hydrogel group.

Experimental groups for *in vivo* study

Five study groups were evaluated using a thoracic-level (T8) lateral hemi-section SCI model in rats (n = 6-8). The sham group was defined in the current study as animals given a SCI with no treatment, and the other four groups were PGel, PHA, PHA/PGel, and PHA/PGel/GNRs (denoted the GNR hydrogel group). Concentrations used were 5 wt% PGel for all PGel-containing groups, and 4 wt% PHA for all PHA-containing groups. The concentration of GNRs in the GNR hydrogel group was 0.8 mg/mL. Hydrogel precursors were formed as described in previous sections.

Surgical procedure

All animal experiments were approved by the Institutional Animal Care and Use Committee of the University of Oklahoma Health Sciences Center (protocol #19-005-SA). Adult female Sprague-Dawley rats (225-275 g) were purchased from Charles River Laboratories (38 total) and were acclimated for at least 72 hours before surgery. Rats were anesthetized with 4% isoflurane with oxygen and maintained with 1-4% isoflurane as needed. Immediately prior to surgery, buprenorphine SR (1-1.2 mg/kg, subcutaneous (SC) injection, ZooPharm, Laramie, WY) was given as an analgesic, meloxicam SR (4 mg/kg, SC, ZooPharm) was delivered as an analgesic and anti-inflammatory, and oxytetracycline (50-60 mg/kg, SC, Covetrus, Portland, ME) was given for preventing infection, including bladder infection. Animals were on a heated pad during pre-operative, intra-operative, and postoperative periods to prevent hypothermia. The dorsal midline was shaved and aseptically prepared with three rounds of alternating chlorohexidine (Covetrus) with 70% alcohol. Immediately before surgery, animals received three scrubs of povidone iodine (Covetrus) and an ophthalmic lubricant (Covetrus) applied to both eyes. Surgery was performed under sterile conditions with intra-operative monitoring, as per IACUC guidelines.

A single midline incision was made through the skin on the back from just above the scapulae and extended 3-4 cm in the caudal direction, followed by blunt dissection that exposed the muscular layer. Parallel cuts were made on either side of the spinal cord from T6 to T10 and the muscles along the spinal

cord were retracted. To expose the spinal cord, a multilevel dorsal laminectomy from T7-9 was performed using fine tipped rongeurs, and the dura mater was removed with fine-tipped forceps. To ensure a consistent T8 lateral spinal cord hemi-section, one midline cut and two medial to lateral cuts approximately 2.0-2.5 mm apart were made on the right side of the cord followed by removal with forceps. Approximately ~50-100 µL of hydrogel precursor was injected through a tapered nozzle (1 mL syringe, 27G nozzle) into the spinal cord injury cavity and crosslinked *in situ* with a handheld UV light (312 nm, EB-160C, Spectroline). A sterile drape with a fenestration was placed over the animal to shield and protect the animal from UV light exposure during material crosslinking (~2 minutes for the hydrogel groups, except ~5 min for GNR hydrogel group). For the sham group, a hemi-section injury was performed but no material was implanted.

Following the hemi-section and material implant, the muscular, subcutaneous, and subcuticular/skin layers were all closed with 4-0 Vicryl sutures in an interrupted pattern. Triple antibiotic ointment was given topically for infection prevention as needed. Additional doses of the buprenorphine SR and meloxicam SR were given every 72 hours if needed. Manual bladder expression was performed twice daily until bladder function recovered (~7-9 days post-injury).

Tissue/organ processing

8 weeks post-injury, animals were humanely euthanized according to American Veterinary Medical Association (AVMA) guidelines by cardiac perfusion after being anesthetized with 4% isoflurane and maintained with

intraperitoneal injections of ketamine (89-100 mg/kg, Covetrus) and xylazine (5-10 mg/kg, Covetrus). Once deeply anesthetized, the chest cavity was exposed and a butterfly catheter was placed into the left ventricle of the heart, while a cut was made into the right auricle. The aortic arch was clamped, and PBS (~105 mL) was slowly injected via syringe pump to remove the blood, followed by 4% formaldehyde (~105 mL) for fixation.

For all rats, a segment of the spinal column was removed and fixed (48 h) in 10% formalin, followed by removal of the spinal cord, and storage in 70% ethanol until histological and immunohistochemistry (IHC) analyses. For the sham group (n = 3) and the GNR hydrogel group (n = 3), the blood, brain, kidney, liver, and spleen were collected for histological and ICP-MS analyses to determine gold content. Blood was collected from the heart using a syringe before the system was flushed with PBS and 4% formaldehyde. The blood was stored at –20°C until analyzed by ICP-MS analysis. The brain, kidney, liver, and spleen were isolated, weighed, and fixed in 10% formalin for 48 hours before a cross-section was removed and stored in 70% ethanol for histological analysis. The remaining amount of each organ was frozen at –20°C until analyzed by ICP-MS.

Functional recovery assessment

Functional recovery for all rats was recorded using a Nikon D5500 (B&H Video, New York City, NY) during a 5-minute open field test using a fabricated acrylic box (40 x 40 x 40 cm). Measurements were taken weekly, starting from prior to surgery (week 0) to the 8-week endpoint (week 8). Videos were

randomized and the affected (right) limb was scored using the Basso, Beattie, and Bresnahan (BBB) Open-Field Locomotion Scoring by a blinded scorer. The BBB scale measures hindlimb movement by accounting for use of individual joints, coordinated limb movement, and weight-bearing movement on a scale of 0 to 21, where 0 indicates no movements and 21 is normal movements.(288) Any rats with bilateral injuries were excluded from the analyses.

Histology & immunohistochemistry

Spinal cords and organs stored in 70% ethanol were paraffin embedded, sectioned, and stained using conventional methods. Spinal cords were sectioned in the coronal plane and organs were sectioned transversely (4 μm thickness). For histological analysis on spinal cords and organs, the Leica ST5020 multistainer (Leica Biosystems, Wetzlar, Germany) was used with the SelecTech hematoxylin and eosin (H&E) staining system (Leica Biosystems), following the manufacturer's protocol. All staining was evaluated by a hospital pathologist.

For IHC, the spinal cord sections were stained for neurons and axons using a neurofilament medium/heavy antibody (NF-M/H, dilution: 1:400, mouse monoclonal IgG_1, cat # sc-32273, Santa Cruz Biotechnology, Dallas, TX), astrocytes using a glial fibrillary acidic protein (GFAP) antibody (dilution: 1:1500, cat # ab33922, rabbit monoclonal IgG, Abcam), oligodendrocytes using an ionized calcium-binding adaptor molecule 1 antibody (Iba1, dilution: 1:6000, cat # ab178846, rabbit monoclonal IgG, Abcam), new neurons using a nestin antibody (dilution: 1:1500, cat # ab221660, rabbit monoclonal IgG, Abcam), and

CSPGs using a chondroitin sulfate-56 (CS-56) antibody (dilution: 1:400, cat # C8035-.2ML, mouse monoclonal IgM, Sigma Aldrich). The IHC was performed on a Leica Bond RX platform (Leica Biosystems) using Polymer Refine Detection system (DS9800). In brief, formalin-fixed, paraffin-embedded (FFPE) tissues were sectioned at 4-8 µm and mounted on positively charged slides. The slides were dried overnight at room temperature and incubated at 60°C for 45 minutes. Slides were transferred to the Leica Bond RX for dewax and then treated for target retrieval at 100°C for 20 minutes in a retrieval solution, either at pH 6.0 (for NF-M/H, GFAP, and CSPG antibodies) or pH 9.0 (for Iba1 and Nestin antibodies). The sections were incubated with 5% goat serum (cat # 01-6201, Thermo Fisher Scientific) for 30 minutes. Endogenous peroxidase was blocked using peroxidase-blocking reagent, followed by the selected incubation for 60 minutes. For the secondary antibody, post-primary IgG-linker and/or Poly-HRP IgG reagents was used. Detection was done using 3, 3-diaminobenzidine tetrahydrochloride (DAB) as chromogen (10 minutes) and counter stained with hematoxylin. Completed slides were dehydrated (Leica ST5020), and mounted (Leica MM24). Antibody specific positive control and negative control (omission of primary antibody) were stained in parallel.

ICP-MS on organs

For ICP-MS analysis of the gold content in the blood and organs, the samples were thawed, and a small section of the organs (~200-700 mg) was weighed, minced, and digested in 20-mL borosilicate scintillation vials. For the

blood, ~100 mL was pipetted directly into the scintillation vial. Nitric acid (800 µL) was added to each sample and samples were digested in a 60°C water bath for 3 hours, followed by addition of hydrochloric acid (200 µL) for another 3 hours in a 60°C water bath. Samples (1 mL) were diluted in nanopure water (40-fold for a 2.5% acid concentration) and 5 mL of each sample was passed through a Millex®-GP syringe filter (0.22 µm, PES membrane, MilliporeSigma). Batch ICP-MS was run using the same parameters as mentioned in the GNR Characterization methods. The total mass of gold per organ was calculated by multiplying the measured gold concentration by the total volume (40 mL) and dividing by the mass of tissue that was digested to get the gold per gram of tissue. The gold per milliliter of blood was calculated by multiplying the measured gold concentration by the 40-fold dilution and the initial 11-fold dilution. For each organ, the background (i.e., average amount of gold in the sham rat organs) was subtracted from the amount of gold in the corresponding organ of the rats of the GNR group. Given that 50 to 100 µL of GNR hydrogel was injected into the SCI at a concentration of 0.8 mg/mL of GNRs, the expected total gold that was delivered was 40 to 80 µg, or 60 µg on average. The gold per organ as a percentage of the total estimated gold delivered (i.e., 60 µg) was estimated for each organ by multiplying the gold per gram of organ by the total mass of the organ, dividing by expected total gold delivered, and multiplying by 100%.

Statistical methods

All statistical analyses were performed in GraphPad Prism (GraphPad Software Inc., La Jolla, CA). An unpaired t-test was used to compare the CTAB- and citrate-GNR's aspect ratio, length, and width, and the yield stress, and storage modulus recovery. A one-way analysis of variance (ANOVA) was used to analyze results from hydrogel conductivity, mechanical, swelling, and absorption testing, metabolic activity, and metabolic activity normalized to DNA content, followed by Tukey's *post-hoc* test. A two-way ANOVA was used to analyze the viscosity curves and DNA content. A mixed-effects analysis with repeated measures was used to analyze the BBB scoring and was followed by Tukey's *post-hoc* test. Differences with $p < 0.05$ were considered significant. Results were reported as the mean ± standard deviation.

Results

CTAB- and citrate-GNRs characterization

UV-Vis-NIR spectra in **Fig. 5.3A** of the seed solution (dashed gray line) and CTAB-GNRs (solid black line) confirmed the formation of gold nanorods with longitudinal (LSPR) and transverse surface plasmon resonance (TSPR) peaks at 1125 nm and 507 nm, respectively. The TEM images of CTAB-GNRs in **Fig. 5.3B** (upper left image) further confirmed the formation of nanorods with minimal contamination by spheres. After replacing the CTAB with citrate on GNRs, the UV-Vis-NIR spectrum of citrate-GNRs (**Fig. 5.3A**, solid lighter blue line) confirmed that there were nanorods with the same LSPR and TSPR peaks as the

CTAB-GNRs. **Fig. 5.3B** (upper right) shows a representative TEM image of the citrate-GNRs, with higher magnification images in the lower half, which confirmed that GNRs had not changed shape and appeared better dispersed than CTAB-GNRs. The replacement of CTAB with citrate was verified by a change in surface charge from 37 ± 7 mV of CTAB-GNRs to -25 ± 8 mV of citrate-GNRs (**Fig. 5.3C**, left side), given that CTAB is positively charged and citrate is negatively charged. Gel electrophoresis showed that the citrate-GNRs migrated toward the cathode (**Fig. 5.3C**, right side) and further verified the negatively charged citrate-GNRs, as compared to the CTAB-GNRs, which stayed in the well.

The aspect ratio, length, and width of the CTAB- and citrate GNRs were determined from ImageJ analyses (**Fig. 5.4A-C**, respectively), and the mass distributions were determined from SP-ICP-MS (**Fig. 5.4D**). Citrate-GNRs had ~6% higher aspect ratios (7.7 ± 1.2 vs. 7.1 ± 1.6, $p < 0.0001$) and were ~8% longer (70 ± 10 nm vs. 65 ± 13 nm, $p < 0.0001$) than CTAB-GNRs, but did not have significantly different widths (9.2 ± 0.7 vs. 9.3 ± 0.8 nm). Single-particle ICP-MS showed that CTAB- and citrate-GNRs had similar mass distributions with overlapping mass histograms.

Batch ICP-MS was used to measure the total gold content of the CTAB-GNRs and citrate-GNRs. The synthesis had an ~80% yield, based on the theoretical gold content in a 200-mL batch of GNRs (19.7 mg) and total measured gold content of the CTAB-GNRs (15.8 mg). After replacing the CTAB-coating with citrate and sterile-filtering, there was a ~29% yield as determined by comparing

the starting mass of CTAB-GNRs used for the indirect-ligand exchange (11.4 mg) to the total measured gold content of the citrate-GNRs (3.3 mg). The yield was further confirmed by the 3-fold decrease in absorbance of the UV-Vis-NIR spectrum for citrate-GNRs compared to the CTAB-GNRs (λ_{LSPR} = 1.00 vs 0.33).

Conductivity, swelling, and mechanical performance of GNR hydrogels and bioprintability of the precursor

The conductivity of the PHA/PGel/GNR hydrogels (or GNR hydrogels) were determined with varied amounts of GNRs (i.e., 0, 0.4, 0.6, 0.8, 1.0, and 1.2 mg/mL), where the conductivity increased along with increasing GNR content up to 0.8 mg/mL GNRs (**Fig. 5.5A**). The conductivity of the 0.8 mg/mL GNR hydrogel group ($1.15x10^{-5} \pm 0.19x10^{-5}$ S/cm) had 71% and 58% higher conductivity than the 0 mg/mL and 0.4 mg/mL groups ($p < 0.01$), respectively. The conductivity of the 0.6 mg/mL GNR hydrogel group ($1.07x10^{-5} \pm 0.09x10^{-5}$ S/cm) was 57% and 44% higher than the 0 and 0.4 mg/mL groups ($p < 0.05$), respectively. The conductivity of the 1.0 mg/mL and 1.2 mg/mL GNR hydrogels were not significantly different from any other group, therefore, the 0 to 0.8 mg/mL concentrations were tested *in vitro*.

The compressive elastic moduli, absorption, and swelling ratio of the most conductive GNR hydrogel (i.e., 0.8 mg/mL GNRs) were compared to PHA/PGel, PHA, and PGel hydrogels (**Fig. 5.5B-D**, respectively). As shown in **Fig. 5.5B**, the compressive elastic moduli of the GNR hydrogels were not significantly different from the moduli of PHA/PGel hydrogels (83 ± 30 kPa and 78 ± 10 kPa,

respectively). Compared to PHA or PGel hydrogels alone, the GNR hydrogels were 2.9 times stiffer than PHA hydrogels (29 ± 2 kPa, $p < 0.0001$) and 21 times stiffer than PGel hydrogels (4 ± 2 kPa, $p < 0.0001$). Similarly, PHA/PGel hydrogels were 2.7 and 20 times stiffer than PHA hydrogels ($p < 0.001$) and PGel hydrogels ($p < 0.0001$), respectively. The PHA/PGel hydrogels had greater compressive moduli than PHA or PGel hydrogels alone, but the addition of the GNRs to the PHA/PGel did not improve the compressive elastic modulus.

As shown in **Fig. 5.5C**, the water absorption of the GNR hydrogels was 2.7, 3.2, and 5.6 times greater ($p < 0.0001$) than PHA, PHA/PGel, and PGel hydrogels, respectively. PHA and PHA/PGel hydrogel absorptions were 2.1 and 1.8 times greater ($p < 0.0001$) than those of PGel hydrogels, respectively. Similar trends were observed for swelling in **Fig. 5.5D**, where the swelling ratios of GNR hydrogels were 1.7, 3.1, and 3.4 times greater ($p < 0.0001$) than for PHA, PGel, and PHA/PGel, respectively. PHA hydrogels had a swelling ratio that was 1.8 and 2.0 times greater ($p < 0.0001$) than those of PGel and PHA/PGel, respectively. PGel hydrogels had a swelling ratio 10% greater than those of PHA/PGel ($p < 0.05$). Overall, the addition of GNRs to PHA/PGel increased the absorption of water from fabrication to the swollen state, and increased the swelling ratios of the swollen state to the dry state.

The viscosity, yield stress, and storage modulus recovery (**Fig. 5.6**) of the GNR hydrogel precursor (labeled as PHA/PGel/GNRs in **Fig. 5.6**) are shown compared to the PHA/PGel precursor (with no GNRs). The viscosity (**Fig. 5.6A**)

of GNR hydrogel precursors versus the PHA/PGel precursors were not significantly different over the tested shear rates. However, the yield stress (**Fig. 5.6B**) of the GNR hydrogels precursors (511 ± 20 Pa) was 2.4 times higher than the PHA/PGel hydrogel precursors. The storage modulus recovery (**Fig. 5.6C**) of GNR hydrogel precursors (86 ± 8 Pa) was not significantly different than the PHA/PGel hydrogel precursors. The bioprinted GNR hydrogels precursors (**Fig. 5.6D**) qualitatively showed cleaner printed struts than the PHA/PGel without GNRs. The strut size was 34% greater in the PHA/PGel ($p < 0.01$), which resulted in the GNR hydrogel precursors having 2.3 times larger pore areas ($p < 0.01$).

In vitro toxicity of GNR hydrogels with citrate-GNRs to rat neural stem cells

The cytotoxicity of varied GNR concentrations (0, 0.4, 0.6, 0.8 mg/mL) in PHA/PGel hydrogels was evaluated with seeded rNSCs for 7 days. The adhesion and proliferation of rNSCs were analyzed by the total metabolic activity (**Fig. 5.7A**), DNA content (**Fig. 5.7B**), and the normalized metabolic activity per ng of DNA (**Fig. 5.7C**). The total metabolic activity and DNA content of rNSCs on day 1 were not significantly different between the hydrogel groups. On day 7, the metabolic activity of rNSCs on hydrogels with no GNRs was ~92%, ~89%, and ~67% greater than the 0.4 ($p < 0.01$), 0.6 ($p < 0.01$), and 0.8 ($p < 0.05$) mg/mL GNR hydrogel groups, respectively. Similarly, the total DNA content on day 7 of hydrogels with no GNRs was ~2, ~2.9, and ~2.9 greater than 0.4 ($p < 0.00f1$), 0.6 ($p < 0.0001$), and 0.8 ($p < 0.0001$) mg/mL GNR hydrogels. Additionally, the

hydrogels without GNRs on day 7 had 2.3 times greater DNA content than on day 1 ($p < 0.0001$). On day 1, the metabolic activity normalized to the DNA content did not show any significant differences between groups; however, on day 7, the 0.8 mg/mL GNR hydrogel had 68% and 45% greater metabolic activity per ng of DNA than 0 and 0.4 mg/mL hydrogel groups, respectively ($p < 0.01$). While the 0.6 mg/mL GNR hydrogel group had a higher metabolic activity per ng of DNA than 0 and 0.4 mg/mL groups, the increase was not statistically significant.

The media changes from the GNR hydrogels (0.8 mg/mL of GNRs) with cells were analyzed for released gold by batch ICP-MS (**Fig. 5.7D**). The amount of gold in the 0 mg/mL GNR hydrogels with cells were not higher than the background (data not shown). The amount of gold released on the first and third day were not higher than the background, but there was 0.026 ± 0.043 μg in the day 5 media samples, and 0.11 ± 0.16 μg in the day 7 samples. One of the three samples did not have an amount of gold higher than the background and caused the large standard deviations. Compared to the theoretical maximum gold content per GNR hydrogel, the day 3 and day 5 media samples had released ~0.12% and ~0.49% of the total gold in the hydrogel, respectively.

Behavioral and cellular response to hydrogel treatments in a rat hemi-section SCI

A T8 lateral hemi-section was made in all rats, and PHA, PGel, PHA/PGel, and PHA/PGel/GNRs were injected into the acute hemi-section and UV-

crosslinked (see graphic in **Fig. 5.8A**). The weekly rat videos were scored, and the histology was assessed after 8 weeks post-injury. All rats had full mobility and a BBB score of 21 prior to the surgery. Injuries were made at week 0, and the weekly post-injury videos of the rat gait and the affected right leg were scored (**Fig. 5.8B**). There were no significant differences across the sham and all implanted materials and there were large standard deviations within each group, even after the animals with bilateral injuries had been removed.

H&E and IHC staining was performed on the spinal cords after 8 weeks (**Fig. 5.9-5.14**), and there were wide variations in the degree of injury for each animal (injuries that were visible were outlined in black dashed lines). In the stained horizontal sections of spinal cords in the coronal plane, there was variability seen in the injury size across all rats, regardless of group. Some cords did not show any injury (despite showing a functional deficit), some injuries spanned less than half the cord, some injuries spanned more than half the cord, and some had physical gaps or bi-lateral injuries across the entire cord (while not showing functional bilateral injuries). It was possible that there was variability in the amount of tissue surgically removed because of the gelatinous nature of the rat spinal cord and/or the cord's orientation had deviated before the sectioning process. The resulting sections may not be representative of the injuries, and comparisons across rats and different groups were not able to be made. From the considerable variability without knowing more information about the surrounding spinal cord sections, the histology and IHC were ultimately

inconclusive, but general observations and broad speculations were drawn from the sections with visible injuries.

In the H&E (**Fig 5.9**), several cords showed collagen and a more fibrotic response within the injury. By 8 weeks, the hydrogel materials appeared to have mostly degraded as there were not large amounts of material leftover in any of the hydrogel groups. Although in the GNR hydrogel group, there was a foreign body response around a few small areas that were not tissue and may have been a small amount of leftover material. In a few of the rats, there was some calcification located more laterally in the injury.

IHC was performed on spinal cords after 8 weeks to stain for neurons/axons (NF-M/H), macrophages/microglia (Iba1), activated astrocytes (GFAP), CSPGs (CS-56), and neural stem cells (nestin), which are shown in **Fig. 5.10-5.14**, respectively. The NF-M/H (or NF) (**Fig. 5.10**) stained neuron cell bodies and axons. Medium and heavy neurofilaments are present throughout the cytoplasm of neurons and are more concentrated in axons compared to dendrites. The gray matter with the neuron cell bodies stained darker than the axonal tracts in the white matter, but the axons were visibly stained. In the animals where the injury could be distinguished, the disruption of the axonal pathways within the injury were observed as a lack of stain in the injury that is outlined by dashed lines in **Fig. 5.10**. While no conclusions can be drawn, there was not substantial evidence of any group showing any axon regeneration in the injury.

The GFAP (**Fig. 5.11**) stained for activated astrocytes, and the borders of the injury were distinguished by the lack of staining of the fibrotic tissue response within the injury. In the GFAP stained spinal cords, there were low levels of staining throughout the section of cord around the injury, but there was not substantial evidence of a reduction of activated astrocytes in any of the groups. From the Iba1 staining of activated microglia and macrophages (**Fig. 5.12**), there were activated microglia throughout the entire visible spinal cord sections and a concentration of macrophages near and within the injury (outlined by a dashed black line in **Fig. 5.12**). However, there was not any significant reduction of macrophages in the proximity of the injury in any of the groups. The spinal cords were stained for CS-56 to show CSPGs, which are one of the inhibitory components in the glial scar that prevent axon regeneration (**Fig. 5.13**). There was light staining of CSPGs within some of the injuries, but there was not a significant discernable reduction of CSPGs in any of the groups. Finally, spinal cords were stained for nestin to show NSCs (**Fig. 5.14**), but the lack of stain in any of the spinal cords showed no NSCs were present in any of the groups.

Gold distribution in rat organs

The blood, brains, kidneys, livers, and spleens of the rats in the sham group and GNR hydrogel group were evaluated by ICP-MS for the total gold content and by histology after 8 weeks (**Fig. 5.15**). The amount of gold detected by ICP-MS is shown in **Fig. 5.15A**. The total gold in the brains and the blood were below the background levels. The kidneys, livers, and spleens of the rats that

received the GNR hydrogels had 0.029 ± 0.29 µg of gold, 0.018 ± 0.017 µg, and 0.007 ± 0.012 µg of gold per gram of organ, respectively. After 8 weeks, the amount of gold in the kidneys, livers, and spleens of GNR treated rats as percentages of the estimated total implanted gold was ~0.05 ± 0.05%, ~0.34 ± 0.34%, and ~0.007 ± 0.012% of the total theoretical gold delivered (**Fig 5.15B**).

The histology of the brain, kidney, liver, and spleen (**Fig. 5.15C**) of the rats in the sham group and those that received the GNR hydrogel was evaluated for pathological changes due to accumulation of gold. The histology of the organs of the rat treated with the GNR hydrogel was selected from a rat that had higher amounts of dissolved gold in the kidney, liver, and spleen via ICP-MS. Individual GNRs would not be visible at this magnification; however, if GNRs aggregated or accumulated in cells (e.g., macrophages) over time, the accumulated GNRs may be visible at high magnifications. None of the organs showed visible accumulations of GNRs in the cells or aggregates of GNRs in the tissues. All the normal tissue architectures were observed in each organ of the rats that received the GNR hydrogels.

Discussion

In the current study, we developed a new conductive GNR hydrogel with an injectable and paste-like precursor, and applied the material in a rat SCI model. The developed PHA/PGel/GNR bioink was injectable and had a paste-like rheology, which enabled less invasive surgical delivery and retention of the material in the injury. The feasibility and long-term safety of delivering the GNR

hydrogel was demonstrated in a lateral T8 hemi-section SCI in rats. With the biocompatible gelation conditions of the GNR hydrogel, the hydrogel was crosslinked directly in the injury and formed a conductive hydrogel. The GNR hydrogel provides a translational conductive biomaterial platform and starting point for further refinement and eventually combination with ES to promote axon regeneration, neural plasticity/reorganization, and functional recovery.

High aspect ratio gold particles, such as GNRs, have potential in fabricating conductive composites because they are inert, biocompatible, and highly conductive. Gold nanoparticle-based materials have been applied to SCI, but the purpose of the gold was for drug delivery or to utilize other properties of gold,[24] but not to make a conductive composite. Outside of SCI, conductive GNR hydrogels have been developed and used for cardiac tissue engineering,(203, 206, 207, 210) but have not yet been applied to SCI. There are several limitations of GNRs that may hinder the development of conductive biomaterials for biomedical applications: challenges in the synthesis, low aspect ratios, low synthesis yields, cytotoxicity of the CTAB surfactant, and high concentrations needed for conductivity. The most popular seed-mediated synthesis of GNRs make fairly low aspect ratio GNRs (3 to 4) with low yields (~15% of Au^{3+} ions were reduced to Au in nanorods) and any minor deviations in the reagent concentration results in significant contamination of spherical or other shapes of particles.(289, 290) While one study synthesized a gold nanowire hydrogel,(202) most gold nanorod hydrogels have utilized smaller aspect ratio

GNRs. Use of a bisurfactant growth solution has enable higher aspect ratio GNRs to be formed; however, the yields were still low.(289) In the current study, we employed a robust and repeatable synthesis by Vigderman and Zubarev(281) that used hydroquinone, a different reducing agent in the growth solution compared to the typically used ascorbic acid reducing agent. The synthesis required more time (12 hours versus 3 hours) but had higher yields (~80% in the current study, but Vigderman and Zubarev were able to achieve 100% conversion), higher aspect ratios (7 to 8), and minimal contamination of other shapes (e.g., spheres, dog-bone shapes).

With a robust, high-yield synthesis of high aspect ratio GNRs, one major limitation of GNRs that we needed to overcome was the cytotoxicity of the CTAB surfactant that is required for shape control and rod formation. While Navaei *et al*.(207) found that CTAB-GNRs in methacrylated gelatin hydrogels were not cytotoxic for cardiomyocytes, preliminary studies with PHA/PGel/CTAB-GNRs at various concentrations were cytotoxic within 1 day for seeded rNSCs (data not shown), presumably from the CTAB. Direct ligand exchange for GNRs is challenging because CTAB binds more strongly to gold than many commonly used ligands (e.g., citrate, polyethylene glycol (PEG)). Instead of replacing the CTAB, other studies have coated CTAB-GNRs with non-toxic components (e.g., GelMA(203)); however, given that the hydrogels would eventually release the GNRs, any remaining CTAB may potentially cause toxic *in vivo* side effects. Therefore, in the current studies, an indirect ligand exchange protocol was

adapted from Zhou *et al.*(209) to first displace the CTAB with a thin silver coating on GNRs and then etch away the silver in the presence of sodium citrate to completely replace the toxic CTAB. The silver to gold ratio and initial starting GNR concentration was adjusted for successful exchange of CTAB for citrate on the longer GNRs. For example, not enough silver resulted in aggregation, possibly from incomplete exchange with negatively charged citrate-GNRs aggregating with positively charged CTAB-GNRs. In contrast, too much silver caused silver nanoparticles to form and a thicker silver layer around the GNR, which may result in incomplete etching away of the silver. Silver nanoparticles in the central nervous system have been shown to cause neuroinflammation and disrupt neural cytoskeletons,(193) so silver-coated GNRs were undesirable and complete replacement of CTAB with citrate was necessary. All of the PHA/PGel hydrogels with citrate-GNRs supported rNSC adhesion and viability, further confirming our speculation that the cytotoxicity of the CTAB-GNRs hydrogels was from the CTAB.

Another benefit of the citrate-GNRs was that the citrate coating was a better stabilizer than the CTAB, and citrate-GNRs did not aggregate over time as quickly, compared to CTAB-GNRs, which started aggregating within 1 to 2 days. The wash step after synthesis with PVP was able to extend the shelf-life of CTAB-GNRs to 1-2 weeks because the PVP is a steric stabilizer. Furthermore, sterilization of CTAB-GNRs was challenging, as they could not be sterile-filtered and UV exposure had the potential to cause aggregation. The only feasible

method to sterilize CTAB-GNRs for cytotoxicity studies was to fabricate them under sterile conditions, which had logistical challenges. On the other hand, citrate-GNRs were better dispersed and were able to be sterile filtered while retaining ~66% of the GNRs.

Given that the conductivity of a composite hydrogel is dependent on the conductive filler concentration, the accurate determination of GNR concentration is necessary for comparison across studies internally and across research groups. Batch ICP-MS is the gold standard for directly measuring total dissolved gold in gold nanoparticle solutions but can be costly and not as fast as other alternate indirect methods. An alternative indirect method for measuring molar gold nanoparticle concentrations is to use the Beer-Lambert law with experimentally determined molar extinction coefficients and the UV-Vis absorption of the LSPR peak.(291) The molar extinction coefficients have been characterized for shorter GNRs (i.e., aspect ratios 2 - 5);(292) however, the coefficients have not been characterized for longer GNRs such as the GNRs used in the current study (aspect ratio 7 - 8). Additionally, we found that in our syntheses, the LSPR peak varied from batch to batch and any experimentally determined molar extinction coefficient would vary accordingly and could not be applied to determine the concentrations of batches with different LSPR peaks. Therefore, batch ICP-MS was the superior method compared to using the Beer-Lambert law for determining the concentration of GNRs in our application. Batch ICP-MS ensured consistent GNR concentrations were used across studies, and

enabled comparison to other developed GNR hydrogels in other fields. Given that higher aspect ratio conductive fillers may enable lower concentrations to be sufficient to achieve conductivity, the use of higher aspect ratio GNRs to fabricate a conductive hydrogel may have advantages of requiring fewer GNRs. The 0.6 and 0.8 mg/mL citrate-GNR concentrations were found to be conductive and were in the range of, and slightly lower than, GNR concentrations in other GNR hydrogels (e.g., 1.0 and 1.5 mg/mL GNRs(207)) that used lower aspect ratio GNRs.

With the biocompatible and conductive PHA/PGel/GNR hydrogel, the formulation with 0.8 mg/mL was implanted in the hemi-section SCI model in rats, along with material controls of PHA/PGel, PHA, PGel, and a sham. While the GNR hydrogels did not show discernable improved axon regeneration, reduced CSPGs/inflammation, or better functional recovery than the sham group, the current study did establish the safety and feasibility of implanting the GNR hydrogel. While all the formulations were injectable and easy to deliver, there were differences across the materials in the placement and retainment within the injury. The formulation that the surgeons noted had poor retention in the injury turned out to be the PGel hydrogel precursor. The PGel precursor did not have a paste-like rheology, as evidenced by the lack of a yield stress and a lower viscosity compared to the other formulations. After injection, it was difficult to discern if the PGel precursor was retained in the injury during crosslinking. However, the paste-like hydrogel precursors (i.e., possession of a yield stress,

higher viscosities) were able to stay within the injury during crosslinking and had better retainment than the PGel precursor. The feasibility of delivering an injectable and paste-like bioink to a SCI was therefore demonstrated in the current study.

In addition to the feasibility of the bioink, the current study demonstrated the safety of the GNR hydrogel. The use of the GNR hydrogel did not inhibit spontaneous recovery of locomotion or cause negative clinical side effects (e.g., weight loss). After 8 weeks, there was minimal evidence of material leftover in the injury from the histological analyses of the spinal cords, indicating all the hydrogel groups had been mostly resorbed by 8 weeks post-injury. The GNRs would have been released as the hydrogel degraded and after 8 weeks, the kidney, liver, and spleen each had less than 0.5% of the total implanted gold, and the blood and brain did not have detectable levels of gold. The histological evaluation of the organs from the rats that received GNR hydrogels showed similar healthy tissue as the organs of the rats in the sham group and minimal subchronic toxicity. Other *in vivo* studies have delivered similar amounts of gold as the current study, or more typically, higher amounts because of repeated dosing regimens. For example, one study in rats with a repeated dosing regimen had mild histological changes (e.g., inflammation, necrosis) and no serious side effects after 2 weeks, 3 months, and 6 months.(293) Another single-dose study in mice had higher GNR accumulation in the organs after 1 day to 15 months, but a lack of toxicity in the organ histology, similar to the outcomes of the current

study.(294) Given the low levels of gold in the organs compared to other studies, we speculate the gold may have been excreted in the urine or feces over the course of the 8-week study, taken up by macrophages that traveled to the lymph nodes, or accumulated in other organs such as the lungs or in the spinal cords, which was not available due to histological processing. The feces, urine, lungs, and lymph nodes were not collected and tested in the current study, but testing in future studies may benefit from confirming the accumulation and/or excretion of the GNRs at different timepoints post-injury. Overall, the lack of negative side effects and lack of pathological effect from the low levels of gold in the tested organs demonstrated the safety of the GNR hydrogels and the released GNRs.

There may have been several reasons for the lack of regeneration and functional recovery, including possible premature hydrogel degradation, displacement of the hydrogel post-crosslinking, increased intraspinal pressures, and/or lack of regenerative cues. Ideally, the rate of tissue regeneration would match that of the hydrogel degradation because too slow of hydrogel degradation may prevent new tissue formation and axon growth, and degradation too fast may cause lack of a scaffold for supporting regeneration and/or additional inflammation or scarring.(75) In addition, hydrogel displacement after crosslinking may cause similar effects as too fast of degradation, or additional off-site effects. One study found that high molecular weight HA hydrogels did not degrade after 9 weeks in a rat hemi-section SCI model;(271) however, the inclusion of gelatin in the hydrogels used in the current study most likely

increased the rate of degradation comparatively. As the histology and IHC in the current study showed, some of the injuries were large gaps or had fibrous scar tissue, and there was minimal evidence of remaining hydrogel material in the injuries. It is possible the lack of regeneration may, at least in part, have been from too fast of hydrogel degradation or hydrogel displacement; however, future studies to evaluate the *in vivo* degradation rate and hydrogel retainment post-surgery would be needed to confirm the speculation.

The mechanical performance and swelling properties of hydrogels implanted into a SCI are important to characterize because swelling may result in increased intraspinal pressures, which in turn may result in negative clinical outcomes.(295) The GNR hydrogels had increased swelling and absorption of water, and we speculate the cause was the high GNR concentrations. Despite the higher aspect ratio GNRs, the GNR concentrations in the mg/mL range are high for nanoparticles and resulted in limited crosslinking because of the dark color/opacity of the hydrogels and/or less available crosslinker. The pentenoate functionalization uses thiol-ene click chemistry, where the -enes of the pentenoate group crosslink with a dithiol crosslinker. Thiols bond to gold quickly and with high affinity, which may have trapped some of the dithiol crosslinker and instead aggregated GNRs together or tethered GNRs to PHA or PGel. No visible aggregates were seen in the precursor, but GNR hydrogels had increased swelling and absorption, which was consistent with a less crosslinked network. Lower compressive elastic moduli typically accompany softer hydrogels;

however, the GNR hydrogels did not have significantly different compressive moduli from the PHA/PGel hydrogels. Gold nanoparticles have been used in tissue engineering to generate hydrogels with improved stiffness,(280) therefore, we speculated that the GNRs may have increased the moduli of PHA/PGel, but the inhibited crosslinking may have diminished or counterbalanced that effect. While the GNR hydrogels had high absorption of water that may have increased intraspinal pressure after gelation in the injury, the high absorption may not have necessarily caused high intraspinal pressures. In a comprehensive review on swelling and intraspinal pressures from injectable hydrogels for SCI by Khaing *et al.,*(295) 2% HA hydrogels had higher absorption (denoted as “mass swelling percent” in the review) than 4% poly(ethylene glycol) (PEG) hydrogels, but lower swelling pressure. Swelling pressure experiments or direct measurements of local spinal tissue pressure after hydrogel implantation would be needed to determine how much the high absorption of GNR hydrogels increase intraspinal pressure, and if those intraspinal pressures negatively affect functional outcomes.

The high absorption of water and low conductivity of the GNR hydrogels used in the current study may both be solved by addressing the inhibited crosslinking by using different crosslinkers, hydrogel crosslinking chemistries, and/or incorporation of additional conductive components. Longer UV exposure times were already used in the current study to crosslink the GNR hydrogels (i.e., 5 min) compared to the PHA/PGel only hydrogels (i.e., 2 min), but the gold may

be still be neutralizing the crosslinker. While an increased amount of crosslinker may compensate for the neutralized crosslinker and improve the hydrogel crosslinking, high concentrations of the crosslinker used in the current study (i.e., DTT) are cytotoxic for rNSCs. Different non-cytotoxic dithiol crosslinkers may overcome the limitations of DTT, where high concentrations of a peptide crosslinker with a cysteine on each end may be less toxic and better crosslink the GNR hydrogels. Alternative fast crosslinking chemistries (e.g., alkyne-azide click chemistries) that do not use thiol crosslinkers or crosslinking molecules at all may additionally avoid the crosslinker complications. Improved crosslinking and the reduction of the water absorption may reduce the risks associated with increased intraspinal pressure, and additionally may condense the GNR network and improve conductivity. Furthermore, the hydrogel conductivity may be improved through the addition of other conductive components into the PHA/PGel/GNR precursor, such as poly(3,4-ethylenedioxythiophene) polystyrene sulfonate (PEDOT:PSS), which is one of the few conductive polymers commercially available as a stable colloidal suspension in water that may be able to be easily blended into the PHA/PGel/GNR precursor.

There was not substantial evidence of axonal regeneration (i.e., axons stained by neurofilament) within the injuries of any of the hydrogel *in vivo* groups in the current study and the conductive material by itself may not have been sufficient to encourage axonal regeneration. Additionally, we did not see a substantial reduction in inflammation (e.g., macrophages stained by Iba1) or the

inhibitory environment (e.g., CSPGs stained by CS-56) in any of the hydrogel groups. In other studies, HA hydrogels alone had neuroprotective effects when applied to rat hemi-section SCI models,(271, 296) but no differences in functional recovery compared to sham groups.(296) However, another study that used HA hydrogels combined with growth factors and cells showed some improvements in functional recovery in a rat hemi-section model.(76) Similar to previously used HA hydrogels, the GNR hydrogel used in the current study may need additional bioactive cues to neutralize the inhibitory environment and/or promote axonal regeneration. In contrast to previously used HA hydrogels, the conductivity of the GNR hydrogel enabled it to be a platform that is compatible with ES. The efficacy will need to be evaluated for a GNR hydrogel (with additional bioactive cues) combined with ES to promote neural differentiation and neurite growth *in vitro*, and promote axon regeneration and neural plasticity *in vivo*. In addition to evaluating the effects of conductive materials with and without ES, it will be important to elucidate the effects of the conductive material alone compared to a non-conductive material.

Given the efficacy of combining motor training and ES after SCI in small clinical studies, it may be logical to combine a conductive biomaterial with ES and motor training. Regenerating the tissue and promoting neural plasticity with regenerative rehabilitation approaches may be able to restore supraspinal input for voluntary control and activation of CPGs and other functions for maximal functional recovery after SCI. Overall, conductive bioinks such as the GNR

hydrogel developed in the current study are translational platforms that may synergistically link regenerative medicine and rehabilitation approaches for developing regenerative rehabilitation treatments for SCI.

Conclusions

The rheology of the developed PHA/PGel/GNR hydrogel bioink enabled translational injection for application to a rat hemi-section model of SCI. While no differences in functional recovery were seen across treated groups, the goal of the study was accomplished with the feasibility and safety of injectable GNR hydrogels being established. With no previous studies evaluating a GNR-based conductive hydrogel for application to SCI, this study filled that gap and in the future, may provide a translational platform that can combine regenerative medicine approaches and rehabilitation approaches to maximize functional recovery in differing injury models.

Chapter 6 : Conclusion

Full functional recovery after spinal cord injury (SCI) is uncommon in patients with severe SCI. Rehabilitation strategies, specifically motor training combined with electrical stimulation (ES), are leading to better functional recovery in patients with incomplete injuries, possibly from leveraging spared tissue. Recovery of locomotion may be possible in patients with more severe injuries, who have little to no spared tissue, by targeted activation of intrinsic spinal circuits, or central pattern generators (CPGs), that are related to locomotion and are still intact below the injury. However, determining the necessary ES parameters to enable activation CPGs and identification of other CPGs and/or spinal networks in humans is a challenge. For full functional recovery beyond locomotion, the axons may need to be regenerated and retrained. Regenerative medicine approaches aim to regenerate the axons, but given that regenerative medicine approaches by themselves have not yet resulted in full functional recovery, there is growing evidence in the SCI literature indicating the need for combining rehabilitation and regenerative medicine to maximize functional recovery. Regenerative medicine approaches may be needed for SCI to restore the damaged axons and support rehabilitation approaches in promoting neural plasticity of any newly regenerated axons. Unfortunately, there are limited methods to synergistically combine rehabilitation and regenerative medicine, but conductive biomaterials could be the missing link that enables synergistic combination with ES. There are limited *in vivo* studies using conductive

biomaterials to treat SCI. The problem is that many conductive biomaterials are preformed scaffolds, which may hinder clinical translation to a contusion-type SCI that does not have defined borders. However, an injectable biomaterial that conforms to the shape of the injury may be more translational for contusion SCIs. The field of bioprinting has been developing injectable materials for biomedical applications and the relevant rheology of bioinks enables translation for developing injectable biomaterials for SCI. In the current work, a conductive and bioprintable hydrogel was developed, refined for neural tissue engineering, and applied to a rat spinal cord injury (SCI) model, for potential future application to spinal cord regeneration after severe, contusion SCIs.

In Aim 1, an existing biomaterial, pentenoate-functionalized hyaluronic acid (PHA) was developed into a bioink. While several biomaterials exist, not all biomaterials are printable by extrusion-based bioprinting. Fabrication of most biomaterials generates a solid scaffold and preformed scaffolds are not typically injectable and not suitable for bioprinting. Several hydrogels are uniquely suited for bioprinting with precursors that are able to be extruded through a needle or nozzle, and subsequently crosslinked after printing. To further universalize the bioprinting field, three standard rheological tests were used to characterize the rheology and predict the printability of materials for easier bioink development. Materials with low viscosity are easier to extrude through needles or nozzles, but materials with higher viscosities can be extruded if they demonstrate shear thinning properties. The ability of a material to hold its shape is important for

bioprinting layer-by-layer structures and is related to the possession of a yield stress. Finally, the retention of the shape after experiencing high shear stresses (i.e., extrusion through a nozzle) is related to the storage modulus recovery and is important for retaining the bioprinted shape after printing.

The molecular weight and the concentration of PHA was varied to determine printable formulations. High molecular weight PHA was previously used to develop paste-like biomaterials for applications in cartilage and bone defects and was found to be more suitable than lower molecular weights for bioprinting. The 4, 5, and 6 wt% PHA formulations were printable and retained their shape after extrusion. However, the 5 and 6 wt% required high pressures to overcome the higher yield stresses, which led to overly fast extrusion and thin, non-uniform printed struts. We determined that the viscosity, yield stress, and storage modulus recovery were vital rheological parameters to characterize and determine printability.

With a bioprintable ink, PHA was further developed in Aim 2 to support rNSC adhesion. The problem with PHA was the rNSCs did not adhere to PHA. Other HA-based hydrogels had incorporated gelatin to improve cell adhesion for oligodendrocytes and fibroblasts, therefore, gelatin was functionalized with the same pentenoate chemistry to form crosslinkable hydrogels. PGel functionalization was fully characterized by 2D NMR experiments and the PGel was less functionalized than PHA, despite using the same amount of pentenoic anhydride per unit mass. We speculate that the lower functionality was because

only ~34% of the amino acids (by weight) in gelatin have amines and hydroxyls that can be functionalized. In comparison, every single repeat unit of the repeating disaccharide has hydroxyls that can be functionalized. After polymer characterization, various concentrations and crosslinker concentrations were tested for rNSC adhesion and the 5 and 10% PGel formulations showed the best adhesion. The problem with PGel was the quick *in vitro* degradation (less than 14 days). To solve the problems of PHA not enabling cell adhesion, and PGel degrading too quickly, various concentrations of PHA and PGel in PHA/PGel hydrogels were tested for rNSC adhesion. A few formulations were found that supported rNSC adhesion and the hydrogels did not visibly degrade in 14 days from the stability of the PHA. The rheological properties of composites may change upon addition or subtraction of a material, therefore the bioprintability of the adhesive formulations was tested. The 3/10% PHA/PGel formulation used large volumes of material, and was not bioprintable despite having a yield stress. The poor shape recovery ultimately led to relaxation following extrusion and merging of the printed struts. The 4%/5% PHA/PGel formulation had similar rheological parameters to 4% PHA and printed with good shape fidelity. Through the addition of PGel to PHA, each material solved the problem of the other, and a PHA/PGel hydrogel bioink that supported rNSC adhesion and viability over 7 days was developed.

In Aim 3, the PHA/PGel hydrogels were further developed into a conductive hydrogel. Most conductive materials used to electrically stimulate

cells are metals, which would damage the soft spinal cord if implanted. Conductive composites with biomaterials are gaining attention in biomedical engineering fields because biocompatible conductive materials can provide ES to tissues and stimulate desirable cell responses in cardiac tissue engineering and other fields. There are three main categories of conductive composites: conductive polymers, carbon-based materials, and metal particle-based materials. Most conductive polymers are insoluble in water and mixing with PHA/PGel may not be feasible because PHA/PGel hydrogels form under aqueous conditions. Furthermore, conductive polymer composites are typically less conductive than the carbon-based and metal particle-based composites. Carbon-based materials, such as carbon nanotubes have extremely high aspect ratios and have been utilized to fabricate conductive composites with high conductivities; however, carbon-based materials are highly hydrophobic and require functionalization to ensure a stable dispersion and limit cytotoxicity. Thus, of the metal particles, silver has been found to disrupt neuron cytoskeletons, but gold itself is inert, biocompatible, and highly conductive. With the aid and expertise of collaborators in the gold nanoparticle field, creation of a gold nanoparticle composite in PHA/PGel hydrogels was a viable solution for developing a conductive hydrogel.

While spherical particles require high concentrations to attain conductivity in a composite, higher aspect ratio particles have greater interparticle distances that lower the necessary concentration of conductive filler required for

conductivity. High aspect ratio gold nanorods were synthesized according to the gold nanorod literature, but shape-controlled synthesis of GNRs requires the use of a toxic surfactant, hexadecyltrimethylammonium bromide (CTAB). PHA/PGel hydrogels with CTAB-GNRs were highly cytotoxic for rNSCs, so the CTAB coating was replaced with citrate. Direct ligand exchange is insufficient for replacing the tightly associated CTAB coating on GNRs, so an indirect ligand exchange was used to remove the CTAB and replace with non-toxic sodium citrate. Additionally, the citrate-capping better stabilized the GNR suspension and better prevented aggregation than the CTAB-capping, which enabled sterile-filtering to sterilize the GNRs and made incorporation into the PHA/PGel hydrogel easier.

After successful synthesis of citrate-GNRs, the concentration of GNRs was varied and the 0.8 mg/mL concentration was determined to be conductive. The same concentrations supported the adhesion and viability of seeded rNSCs over 7 days. The 0.8 mg/mL GNR concentration had slightly higher metabolic activity per nanogram of DNA and was selected for the *in vivo* study. The GNR hydrogel was implanted in a lateral hemi-section SCI rat model, which is the least debilitating *in vivo* model of SCI that still enables analysis of functional recovery. The GNR hydrogel, along with a PHA/PGel hydrogel, PHA hydrogel, and PGel hydrogel were tested and compared to rats who received an injury and no treatment (sham). There was a wide variability in the functional recovery (i.e., BBB scores) within each group and no treatment was significantly different from

another. Additionally, in the histological and immunohistochemistry analyses, there was variability in the visible injury size across rats. It was possible that there was variability in the size of surgical defect made, because the gelatinous nature of the rat spinal cord did not easily enable precise removal of half the cord. Rats with less of an injury may have recovered locomotion much faster. Additionally, it is possible that during the preparation process of the spinal cords, the orientation of the injury on the spinal cord may have deviated before the sectioning and the injury may not have been visible in the stained section. Without knowing more information about the surrounding spinal cord sections, the histology and IHC were inconclusive, but general observations and broad speculations were drawn from the sections with visible injuries. The size of the injury was not able to be compared without knowing if the selected section was at the epicenter of each injury. However, the tissue within the injury did not show substantial amounts of axonal staining, decreased macrophages/activated microglia, decreased activated astrocytes, or decreased chondroitin sulfate proteoglycans. Altogether, we speculated there was not robust evidence that any of the materials were promoting axonal regeneration or decreasing the inhibitory injury environment. There may have been several reasons for the lack of regeneration and functional recovery including premature hydrogel degradation, increased intraspinal pressures, and or a lack of regenerative cues. The ideal rate of hydrogel degradation would be the same rate of regeneration to not impede regeneration if degradation were too slow or lacked support for new

tissue if degradation were too quick. While high molecular weight HA has been known to have slow degradation *in vivo*, the inclusion of gelatin in the current thesis may have increased the rate of degradation. It is possible the GNR hydrogels degraded too quickly and influenced the functional recovery.

While the results of the *in vivo* study did not show improved regeneration of the neural tissue or better functional recovery than the sham group, the study did establish the feasibility of implanting the GNR hydrogel and the long-term safety of the GNRs. Surgeons had noted that the precursors of the GNR hydrogel, PHA/PGel hydrogel, and PHA hydrogels were easy to work with in terms of injectability and material retention in the injury. The PGel did not have a yield stress or the paste-like rheology that the other formulations had, and after injection, it was difficult to discern if the material was retained in the injury. Furthermore, the use of the GNR hydrogel did not decrease or inhibit the normal spontaneous recovery of the rats, or cause negative side effects (e.g., weight loss). All of the GNR hydrogels showed a visible injury after 8 weeks, and there was minimal evidence of material within any of the injuries, indicating all the hydrogel groups had mostly degraded by 8 weeks post-injury, which would have released the GNRs. The organs of the rats treated with the GNR hydrogels each had less than 0.5% of the total implanted gold, but there was no visible histological evidence of GNR accumulation in macrophages in the different organs and the organs appeared healthy. Given the low levels of gold in the organs compared to other long-term gold nanoparticle studies, the gold may have

been excreted in the urine or feces, and/or accumulated in the lymph nodes. Together, the safety of GNR hydrogels was established and the rheology of the GNR hydrogel bioink enabled translation for application to rat SCI models.

In the future, the conductive biomaterial that was developed may provide a translational platform for combination and synergy with ES to leverage the principles of regenerative rehabilitation for SCI. Further refinement of the material would overcome several limitations of the conductive hydrogel formulation presented in this dissertation, such as high GNR concentrations, high absorption, and low conductivity. While the GNRs synthesized and used in the current studies had high aspect ratios (7-8) compared to typically synthesized GNRs (3-4), high concentrations (e.g., in range of mg/mL) of GNRs were still required to reach conductivity in the hydrogel.

The high GNR concentration may have disrupted the hydrogel crosslinking from light attenuation or decreasing the amount of available crosslinker. The high concentration increased the opacity/dark color of the hydrogel precursor, which may have resulted in limited crosslinking. Additionally, the pentenoate functionalization relies on thiol-ene click chemistry, where the -enes of the pentenoate group react with a dithiol molecule to crosslink the PHA or PGel polymers in an interconnected network. The high affinity and quick reaction of the gold-thiol bond may trap the dithiol crosslinker and instead aggregate GNRs together or tether GNRs to PHA or PGel. With less available crosslinker, hydrogels would be less crosslinked and thus more compliant. However, in the

evaluated mechanical performance, the GNR hydrogels did not have significantly different compressive moduli than the PHA/PGel hydrogels. Gold nanoparticles have been used in tissue engineering to generate hydrogels with improved stiffness, and we initially expected the GNR hydrogels to have higher moduli than PHA/PGel hydrogels. We speculate the GNRs may have increased the moduli of PHA/PGel but the inhibited crosslinking may have eliminated the effect.

The inhibited crosslinking from high GNR concentrations may additionally cause greater absorption, which was observed. Hydrogel absorption of water after fabrication may have a negative outcome on the spinal cord if the hydrogel swells and increases intraspinal pressure after forming within the injury. Higher intraspinal pressures have been correlated with negative functional recoveries, so reduction of the absorption to values around 1, where no swelling occurs, may be more suitable for application to SCI. However, higher absorption is not always correlated to higher swelling pressures, and swelling pressure experiments or direct measurements of local spinal tissue pressures after hydrogel implantation will be needed to ensure the material does not increase intraspinal pressures and increase the risk of negative functional outcomes. Finally, the high absorption of the hydrogel may increase interparticle distances between GNRs, leading to a reduction in conductivity. While increasing the concentration typically does not result in substantial increases in conductivity once the interconnected network has been achieved, it is possible we have not reached the maximum connectivity between GNRs because of the high absorption disrupting the GNR network.

Overall, the high absorption of water and low conductivity of the GNR hydrogels used in the current thesis may be solved by improving the crosslinking with additional crosslinker, changing hydrogel chemistries, and/or incorporating additional conductive fillers. Longer UV exposure times (i.e., 5 min versus 2 min) were used in the current thesis to crosslink the GNR hydrogels but increasing the concentration of crosslinker may counteract the amount of dithiol crosslinker trapped by the gold and improve hydrogel crosslinking. High concentrations of the crosslinker used in this study (i.e., DTT) are cytotoxic for rNSCs; however, a different non-cytotoxic dithiol crosslinker, such as a peptide crosslinker with a cysteine on each end, may be beneficial in the future. Alternatively, other fast crosslinking chemistries (e.g., alkyne-azide click chemistries) that do not use thiol crosslinkers or crosslinking molecules at all may circumvent the dithiol crosslinker/gold problem entirely. Finally, the conductivity may be improved through addition of other conductive fillers, such as poly(3,4-ethylenedioxythiophene) polystyrene sulfonate (PEDOT:PSS), which is one of the few water stable conductive polymers and is commercially available as a colloidal solution.

In addition to improving the swelling and mechanical performance of the GNR hydrogels, the ability of the material to encourage axon regeneration or reduce the inhibitory environment may be improved in the future with the addition of other regenerative medicine strategies into the current translational system. HA hydrogels have been applied to SCI *in vivo* and found to have neuroprotective

effects but HA alone was not enough to promote axon regeneration. HA hydrogels with growth factors and cells had demonstrated better functional recovery in rat hemi-section model over cell-only controls. Given that there was not substantial evidence of axon regeneration or a decrease in inflammation/the inhibitory environment in the current thesis, additional bioactive cues or neutralizing factors can be incorporated into the GNR hydrogel platform with relative ease. Methods for guiding axon growth that can be controlled non-invasively may be beneficial (e.g., magnetic iron oxide nanofibers, self-assembling peptides, shape-memory polymers). In contrast to the HA hydrogels used to treat SCI so far, the GNR hydrogel used in the current dissertation was conductive, which enables it to be a platform compatible with ES in future work. The efficacy of a refined GNR hydrogel with and without ES in promoting neural differentiation and/or neurite extension *in vitro* will be needed prior to *in vivo* studies. Furthermore, it is important in future studies to elucidate the effects of the conductive material versus a non-conductive material and determine if the conductive biomaterial by itself may be sufficient, or if ES with any material is sufficient, or if there is truly a synergistic effect of using a conductive material with ES. Finally, given the efficacy of combining motor training with ES after SCI that has been demonstrated in a few human patients, it may be logical to combine a conductive biomaterial with ES and motor training in future studies. Conductive bioinks may facilitate axon regeneration and the ES and motor training may enable reorganization of the regenerated axons for restoration of the supraspinal

input needed for voluntary control and activation of CPGs for locomotion among other functions for full functional recovery after SCI. Conductive bioinks may be a method to synergistically link regenerative medicine approaches and rehabilitation approaches to promote maximum functional recovery after SCI.

While the rat lateral hemi-section model was a logical first step from being the least debilitating while allowing evaluation of functional recovery after SCI, there were several challenges and other animal models (e.g., species, types of injury, level) may be explored in future studies. In rodents, there are several types of cut injuries (e.g., dorsal hemi-section, lateral hemi-section, transection) and contusion injuries (e.g., bilateral contusion, crush),(297) where cut injuries allow for easier analysis of axon regeneration and contusion injuries better represent human injuries and pathologies. Cut injuries may be easier to analyze axon growth compared to contusion injuries that leave some spared tissue; however, rats have significant recovery after hemi-section injuries, most likely due to increased axonal sprouting from the unlesioned side, and are challenging to perform, as evident from the variable scores compared between different laboratories. Furthermore, transection injuries are challenging from cord retraction on both ends of a cut cord, and are the least representative of typical human injuries. Contusion injuries are more difficult to analyze because of spared tissue, but are the industry standard because they better represent human injuries and are easier to perform consistently with the use of commercial

impactors. A rat thoracic level contusion injury would be the most useful model to use moving forward.

In addition to the type of injury, different species are used including rodents, felines, canines, swine, and non-human primates (e.g., macaques, marmosets, squirrel monkeys).(298) Mice and rats are the most widely used for SCI, but rats better mimic the human pathologies compared to mice, which recover better than rats or humans after SCI. An inherent limitation and consideration for rodent and feline models of SCI is that rehabilitation approaches (e.g., ES, pharmacological stimulation) can enable recovery of locomotion in animals with complete transections. Proper controls are needed to elucidate the effects of treatments. There are limited larger animal models of SCI (e.g., swine, canine), but all laboratory animal SCI models do not accurately represent the heterogeneity across human injuries. Given the high occurrence of naturally occurring SCI in pet dogs, the Canine Spinal Cord Injury Consortium was established in 2015 to promote the value of the clinical dog model of SCI.(299) The population of dogs with chronic SCI may be valuable in the future for evaluating efficacy of SCI treatments in larger animal models and eventual translation to human patients.

In the current dissertation, a conductive hydrogel was developed that supported rat neural stem cell viability and was an injectable bioink. The material was successfully applied in a hemi-section rat SCI model and was feasibly delivered without negative side effects. The significance of the research in this

dissertation was, to the best of our knowledge, the first application of a conductive gold-based hydrogel to treat SCI. Gold nanoparticle hydrogels have been developed to deliver drugs for SCI, but the hydrogels were not conductive. On the other hand, gold-based conductive hydrogels have been fabricated for cardiac tissue engineering and other biomedical applications, but not applied to SCI. In the future, the rheology of the PHA/PGel bioink hydrogel may enable the material to be translated to a more clinically relevant contusion SCI rat model. Furthermore, the conductivity of the hydrogel may enable combination with ES as a regenerative rehabilitation approach to leverage the beneficial cellular effects of stimulation, enhance neural plasticity, and promote better functional recovery after SCI.

References

1. Rose LF, Wolf EJ, Brindle T, Cernich A, Dean WK, Dearth CL, Grimm M, Kusiak A, Nitkin R, Potter K, Randolph BJ, Wang F, Yamaguchi D. The convergence of regenerative medicine and rehabilitation: federal perspectives. NPJ Regen Med. 2018;3:19. Epub 2018/10/17. doi: 10.1038/s41536-018-0056-1. PubMed PMID: 30323950; PMCID: PMC6180133.

2. Krucoff MO, Miller JP, Saxena T, Bellamkonda R, Rahimpour S, Harward SC, Lad SP, Turner DA. Toward Functional Restoration of the Central Nervous System: A Review of Translational Neuroscience Principles. Neurosurgery. 2019;84(1):30-40. doi: 10.1093/neuros/nyy128. PubMed PMID: 29800461; PMCID: PMC6292792.

3. Courtine G, Sofroniew MV. Spinal cord repair: advances in biology and technology. Nat Med. 2019;25(6):898-908. Epub 2019/06/05. doi: 10.1038/s41591-019-0475-6. PubMed PMID: 31160817.

4. Hutson TH, Di Giovanni S. The translational landscape in spinal cord injury: focus on neuroplasticity and regeneration. Nat Rev Neurol. 2019;15(12):732-45. Epub 2019/11/16. doi: 10.1038/s41582-019-0280-3. PubMed PMID: 31728042.

5. Ambrosio F, Rando TA. The regenerative rehabilitation collection: a forum for an emerging field. NPJ Regen Med. 2018;3:20. Epub 2018/10/31. doi: 10.1038/s41536-018-0058-z. PubMed PMID: 30374410; PMCID: PMC6195606.

6. Ambrosio F, Russell A. Regenerative rehabilitation: a call to action. J Rehabil Res Dev. 2010;47(3):xi-xv. Epub 2010/07/29. doi: 10.1682/jrrd.2010.03.0021. PubMed PMID: 20665343.

7. Willett NJ, Boninger ML, Miller LJ, Alvarez L, Aoyama T, Bedoni M, Brix KA, Chisari C, Christ G, Dearth CL, Dyson-Hudson TA, Evans CH, Goldman SM, Gregory K, Gualerzi A, Hart J, Ito A, Kuroki H, Loghmani MT, Mack DL, Malanga GA, Noble-Haeusslein L, Pasquina P, Roche JA, Rose L, Stoddart MJ, Tajino J, Terzic C, Topp KS, Wagner WR, Warden SJ, Wolf SL, Xie H, Rando TA, Ambrosio F. Taking the Next Steps in Regenerative Rehabilitation: Establishment of a New Interdisciplinary Field. Arch Phys Med Rehabil. 2020;101(5):917-23. Epub 2020/02/09. doi: 10.1016/j.apmr.2020.01.007. PubMed PMID: 32035141.

8. Lin J, Anopas D, Milbreta U, Lin PH, Chin JS, Zhang N, Wee SK, Tow A, Ang WT, Chew SY. Regenerative rehabilitation: exploring the synergistic effects of rehabilitation and implantation of a bio-functional scaffold in

enhancing nerve regeneration. Biomater Sci. 2019;7(12):5150-60. Epub 2019/10/04. doi: 10.1039/c9bm01095e. PubMed PMID: 31580337.

9. Zhu H, Poon W, Liu Y, Leung GK, Wong Y, Feng Y, Ng SCP, Tsang KS, Sun DTF, Yeung DK, Shen C, Niu F, Xu Z, Tan P, Tang S, Gao H, Cha Y, So KF, Fleischaker R, Sun D, Chen J, Lai J, Cheng W, Young W. Phase I-II Clinical Trial Assessing Safety and Efficacy of Umbilical Cord Blood Mononuclear Cell Transplant Therapy of Chronic Complete Spinal Cord Injury. Cell Transplant. 2016;25(11):1925-43. Epub 2016/04/15. doi: 10.3727/096368916X691411. PubMed PMID: 27075659.

10. Rajnicek AM, Zhao Z, Moral-Vico J, Cruz AM, McCaig CD, Casan-Pastor N. Controlling Nerve Growth with an Electric Field Induced Indirectly in Transparent Conductive Substrate Materials. Adv Healthc Mater. 2018;7(17):e1800473. Epub 2018/07/06. doi: 10.1002/adhm.201800473. PubMed PMID: 29975820.

11. Pires F, Ferreira Q, Rodrigues CA, Morgado J, Ferreira FC. Neural stem cell differentiation by electrical stimulation using a cross-linked PEDOT substrate: Expanding the use of biocompatible conjugated conductive polymers for neural tissue engineering. Biochim Biophys Acta. 2015;1850(6):1158-68. Epub 2015/02/11. doi: 10.1016/j.bbagen.2015.01.020. PubMed PMID: 25662071.

12. Borah R, Ingavle GC, Sandeman SR, Kumar A, Mikhalovsky S. Electrically conductive MEH-PPV:PCL electrospun nanofibres for electrical stimulation of rat PC12 pheochromocytoma cells. Biomater Sci. 2018;6(9):2342-59. Epub 2018/07/19. doi: 10.1039/c8bm00559a. PubMed PMID: 30019048.

13. Koppes AN, Keating KW, McGregor AL, Koppes RA, Kearns KR, Ziemba AM, McKay CA, Zuidema JM, Rivet CJ, Gilbert RJ, Thompson DM. Robust neurite extension following exogenous electrical stimulation within single walled carbon nanotube-composite hydrogels. Acta Biomaterialia. 2016;39:34-43. doi: https://doi.org/10.1016/j.actbio.2016.05.014.

14. Imaninezhad M, Pemberton K, Xu F, Kalinowski K, Bera R, Zustiak SP. Directed and enhanced neurite outgrowth following exogenous electrical stimulation on carbon nanotube-hydrogel composites. J Neural Eng. 2018;15(5):056034. Epub 2018/07/28. doi: 10.1088/1741-2552/aad65b. PubMed PMID: 30051883.

15. Wang J, Tian L, Chen N, Ramakrishna S, Mo X. The cellular response of nerve cells on poly-l-lysine coated PLGA-MWCNTs aligned nanofibers under electrical stimulation. Mater Sci Eng C Mater Biol Appl. 2018;91:715-26. Epub 2018/07/24. doi: 10.1016/j.msec.2018.06.025. PubMed PMID: 30033306.

16. Zhou Z, Liu X, Wu W, Park S, Miller Ii AL, Terzic A, Lu L. Effective nerve cell modulation by electrical stimulation of carbon nanotube embedded conductive polymeric scaffolds. Biomater Sci. 2018;6(9):2375-85. Epub 2018/07/19. doi: 10.1039/c8bm00553b. PubMed PMID: 30019709.

17. Thornton MA, Mehta MD, Morad TT, Ingraham KL, Khankan RR, Griffis KG, Yeung AK, Zhong H, Roy RR, Edgerton VR, Phelps PE. Evidence of axon connectivity across a spinal cord transection in rats treated with epidural stimulation and motor training combined with olfactory ensheathing cell transplantation. Exp Neurol. 2018;309:119-33. Epub 2018/07/30. doi: 10.1016/j.expneurol.2018.07.015. PubMed PMID: 30056160; PMCID: PMC6365019.

18. Aravamudhan S, Bellamkonda RV. Toward a convergence of regenerative medicine, rehabilitation, and neuroprosthetics. J Neurotrauma. 2011;28(11):2329-47. Epub 2011/06/15. doi: 10.1089/neu.2010.1542. PubMed PMID: 21663399.

19. Ross HH, Ambrosio F, Trumbower RD, Reier PJ, Behrman AL, Wolf SL. Neural Stem Cell Therapy and Rehabilitation in the Central Nervous System: Emerging Partnerships. Phys Ther. 2016;96(5):734-42. Epub 2016/02/06. doi: 10.2522/ptj.20150063. PubMed PMID: 26847015; PMCID: PMC6281018.

20. Zheng Y, Mao YR, Yuan TF, Xu DS, Cheng LM. Multimodal treatment for spinal cord injury: a sword of neuroregeneration upon neuromodulation. Neural Regen Res. 2020;15(8):1437-50. Epub 2020/01/31. doi: 10.4103/1673-5374.274332. PubMed PMID: 31997803; PMCID: PMC7059565.

21. Palza H, Zapata PA, Angulo-Pineda C. Electroactive Smart Polymers for Biomedical Applications. Materials (Basel). 2019;12(2). Epub 2019/01/19. doi: 10.3390/ma12020277. PubMed PMID: 30654487; PMCID: PMC6357059.

22. Min JH, Patel M, Koh WG. Incorporation of Conductive Materials into Hydrogels for Tissue Engineering Applications. Polymers (Basel). 2018;10(10). Epub 2019/04/10. doi: 10.3390/polym10101078. PubMed PMID: 30961003; PMCID: PMC6404001.

23. Distler T, Boccaccini AR. 3D printing of electrically conductive hydrogels for tissue engineering and biosensors - A review. Acta Biomater. 2019. Epub 2019/09/03. doi: 10.1016/j.actbio.2019.08.044. PubMed PMID: 31476385.

24. Ghasemi-Mobarakeh L, Prabhakaran MP, Morshed M, Nasr-Esfahani MH, Baharvand H, Kiani S, Al-Deyab SS, Ramakrishna S. Application of conductive polymers, scaffolds and electrical stimulation for nerve tissue

engineering. J Tissue Eng Regen Med. 2011;5(4):e17-35. Epub 2011/03/18. doi: 10.1002/term.383. PubMed PMID: 21413155.

25. Center NSCIS. Facts and Figures at a Glance. Birmingham, AL: University of Alabama at Birmingham, 2020 2020. Report No.

26. Szuflita NS, Neal CJ, Rosner MK, Frankowski RF, Grossman RG. Spine Injuries Sustained by U.S. Military Personnel in Combat are Different From Non-Combat Spine Injuries. Mil Med. 2016;181(10):1314-23. Epub 2016/10/19. doi: 10.7205/MILMED-D-15-00332. PubMed PMID: 27753570.

27. Roberts TT, Leonard GR, Cepela DJ. Classifications In Brief: American Spinal Injury Association (ASIA) Impairment Scale. Clin Orthop Relat Res. 2017;475(5):1499-504. Epub 2016/11/07. doi: 10.1007/s11999-016-5133-4. PubMed PMID: 27815685; PMCID: PMC5384910.

28. Ehsanian R, Haefeli J, Quach N, Kosarchuk J, Torres D, Stuck ED, Endo J, Crew JD, Dirlikov B, Bresnahan JC, Beattie MS, Ferguson AR, McKenna SL. Exploration of surgical blood pressure management and expected motor recovery in individuals with traumatic spinal cord injury. Spinal Cord. 2020;58(3):377-86. Epub 2019/10/28. doi: 10.1038/s41393-019-0370-5. PubMed PMID: 31649323; PMCID: PMC7062632.

29. Ahuja CS, Wilson JR, Nori S, Kotter MRN, Druschel C, Curt A, Fehlings MG. Traumatic spinal cord injury. Nat Rev Dis Primers. 2017;3:17018. Epub 2017/04/28. doi: 10.1038/nrdp.2017.18. PubMed PMID: 28447605.

30. Dietrich WD, Levi AD, Wang M, Green BA. Hypothermic treatment for acute spinal cord injury. Neurotherapeutics. 2011;8(2):229-39. Epub 2011/03/19. doi: 10.1007/s13311-011-0035-3. PubMed PMID: 21416406; PMCID: PMC3101829.

31. Khorasanizadeh M, Yousefifard M, Eskian M, Lu Y, Chalangari M, Harrop JS, Jazayeri SB, Seyedpour S, Khodaei B, Hosseini M, Rahimi-Movaghar V. Neurological recovery following traumatic spinal cord injury: a systematic review and meta-analysis. J Neurosurg Spine. 2019:1-17. Epub 2019/02/17. doi: 10.3171/2018.10.SPINE18802. PubMed PMID: 30771786.

32. Center NSCIS. 2019 Annual Report - Complete Public Version. Birmingham, AL: University of Alabama at Birmingham, 2019 2019. Report No.

33. Tsintou M, Dalamagkas K, Seifalian AM. Advances in regenerative therapies for spinal cord injury: a biomaterials approach. Neural Regen Res. 2015;10(5):726-42. doi: 10.4103/1673-5374.156966.

34. Chhabra HS, Sarda K. Clinical translation of stem cell based interventions for spinal cord injury - Are we there yet? Adv Drug Deliv Rev. 2017;120:41-9. Epub 2017/10/02. doi: 10.1016/j.addr.2017.09.021. PubMed PMID: 28964881.

35. Gaudet AD, Popovich PG. Extracellular matrix regulation of inflammation in the healthy and injured spinal cord. Exp Neurol. 2014;0:24-34. doi: 10.1016/j.expneurol.2013.11.020.

36. Bradbury EJ, Burnside ER. Moving beyond the glial scar for spinal cord repair. Nat Commun. 2019;10(1):3879. Epub 2019/08/30. doi: 10.1038/s41467-019-11707-7. PubMed PMID: 31462640; PMCID: PMC6713740.

37. Sabelström H, Stenudd M, Frisén J. Neural stem cells in the adult spinal cord. Exp Neurol. 2014;260:44-9. doi: 10.1016/j.expneurol.2013.01.026.

38. Ohtake Y, Saito A, Li S. Diverse functions of protein tyrosine phosphatase sigma in the nervous and immune systems. Exp Neurol. 2018;302:196-204. Epub 2018/01/29. doi: 10.1016/j.expneurol.2018.01.014. PubMed PMID: 29374568; PMCID: PMC6275553.

39. Vecino E. The Extracellular Matrix in the Nervous System: The Good and the Bad Aspects. In: Travascio JCFKE-F, editor. Composition and Function of the Extracellular Matrix in the Human Body. Rijeka: IntechOpen; 2016. p. Ch. 5.

40. Fawcett J. Repair of spinal cord injuries: where are we, where are we going? Spinal Cord. 2002;40(12):615-23. doi: 10.1038/sj.sc.3101328.

41. Tang Y, Yu P, Cheng L. Current progress in the derivation and therapeutic application of neural stem cells. Cell Death Dis. 2017;8(10):e3108. Epub 2017/10/13. doi: 10.1038/cddis.2017.504. PubMed PMID: 29022921; PMCID: PMC5682670.

42. Alessandrini M, Preynat-Seauve O, De Bruin K, Pepper MS. Stem cell therapy for neurological disorders. S Afr Med J. 2019;109(8b):70-7. Epub 2019/10/31. doi: 10.7196/SAMJ.2019.v109i8b.14009. PubMed PMID: 31662153.

43. Ramotowski C, Qu X, Villa-Diaz LG. Progress in the Use of Induced Pluripotent Stem Cell-Derived Neural Cells for Traumatic Spinal Cord Injuries in Animal Populations: Meta-Analysis and Review. Stem Cells Transl Med. 2019;8(7):681-93. Epub 2019/03/25. doi: 10.1002/sctm.18-0225. PubMed PMID: 30903654; PMCID: PMC6591555.

44. Binan L, Ajji A, De Crescenzo G, Jolicoeur M. Approaches for neural tissue regeneration. Stem Cell Rev Rep. 2014;10(1):44-59. Epub 2013/10/05. doi: 10.1007/s12015-013-9474-z. PubMed PMID: 24092527.

45. Cofano F, Boido M, Monticelli M, Zenga F, Ducati A, Vercelli A, Garbossa D. Mesenchymal Stem Cells for Spinal Cord Injury: Current Options, Limitations, and Future of Cell Therapy. Int J Mol Sci. 2019;20(11). Epub 2019/06/05. doi: 10.3390/ijms20112698. PubMed PMID: 31159345; PMCID: PMC6600381.

46. Yao R, Murtaza M, Velasquez JT, Todorovic M, Rayfield A, Ekberg J, Barton M, St John J. Olfactory Ensheathing Cells for Spinal Cord Injury: Sniffing Out the Issues. Cell Transplant. 2018;27(6):879-89. Epub 2018/06/09. doi: 10.1177/0963689718779353. PubMed PMID: 29882418; PMCID: PMC6050914.

47. Nakhjavan-Shahraki B, Yousefifard M, Rahimi-Movaghar V, Baikpour M, Nasirinezhad F, Safari S, Yaseri M, Moghadas Jafari A, Ghelichkhani P, Tafakhori A, Hosseini M. Transplantation of olfactory ensheathing cells on functional recovery and neuropathic pain after spinal cord injury; systematic review and meta-analysis. Sci Rep. 2018;8(1):325. Epub 2018/01/13. doi: 10.1038/s41598-017-18754-4. PubMed PMID: 29321494; PMCID: PMC5762885.

48. Dalamagkas K, Tsintou M, Seifalian A, Seifalian AM. Translational Regenerative Therapies for Chronic Spinal Cord Injury. Int J Mol Sci. 2018;19(6). Epub 2018/06/20. doi: 10.3390/ijms19061776. PubMed PMID: 29914060; PMCID: PMC6032191.

49. Zhou P, Guan J, Xu P, Zhao J, Zhang C, Zhang B, Mao Y, Cui W. Cell Therapeutic Strategies for Spinal Cord Injury. Adv Wound Care (New Rochelle). 2019;8(11):585-605. Epub 2019/10/23. doi: 10.1089/wound.2019.1046. PubMed PMID: 31637103; PMCID: PMC6798812.

50. Badhiwala JH, Ahuja CS, Fehlings MG. Time is spine: a review of translational advances in spinal cord injury. J Neurosurg Spine. 2018;30(1):1-18. Epub 2019/01/06. doi: 10.3171/2018.9.SPINE18682. PubMed PMID: 30611186.

51. Keefe KM, Sheikh IS, Smith GM. Targeting Neurotrophins to Specific Populations of Neurons: NGF, BDNF, and NT-3 and Their Relevance for Treatment of Spinal Cord Injury. Int J Mol Sci. 2017;18(3). doi: 10.3390/ijms18030548.

52. Jones LL, Oudega M, Bunge MB, Tuszynski MH. Neurotrophic factors, cellular bridges and gene therapy for spinal cord injury. J Physiol (Lond). 2001;533(Pt 1):83-9. doi: 10.1111/j.1469-7793.2001.0083b.x.

53. Song YH, Agrawal NK, Griffin JM, Schmidt CE. Recent advances in nanotherapeutic strategies for spinal cord injury repair. Adv Drug Deliv

Rev. 2018. Epub 2018/12/26. doi: 10.1016/j.addr.2018.12.011. PubMed PMID: 30582938.

54. Hayta E, Elden H. Acute spinal cord injury: A review of pathophysiology and potential of non-steroidal anti-inflammatory drugs for pharmacological intervention. J Chem Neuroanat. 2018;87:25-31. Epub 2017/08/15. doi: 10.1016/j.jchemneu.2017.08.001. PubMed PMID: 28803968.

55. Jorge A, Taylor T, Agarwal N, Hamilton DK. Current Agents and Related Therapeutic Targets for Inflammation After Acute Traumatic Spinal Cord Injury. World Neurosurg. 2019;132:138-47. Epub 2019/08/31. doi: 10.1016/j.wneu.2019.08.108. PubMed PMID: 31470153.

56. Orr MB, Gensel JC. Spinal Cord Injury Scarring and Inflammation: Therapies Targeting Glial and Inflammatory Responses. Neurotherapeutics. 2018;15(3):541-53. Epub 2018/05/03. doi: 10.1007/s13311-018-0631-6. PubMed PMID: 29717413; PMCID: PMC6095779.

57. Jain A, Kim YT, McKeon RJ, Bellamkonda RV. In situ gelling hydrogels for conformal repair of spinal cord defects, and local delivery of BDNF after spinal cord injury. Biomaterials. 2006;27(3):497-504. Epub 2005/08/16. doi: 10.1016/j.biomaterials.2005.07.008. PubMed PMID: 16099038.

58. Lee H, McKeon RJ, Bellamkonda RV. Sustained delivery of thermostabilized chABC enhances axonal sprouting and functional recovery after spinal cord injury. Proc Natl Acad Sci U S A. 2010;107(8):3340-5. Epub 2009/11/04. doi: 10.1073/pnas.0905437106. PubMed PMID: 19884507; PMCID: PMC2840440.

59. Haggerty AE, Oudega M. Biomaterials for spinal cord repair. Neurosci Bull. 2013;29(4):445-59. doi: 10.1007/s12264-013-1362-7.

60. Wang ZZ, Sakiyama-Elbert SE. Matrices, scaffolds & carriers for cell delivery in nerve regeneration. Exp Neurol. 2019;319:112837. Epub 2018/10/07. doi: 10.1016/j.expneurol.2018.09.020. PubMed PMID: 30291854; PMCID: PMC6447476.

61. Theodore N, Hlubek R, Danielson J, Neff K, Vaickus L, Ulich TR, Ropper AE. First Human Implantation of a Bioresorbable Polymer Scaffold for Acute Traumatic Spinal Cord Injury: A Clinical Pilot Study for Safety and Feasibility. Neurosurgery. 2016;79(2):E305-12. Epub 2016/06/17. doi: 10.1227/NEU.0000000000001283. PubMed PMID: 27309344.

62. Zhao Y, Tang F, Xiao Z, Han G, Wang N, Yin N, Chen B, Jiang X, Yun C, Han W, Zhao C, Cheng S, Zhang S, Dai J. Clinical Study of NeuroRegen Scaffold Combined With Human Mesenchymal Stem Cells for the Repair of Chronic Complete Spinal Cord Injury. Cell Transplant. 2017;26(5):891-

900. Epub 2017/02/12. doi: 10.3727/096368917X695038. PubMed PMID: 28185615; PMCID: PMC5657723.

63. Xiao Z, Tang F, Zhao Y, Han G, Yin N, Li X, Chen B, Han S, Jiang X, Yun C, Zhao C, Cheng S, Zhang S, Dai J. Significant Improvement of Acute Complete Spinal Cord Injury Patients Diagnosed by a Combined Criteria Implanted with NeuroRegen Scaffolds and Mesenchymal Stem Cells. Cell Transplant. 2018;27(6):907-15. Epub 2018/06/07. doi: 10.1177/0963689718766279. PubMed PMID: 29871514; PMCID: PMC6050906.

64. Katoh H, Yokota K, Fehlings MG. Regeneration of Spinal Cord Connectivity Through Stem Cell Transplantation and Biomaterial Scaffolds. Front Cell Neurosci. 2019;13:248. Epub 2019/06/28. doi: 10.3389/fncel.2019.00248. PubMed PMID: 31244609; PMCID: PMC6563678.

65. Ham TR, Leipzig ND. Biomaterial strategies for limiting the impact of secondary events following spinal cord injury. Biomed Mater. 2018;13(2):024105. Epub 2017/11/21. doi: 10.1088/1748-605X/aa9bbb. PubMed PMID: 29155409; PMCID: PMC5824690.

66. Liu T, Houle JD, Xu J, Chan BP, Chew SY. Nanofibrous collagen nerve conduits for spinal cord repair. Tissue Eng Part A. 2012;18(9-10):1057-66. Epub 2012/01/10. doi: 10.1089/ten.TEA.2011.0430. PubMed PMID: 22220714; PMCID: PMC3338103.

67. Milbreta U, Nguyen LH, Diao H, Lin J, Wu W, Sun C-Y, Wang J, Chew SY. Three-Dimensional Nanofiber Hybrid Scaffold Directs and Enhances Axonal Regeneration after Spinal Cord Injury. ACS Biomaterials Science & Engineering. 2016;2(8):1319-29. doi: 10.1021/acsbiomaterials.6b00248.

68. Gelain F, Panseri S, Antonini S, Cunha C, Donega M, Lowery J, Taraballi F, Cerri G, Montagna M, Baldissera F, Vescovi A. Transplantation of nanostructured composite scaffolds results in the regeneration of chronically injured spinal cords. ACS Nano. 2011;5(1):227-36. Epub 2010/12/30. doi: 10.1021/nn102461w. PubMed PMID: 21189038.

69. Amr SM, Gouda A, Koptan WT, Galal AA, Abdel-Fattah DS, Rashed LA, Atta HM, Abdel-Aziz MT. Bridging defects in chronic spinal cord injury using peripheral nerve grafts combined with a chitosan-laminin scaffold and enhancing regeneration through them by co-transplantation with bone-marrow-derived mesenchymal stem cells: case series of 14 patients. J Spinal Cord Med. 2014;37(1):54-71. Epub 2013/10/05. doi: 10.1179/2045772312Y.0000000069. PubMed PMID: 24090088; PMCID: PMC4066552.

70. Wang C, Yue H, Feng Q, Xu B, Bian L, Shi P. Injectable Nanoreinforced Shape-Memory Hydrogel System for Regenerating Spinal Cord Tissue from Traumatic Injury. ACS Appl Mater Interfaces. 2018;10(35):29299-307. Epub 2018/08/10. doi: 10.1021/acsami.8b08929. PubMed PMID: 30091362.

71. Bencherif SA, Sands RW, Bhatta D, Arany P, Verbeke CS, Edwards DA, Mooney DJ. Injectable preformed scaffolds with shape-memory properties. Proc Natl Acad Sci U S A. 2012;109(48):19590-5. Epub 2012/11/15. doi: 10.1073/pnas.1211516109. PubMed PMID: 23150549; PMCID: PMC3511752.

72. Pakulska MM, Ballios BG, Shoichet MS. Injectable hydrogels for central nervous system therapy. Biomed Mater. 2012;7(2):024101. Epub 2012/03/30. doi: 10.1088/1748-6041/7/2/024101. PubMed PMID: 22456684.

73. Ziemba AM, Gilbert RJ. Biomaterials for Local, Controlled Drug Delivery to the Injured Spinal Cord. Front Pharmacol. 2017;8:245. doi: 10.3389/fphar.2017.00245.

74. Assunção-Silva RC, Gomes ED, Sousa N, Silva NA, Salgado AJ. Hydrogels and Cell Based Therapies in Spinal Cord Injury Regeneration. Stem Cells Int. 2015;2015. doi: 10.1155/2015/948040.

75. Macaya D, Spector M. Injectable hydrogel materials for spinal cord regeneration: a review. Biomed Mater. 2012;7(1):012001. Epub 2012/01/14. doi: 10.1088/1748-6041/7/1/012001. PubMed PMID: 22241481.

76. Mothe AJ, Tam RY, Zahir T, Tator CH, Shoichet MS. Repair of the injured spinal cord by transplantation of neural stem cells in a hyaluronan-based hydrogel. Biomaterials. 2013;34(15):3775-83. doi: 10.1016/j.biomaterials.2013.02.002.

77. Hong LTA, Kim YM, Park HH, Hwang DH, Cui Y, Lee EM, Yahn S, Lee JK, Song SC, Kim BG. An injectable hydrogel enhances tissue repair after spinal cord injury by promoting extracellular matrix remodeling. Nat Commun. 2017;8(1):533. Epub 2017/09/16. doi: 10.1038/s41467-017-00583-8. PubMed PMID: 28912446; PMCID: PMC5599609.

78. Zaviskova K, Tukmachev D, Dubisova J, Vackova I, Hejcl A, Bystronova J, Pravda M, Scigalkova I, Sulakova R, Velebny V, Wolfova L, Kubinova S. Injectable hydroxyphenyl derivative of hyaluronic acid hydrogel modified with RGD as scaffold for spinal cord injury repair. J Biomed Mater Res A. 2018;106(4):1129-40. Epub 2017/12/22. doi: 10.1002/jbm.a.36311. PubMed PMID: 29266693.

79. Hassannejad Z, Zadegan SA, Vaccaro AR, Rahimi-Movaghar V, Sabzevari O. Biofunctionalized peptide-based hydrogel as an injectable scaffold for BDNF delivery can improve regeneration after spinal cord injury. Injury. 2019;50(2):278-85. Epub 2019/01/01. doi: 10.1016/j.injury.2018.12.027. PubMed PMID: 30595411.

80. Townsend JM, Beck EC, Gehrke SH, Berkland CJ, Detamore MS. Flow Behavior Prior to Crosslinking: The Need for Precursor Rheology for Placement of Hydrogels in Medical Applications and for 3D Bioprinting. Prog Polym Sci. 2019;91:126-40. Epub 2019/10/02. doi: 10.1016/j.progpolymsci.2019.01.003. PubMed PMID: 31571701; PMCID: PMC6768569.

81. Kiyotake EA, Douglas AW, Thomas EE, Detamore MS. Development and Quantitative Characterization of the Precursor Rheology of Hyaluronic acid Hydrogels for Bioprinting. Acta Biomater. 2019. Epub 2019/01/23. doi: 10.1016/j.actbio.2019.01.041. PubMed PMID: 30669003.

82. Beck EC, Lohman BL, Tabakh DB, Kieweg SL, Gehrke SH, Berkland CJ, Detamore MS. Enabling Surgical Placement of Hydrogels Through Achieving Paste-Like Rheological Behavior in Hydrogel Precursor Solutions. Ann Biomed Eng. 2015;43(10):2569-76. Epub 2015/02/19. doi: 10.1007/s10439-015-1277-8. PubMed PMID: 25691398; PMCID: PMC4540702.

83. Beck EC, Barragan M, Tadros MH, Kiyotake EA, Acosta FM, Kieweg SL, Detamore MS. Chondroinductive Hydrogel Pastes Composed of Naturally Derived Devitalized Cartilage. Ann Biomed Eng. 2016;44(6):1863-80. doi: 10.1007/s10439-015-1547-5. PubMed PMID: 26744243.

84. Shah PK, Lavrov I. Spinal Epidural Stimulation Strategies: Clinical Implications of Locomotor Studies in Spinal Rats. Neuroscientist. 2017;23(6):664-80. doi: 10.1177/1073858417699554. PubMed PMID: 28345483.

85. Rossignol S, Martinez M, Escalona M, Kundu A, Delivet-Mongrain H, Alluin O, Gossard JP. The "beneficial" effects of locomotor training after various types of spinal lesions in cats and rats. Prog Brain Res. 2015;218:173-98. Epub 2015/04/19. doi: 10.1016/bs.pbr.2014.12.009. PubMed PMID: 25890137.

86. Courtine G, Gerasimenko Y, van den Brand R, Yew A, Musienko P, Zhong H, Song B, Ao Y, Ichiyama RM, Lavrov I, Roy RR, Sofroniew MV, Edgerton VR. Transformation of nonfunctional spinal circuits into functional states after the loss of brain input. Nat Neurosci. 2009;12(10):1333-42. Epub 2009/09/22. doi: 10.1038/nn.2401. PubMed PMID: 19767747; PMCID: PMC2828944.

87. Peña Pino I, Hoover C, Venkatesh S, Ahmadi A, Sturtevant D, Patrick N, Freeman D, Parr A, Samadani U, Balser D, Krassioukov A, Phillips A, Netoff TI, Darrow D. Long-Term Spinal Cord Stimulation After Chronic Complete Spinal Cord Injury Enables Volitional Movement in the Absence of Stimulation. Frontiers in Systems Neuroscience. 2020;14:35.

88. Angeli CA, Boakye M, Morton RA, Vogt J, Benton K, Chen Y, Ferreira CK, Harkema SJ. Recovery of Over-Ground Walking after Chronic Motor Complete Spinal Cord Injury. New England Journal of Medicine. 2018;379(13):1244-50. doi: 10.1056/NEJMoa1803588.

89. Wagner FB, Mignardot JB, Le Goff-Mignardot CG, Demesmaeker R, Komi S, Capogrosso M, Rowald A, Seanez I, Caban M, Pirondini E, Vat M, McCracken LA, Heimgartner R, Fodor I, Watrin A, Seguin P, Paoles E, Van Den Keybus K, Eberle G, Schurch B, Pralong E, Becce F, Prior J, Buse N, Buschman R, Neufeld E, Kuster N, Carda S, von Zitzewitz J, Delattre V, Denison T, Lambert H, Minassian K, Bloch J, Courtine G. Targeted neurotechnology restores walking in humans with spinal cord injury. Nature. 2018;563(7729):65-71. Epub 2018/11/02. doi: 10.1038/s41586-018-0649-2. PubMed PMID: 30382197.

90. Gill ML, Grahn PJ, Calvert JS, Linde MB, Lavrov IA, Strommen JA, Beck LA, Sayenko DG, Van Straaten MG, Drubach DI, Veith DD, Thoreson AR, Lopez C, Gerasimenko YP, Edgerton VR, Lee KH, Zhao KD. Neuromodulation of lumbosacral spinal networks enables independent stepping after complete paraplegia. Nat Med. 2018;24(11):1677-82. Epub 2018/09/27. doi: 10.1038/s41591-018-0175-7. PubMed PMID: 30250140.

91. Hofer AS, Schwab ME. Enhancing rehabilitation and functional recovery after brain and spinal cord trauma with electrical neuromodulation. Curr Opin Neurol. 2019;32(6):828-35. Epub 2019/10/01. doi: 10.1097/WCO.0000000000000750. PubMed PMID: 31567546; PMCID: PMC6855343.

92. Megia Garcia A, Serrano-Munoz D, Taylor J, Avendano-Coy J, Gomez-Soriano J. Transcutaneous Spinal Cord Stimulation and Motor Rehabilitation in Spinal Cord Injury: A Systematic Review. Neurorehabil Neural Repair. 2020;34(1):3-12. Epub 2019/12/21. doi: 10.1177/1545968319893298. PubMed PMID: 31858871.

93. de Araujo AVL, Ribeiro FPG, Massetti T, Potter-Baker KA, Cortes M, Plow EB, da Silva TD, Tonks J, Anghinah R, Magalhaes FH, Fregni F, de Mello Monteiro CB. Effectiveness of anodal transcranial direct current stimulation to improve muscle strength and motor functionality after incomplete spinal cord injury: a systematic review and meta-analysis. Spinal Cord. 2020. Epub 2020/02/19. doi: 10.1038/s41393-020-0438-2. PubMed PMID: 32066873.

94. de Paz RH, Serrano-Munoz D, Perez-Nombela S, Bravo-Esteban E, Avendano-Coy J, Gomez-Soriano J. Combining transcranial direct-current stimulation with gait training in patients with neurological disorders: a systematic review. J Neuroeng Rehabil. 2019;16(1):114. Epub 2019/09/16. doi: 10.1186/s12984-019-0591-z. PubMed PMID: 31521179; PMCID: PMC6744683.

95. Hayashi Y, Jacob-Vadakot S, Dugan EA, McBride S, Olexa R, Simansky K, Murray M, Shumsky JS. 5-HT precursor loading, but not 5-HT receptor agonists, increases motor function after spinal cord contusion in adult rats. Exp Neurol. 2010;221(1):68-78. Epub 2009/10/21. doi: 10.1016/j.expneurol.2009.10.003. PubMed PMID: 19840787; PMCID: PMC2812640.

96. Perrin FE, Noristani HN. Serotonergic mechanisms in spinal cord injury. Exp Neurol. 2019;318:174-91. Epub 2019/05/16. doi: 10.1016/j.expneurol.2019.05.007. PubMed PMID: 31085200.

97. Ghosh M, Pearse DD. The role of the serotonergic system in locomotor recovery after spinal cord injury. Front Neural Circuits. 2014;8:151. Epub 2015/02/25. doi: 10.3389/fncir.2014.00151. PubMed PMID: 25709569; PMCID: PMC4321350.

98. Zhu R, Sun Z, Li C, Ramakrishna S, Chiu K, He L. Electrical stimulation affects neural stem cell fate and function in vitro. Exp Neurol. 2019;319:112963. Epub 2019/05/28. doi: 10.1016/j.expneurol.2019.112963. PubMed PMID: 31125549.

99. Zare EN, Makvandi P, Ashtari B, Rossi F, Motahari A, Perale G. Progress in Conductive Polyaniline-Based Nanocomposites for Biomedical Applications: A Review. J Med Chem. 2019. Epub 2019/09/11. doi: 10.1021/acs.jmedchem.9b00803. PubMed PMID: 31502840.

100. Kaur G, Adhikari R, Cass P, Bown M, Gunatillake P. Electrically conductive polymers and composites for biomedical applications. RSC Advances. 2015;5(47):37553-67. doi: 10.1039/C5RA01851J.

101. Xu Y, Huang Z, Pu X, Yin G, Zhang J. Fabrication of Chitosan/Polypyrrole-coated poly(L-lactic acid)/Polycaprolactone aligned fibre films for enhancement of neural cell compatibility and neurite growth. Cell Prolif. 2019;52(3):e12588. Epub 2019/04/12. doi: 10.1111/cpr.12588. PubMed PMID: 30972893.

102. You JO, Rafat M, Ye GJ, Auguste DT. Nanoengineering the heart: conductive scaffolds enhance connexin 43 expression. Nano Lett. 2011;11(9):3643-8. Epub 2011/08/02. doi: 10.1021/nl201514a. PubMed PMID: 21800912.

103. Pourjavadi A, Doroudian M, Ahadpour A, Azari S. Injectable chitosan/kappa-carrageenan hydrogel designed with au nanoparticles: A conductive scaffold for tissue engineering demands. Int J Biol Macromol. 2019;126:310-7. Epub 2018/12/07. doi: 10.1016/j.ijbiomac.2018.11.256. PubMed PMID: 30502431.

104. Baei P, Jalili-Firoozinezhad S, Rajabi-Zeleti S, Tafazzoli-Shadpour M, Baharvand H, Aghdami N. Electrically conductive gold nanoparticle-chitosan thermosensitive hydrogels for cardiac tissue engineering. Mater Sci Eng C Mater Biol Appl. 2016;63:131-41. Epub 2016/04/05. doi: 10.1016/j.msec.2016.02.056. PubMed PMID: 27040204.

105. Wu H, Yu G, Pan L, Liu N, McDowell MT, Bao Z, Cui Y. Stable Li-ion battery anodes by in-situ polymerization of conducting hydrogel to conformally coat silicon nanoparticles. Nat Commun. 2013;4:1943. Epub 2013/06/05. doi: 10.1038/ncomms2941. PubMed PMID: 23733138.

106. Huang H, Yao J, Liu Y, Tuo X, Da Y, Zeng X, Li L. 3D Nanostructured Polypyrrole/Sodium Alginate Conducting Hydrogel from self-assembly with High Supercapacitor Performance. Journal of Macromolecular Science, Part B. 2017;56(8):532-40. doi: 10.1080/00222348.2017.1342951.

107. Su D, Zhou J, Ahmed KS, Ma Q, Lv G, Chen J. Fabrication and characterization of collagen-heparin-polypyrrole composite conductive film for neural scaffold. Int J Biol Macromol. 2019;129:895-903. Epub 2019/02/19. doi: 10.1016/j.ijbiomac.2019.02.087. PubMed PMID: 30776438.

108. Le TH, Kim Y, Yoon H. Electrical and Electrochemical Properties of Conducting Polymers. Polymers (Basel). 2017;9(4). Epub 2017/04/23. doi: 10.3390/polym9040150. PubMed PMID: 30970829; PMCID: PMC6432010.

109. Balint R, Cassidy NJ, Cartmell SH. Conductive polymers: towards a smart biomaterial for tissue engineering. Acta Biomater. 2014;10(6):2341-53. Epub 2014/02/22. doi: 10.1016/j.actbio.2014.02.015. PubMed PMID: 24556448.

110. Hackett AJ, Malmström J, Travas-Sejdic J. Functionalization of conducting polymers for biointerface applications. Progress in Polymer Science. 2017;70:18-33. doi: https://doi.org/10.1016/j.progpolymsci.2017.03.004.

111. Ateh DD, Navsaria HA, Vadgama P. Polypyrrole-based conducting polymers and interactions with biological tissues. J R Soc Interface. 2006;3(11):741-52. Epub 2006/10/04. doi: 10.1098/rsif.2006.0141. PubMed PMID: 17015302; PMCID: PMC1885362.

112. Bechara S, Wadman L, Popat KC. Electroconductive polymeric nanowire templates facilitates in vitro C17.2 neural stem cell line adhesion, proliferation and differentiation. Acta Biomater. 2011;7(7):2892-901. Epub 2011/05/03. doi: 10.1016/j.actbio.2011.04.009. PubMed PMID: 21530693; PMCID: PMC3116238.

113. Runge MB, Dadsetan M, Baltrusaitis J, Ruesink T, Lu L, Windebank AJ, Yaszemski MJ. Development of electrically conductive oligo(polyethylene glycol) fumarate-polypyrrole hydrogels for nerve regeneration. Biomacromolecules. 2010;11(11):2845-53. Epub 2010/10/15. doi: 10.1021/bm100526a. PubMed PMID: 20942380; PMCID: PMC3947846.

114. Lee JY, Bashur CA, Goldstein AS, Schmidt CE. Polypyrrole-coated electrospun PLGA nanofibers for neural tissue applications. Biomaterials. 2009;30(26):4325-35. Epub 2009/06/09. doi: 10.1016/j.biomaterials.2009.04.042. PubMed PMID: 19501901; PMCID: PMC2713816.

115. Zou Y, Qin J, Huang Z, Yin G, Pu X, He D. Fabrication of Aligned Conducting PPy-PLLA Fiber Films and Their Electrically Controlled Guidance and Orientation for Neurites. ACS Appl Mater Interfaces. 2016;8(20):12576-82. Epub 2016/05/14. doi: 10.1021/acsami.6b00957. PubMed PMID: 27172537.

116. Sun B, Zhou Z, Li D, Wu T, Zheng H, Liu J, Wang G, Yu Y, Mo X. Polypyrrole-coated poly(l-lactic acid-co-epsilon-caprolactone)/silk fibroin nanofibrous nerve guidance conduit induced nerve regeneration in rat. Mater Sci Eng C Mater Biol Appl. 2019;94:190-9. Epub 2018/11/15. doi: 10.1016/j.msec.2018.09.021. PubMed PMID: 30423701.

117. Xu H, Holzwarth JM, Yan Y, Xu P, Zheng H, Yin Y, Li S, Ma PX. Conductive PPY/PDLLA conduit for peripheral nerve regeneration. Biomaterials. 2014;35(1):225-35. Epub 2013/10/22. doi: 10.1016/j.biomaterials.2013.10.002. PubMed PMID: 24138830; PMCID: PMC3884072.

118. Shu B, Sun X, Liu R, Jiang F, Yu H, Xu N, An Y. Restoring electrical connection using a conductive biomaterial provides a new therapeutic strategy for rats with spinal cord injury. Neurosci Lett. 2019;692:33-40. Epub 2018/10/28. doi: 10.1016/j.neulet.2018.10.031. PubMed PMID: 30367954.

119. Raynald, Shu B, Liu XB, Zhou JF, Huang H, Wang JY, Sun XD, Qin C, An YH. Polypyrrole/polylactic acid nanofibrous scaffold cotransplanted with bone marrow stromal cells promotes the functional recovery of spinal cord injury in rats. CNS Neurosci Ther. 2019;25(9):951-64. Epub 2019/09/06.

doi: 10.1111/cns.13135. PubMed PMID: 31486601; PMCID: PMC6698972.

120. Ribeiro J, Caseiro AR, Pereira T, Armada-da-Silva PA, Pires I, Prada J, Amorim I, Leal Reis I, Amado S, Santos JD, Bompasso S, Raimondo S, Varejao AS, Geuna S, Luis AL, Mauricio AC. Evaluation of PVA biodegradable electric conductive membranes for nerve regeneration in axonotmesis injuries: the rat sciatic nerve animal model. J Biomed Mater Res A. 2017;105(5):1267-80. Epub 2017/01/13. doi: 10.1002/jbm.a.35998. PubMed PMID: 28078802.

121. Ma C, Jiang L, Wang Y, Gang F, Xu N, Li T, Liu Z, Chi Y, Wang X, Zhao L, Feng Q, Sun X. 3D Printing of Conductive Tissue Engineering Scaffolds Containing Polypyrrole Nanoparticles with Different Morphologies and Concentrations. Materials (Basel). 2019;12(15). Epub 2019/08/09. doi: 10.3390/ma12152491. PubMed PMID: 31390733; PMCID: PMC6696326.

122. Wu C, Liu A, Chen S, Zhang X, Chen L, Zhu Y, Xiao Z, Sun J, Luo H, Fan H. Cell-Laden Electroconductive Hydrogel Simulating Nerve Matrix To Deliver Electrical Cues and Promote Neurogenesis. ACS Appl Mater Interfaces. 2019;11(25):22152-63. Epub 2019/06/14. doi: 10.1021/acsami.9b05520. PubMed PMID: 31194504.

123. Zhou L, Fan L, Yi X, Zhou Z, Liu C, Fu R, Dai C, Wang Z, Chen X, Yu P, Chen D, Tan G, Wang Q, Ning C. Soft Conducting Polymer Hydrogels Cross-Linked and Doped by Tannic Acid for Spinal Cord Injury Repair. ACS Nano. 2018;12(11):10957-67. Epub 2018/10/05. doi: 10.1021/acsnano.8b04609. PubMed PMID: 30285411.

124. Yang J, Choe G, Yang S, Jo H, Lee JY. Polypyrrole-incorporated conductive hyaluronic acid hydrogels. Biomater Res. 2016;20. doi: 10.1186/s40824-016-0078-y.

125. Guarino V, Alvarez-Perez MA, Borriello A, Napolitano T, Ambrosio L. Conductive PANi/PEGDA macroporous hydrogels for nerve regeneration. Adv Healthc Mater. 2013;2(1):218-27. Epub 2012/11/28. doi: 10.1002/adhm.201200152. PubMed PMID: 23184787.

126. Humpolicek P, Radaszkiewicz KA, Capakova Z, Pachernik J, Bober P, Kasparkova V, Rejmontova P, Lehocky M, Ponizil P, Stejskal J. Polyaniline cryogels: Biocompatibility of novel conducting macroporous material. Sci Rep. 2018;8(1):135. Epub 2018/01/11. doi: 10.1038/s41598-017-18290-1. PubMed PMID: 29317683; PMCID: PMC5760658.

127. Stejskal J, Bober P, Trchová M, Kovalcik A, Hodan J, Hromádková J, Prokeš J. Polyaniline Cryogels Supported with Poly(vinyl alcohol): Soft and Conducting. Macromolecules. 2017;50(3):972-8. doi: 10.1021/acs.macromol.6b02526.

128. Das S, Sharma M, Saharia D, Sarma KK, Muir EM, Bora U. Electrospun silk-polyaniline conduits for functional nerve regeneration in rat sciatic nerve injury model. Biomed Mater. 2017;12(4):045025. Epub 2017/06/21. doi: 10.1088/1748-605X/aa7802. PubMed PMID: 28632137.

129. Khorshidi S, Karkhaneh A. Particle-coated electrospun scaffold: A semi-conductive drug eluted scaffold with layered fiber/particle arrangement. J Biomed Mater Res A. 2018;106(12):3248-54. Epub 2018/10/26. doi: 10.1002/jbm.a.36522. PubMed PMID: 30358083.

130. Abasi S, Aggas JR, Guiseppi-Elie A. Physiochemical and morphological dependent growth of NIH/3T3 and PC-12 on polyaniline-chloride/chitosan bionanocomposites. Mater Sci Eng C Mater Biol Appl. 2019;99:1304-12. Epub 2019/03/21. doi: 10.1016/j.msec.2019.02.018. PubMed PMID: 30889665.

131. Zarrintaj P, Urbanska AM, Gholizadeh SS, Goodarzi V, Saeb MR, Mozafari M. A facile route to the synthesis of anilinic electroactive colloidal hydrogels for neural tissue engineering applications. J Colloid Interface Sci. 2018;516:57-66. Epub 2018/02/07. doi: 10.1016/j.jcis.2018.01.044. PubMed PMID: 29408144.

132. Atoufi Z, Zarrintaj P, Motlagh GH, Amiri A, Bagher Z, Kamrava SK. A novel bio electro active alginate-aniline tetramer/ agarose scaffold for tissue engineering: synthesis, characterization, drug release and cell culture study. J Biomater Sci Polym Ed. 2017;28(15):1617-38. Epub 2017/06/08. doi: 10.1080/09205063.2017.1340044. PubMed PMID: 28589747.

133. Zarrintaj P, Bakhshandeh B, Rezaeian I, Heshmatian B, Ganjali MR. A Novel Electroactive Agarose-Aniline Pentamer Platform as a Potential Candidate for Neural Tissue Engineering. Sci Rep. 2017;7(1):17187. Epub 2017/12/08. doi: 10.1038/s41598-017-17486-9. PubMed PMID: 29215076; PMCID: PMC5719440.

134. Wang G, Wu W, Yang H, Zhang P, Wang JY. Intact polyaniline coating as a conductive guidance is beneficial to repairing sciatic nerve injury. J Biomed Mater Res B Appl Biomater. 2019. Epub 2019/03/27. doi: 10.1002/jbm.b.34372. PubMed PMID: 30912286.

135. Xu D, Fan L, Gao L, Xiong Y, Wang Y, Ye Q, Yu A, Dai H, Yin Y, Cai J, Zhang L. Micro-Nanostructured Polyaniline Assembled in Cellulose Matrix via Interfacial Polymerization for Applications in Nerve Regeneration. ACS Appl Mater Interfaces. 2016;8(27):17090-7. Epub 2016/06/18. doi: 10.1021/acsami.6b03555. PubMed PMID: 27314673.

136. Das S, Chatterjee DP, Ghosh R, Nandi AK. Water soluble polythiophenes: preparation and applications. RSC Advances. 2015;5(26):20160-77. doi: 10.1039/C4RA16496B.

137. Yano H, Kudo K, Marumo K, Okuzaki H. Fully soluble self-doped poly(3,4-ethylenedioxythiophene) with an electrical conductivity greater than 1000 S cm(-1). Sci Adv. 2019;5(4):eaav9492. Epub 2019/04/18. doi: 10.1126/sciadv.aav9492. PubMed PMID: 30993206; PMCID: PMC6461456.

138. Stritesky S, Markova A, Vitecek J, Safarikova E, Hrabal M, Kubac L, Kubala L, Weiter M, Vala M. Printing inks of electroactive polymer PEDOT:PSS: The study of biocompatibility, stability, and electrical properties. J Biomed Mater Res A. 2018;106(4):1121-8. Epub 2017/12/24. doi: 10.1002/jbm.a.36314. PubMed PMID: 29274101.

139. Wang S, Guan S, Li W, Ge D, Xu J, Sun C, Liu T, Ma X. 3D culture of neural stem cells within conductive PEDOT layer-assembled chitosan/gelatin scaffolds for neural tissue engineering. Mater Sci Eng C Mater Biol Appl. 2018;93:890-901. Epub 2018/10/03. doi: 10.1016/j.msec.2018.08.054. PubMed PMID: 30274126.

140. Xu C, Guan S, Wang S, Gong W, Liu T, Ma X, Sun C. Biodegradable and electroconductive poly(3,4-ethylenedioxythiophene)/carboxymethyl chitosan hydrogels for neural tissue engineering. Mater Sci Eng C Mater Biol Appl. 2018;84:32-43. Epub 2018/03/10. doi: 10.1016/j.msec.2017.11.032. PubMed PMID: 29519441.

141. Alves-Sampaio A, Garcia-Rama C, Collazos-Castro JE. Biofunctionalized PEDOT-coated microfibers for the treatment of spinal cord injury. Biomaterials. 2016;89:98-113. Epub 2016/03/11. doi: 10.1016/j.biomaterials.2016.02.037. PubMed PMID: 26963900.

142. Wang S, Guan S, Wang J, Liu H, Liu T, Ma X, Cui Z. Fabrication and characterization of conductive poly (3,4-ethylenedioxythiophene) doped with hyaluronic acid/poly (l-lactic acid) composite film for biomedical application. J Biosci Bioeng. 2017;123(1):116-25. Epub 2016/08/09. doi: 10.1016/j.jbiosc.2016.07.010. PubMed PMID: 27498308.

143. Spencer AR, Shirzaei Sani E, Soucy JR, Corbet CC, Primbetova A, Koppes RA, Annabi N. Bioprinting of a Cell-Laden Conductive Hydrogel Composite. ACS Appl Mater Interfaces. 2019;11(34):30518-33. Epub 2019/08/03. doi: 10.1021/acsami.9b07353. PubMed PMID: 31373791.

144. Wang S, Guan S, Zhu Z, Li W, Liu T, Ma X. Hyaluronic acid doped-poly(3,4-ethylenedioxythiophene)/chitosan/gelatin (PEDOT-HA/Cs/Gel) porous conductive scaffold for nerve regeneration. Mater Sci Eng C Mater Biol Appl. 2017;71:308-16. Epub 2016/12/19. doi: 10.1016/j.msec.2016.10.029. PubMed PMID: 27987712.

145. Sirivisoot S, Pareta R, Harrison BS. Protocol and cell responses in three-dimensional conductive collagen gel scaffolds with conductive polymer

nanofibres for tissue regeneration. Interface Focus. 2014;4(1):20130050. Epub 2014/02/07. doi: 10.1098/rsfs.2013.0050. PubMed PMID: 24501678; PMCID: PMC3886315.

146. Feig VR, Tran H, Lee M, Liu K, Huang Z, Beker L, Mackanic DG, Bao Z. An Electrochemical Gelation Method for Patterning Conductive PEDOT:PSS Hydrogels. Adv Mater. 2019;31(39):e1902869. Epub 2019/08/16. doi: 10.1002/adma.201902869. PubMed PMID: 31414520.

147. Abidian MR, Daneshvar ED, Egeland BM, Kipke DR, Cederna PS, Urbanchek MG. Hybrid conducting polymer-hydrogel conduits for axonal growth and neural tissue engineering. Adv Healthc Mater. 2012;1(6):762-7. Epub 2012/11/28. doi: 10.1002/adhm.201200182. PubMed PMID: 23184828.

148. Heo DN, Lee SJ, Timsina R, Qiu X, Castro NJ, Zhang LG. Development of 3D printable conductive hydrogel with crystallized PEDOT:PSS for neural tissue engineering. Mater Sci Eng C Mater Biol Appl. 2019;99:582-90. Epub 2019/03/21. doi: 10.1016/j.msec.2019.02.008. PubMed PMID: 30889733.

149. Heo DN, Acquah N, Kim J, Lee SJ, Castro NJ, Zhang LG. Directly Induced Neural Differentiation of Human Adipose-Derived Stem Cells Using Three-Dimensional Culture System of Conductive Microwell with Electrical Stimulation. Tissue Eng Part A. 2018;24(7-8):537-45. Epub 2017/07/26. doi: 10.1089/ten.TEA.2017.0150. PubMed PMID: 28741412.

150. Gagnon DR, Capistran JD, Karasz FE, Lenz RW, Antoun S. Synthesis, doping, and electrical conductivity of high molecular weight poly(p-phenylene vinylene). Polymer. 1987;28(4):567-73. doi: https://doi.org/10.1016/0032-3861(87)90471-X.

151. Niamlang S, Buranut T, Niansiri A, Sirivat A. Controlled Aloin Release from Crosslinked Polyacrylamide Hydrogels: Effects of Mesh Size, Electric Field Strength and a Conductive Polymer. Materials (Basel). 2013;6(10):4787-800. Epub 2013/10/22. doi: 10.3390/ma6104787. PubMed PMID: 28788360; PMCID: PMC5452847.

152. Zheng Z, Huang L, Yan L, Yuan F, Wang L, Wang K, Lawson T, Lin M, Liu Y. Polyaniline Functionalized Graphene Nanoelectrodes for the Regeneration of PC12 Cells via Electrical Stimulation. Int J Mol Sci. 2019;20(8). Epub 2019/04/27. doi: 10.3390/ijms20082013. PubMed PMID: 31022890; PMCID: PMC6515035.

153. Guo W, Zhang X, Yu X, Wang S, Qiu J, Tang W, Li L, Liu H, Wang ZL. Self-Powered Electrical Stimulation for Enhancing Neural Differentiation of Mesenchymal Stem Cells on Graphene-Poly(3,4-ethylenedioxythiophene)

Hybrid Microfibers. ACS Nano. 2016;10(5):5086-95. Epub 2016/05/05. doi: 10.1021/acsnano.6b00200. PubMed PMID: 27144593.

154. Zheng X, Woeppel KM, Griffith AY, Chang E, Looker MJ, Fisher LE, Clapsaddle BJ, Cui XT. Soft Conducting Elastomer for Peripheral Nerve Interface. Adv Healthc Mater. 2019;8(9):e1801311. Epub 2019/03/08. doi: 10.1002/adhm.201801311. PubMed PMID: 30843365.

155. Wang K, Tian L, Wang T, Zhang Z, Gao X, Wu L, Fu B, Liu X. Electrodeposition of alginate with PEDOT/PSS coated MWCNTs to make an interpenetrating conducting hydrogel for neural interface. Composite Interfaces. 2019;26(1):27-40. doi: 10.1080/09276440.2018.1465766.

156. Shin J, Choi EJ, Cho JH, Cho AN, Jin Y, Yang K, Song C, Cho SW. Three-Dimensional Electroconductive Hyaluronic Acid Hydrogels Incorporated with Carbon Nanotubes and Polypyrrole by Catechol-Mediated Dispersion Enhance Neurogenesis of Human Neural Stem Cells. Biomacromolecules. 2017;18(10):3060-72. Epub 2017/09/07. doi: 10.1021/acs.biomac.7b00568. PubMed PMID: 28876908.

157. Rong Q, Han H, Feng F, Ma Z. Network nanostructured polypyrrole hydrogel/Au composites as enhanced electrochemical biosensing platform. Sci Rep. 2015;5:11440. Epub 2015/06/16. doi: 10.1038/srep11440. PubMed PMID: 26074185; PMCID: PMC4466777.

158. Youssef AM, El-Aziz MEA, Abd El-Sayed ES, Moussa MA, Turky G, Kamel S. Rational design and electrical study of conducting bionanocomposites hydrogel based on chitosan and silver nanoparticles. Int J Biol Macromol. 2019;140:886-94. Epub 2019/08/27. doi: 10.1016/j.ijbiomac.2019.08.199. PubMed PMID: 31449867.

159. Bitounis D, Ali-Boucetta H, Hong BH, Min DH, Kostarelos K. Prospects and challenges of graphene in biomedical applications. Adv Mater. 2013;25(16):2258-68. Epub 2013/03/16. doi: 10.1002/adma.201203700. PubMed PMID: 23494834.

160. Kim TH, Lee T, El-Said WA, Choi JW. Graphene-Based Materials for Stem Cell Applications. Materials (Basel). 2015;8(12):8674-90. Epub 2015/12/11. doi: 10.3390/ma8125481. PubMed PMID: 28793737; PMCID: PMC5458813.

161. Dominguez-Bajo A, Gonzalez-Mayorga A, Lopez-Dolado E, Serrano MC. Graphene-Derived Materials Interfacing the Spinal Cord: Outstanding in Vitro and in Vivo Findings. Front Syst Neurosci. 2017;11:71. Epub 2017/11/01. doi: 10.3389/fnsys.2017.00071. PubMed PMID: 29085285; PMCID: PMC5649236.

162. Hwang JY, Shin US, Jang WC, Hyun JK, Wall IB, Kim HW. Biofunctionalized carbon nanotubes in neural regeneration: a mini-review. Nanoscale. 2013;5(2):487-97. Epub 2012/12/12. doi: 10.1039/c2nr31581e. PubMed PMID: 23223857.

163. Facciola A, Visalli G, La Maestra S, Ceccarelli M, D'Aleo F, Nunnari G, Pellicano GF, Di Pietro A. Carbon nanotubes and central nervous system: Environmental risks, toxicological aspects and future perspectives. Environ Toxicol Pharmacol. 2019;65:23-30. Epub 2018/12/01. doi: 10.1016/j.etap.2018.11.006. PubMed PMID: 30500734.

164. Sahni D, Jea A, Mata JA, Marcano DC, Sivaganesan A, Berlin JM, Tatsui CE, Sun Z, Luerssen TG, Meng S, Kent TA, Tour JM. Biocompatibility of pristine graphene for neuronal interface. J Neurosurg Pediatr. 2013;11(5):575-83. Epub 2013/03/12. doi: 10.3171/2013.1.PEDS12374. PubMed PMID: 23473006.

165. Park SY, Park J, Sim SH, Sung MG, Kim KS, Hong BH, Hong S. Enhanced differentiation of human neural stem cells into neurons on graphene. Adv Mater. 2011;23(36):H263-7. Epub 2011/08/09. doi: 10.1002/adma.201101503. PubMed PMID: 21823178.

166. Dominguez-Bajo A, Gonzalez-Mayorga A, Guerrero CR, Palomares FJ, Garcia R, Lopez-Dolado E, Serrano MC. Myelinated axons and functional blood vessels populate mechanically compliant rGO foams in chronic cervical hemisected rats. Biomaterials. 2019;192:461-74. Epub 2018/12/05. doi: 10.1016/j.biomaterials.2018.11.024. PubMed PMID: 30502723.

167. Lopez-Dolado E, Gonzalez-Mayorga A, Portoles MT, Feito MJ, Ferrer ML, Del Monte F, Gutierrez MC, Serrano MC. Subacute Tissue Response to 3D Graphene Oxide Scaffolds Implanted in the Injured Rat Spinal Cord. Adv Healthc Mater. 2015;4(12):1861-8. Epub 2015/06/27. doi: 10.1002/adhm.201500333. PubMed PMID: 26115359.

168. Palejwala AH, Fridley JS, Mata JA, Samuel EL, Luerssen TG, Perlaky L, Kent TA, Tour JM, Jea A. Biocompatibility of reduced graphene oxide nanoscaffolds following acute spinal cord injury in rats. Surg Neurol Int. 2016;7:75. Epub 2016/09/15. doi: 10.4103/2152-7806.188905. PubMed PMID: 27625885; PMCID: PMC5009578.

169. Lopez-Dolado E, Gonzalez-Mayorga A, Gutierrez MC, Serrano MC. Immunomodulatory and angiogenic responses induced by graphene oxide scaffolds in chronic spinal hemisected rats. Biomaterials. 2016;99:72-81. Epub 2016/05/24. doi: 10.1016/j.biomaterials.2016.05.012. PubMed PMID: 27214651.

170. Zhang K, Zheng H, Liang S, Gao C. Aligned PLLA nanofibrous scaffolds coated with graphene oxide for promoting neural cell growth. Acta Biomater. 2016;37:131-42. Epub 2016/04/12. doi: 10.1016/j.actbio.2016.04.008. PubMed PMID: 27063493.

171. Shah S, Yin PT, Uehara TM, Chueng ST, Yang L, Lee KB. Guiding stem cell differentiation into oligodendrocytes using graphene-nanofiber hybrid scaffolds. Adv Mater. 2014;26(22):3673-80. Epub 2014/03/29. doi: 10.1002/adma.201400523. PubMed PMID: 24668911; PMCID: PMC4048813.

172. Pan S, Qi Z, Li Q, Ma Y, Fu C, Zheng S, Kong W, Liu Q, Yang X. Graphene oxide-PLGA hybrid nanofibres for the local delivery of IGF-1 and BDNF in spinal cord repair. Artif Cells Nanomed Biotechnol. 2019;47(1):651-64. Epub 2019/03/05. doi: 10.1080/21691401.2019.1575843. PubMed PMID: 30829545.

173. Gonzalez-Mayorga A, Lopez-Dolado E, Gutierrez MC, Collazos-Castro JE, Ferrer ML, Del Monte F, Serrano MC. Favorable Biological Responses of Neural Cells and Tissue Interacting with Graphene Oxide Microfibers. ACS Omega. 2017;2(11):8253-63. Epub 2018/07/20. doi: 10.1021/acsomega.7b01354. PubMed PMID: 30023578; PMCID: PMC6044865.

174. Fabbro A, Sucapane A, Toma FM, Calura E, Rizzetto L, Carrieri C, Roncaglia P, Martinelli V, Scaini D, Masten L, Turco A, Gustincich S, Prato M, Ballerini L. Adhesion to carbon nanotube conductive scaffolds forces action-potential appearance in immature rat spinal neurons. PLoS One. 2013;8(8):e73621. Epub 2013/08/21. doi: 10.1371/journal.pone.0073621. PubMed PMID: 23951361; PMCID: PMC3741175.

175. Chen W, Xiong Q, Ren Q, Guo Y, Li G. Can amino-functionalized carbon nanotubes carry functional nerve growth factor? Neural Regen Res. 2014;9(3):285-92. Epub 2014/09/11. doi: 10.4103/1673-5374.128225. PubMed PMID: 25206814; PMCID: PMC4146147.

176. Roman JA, Niedzielko TL, Haddon RC, Parpura V, Floyd CL. Single-walled carbon nanotubes chemically functionalized with polyethylene glycol promote tissue repair in a rat model of spinal cord injury. J Neurotrauma. 2011;28(11):2349-62. Epub 2011/02/10. doi: 10.1089/neu.2010.1409. PubMed PMID: 21303267; PMCID: PMC3218389.

177. Usmani S, Aurand ER, Medelin M, Fabbro A, Scaini D, Laishram J, Rosselli FB, Ansuini A, Zoccolan D, Scarselli M, De Crescenzi M, Bosi S, Prato M, Ballerini L. 3D meshes of carbon nanotubes guide functional reconnection of segregated spinal explants. Sci Adv. 2016;2(7):e1600087.

Epub 2016/07/28. doi: 10.1126/sciadv.1600087. PubMed PMID: 27453939; PMCID: PMC4956187.

178. Wang C, Oh S, Lee HA, Kang J, Jeong KJ, Kang SW, Hwang DY, Lee J. In vivo feasibility test using transparent carbon nanotube-coated polydimethylsiloxane sheet at brain tissue and sciatic nerve. J Biomed Mater Res A. 2017;105(6):1736-45. Epub 2017/01/12. doi: 10.1002/jbm.a.36001. PubMed PMID: 28076883.

179. Imaninezhad M, Kuljanishvili I, Zustiak SP. A Two-Step Method for Transferring Single-Walled Carbon Nanotubes onto a Hydrogel Substrate. Macromol Biosci. 2017;17(3). Epub 2016/10/05. doi: 10.1002/mabi.201600261. PubMed PMID: 27701819.

180. Wang J, Chen N, Ramakrishna S, Tian L, Mo X. The Effect of Plasma Treated PLGA/MWCNTs-COOH Composite Nanofibers on Nerve Cell Behavior. Polymers (Basel). 2017;9(12). Epub 2017/12/14. doi: 10.3390/polym9120713. PubMed PMID: 30966009; PMCID: PMC6418518.

181. Wang L, Wu Y, Hu T, Ma PX, Guo B. Aligned conductive core-shell biomimetic scaffolds based on nanofiber yarns/hydrogel for enhanced 3D neurite outgrowth alignment and elongation. Acta Biomater. 2019;96:175-87. Epub 2019/07/02. doi: 10.1016/j.actbio.2019.06.035. PubMed PMID: 31260823.

182. Shrestha S, Shrestha BK, Lee J, Joong OK, Kim BS, Park CH, Kim CS. A conducting neural interface of polyurethane/silk-functionalized multiwall carbon nanotubes with enhanced mechanical strength for neuroregeneration. Mater Sci Eng C Mater Biol Appl. 2019;102:511-23. Epub 2019/05/31. doi: 10.1016/j.msec.2019.04.053. PubMed PMID: 31147022.

183. Chen CS, Soni S, Le C, Biasca M, Farr E, Chen EY, Chin WC. Human stem cell neuronal differentiation on silk-carbon nanotube composite. Nanoscale Res Lett. 2012;7(1):126. Epub 2012/02/16. doi: 10.1186/1556-276X-7-126. PubMed PMID: 22333433; PMCID: PMC3292945.

184. Wu S, Duan B, Lu A, Wang Y, Ye Q, Zhang L. Biocompatible chitin/carbon nanotubes composite hydrogels as neuronal growth substrates. Carbohydr Polym. 2017;174:830-40. Epub 2017/08/20. doi: 10.1016/j.carbpol.2017.06.101. PubMed PMID: 28821138.

185. Salehi M, Naseri-Nosar M, Ebrahimi-Barough S, Nourani M, Khojasteh A, Hamidieh AA, Amani A, Farzamfar S, Ai J. Sciatic nerve regeneration by transplantation of Schwann cells via erythropoietin controlled-releasing polylactic acid/multiwalled carbon nanotubes/gelatin nanofibrils neural guidance conduit. J Biomed Mater Res B Appl Biomater.

2018;106(4):1463-76. Epub 2017/07/05. doi: 10.1002/jbm.b.33952. PubMed PMID: 28675568.

186. Serrano MC, Nardecchia S, Garcia-Rama C, Ferrer ML, Collazos-Castro JE, del Monte F, Gutierrez MC. Chondroitin sulphate-based 3D scaffolds containing MWCNTs for nervous tissue repair. Biomaterials. 2014;35(5):1543-51. Epub 2013/12/03. doi: 10.1016/j.biomaterials.2013.11.017. PubMed PMID: 24290440.

187. Nardecchia S, Serrano MC, Gutiérrez MC, Ferrer ML, Monte Fd. Modulating the cytocompatibility of tridimensional carbon nanotube-based scaffolds. Journal of Materials Chemistry B. 2013;1(24):3064-72. doi: 10.1039/C3TB20253D.

188. Nawrotek K, Tylman M, Decherchi P, Marqueste T, Rudnicka K, Gatkowska J, Wieczorek M. Assessment of degradation and biocompatibility of electrodeposited chitosan and chitosan-carbon nanotube tubular implants. J Biomed Mater Res A. 2016;104(11):2701-11. Epub 2016/06/22. doi: 10.1002/jbm.a.35812. PubMed PMID: 27325550.

189. Lee SJ, Zhu W, Nowicki M, Lee G, Heo DN, Kim J, Zuo YY, Zhang LG. 3D printing nano conductive multi-walled carbon nanotube scaffolds for nerve regeneration. J Neural Eng. 2018;15(1):016018. Epub 2017/10/25. doi: 10.1088/1741-2552/aa95a5. PubMed PMID: 29064377.

190. Shin SR, Farzad R, Tamayol A, Manoharan V, Mostafalu P, Zhang YS, Akbari M, Jung SM, Kim D, Comotto M, Annabi N, Al-Hazmi FE, Dokmeci MR, Khademhosseini A. A Bioactive Carbon Nanotube-Based Ink for Printing 2D and 3D Flexible Electronics. Adv Mater. 2016;28(17):3280-9. Epub 2016/02/27. doi: 10.1002/adma.201506420. PubMed PMID: 26915715; PMCID: PMC4850092.

191. Cooper RJ, Menking-Colby MN, Humphrey KA, Victory JH, Kipps DW, Spitzer N. Involvement of beta-catenin in cytoskeleton disruption following adult neural stem cell exposure to low-level silver nanoparticles. Neurotoxicology. 2019;71:102-12. Epub 2019/01/04. doi: 10.1016/j.neuro.2018.12.010. PubMed PMID: 30605761.

192. Sharma HS, Muresanu DF, Lafuente JV, Sjoquist PO, Patnaik R, Sharma A. Nanoparticles Exacerbate Both Ubiquitin and Heat Shock Protein Expressions in Spinal Cord Injury: Neuroprotective Effects of the Proteasome Inhibitor Carfilzomib and the Antioxidant Compound H-290/51. Mol Neurobiol. 2015;52(2):882-98. Epub 2015/07/02. doi: 10.1007/s12035-015-9297-9. PubMed PMID: 26126513.

193. Wu T, Tang M. The inflammatory response to silver and titanium dioxide nanoparticles in the central nervous system. Nanomedicine (Lond).

2018;13(2):233-49. Epub 2017/12/05. doi: 10.2217/nnm-2017-0270. PubMed PMID: 29199887.

194. Nguyen TNH, Nolan JK, Park H, Lam S, Fattah M, Page JC, Joe HE, Jun MBG, Lee H, Kim SJ, Shi R, Lee H. Facile fabrication of flexible glutamate biosensor using direct writing of platinum nanoparticle-based nanocomposite ink. Biosens Bioelectron. 2019;131:257-66. Epub 2019/03/09. doi: 10.1016/j.bios.2019.01.051. PubMed PMID: 30849725.

195. Laomeephol C, Ferreira H, Yodmuang S, Reis RL, Damrongsakkul S, Neves NM. Exploring the Gelation Mechanisms and Cytocompatibility of Gold (III)-Mediated Regenerated and Thiolated Silk Fibroin Hydrogels. Biomolecules. 2020;10(3). Epub 2020/03/22. doi: 10.3390/biom10030466. PubMed PMID: 32197484.

196. Yan K, Xu F, Li S, Li Y, Chen Y, Wang D. Ice-templating of chitosan/agarose porous composite hydrogel with adjustable water-sensitive shape memory property and multi-staged degradation performance. Colloids Surf B Biointerfaces. 2020;190:110907. Epub 2020/03/03. doi: 10.1016/j.colsurfb.2020.110907. PubMed PMID: 32120129.

197. Skardal A, Zhang J, McCoard L, Oottamasathien S, Prestwich GD. Dynamically crosslinked gold nanoparticle - hyaluronan hydrogels. Adv Mater. 2010;22(42):4736-40. Epub 2010/08/24. doi: 10.1002/adma.201001436. PubMed PMID: 20730818.

198. Eguchi Y, Kato T, Tanaka T, Maruyama T. A DNA–gold nanoparticle hybrid hydrogel network prepared by enzymatic reaction. Chemical Communications. 2017;53(43):5802-5. doi: 10.1039/C7CC02435E.

199. An H, Li Q, Wen J. Bone marrow mesenchymal stem cells encapsulated thermal-responsive hydrogel network bridges combined photo-plasmonic nanoparticulate system for the treatment of urinary bladder dysfunction after spinal cord injury. J Photochem Photobiol B. 2020;203:111741. Epub 2020/01/07. doi: 10.1016/j.jphotobiol.2019.111741. PubMed PMID: 31901721.

200. Shevach M, Maoz BM, Feiner R, Shapira A, Dvir T. Nanoengineering gold particle composite fibers for cardiac tissue engineering. J Mater Chem B. 2013;1(39):5210-7. Epub 2013/10/21. doi: 10.1039/c3tb20584c. PubMed PMID: 32263327.

201. Shevach M, Fleischer S, Shapira A, Dvir T. Gold nanoparticle-decellularized matrix hybrids for cardiac tissue engineering. Nano Lett. 2014;14(10):5792-6. Epub 2014/09/02. doi: 10.1021/nl502673m. PubMed PMID: 25176294.

202. Dvir T, Timko BP, Brigham MD, Naik SR, Karajanagi SS, Levy O, Jin H, Parker KK, Langer R, Kohane DS. Nanowired three-dimensional cardiac patches. Nat Nanotechnol. 2011;6(11):720-5. Epub 2011/09/29. doi: 10.1038/nnano.2011.160. PubMed PMID: 21946708; PMCID: PMC3208725.

203. Zhu K, Shin SR, van Kempen T, Li YC, Ponraj V, Nasajpour A, Mandla S, Hu N, Liu X, Leijten J, Lin YD, Hussain MA, Zhang YS, Tamayol A, Khademhosseini A. Gold Nanocomposite Bioink for Printing 3D Cardiac Constructs. Adv Funct Mater. 2017;27(12). Epub 2017/03/24. doi: 10.1002/adfm.201605352. PubMed PMID: 30319321; PMCID: PMC6181228.

204. McKeon-Fischer KD, Freeman JW. Characterization of electrospun poly(L-lactide) and gold nanoparticle composite scaffolds for skeletal muscle tissue engineering. J Tissue Eng Regen Med. 2011;5(7):560-8. Epub 2011/06/23. doi: 10.1002/term.348. PubMed PMID: 21695797.

205. Zhang Y, Fan W, Wang K, Wei H, Zhang R, Wu Y. Novel preparation of Au nanoparticles loaded Laponite nanoparticles/ECM injectable hydrogel on cardiac differentiation of resident cardiac stem cells to cardiomyocytes. J Photochem Photobiol B. 2019;192:49-54. Epub 2019/01/27. doi: 10.1016/j.jphotobiol.2018.12.022. PubMed PMID: 30682654.

206. Navaei A, Rahmani Eliato K, Ros R, Migrino RQ, Willis BC, Nikkhah M. The influence of electrically conductive and non-conductive nanocomposite scaffolds on the maturation and excitability of engineered cardiac tissues. Biomater Sci. 2019;7(2):585-95. Epub 2018/11/15. doi: 10.1039/c8bm01050a. PubMed PMID: 30426116.

207. Navaei A, Saini H, Christenson W, Sullivan RT, Ros R, Nikkhah M. Gold nanorod-incorporated gelatin-based conductive hydrogels for engineering cardiac tissue constructs. Acta Biomater. 2016;41:133-46. Epub 2016/05/24. doi: 10.1016/j.actbio.2016.05.027. PubMed PMID: 27212425.

208. Nezhad-Mokhtari P, Akrami-Hasan-Kohal M, Ghorbani M. An injectable chitosan-based hydrogel scaffold containing gold nanoparticles for tissue engineering applications. Int J Biol Macromol. 2020;154:198-205. Epub 2020/03/19. doi: 10.1016/j.ijbiomac.2020.03.112. PubMed PMID: 32184143.

209. Zhou S, Huo D, Goines S, Yang TH, Lyu Z, Zhao M, Gilroy KD, Wu Y, Hood ZD, Xie M, Xia Y. Enabling Complete Ligand Exchange on the Surface of Gold Nanocrystals through the Deposition and Then Etching of Silver. J Am Chem Soc. 2018;140(38):11898-901. Epub 2018/09/05. doi: 10.1021/jacs.8b06464. PubMed PMID: 30179474.

210. Navaei A, Moore N, Sullivan RT, Truong D, Migrino RQ, Nikkhah M. Electrically conductive hydrogel-based micro-topographies for the development of organized cardiac tissues. RSC Advances. 2017;7(6):3302-12. doi: 10.1039/C6RA26279A.

211. Zhou C, Huang J, Yang Q, Li T, Liu J, Qian Z. Gold nanorods-based thermosensitive hydrogel produces selective long-lasting regional anesthesia triggered by photothermal activation of Transient Receptor Potential Vanilloid Type-1 channels. Colloids Surf B Biointerfaces. 2018;171:17-23. Epub 2018/07/14. doi: 10.1016/j.colsurfb.2018.07.002. PubMed PMID: 30005286.

212. Afjeh-Dana E, Naserzadeh P, Nazari H, Mottaghitalab F, Shabani R, Aminii N, Mehravi B, Rostami FT, Joghataei MT, Mousavizadeh K, Ashtari K. Gold nanorods reinforced silk fibroin nanocomposite for peripheral nerve tissue engineering applications. Int J Biol Macromol. 2019;129:1034-9. Epub 2019/02/12. doi: 10.1016/j.ijbiomac.2019.02.050. PubMed PMID: 30742919.

213. Paviolo C, Haycock JW, Yong J, Yu A, Stoddart PR, McArthur SL. Laser exposure of gold nanorods can increase neuronal cell outgrowth. Biotechnol Bioeng. 2013;110(8):2277-91. Epub 2013/03/05. doi: 10.1002/bit.24889. PubMed PMID: 23456616.

214. Paviolo C, Haycock JW, Cadusch PJ, McArthur SL, Stoddart PR. Laser exposure of gold nanorods can induce intracellular calcium transients. J Biophotonics. 2014;7(10):761-5. Epub 2013/06/26. doi: 10.1002/jbio.201300043. PubMed PMID: 23798060.

215. Naderi MS, Moghadam TT, Khajeh K, Ranjbar B. Improving the stability of chondroitinase ABC I via interaction with gold nanorods. Int J Biol Macromol. 2018;107(Pt A):297-304. Epub 2017/09/05. doi: 10.1016/j.ijbiomac.2017.08.167. PubMed PMID: 28867227.

216. Kamei N, Adachi N, Ochi M. Magnetic cell delivery for the regeneration of musculoskeletal and neural tissues. Regen Ther. 2018;9:116-9. Epub 2018/12/14. doi: 10.1016/j.reth.2018.10.001. PubMed PMID: 30525082; PMCID: PMC6222975.

217. Adams CF, Delaney AM, Carwardine DR, Tickle J, Granger N, Chari DM. Nanoparticle-Based Imaging of Clinical Transplant Populations Encapsulated in Protective Polymer Matrices. Macromol Biosci. 2019;19(2):e1800389. Epub 2018/12/05. doi: 10.1002/mabi.201800389. PubMed PMID: 30511815.

218. Gao J, Xia B, Li S, Huang L, Ma T, Shi X, Luo K, Yang Y, Zhao L, Zhang H, Luo B, Huang J. Magnetic Field Promotes Migration of Schwann Cells with Chondroitinase ABC (ChABC)-Loaded Superparamagnetic

Nanoparticles Across Astrocyte Boundary in vitro. Int J Nanomedicine. 2020;15:315-32. Epub 2020/02/06. doi: 10.2147/IJN.S227328. PubMed PMID: 32021182; PMCID: PMC6980842.

219. Pal A, Kumar S, Jain S, Nag TC, Mathur R. Neuroregenerative Effects of Electromagnetic Field and Magnetic Nanoparticles on Spinal Cord Injury in Rats. J Nanosci Nanotechnol. 2018;18(10):6756-64. Epub 2018/06/30. doi: 10.1166/jnn.2018.15820. PubMed PMID: 29954491.

220. Lacko CS, Singh I, Wall MA, Garcia AR, Porvasnik SL, Rinaldi C, Schmidt CE. Magnetic particle templating of hydrogels: engineering naturally derived hydrogel scaffolds with 3D aligned microarchitecture for nerve repair. J Neural Eng. 2020;17(1):016057. Epub 2019/10/03. doi: 10.1088/1741-2552/ab4a22. PubMed PMID: 31577998.

221. Rose JC, Camara-Torres M, Rahimi K, Kohler J, Moller M, De Laporte L. Nerve Cells Decide to Orient inside an Injectable Hydrogel with Minimal Structural Guidance. Nano Lett. 2017;17(6):3782-91. Epub 2017/03/23. doi: 10.1021/acs.nanolett.7b01123. PubMed PMID: 28326790; PMCID: PMC5537692.

222. Johnson CDL, Ganguly D, Zuidema JM, Cardinal TJ, Ziemba AM, Kearns KR, McCarthy SM, Thompson DM, Ramanath G, Borca-Tasciuc DA, Dutz S, Gilbert RJ. Injectable, Magnetically Orienting Electrospun Fiber Conduits for Neuron Guidance. ACS Appl Mater Interfaces. 2019;11(1):356-72. Epub 2018/12/06. doi: 10.1021/acsami.8b18344. PubMed PMID: 30516370; PMCID: PMC6520652.

223. Omidinia-Anarkoli A, Boesveld S, Tuvshindorj U, Rose JC, Haraszti T, De Laporte L. An Injectable Hybrid Hydrogel with Oriented Short Fibers Induces Unidirectional Growth of Functional Nerve Cells. Small. 2017;13(36). Epub 2017/08/08. doi: 10.1002/smll.201702207. PubMed PMID: 28783255.

224. Gungor-Ozkerim PS, Inci I, Zhang YS, Khademhosseini A, Dokmeci MR. Bioinks for 3D bioprinting: an overview. Biomater Sci. 2018;6(5):915-46. doi: 10.1039/c7bm00765e. PubMed PMID: 29492503.

225. Vijayavenkataraman S, Yan WC, Lu WF, Wang CH, Fuh JYH. 3D bioprinting of tissues and organs for regenerative medicine. Adv Drug Deliv Rev. 2018. doi: 10.1016/j.addr.2018.07.004. PubMed PMID: 29990578.

226. Gopinathan J, Noh I. Recent trends in bioinks for 3D printing. Biomater Res. 2018;22:11. Epub 2018/04/11. doi: 10.1186/s40824-018-0122-1. PubMed PMID: 29636985; PMCID: PMC5889544.

227. Jammalamadaka U, Tappa K. Recent Advances in Biomaterials for 3D Printing and Tissue Engineering. J Funct Biomater. 2018;9(1). doi: 10.3390/jfb9010022. PubMed PMID: 29494503; PMCID: PMC5872108.

228. Murphy SV, Atala A. 3D bioprinting of tissues and organs. Nat Biotechnol. 2014;32(8):773-85. Epub 2014/08/06. doi: 10.1038/nbt.2958. PubMed PMID: 25093879.

229. Daly AC, Freeman FE, Gonzalez-Fernandez T, Critchley SE, Nulty J, Kelly DJ. 3D Bioprinting for Cartilage and Osteochondral Tissue Engineering. Adv Healthc Mater. 2017;6(22). Epub 2017/08/15. doi: 10.1002/adhm.201700298. PubMed PMID: 28804984.

230. Panwar A, Tan LP. Current Status of Bioinks for Micro-Extrusion-Based 3D Bioprinting. Molecules. 2016;21(6). doi: 10.3390/molecules21060685. PubMed PMID: 27231892.

231. Derakhshanfar S, Mbeleck R, Xu K, Zhang X, Zhong W, Xing M. 3D bioprinting for biomedical devices and tissue engineering: A review of recent trends and advances. Bioact Mater. 2018;3(2):144-56. doi: 10.1016/j.bioactmat.2017.11.008. PubMed PMID: 29744452; PMCID: PMC5935777.

232. Holzl K, Lin S, Tytgat L, Van Vlierberghe S, Gu L, Ovsianikov A. Bioink properties before, during and after 3D bioprinting. Biofabrication. 2016;8(3):032002. doi: 10.1088/1758-5090/8/3/032002. PubMed PMID: 27658612.

233. Malda J, Visser J, Melchels FP, Jungst T, Hennink WE, Dhert WJ, Groll J, Hutmacher DW. 25th anniversary article: Engineering hydrogels for biofabrication. Adv Mater. 2013;25(36):5011-28. Epub 2013/09/17. doi: 10.1002/adma.201302042. PubMed PMID: 24038336.

234. Stichler S, Bock T, Paxton N, Bertlein S, Levato R, Schill V, Smolan W, Malda J, Tessmar J, Blunk T, Groll J. Double printing of hyaluronic acid/poly(glycidol) hybrid hydrogels with poly(epsilon-caprolactone) for MSC chondrogenesis. Biofabrication. 2017;9(4):044108. Epub 2017/09/15. doi: 10.1088/1758-5090/aa8cb7. PubMed PMID: 28906257.

235. Wenz A, Borchers K, Tovar GEM, Kluger PJ. Bone matrix production in hydroxyapatite-modified hydrogels suitable for bone bioprinting. Biofabrication. 2017;9(4):044103. Epub 2017/10/11. doi: 10.1088/1758-5090/aa91ec. PubMed PMID: 28990579.

236. Sakai S, Ohi H, Hotta T, Kamei H, Taya M. Differentiation potential of human adipose stem cells bioprinted with hyaluronic acid/gelatin-based bioink through microextrusion and visible light-initiated crosslinking.

Biopolymers. 2018;109(2). Epub 2017/11/16. doi: 10.1002/bip.23080. PubMed PMID: 29139103.

237. Law N, Doney B, Glover H, Qin Y, Aman ZM, Sercombe TB, Liew LJ, Dilley RJ, Doyle BJ. Characterisation of hyaluronic acid methylcellulose hydrogels for 3D bioprinting. J Mech Behav Biomed Mater. 2018;77:389-99. Epub 2017/10/11. doi: 10.1016/j.jmbbm.2017.09.031. PubMed PMID: 29017117.

238. Skardal A, Devarasetty M, Kang HW, Seol YJ, Forsythe SD, Bishop C, Shupe T, Soker S, Atala A. Bioprinting Cellularized Constructs Using a Tissue-specific Hydrogel Bioink. J Vis Exp. 2016(110):e53606. Epub 2016/05/12. doi: 10.3791/53606. PubMed PMID: 27166839; PMCID: PMC4941985.

239. Diamantides N, Wang L, Pruiksma T, Siemiatkoski J, Dugopolski C, Shortkroff S, Kennedy S, Bonassar LJ. Correlating rheological properties and printability of collagen bioinks: the effects of riboflavin photocrosslinking and pH. Biofabrication. 2017;9(3):034102. Epub 2017/07/06. doi: 10.1088/1758-5090/aa780f. PubMed PMID: 28677597.

240. Muller M, Becher J, Schnabelrauch M, Zenobi-Wong M. Nanostructured Pluronic hydrogels as bioinks for 3D bioprinting. Biofabrication. 2015;7(3):035006. Epub 2015/08/12. doi: 10.1088/1758-5090/7/3/035006. PubMed PMID: 26260872.

241. Mouser VHM, Melchels FPW, Visser J, Dhert WJA, Gawlitta D, Malda J. Yield stress determines bioprintability of hydrogels based on gelatin-methacryloyl and gellan gum for cartilage bioprinting. Biofabrication. 2016;8(3):035003. doi: 10.1088/1758-5090/8/3/035003.

242. Ribeiro A, Blokzijl MM, Levato R, Visser CW, Castilho M, Hennink WE, Vermonden T, Malda J. Assessing bioink shape fidelity to aid material development in 3D bioprinting. Biofabrication. 2017;10(1):014102. Epub 2017/10/05. doi: 10.1088/1758-5090/aa90e2. PubMed PMID: 28976364.

243. Gao T, Gillispie GJ, Copus JS, Pr AK, Seol YJ, Atala A, Yoo JJ, Lee SJ. Optimization of gelatin-alginate composite bioink printability using rheological parameters: a systematic approach. Biofabrication. 2018;10(3):034106. Epub 2018/06/21. doi: 10.1088/1758-5090/aacdc7. PubMed PMID: 29923501; PMCID: PMC6040670.

244. Paxton N, Smolan W, Bock T, Melchels F, Groll J, Jungst T. Proposal to assess printability of bioinks for extrusion-based bioprinting and evaluation of rheological properties governing bioprintability. Biofabrication. 2017;9(4):044107. Epub 2017/09/21. doi: 10.1088/1758-5090/aa8dd8. PubMed PMID: 28930091.

245. Wilson SA, Cross LM, Peak CW, Gaharwar AK. Shear-Thinning and Thermo-Reversible Nanoengineered Inks for 3D Bioprinting. ACS Appl Mater Interfaces. 2017;9(50):43449-58. Epub 2017/12/08. doi: 10.1021/acsami.7b13602. PubMed PMID: 29214803.

246. Skardal A, Devarasetty M, Kang HW, Mead I, Bishop C, Shupe T, Lee SJ, Jackson J, Yoo J, Soker S, Atala A. A hydrogel bioink toolkit for mimicking native tissue biochemical and mechanical properties in bioprinted tissue constructs. Acta Biomater. 2015;25:24-34. Epub 2015/07/27. doi: 10.1016/j.actbio.2015.07.030. PubMed PMID: 26210285.

247. Jungst T, Smolan W, Schacht K, Scheibel T, Groll J. Strategies and Molecular Design Criteria for 3D Printable Hydrogels. Chem Rev. 2016;116(3):1496-539. Epub 2015/10/27. doi: 10.1021/acs.chemrev.5b00303. PubMed PMID: 26492834.

248. Hospodiuk M, Dey M, Sosnoski D, Ozbolat IT. The bioink: A comprehensive review on bioprintable materials. Biotechnol Adv. 2017;35(2):217-39. Epub 2017/01/07. doi: 10.1016/j.biotechadv.2016.12.006. PubMed PMID: 28057483.

249. Tiwari S, Bahadur P. Modified hyaluronic acid based materials for biomedical applications. Int J Biol Macromol. 2019;121:556-71. Epub 2018/10/16. doi: 10.1016/j.ijbiomac.2018.10.049. PubMed PMID: 30321638.

250. Beck EC, Barragan M, Libeer TB, Kieweg SL, Converse GL, Hopkins RA, Berkland CJ, Detamore MS. Chondroinduction from Naturally Derived Cartilage Matrix: A Comparison Between Devitalized and Decellularized Cartilage Encapsulated in Hydrogel Pastes. Tissue Eng Part A. 2016;22(7-8):665-79. doi: 10.1089/ten.TEA.2015.0546. PubMed PMID: 27001140; PMCID: PMC4840832.

251. Townsend JM, Andrews BT, Feng Y, Wang J, Nudo RJ, Van Kampen E, Gehrke SH, Berkland CJ, Detamore MS. Superior calvarial bone regeneration using pentenoate-functionalized hyaluronic acid hydrogels with devitalized tendon particles. Acta Biomater. 2018;71:148-55. doi: 10.1016/j.actbio.2018.02.013. PubMed PMID: 29496620; PMCID: PMC5899926.

252. Townsend JM, Dennis SC, Whitlow J, Feng Y, Wang J, Andrews B, Nudo RJ, Detamore MS, Berkland CJ. Colloidal Gels with Extracellular Matrix Particles and Growth Factors for Bone Regeneration in Critical Size Rat Calvarial Defects. AAPS J. 2017;19(3):703-11. Epub 2017/02/01. doi: 10.1208/s12248-017-0045-0. PubMed PMID: 28138909.

253. Skardal A, Zhang J, McCoard L, Xu X, Oottamasathien S, Prestwich GD. Photocrosslinkable hyaluronan-gelatin hydrogels for two-step bioprinting.

Tissue Eng Part A. 2010;16(8):2675-85. doi: 10.1089/ten.TEA.2009.0798. PubMed PMID: 20387987; PMCID: PMC3135254.

254. Mergy J, Fournier A, Hachet E, Auzély-Velty R. Modification of polysaccharides via thiol-ene chemistry: A versatile route to functional biomaterials. J Polym Sci A Polym Chem. 2012;50(19):4019-28. doi: 10.1002/pola.26201.

255. Gottlieb HE, Kotlyar V, Nudelman A. NMR chemical shifts of common laboratory solvents as trace impurities. Journal of Organic Chemistry. 1997;62(21):7512-5. doi: DOI 10.1021/jo971176v. PubMed PMID: WOS:A1997YC65700083.

256. Townsend JM, Zabel TA, Feng Y, Wang J, Andrews BT, Nudo RJ, Berkland CJ, Detamore MS. Effects of tissue processing on bioactivity of cartilage matrix-based hydrogels encapsulating osteoconductive particles. Biomed Mater. 2018;13(3):034108. Epub 2018/02/08. doi: 10.1088/1748-605X/aaad77. PubMed PMID: 29411714; PMCID: PMC5892836.

257. Beck EC, Barragan M, Tadros MH, Gehrke SH, Detamore MS. Approaching the compressive modulus of articular cartilage with a decellularized cartilage-based hydrogel. Acta Biomater. 2016;38:94-105. doi: 10.1016/j.actbio.2016.04.019. PubMed PMID: 27090590; PMCID: PMC4903909.

258. Ouyang L, Yao R, Zhao Y, Sun W. Effect of bioink properties on printability and cell viability for 3D bioplotting of embryonic stem cells. Biofabrication. 2016;8(3):035020. Epub 2016/09/17. doi: 10.1088/1758-5090/8/3/035020. PubMed PMID: 27634915.

259. Billiet T, Gevaert E, De Schryver T, Cornelissen M, Dubruel P. The 3D printing of gelatin methacrylamide cell-laden tissue-engineered constructs with high cell viability. Biomaterials. 2014;35(1):49-62. Epub 2013/10/12. doi: 10.1016/j.biomaterials.2013.09.078. PubMed PMID: 24112804.

260. Wang LL, Highley CB, Yeh YC, Galarraga JH, Uman S, Burdick JA. Three-dimensional extrusion bioprinting of single- and double-network hydrogels containing dynamic covalent crosslinks. J Biomed Mater Res A. 2018;106(4):865-75. Epub 2018/01/10. doi: 10.1002/jbm.a.36323. PubMed PMID: 29314616; PMCID: PMC5826872.

261. Ooi HW, Mota C, Ten Cate AT, Calore A, Moroni L, Baker MB. Thiol-Ene Alginate Hydrogels as Versatile Bioinks for Bioprinting. Biomacromolecules. 2018;19(8):3390-400. Epub 2018/06/26. doi: 10.1021/acs.biomac.8b00696. PubMed PMID: 29939754.

262. Nair K, Gandhi M, Khalil S, Yan KC, Marcolongo M, Barbee K, Sun W. Characterization of cell viability during bioprinting processes. Biotechnol

J. 2009;4(8):1168-77. Epub 2009/06/10. doi: 10.1002/biot.200900004. PubMed PMID: 19507149.

263. Koo Y, Kim G. New strategy for enhancing in situ cell viability of cell-printing process via piezoelectric transducer-assisted three-dimensional printing. Biofabrication. 2016;8(2):025010. Epub 2016/05/21. doi: 10.1088/1758-5090/8/2/025010. PubMed PMID: 27203798.

264. Bhatnagar D, Dube K, Damodaran VB, Subramanian G, Aston K, Halperin F, Mao M, Pricer K, Murthy NS, Kohn J. Effects of Terminal Sterilization on PEG-Based Bioresorbable Polymers Used in Biomedical Applications. Macromol Mater Eng. 2016;301(10):1211-24. doi: 10.1002/mame.201600133. PubMed PMID: 28280451; PMCID: PMC5340269.

265. Phillip E, Jr., Murthy NS, Bolikal D, Narayanan P, Kohn J, Lavelle L, Bodnar S, Pricer K. Ethylene oxide's role as a reactive agent during sterilization: effects of polymer composition and device architecture. J Biomed Mater Res B Appl Biomater. 2013;101(4):532-40. doi: 10.1002/jbm.b.32853. PubMed PMID: 23296710.

266. Kanjickal D, Lopina S, Evancho-Chapman MM, Schmidt S, Donovan D. Effects of sterilization on poly(ethylene glycol) hydrogels. J Biomed Mater Res A. 2008;87(3):608-17. doi: 10.1002/jbm.a.31811. PubMed PMID: 18186054.

267. Hooper KA, Cox JD, Kohn J. Comparison of the effect of ethylene oxide and γ-irradiation on selected tyrosine-derived polycarbonates and poly(L-lactic acid). Journal of Applied Polymer Science. 1997;63(11):1499-510. doi: 10.1002/(SICI)1097-4628(19970314)63:11<1499::AID-APP12>3.0.CO;2-Y.

268. Li X, Liu X, Cui L, Brunson C, Zhao W, Bhat NR, Zhang N, Wen X. Engineering an in situ crosslinkable hydrogel for enhanced remyelination. FASEB J. 2013;27(3):1127-36. doi: 10.1096/fj.12-211151.

269. Claassen C, Claassen MH, Truffault V, Sewald L, Tovar GEM, Borchers K, Southan A. Quantification of Substitution of Gelatin Methacryloyl: Best Practice and Current Pitfalls. Biomacromolecules. 2018;19(1):42-52. Epub 2017/12/07. doi: 10.1021/acs.biomac.7b01221. PubMed PMID: 29211461.

270. Townsend JM, Sali G, Homburg HB, Cassidy NT, Sanders ME, Fung KM, Andrews BT, Nudo RJ, Bohnstedt BN, Detamore MS. Thiolated bone and tendon tissue particles covalently bound in hydrogels for in vivo calvarial bone regeneration. Acta Biomater. 2020;104:66-75. Epub 2020/01/07. doi: 10.1016/j.actbio.2019.12.035. PubMed PMID: 31904561.

271. Khaing ZZ, Milman BD, Vanscoy JE, Seidlits SK, Grill RJ, Schmidt CE. High molecular weight hyaluronic acid limits astrocyte activation and scar formation after spinal cord injury. J Neural Eng. 2011;8(4):046033. doi: 10.1088/1741-2560/8/4/046033.

272. Karimi A, Shojaei A, Tehrani P. Mechanical properties of the human spinal cord under the compressive loading. J Chem Neuroanat. 2017;86:15-8. Epub 2017/07/20. doi: 10.1016/j.jchemneu.2017.07.004. PubMed PMID: 28720407.

273. Huerta-Angeles G, Nemcova M, Prikopova E, Smejkalova D, Pravda M, Kucera L, Velebny V. Reductive alkylation of hyaluronic acid for the synthesis of biocompatible hydrogels by click chemistry. Carbohydr Polym. 2012;90(4):1704-11. Epub 2012/09/05. doi: 10.1016/j.carbpol.2012.07.054. PubMed PMID: 22944436.

274. Hoch E, Hirth T, Tovar GEM, Borchers K. Chemical tailoring of gelatin to adjust its chemical and physical properties for functional bioprinting. J Mater Chem B. 2013;1(41):5675-85. Epub 2013/11/07. doi: 10.1039/c3tb20745e. PubMed PMID: 32261191.

275. Vigata M, Meinert C, Pahoff S, Bock N, Hutmacher DW. Gelatin Methacryloyl Hydrogels Control the Localized Delivery of Albumin-Bound Paclitaxel. Polymers (Basel). 2020;12(2). Epub 2020/02/28. doi: 10.3390/polym12020501. PubMed PMID: 32102478; PMCID: PMC7077643.

276. Li X, Chen S, Li J, Wang X, Zhang J, Kawazoe N, Chen G. 3D Culture of Chondrocytes in Gelatin Hydrogels with Different Stiffness. Polymers (Basel). 2016;8(8). Epub 2016/07/26. doi: 10.3390/polym8080269. PubMed PMID: 30974547; PMCID: PMC6431829.

277. Habeeb AF. Determination of free amino groups in proteins by trinitrobenzenesulfonic acid. Anal Biochem. 1966;14(3):328-36. Epub 1966/03/01. doi: 10.1016/0003-2697(66)90275-2. PubMed PMID: 4161471.

278. Sutter M, Siepmann J, Hennink WE, Jiskoot W. Recombinant gelatin hydrogels for the sustained release of proteins. J Control Release. 2007;119(3):301-12. Epub 2007/05/01. doi: 10.1016/j.jconrel.2007.03.003. PubMed PMID: 17467099.

279. Yarrow JF, Kok HJ, Phillips EG, Conover CF, Lee J, Bassett TE, Buckley KH, Reynolds MC, Wnek RD, Otzel DM, Chen C, Jiron JM, Graham ZA, Cardozo C, Vandenborne K, Bose PK, Aguirre JI, Borst SE, Ye F. Locomotor training with adjuvant testosterone preserves cancellous bone and promotes muscle plasticity in male rats after severe spinal cord injury.

J Neurosci Res. 2020;98(5):843-68. Epub 2019/12/05. doi: 10.1002/jnr.24564. PubMed PMID: 31797423; PMCID: PMC7072003.

280. Yadid M, Feiner R, Dvir T. Gold Nanoparticle-Integrated Scaffolds for Tissue Engineering and Regenerative Medicine. Nano Lett. 2019;19(4):2198-206. Epub 2019/03/19. doi: 10.1021/acs.nanolett.9b00472. PubMed PMID: 30884238.

281. Vigderman L, Zubarev ER. High-Yield Synthesis of Gold Nanorods with Longitudinal SPR Peak Greater than 1200 nm Using Hydroquinone as a Reducing Agent. Chemistry of Materials. 2013;25(8):1450-7. doi: 10.1021/cm303661d.

282. Donahue ND, Francek ER, Kiyotake E, Thomas EE, Yang W, Wang L, Detamore MS, Wilhelm S. Assessing nanoparticle colloidal stability with single-particle inductively coupled plasma mass spectrometry (SP-ICP-MS). Anal Bioanal Chem. 2020;412(22):5205-16. Epub 2020/07/07. doi: 10.1007/s00216-020-02783-6. PubMed PMID: 32627086.

283. Lee JC, Donahue ND, Mao AS, Karim A, Komarneni M, Thomas EE, Francek ER, Yang W, Wilhelm S. Exploring Maleimide-Based Nanoparticle Surface Engineering to Control Cellular Interactions. ACS Applied Nano Materials. 2020;3(3):2421-9. doi: 10.1021/acsanm.9b02541.

284. Pace HE, Rogers NJ, Jarolimek C, Coleman VA, Gray EP, Higgins CP, Ranville JF. Single Particle Inductively Coupled Plasma-Mass Spectrometry: A Performance Evaluation and Method Comparison in the Determination of Nanoparticle Size. Environmental Science & Technology. 2012;46(22):12272-80. doi: 10.1021/es301787d.

285. Merrifield RC, Stephan C, Lead JR. Quantification of Au Nanoparticle Biouptake and Distribution to Freshwater Algae Using Single Cell – ICP-MS. Environmental Science & Technology. 2018;52(4):2271-7. doi: 10.1021/acs.est.7b04968.

286. Laborda F, Jiménez-Lamana J, Bolea E, Castillo JR. Critical considerations for the determination of nanoparticle number concentrations, size and number size distributions by single particle ICP-MS. Journal of Analytical Atomic Spectrometry. 2013;28(8):1220-32. doi: 10.1039/C3JA50100K.

287. Herren B, Charara M, Saha MC, Altan MC, Liu Y. Rapid Microwave Polymerization of Porous Nanocomposites with Piezoresistive Sensing Function. Nanomaterials (Basel). 2020;10(2). Epub 2020/02/06. doi: 10.3390/nano10020233. PubMed PMID: 32013133; PMCID: PMC7075205.

288. Basso DM, Beattie MS, Bresnahan JC. A sensitive and reliable locomotor rating scale for open field testing in rats. Journal of Neurotrauma. 1995;12(1):1-21. doi: 10.1089/neu.1995.12.1.

289. Nikoobakht B, El-Sayed MA. Preparation and Growth Mechanism of Gold Nanorods (NRs) Using Seed-Mediated Growth Method. Chemistry of Materials. 2003;15(10):1957-62. doi: 10.1021/cm020732l.

290. Orendorff CJ, Murphy CJ. Quantitation of metal content in the silver-assisted growth of gold nanorods. J Phys Chem B. 2006;110(9):3990-4. Epub 2006/03/03. doi: 10.1021/jp0570972. PubMed PMID: 16509687.

291. Hu ZJ, Hou S, Ji YL, Wen T, Liu WQ, Zhang H, Shi XW, Yan J, Wu XC. Fast characterization of gold nanorods ensemble by correlating its structure with optical extinction spectral features. AIP Advances. 2014;4(11):117137. doi: 10.1063/1.4903163.

292. Near RD, Hayden SC, Hunter RE, Thackston D, El-Sayed MA. Rapid and Efficient Prediction of Optical Extinction Coefficients for Gold Nanospheres and Gold Nanorods. The Journal of Physical Chemistry C. 2013;117(45):23950-5. doi: 10.1021/jp4082596.

293. Mostafa AE-s, Nemat AY, Ali AS, Osama AE-s, Sawsan SM, Siham ME-s, Marwa AE-s, Nabila SH, Emad AA-a, Wael HE, Rehab FA-r. Toxicological and pharmacological assessment of gold nanorods in normal rats. International Journal of Pharmacy and Pharmaceutical Sciences. 2015;7(12).

294. Ali MRK, Rahman MA, Wu Y, Han T, Peng X, Mackey MA, Wang D, Shin HJ, Chen ZG, Xiao H, Wu R, Tang Y, Shin DM, El-Sayed MA. Efficacy, long-term toxicity, and mechanistic studies of gold nanorods photothermal therapy of cancer in xenograft mice. Proceedings of the National Academy of Sciences. 2017;114(15):E3110. doi: 10.1073/pnas.1619302114.

295. Khaing ZZ, Ehsanipour A, Hofstetter CP, Seidlits SK. Injectable Hydrogels for Spinal Cord Repair: A Focus on Swelling and Intraspinal Pressure. Cells Tissues Organs. 2016;202(1-2):67-84. Epub 2016/10/18. doi: 10.1159/000446697. PubMed PMID: 27701162.

296. Kushchayev SV, Giers MB, Hom Eng D, Martirosyan NL, Eschbacher JM, Mortazavi MM, Theodore N, Panitch A, Preul MC. Hyaluronic acid scaffold has a neuroprotective effect in hemisection spinal cord injury. J Neurosurg Spine. 2016;25(1):114-24. doi: 10.3171/2015.9.SPINE15628.

297. Steward O, Willenberg R. Rodent spinal cord injury models for studies of axon regeneration. Exp Neurol. 2017;287(Pt 3):374-83. doi: 10.1016/j.expneurol.2016.06.029.

298. Cheriyan T, Ryan DJ, Weinreb JH, Cheriyan J, Paul JC, Lafage V, Kirsch T, Errico TJ. Spinal cord injury models: a review. Spinal Cord. 2014;52(8):588-95. Epub 2014/06/11. doi: 10.1038/sc.2014.91. PubMed PMID: 24912546.

299. Moore SA, Granger N, Olby NJ, Spitzbarth I, Jeffery ND, Tipold A, Nout-Lomas YS, da Costa RC, Stein VM, Noble-Haeusslein LJ, Blight AR, Grossman RG, Basso DM, Levine JM. Targeting Translational Successes through CANSORT-SCI: Using Pet Dogs To Identify Effective Treatments for Spinal Cord Injury. J Neurotrauma. 2017;34(12):2007-18. Epub 2017/02/24. doi: 10.1089/neu.2016.4745. PubMed PMID: 28230415; PMCID: PMC5467140.

300. Curtis E, Martin JR, Gabel B, Sidhu N, Rzesiewicz TK, Mandeville R, Van Gorp S, Leerink M, Tadokoro T, Marsala S, Jamieson C, Marsala M, Ciacci JD. A First-in-Human, Phase I Study of Neural Stem Cell Transplantation for Chronic Spinal Cord Injury. Cell Stem Cell. 2018;22(6):941-50 e6. Epub 2018/06/03. doi: 10.1016/j.stem.2018.05.014. PubMed PMID: 29859175.

301. Xiao Z, Tang F, Tang J, Yang H, Zhao Y, Chen B, Han S, Wang N, Li X, Cheng S, Han G, Zhao C, Yang X, Chen Y, Shi Q, Hou S, Zhang S, Dai J. One-year clinical study of NeuroRegen scaffold implantation following scar resection in complete chronic spinal cord injury patients. Sci China Life Sci. 2016;59(7):647-55. doi: 10.1007/s11427-016-5080-z.

Appendix A: Figures

Chapter 1: No Figures

Chapter 2: Figures 2.1-2.2

Chapter 3: Figures 3.1-3.5

Chapter 4: Figures 4.1-4.8

Chapter 5: Figures 5.1-5.15

Chapter 6: No Figures

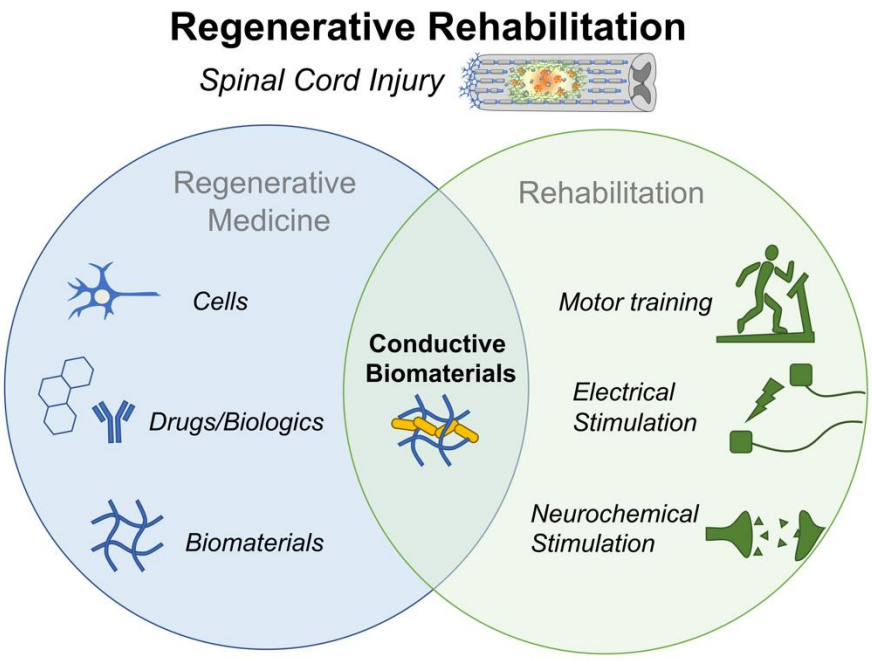

Figure 2.1: A Venn Diagram Illustrating Conductive Biomaterials in Regenerative Rehabilitation

A Venn diagram of the concept of regenerative rehabilitation for spinal cord injury (SCI). Regenerative medicine approaches include cells, drugs, biologics, and biomaterials. Rehabilitation approaches for SCI include motor training, electrical stimulation, and neurochemical stimulation. Conductive biomaterials can link these two disparate fields together by providing a substrate to deliver electrical stimulation (ES) through the injury to elicit neural plasticity and by delivering cell, drugs, and/or biologics to regenerate the injured tissue.

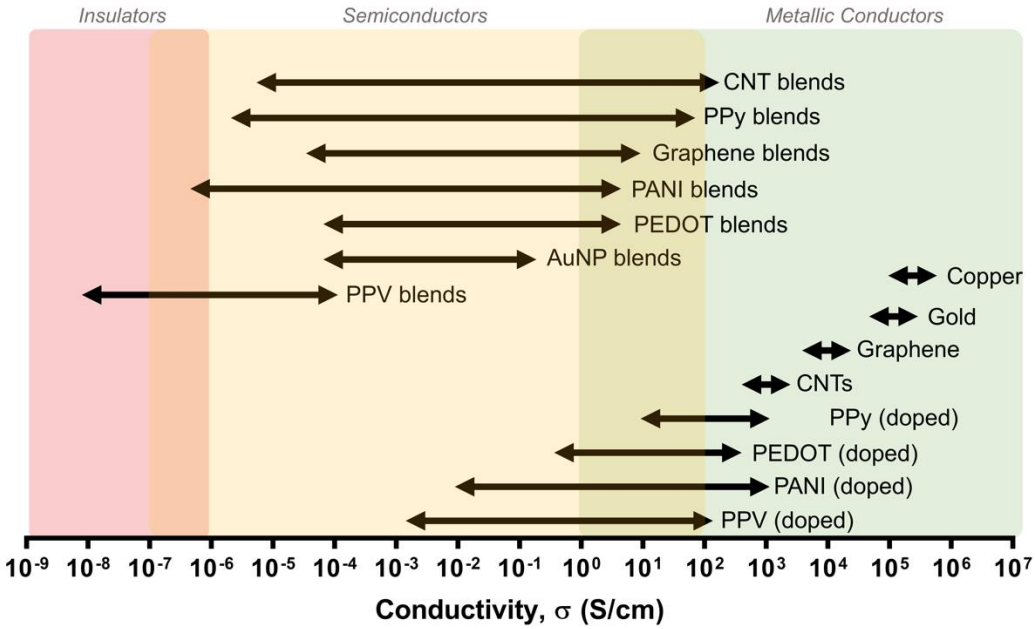

Figure 2.2: Illustration of the of Conductive Composites

The range of conductivities for conductive substrates by themselves and conductive composites. The region of insulators is $<10^{-6}$ S/cm (red area), the region of semiconductors is ~10^{-7} to ~10^{2} (yellow area), and metallic conductors range from ~10^{0} to 10^{7} (green area). Abbreviations: CNTs, carbon nanotubes; PPy, polypyrrole; PANI, polyaniline; PEDOT, poly(3,4-ethylenedioxythiophene); AuNP, gold nanoparticle; PPV, poly(p-phenylene vinylene.

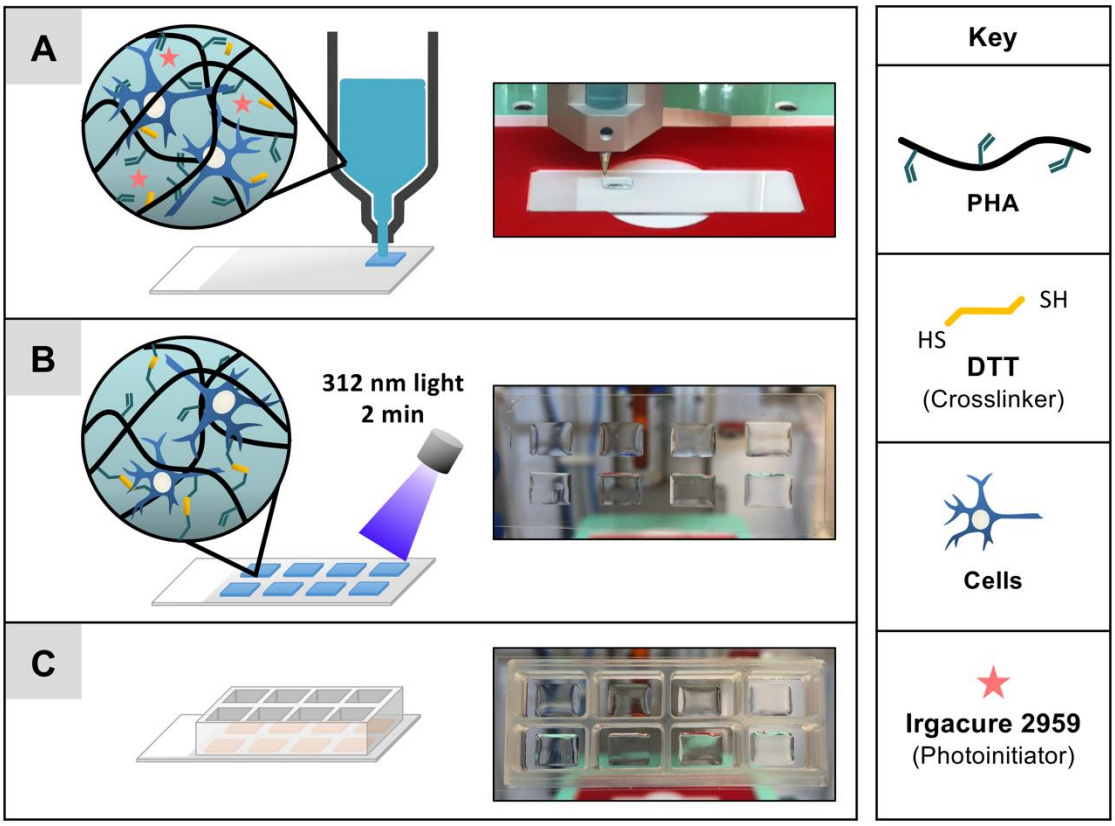

Figure 3.1: Aim 1 Illustration of Bioprinting and Hydrogel Formation

Graphic of the bioprinting, hydrogel formation, and cell culture. **A)** Hydrogel precursor containing pentenoate-functionalized hyaluronic acid (PHA), dithiothreitol (DTT), Irgacure 2959, and PBS with cells were mixed and loaded into UV-protected cartridges. PHA precursors were bioprinted in a 2 x 4 grid of rectangular prisms (8 x 6 x 0.3 mm, L x W x H) and onto a 24 x 76 mm glass microscope slide. **B)** Hydrogels were crosslinked after exposure to 312 nm UV light for 2 min. **C)** Silicon well chambers were sealed around the hydrogels and medium was added. Cells were cultured for 7 days.

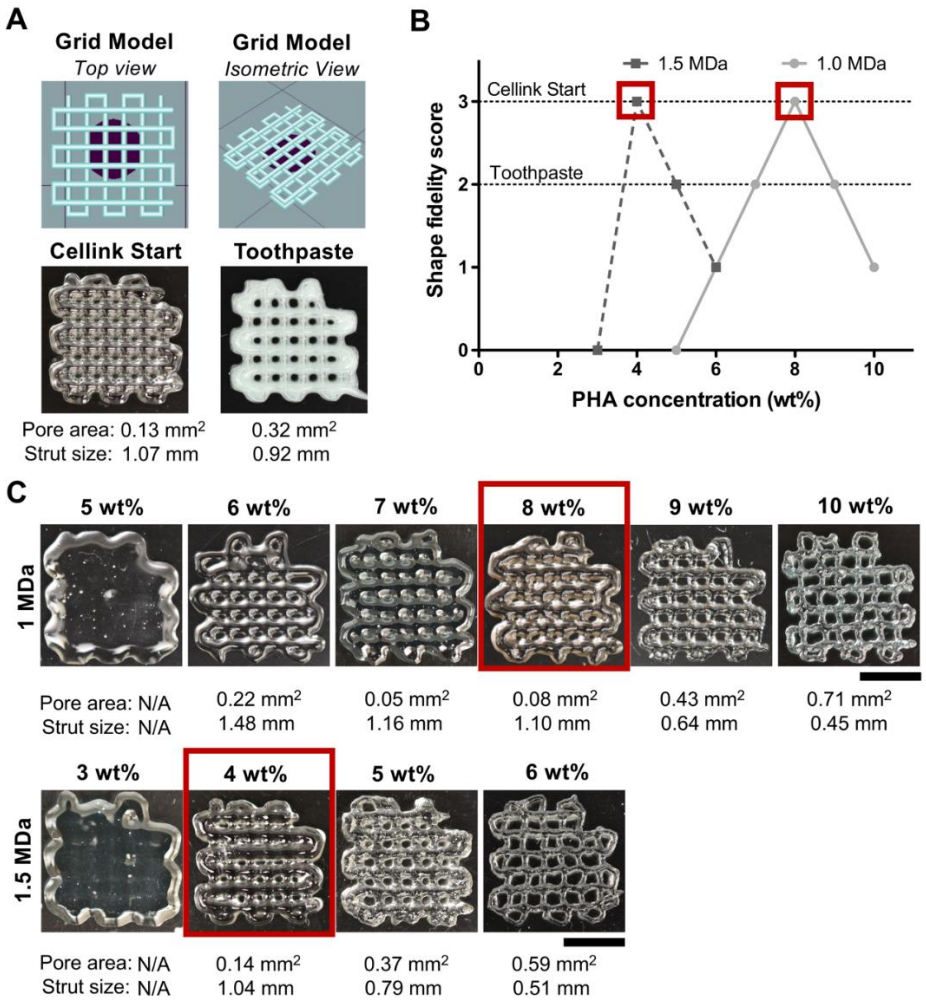

Figure 3.2: Aim 1 Shape Fidelity of PHA Precursor Formulations

Shape fidelity of 1 and 1.5 MDa PHA at varying concentrations. The 1.5 MDa 4 wt% and 1 MDa 8 wt% formulations printed the best (outlined in red boxes). **A)** The printed object was a 3-layer grid with alternating layers of 6 horizontal or 6 vertical lines in a rectilinear pattern. Cellink Start had good shape fidelity after printing, while toothpaste only had medium shape fidelity due to quick material relaxation and loss of defined edges shortly after printing. **B)** Shape fidelity scores for 1 and 1.5 MDa PHA formulations. For both molecular weights, the shape fidelity increased, reached a peak, and decreased as the concentration of PHA increased. **C)** Macro images within 1 min after printing and before crosslinking from a top view to show the shape fidelity. Pore areas appeared to generally increase while strut sizes generally decreased with increasing PHA concentrations. Scale bars: 5 mm.

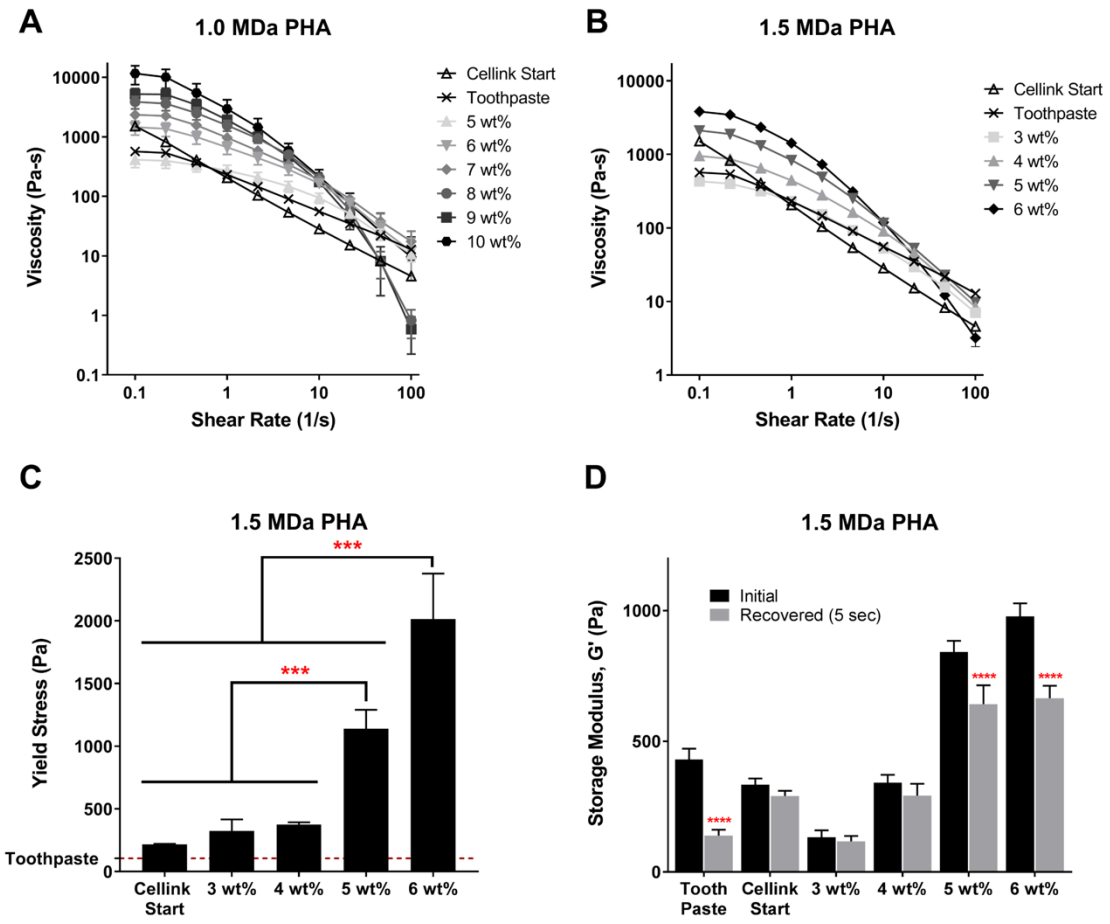

Figure 3.3. Aim 1 Rheology of PHA Precursor Formulations

Rheological testing of varying PHA concentrations of 1 and 1.5 MDa PHA precursors. Viscosity data by itself did not indicate printability; however, the printable formulations had a yield stress between 0 and 1000 Pa and recovered 85% or greater of their initial storage modulus. **A)** The viscosities of the 1 MDa PHA increased as the PHA concentration increased; however, all groups' viscosities decreased to below 18 Pa-s at the highest tested shear rate and demonstrated shear thinning behavior. **B)** Similar to the 1 MDa PHA groups, the viscosity behavior of the 1.5 MDa PHA was shear thinning and increased as the PHA concentration increased. **C)** 1.5 MDa - 3 and 4 wt% had similar yield stresses to Cellink! Start and were less than 1000 Pa. The 1 MDa PHA groups did not have measurable yield stresses. **D)** Cellink Start®, 1.5 MDa - 3 wt%, and 1.5 MDa - 4 wt% recovered greater than 85% of their initial storage moduli after being disrupted by a high shear stress. *p < 0.05, **p < 0.01, ***p < 0.001, **** p < 0.0001.

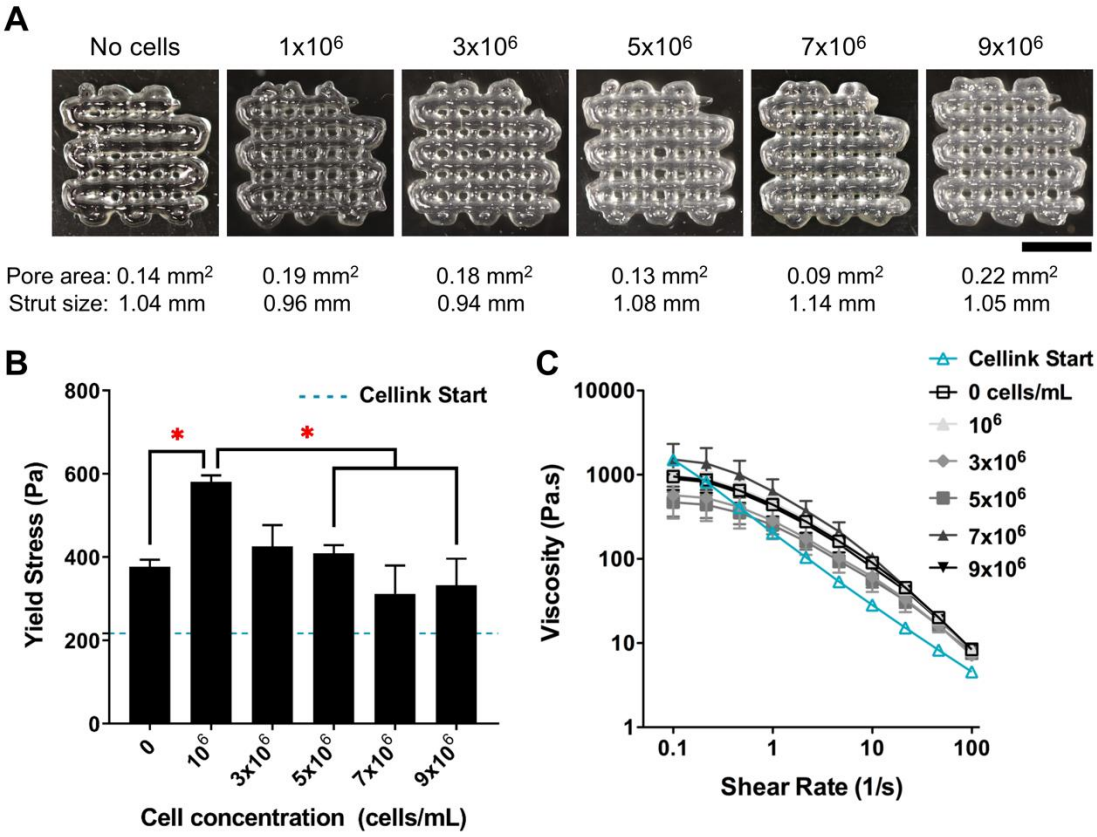

Figure 3.4: Aim 1 Shape Fidelity and Rheology of PHA Precursors with Cells

The printability, yield stress, and viscosity of varying cell concentrations in a 1.5 MDa - 4 wt% PHA precursor. The printability, yield stress, and viscosity were minimally affected by increasing cell concentrations, up to 9 x 10^6 cells/mL. **A)** The shape fidelity of the PHA precursor remained high for all cell concentrations tested (1 – 9 x 10^6 cells/mL). All cell concentrations had similar pore areas and strut sizes. **B)** The yield stress of PHA with 1 x 10^6 cells/mL was increased compared to PHA without cells; however, all higher concentrations had similar yield stresses to PHA without cells. **C)** The viscosity of the PHA groups with cells all showed similar shear thinning behavior to that of the PHA without cells. Scale bar: 5 mm. * $p < 0.05$.

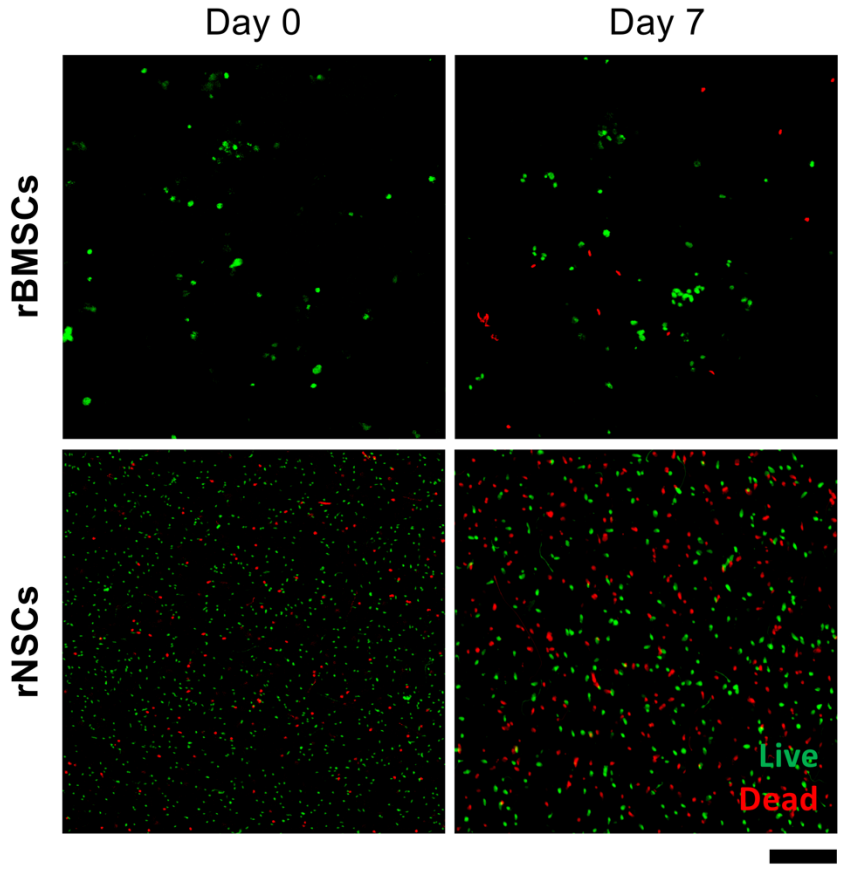

Figure 3.5: Aim 1 Viability of Printed Cells

Viability of rat bone marrow mesenchymal stem cells (rBMSCs) and rat neural stem cells (rNSCs) after bioprinting into rectangular scaffolds (8 x 6 x 0.3 mm) with 100% infill after 0 days and 7 days of culture. The viability was high for both rBMSCs and rNSCs after bioprinting and cells survived for 7 days in culture. After rBMSCs or rNSCs were bioprinted in PHA hydrogels (day 0), there was high viability of both cell types (>87%) (green, live cells; red, dead cells). Over 7 days of culture, rBMSCs maintained a high viability (~85%) but the rNSC viability decreased (~55%). Scale bar: 200 μm.

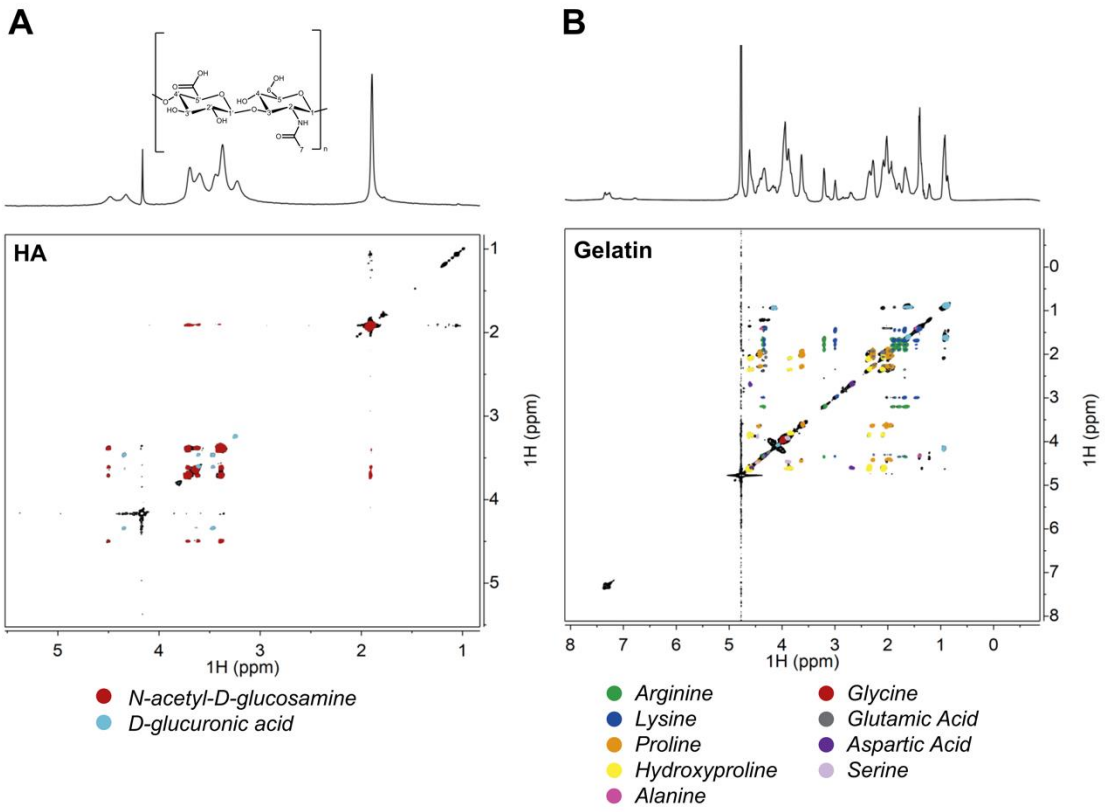

Figure 4.1: Aim 2 Fully Assigned 2D NMR of HA and Gelatin

The 2D TOCSY (TOtal Correlation SpectroscopY) spectra of hyaluronic acid (HA) and gelatin significantly aided the assignment of the signals. **A)** Distinct correlations patterns were observed for each sugar ring allowing for the absolute proton resonance assignment for HA. The N-acetyl-D-glucosamine spin system, shown in red, displayed the correlation of protons 2, 3, 4, 5 and 6 to each other and to the anomeric proton signal 1 at 4.47 ppm. Correlations are also observed from the methyl on the acetyl group at 1.9 ppm to the protons on its attached ring. The of D-glucuronic acid spin system, shown in light blue, displayed the correlation of protons 2', 3', 4', and 5' correlated to each other and to the anomeric proton signal, 1' at 4.33 ppm. **B)** The gelatin TOCSY displayed a distinct correlation pattern for each amino acid. The spin systems of arginine (green), lysine (dark blue), proline (orange), hydroxyproline (yellow), alanine (pink), glycine (red), glutamic acid (grey), aspartic acid (dark purple), and serine (light purple) were all identified.

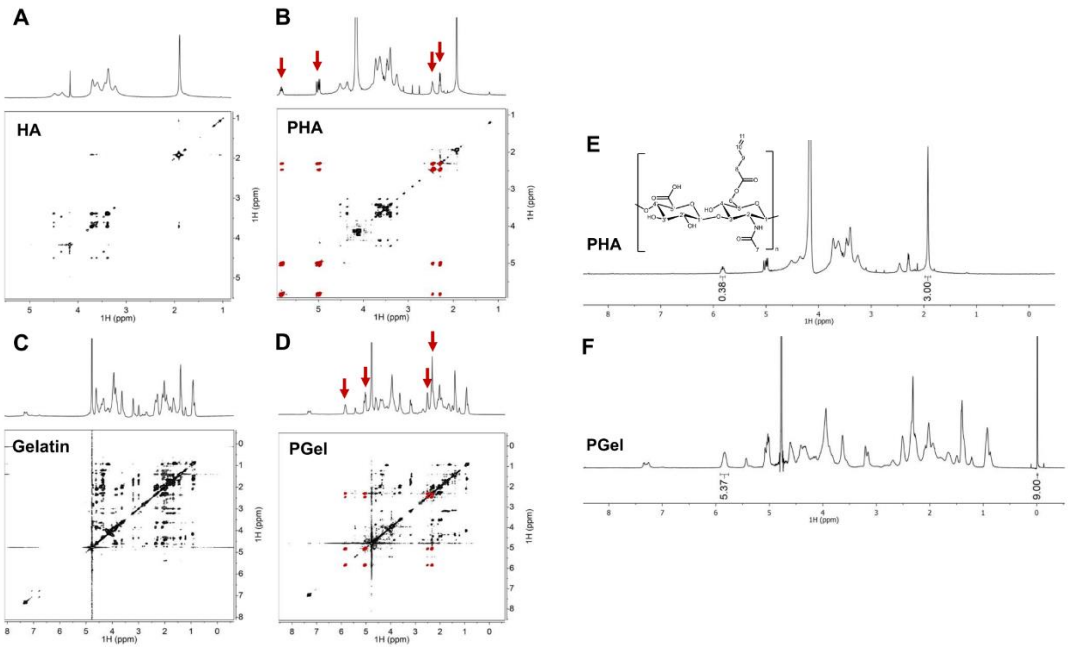

Figure 4.2: Aim 2 2D NMR of PHA or PGel

The 2D TOCSY spectra of HA or gelatin versus PHA or PGel, respectively, showed the original polymer peaks and the appearance of new peaks of the pentenoate group. The integration of the PHA or PGel ^{1}H spectra showed the degree of functionalization with the pentenoate group. **A)** The HA 2D TOCSY showed the original polymer signals of each sugar ring. **B)** The PHA 2D TOCSY displayed the appearance of the pentenoate group spin system. The correlation of the four new peaks (2.27, 2.46, 5.00, 5.82 ppm) is shown in red. **C)** The gelatin 2D TOCSY shows the original polymer signals of each amino acid. **D)** The PGel 2D TOCSY displayed the appearance of the pentenoate group spin system. The correlation of the four new peaks (2.33, 2.51, 5.04, 5.84 ppm) is shown in red. **E)** The PHA proton signal (10) at 5.82 ppm was integrated and normalized to the 3 protons of the methyl group of proton signal (7) at 1.9 ppm revealing that 38% of the repeating disaccharide units were functionalized with a pentenoate group, or there was ~0.108 millimoles of the pentenoate group per gram of PHA. **F)** The same proton signal (10) of the pentenoate group at 5.84 ppm was integrated on the PGel ^{1}H signal and quantified with an internal standard (TMSP, 9 protons, 0 ppm). There was ~0.025 millimoles of the pentenoate group per gram of PGel.

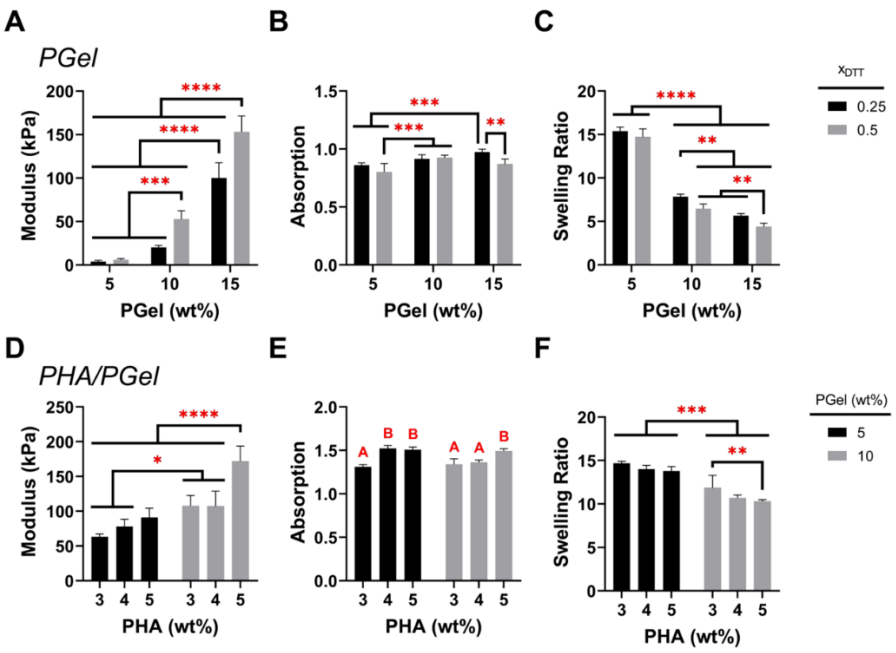

Figure 4.3: Aim 2 Mechanical Performance and Swelling of PGel and PHA/PGel Hydrogels

The mechanical performance and swelling were characterized for different formulations of PGel and PHA/PGel. **A)** The compressive modulus of PGel hydrogels (n = 5-6) showed increased compressive moduli with increased polymer content. The higher concentration of DTT crosslinker (gray bars) additionally increased the moduli compared to the lower DTT concentration (black bars) in all groups except the 5 wt% PGel hydrogels. **B)** The absorption of all tested PGel hydrogels (n = 6) were close to or less than 1, showing minimal swelling or slight contraction after fabrication, despite the PGel concentration and DTT concentration. **C)** The swelling ratio of PGel hydrogels (n = 6) decreased with increasing PGel concentration, and the effect of the different DTT concentrations was minimal. **D)** The compressive moduli of the PHA/PGel hydrogels (n = 5-6) showed increased moduli with increased PHA content. The 10% PGel concentrations (gray bars) additionally increased the moduli compared to the 5% PGel concentrations (black bars). **E)** The absorption of all tested PHA/PGel hydrogels (n = 6) was between 1 and 1.5, showing absorption of water after fabrication and greater absorption with increased PHA content. Significance was marked with ‘A’ or ‘B’, where groups denoted by ‘B’ were significantly greater than those denoted by ‘A’, and those with the same letter were not significantly different from each other. **F)** The PHA/PGel hydrogels had decreased swelling ratios (n = 6) with increased PGel content and there was a minimal effect of the varied PHA concentration. * $p < 0.05$, ** $p < 0.01$, *** $p < 0.001$, **** $p < 0.0001$.

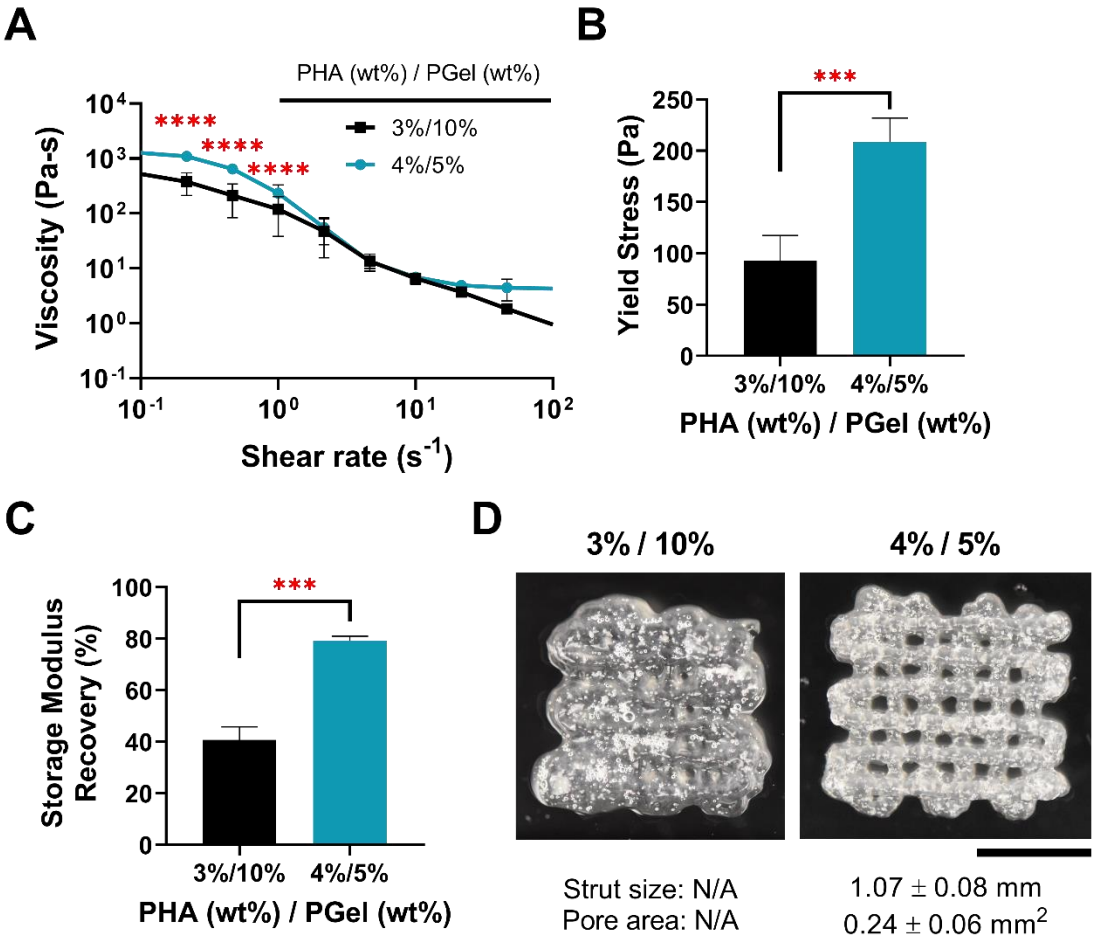

Figure 4.4: Aim 2 Rheology of PHA/PGel Precursors

The rheology of the PHA/PGel precursor formulations that were adhesive for rNSCs show that the 4%/5% formulation was shear thinning, had a higher yield stress, and higher storage modulus recovery than the 3%/10% formulation. **A)** The viscosity (n = 3) of the 4%/5% precursor (blue line, circle points), was higher at the three lowest tested shear rates than the 3%/10% (black line, square points). Both formulations were shear thinning. **B)** The yield stress (n = 3-5) of the 4%/5% precursor (blue bar) was higher than the 3%/10% precursor (black bar). **C)** The storage modulus recovery (n = 3) of the 4%/5% precursor (blue bar) was higher than the 3%/10% precursor (black bar). **D)** Given the higher yield stress and better storage modulus recovery, the 4%/5% formulation was bioprinted in a 3-layer grid pattern, and the strut size (1.07 ± 0.08 mm) and pore area (0.24 ± 0.03 mm^2) were determined. *** $p < 0.001$, **** $p < 0.0001$.

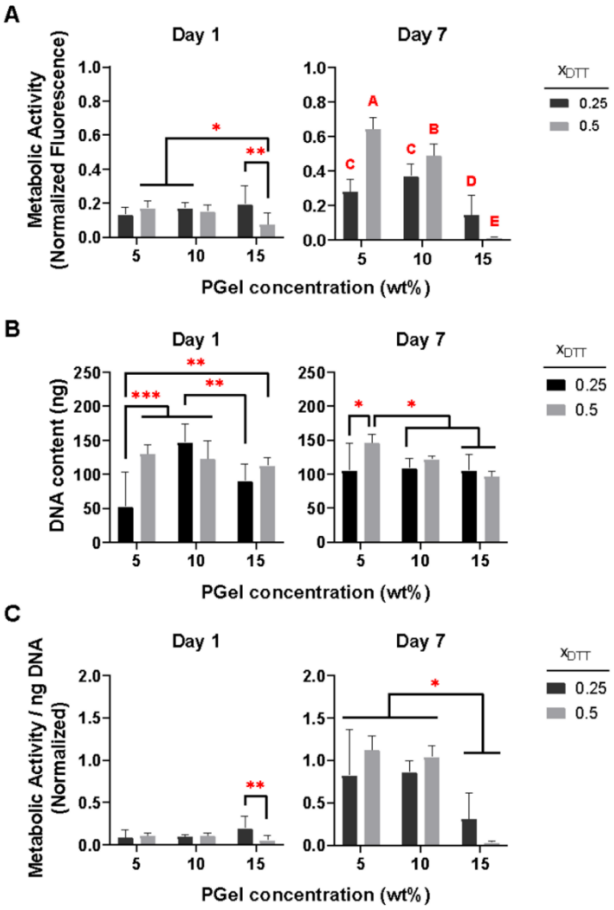

Figure 4.5: Aim 2 Cell Viability on PGel Hydrogels

Across varied PGel and DTT crosslinker concentrations, seeded rat neural stem cells (rNSCs) had the highest normalized metabolic activity after 7 days on the 5% and 10% PGel hydrogels (n = 6-8). **A)** The metabolic activity of seeded rNSCs the PGel hydrogels were similar on day 1, and higher for the 5% and 10% PGel hydrogels with 0.5 x_{DTT} on day 7 compared to all other groups. Significance is denoted by letters, where groups marked by 'A' were significantly higher than 'B', 'C', 'D', and 'E', and groups marked by 'B' were significantly higher than those marked by 'C', 'D', and 'E', etc. **B)** On day 1, the DNA content was lower on the 5%/0.25 x_{DTT} hydrogel than most of the other groups. On day 7, the 5%/0.5 x_{DTT} hydrogel had higher DNA content than all groups except the 10%/0.5 x_{DTT} hydrogel. **C)** The metabolic activity normalized to the DNA content and to the plated cells group, showed similar activity of all hydrogels on day 1, and higher activity of the 5% and 10% PGel hydrogels on day 7. * $p < 0.05$, ** $p < 0.01$, *** $p < 0.001$.

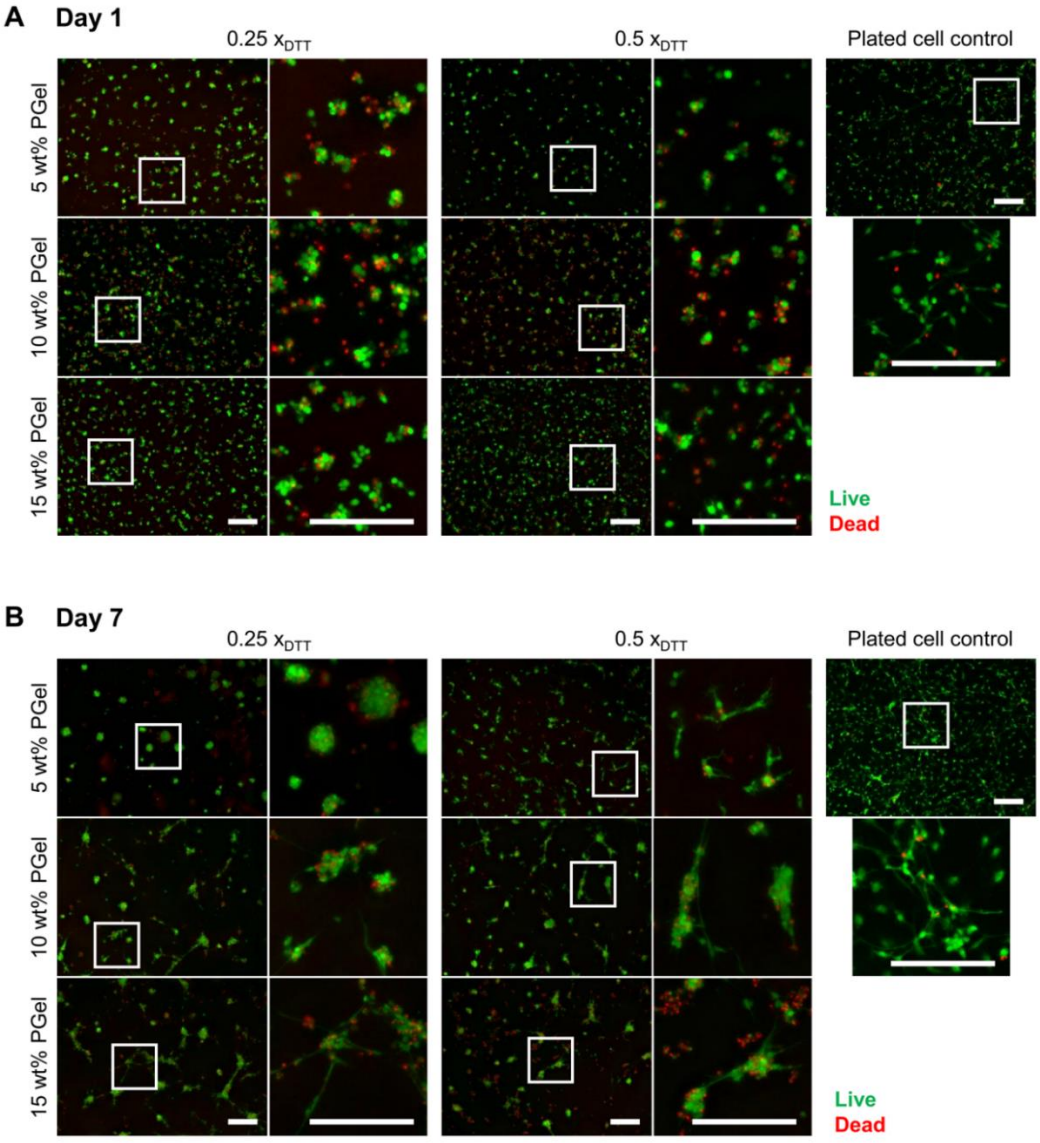

Figure 4.6: Aim 2 LIVE/DEAD Staining of Cells on PGel Hydrogels

The LIVE/DEAD staining of rNSCs on PGel hydrogels had similar cell densities after 1 day and similar spread morphologies on day 7. **A)** 1 day after seeding, the rNSCs had qualitatively adhered to all PGel hydrogels in similar densities of live and dead cells with minimal spread morphologies. **B)** After 7 days, the rNSCs had spread morphologies on all PGel hydrogels except the 5%/0.25 x_{DTT} hydrogels, where PGel hydrogels had become very soft and rNSCs had formed neurospheres instead of adhering and spreading on the material. The 15% PGel hydrogels appeared to have more dead cells than the 5% and 10% PGel hydrogels. Scale bars: 200 µm.

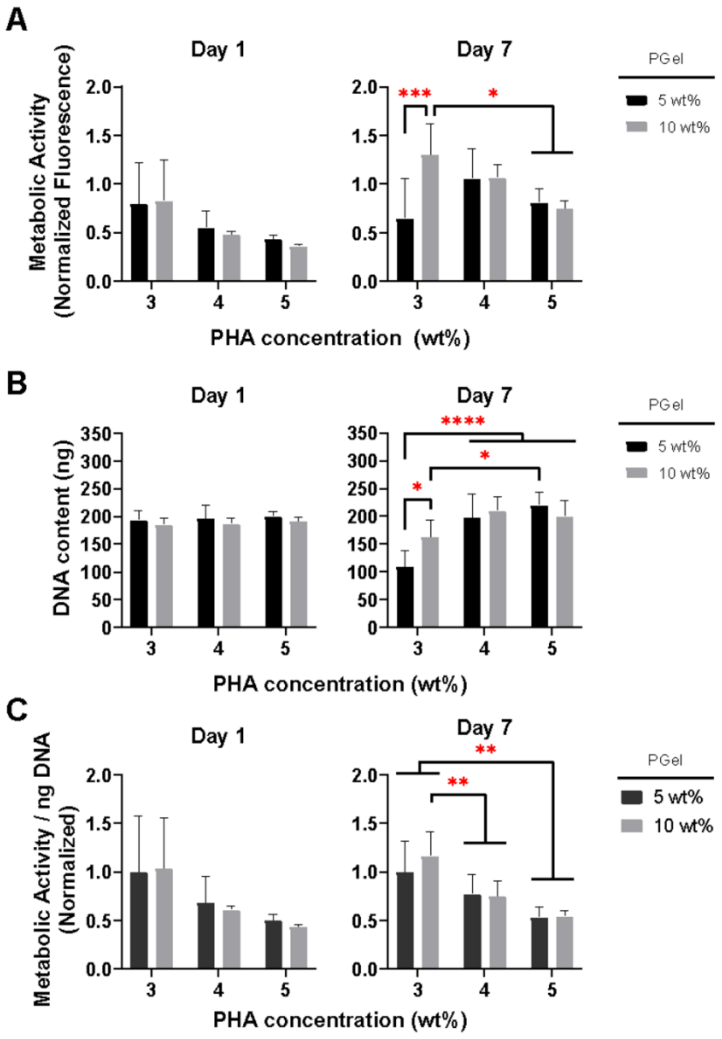

Figure 4.7: Aim 2 Cell Viability on PHA/PGel Hydrogels

The PHA and PGel concentrations were varied in PHA/PGel hydrogels and the 3%/10%, 4%/5%, and 4%/10% hydrogels had the best adhesion and normalized metabolic activity (n = 5-7). **A)** On day 1, the metabolic activity of seeded rNSCs across all groups was similar and on day 7, the activity decreased with increasing PHA content, except for the 3%/5% hydrogel, which additionally had lower metabolic activity. **B)** On day 1, the DNA content was similar across all hydrogels and on day 7, the 4% and 5% PHA hydrogels had higher DNA content than the 3%/5% group. **C)** The metabolic activity normalized to the DNA content and further normalized to the 3%/5% hydrogel group showed that the normalized metabolic activity decreased with increasing PHA content with minimal differences between PGel concentrations. * $p < 0.05$, ** $p < 0.01$, *** $p < 0.001$, **** $p < 0.0001$.

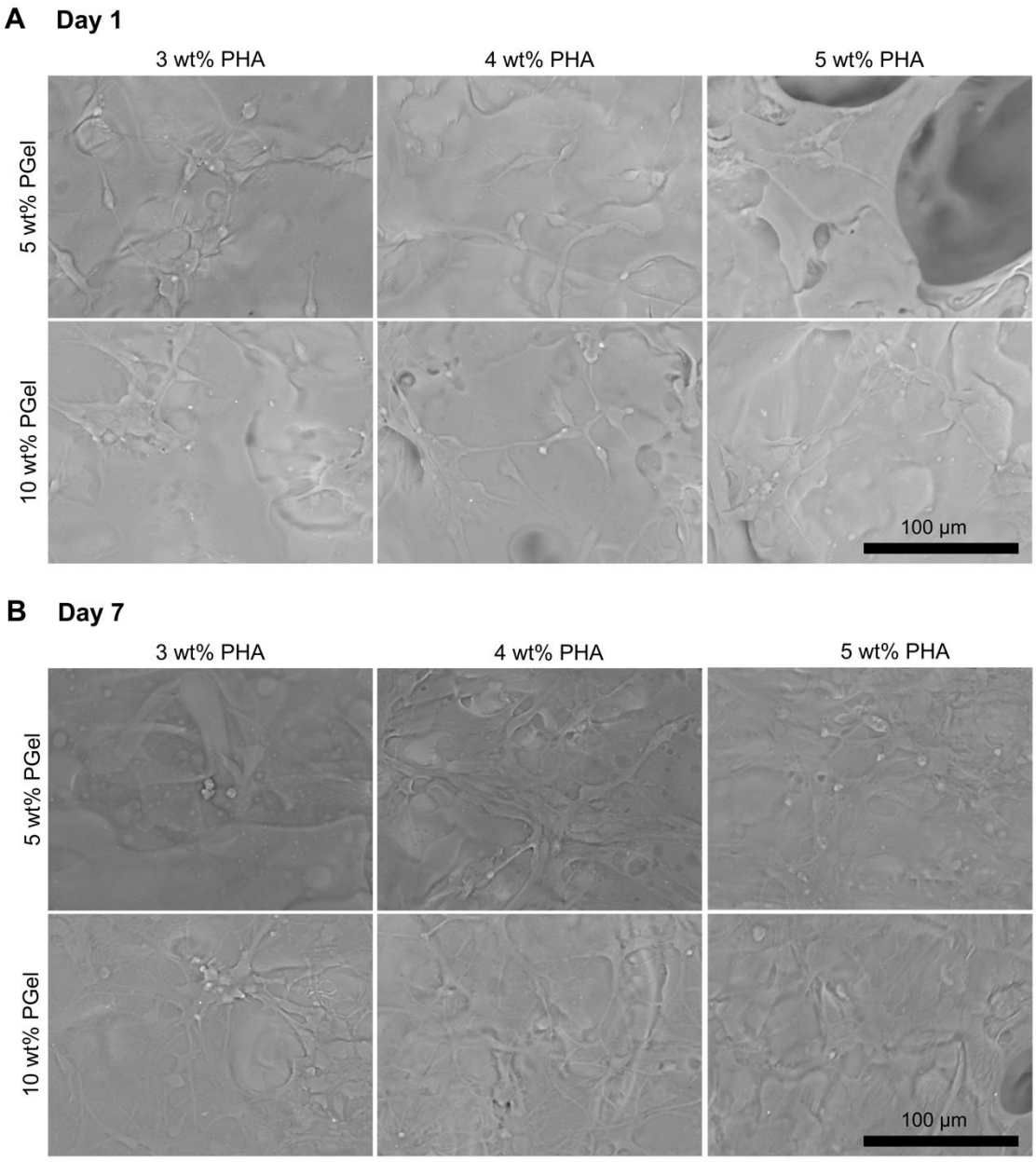

Figure 4.8: Aim 2 SEM Images of Cells on PHA/PGel Hydrogels

The scanning electron microscopy (SEM) images on day 7 showed greater spread cell morphologies across PHA/PGel hydrogels, except for cells on the 3%/5% hydrogel. **A)** On day 1, there were qualitatively similar densities and cell morphologies of rNSCs adhered across all PHA/PGel formulations. **B)** On day 7, rNSCs had greater spread morphologies on all the PHA/PGel hydrogels except for the 3%/5% hydrogels, where there were minimal numbers of cells that had rounded morphologies.

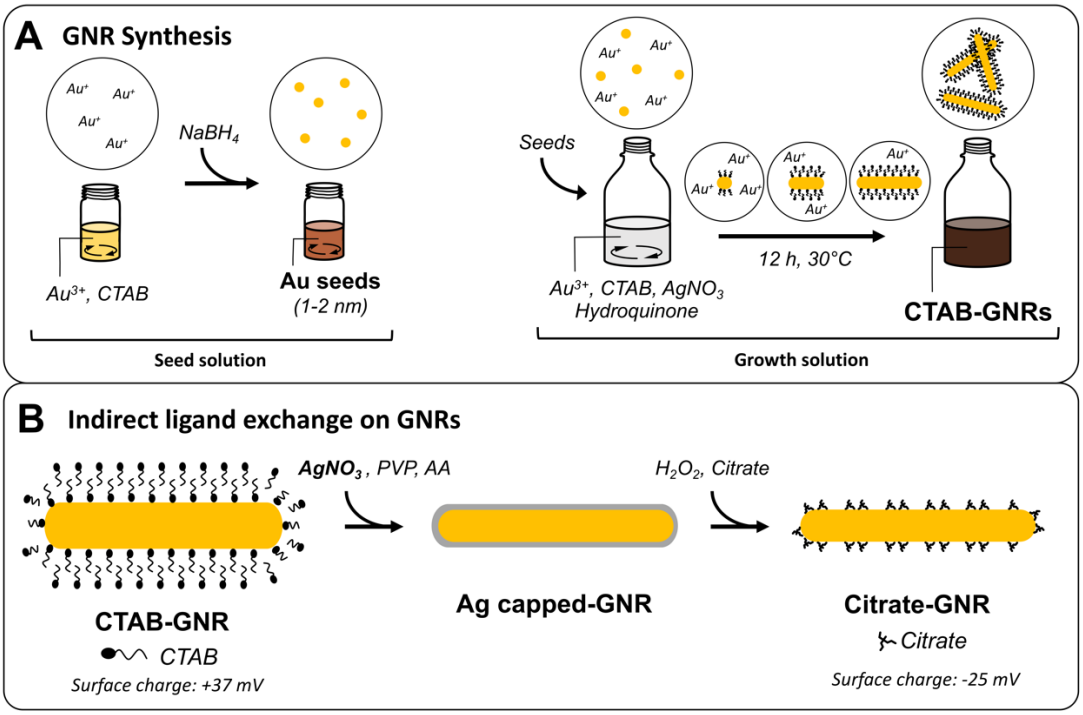

Figure 5.1: Aim 3 Illustration of the GNR Synthesis and Citrate-capping

A graphic depicting the synthesis of citrate-capped gold nanorods (GNRs). **A)** GNRs were synthesized using a seed-mediated growth method using hydroquinone as a reducing agent for longer aspect ratio, higher purity, and higher yields of GNRs than the ascorbic-acid based synthesis. The seed solution was made by quick addition of ice-cold sodium borohydride ($NaBH_4$) to a solution of gold chloride and hexadecyltrimethylammonium bromide (CTAB). A small amount of seed solution was added to the growth solution, which contained gold chloride, CTAB, silver nitrate ($AgNO_3$), and hydroquinone. The solution was left for 12 hours in a 30°C water bath for GNRs to grow. **B)** The toxic CTAB on CTAB-GNRs were replaced with non-toxic citrate through an indirect ligand exchange protocol. Silver nitrate was used to coat GNRs and displace the CTAB, followed by the etching away of the silver with hydrogen peroxide (H_2O_2) in a sodium citrate solution. GNRs were left in sodium citrate to generate citrate-GNRs.

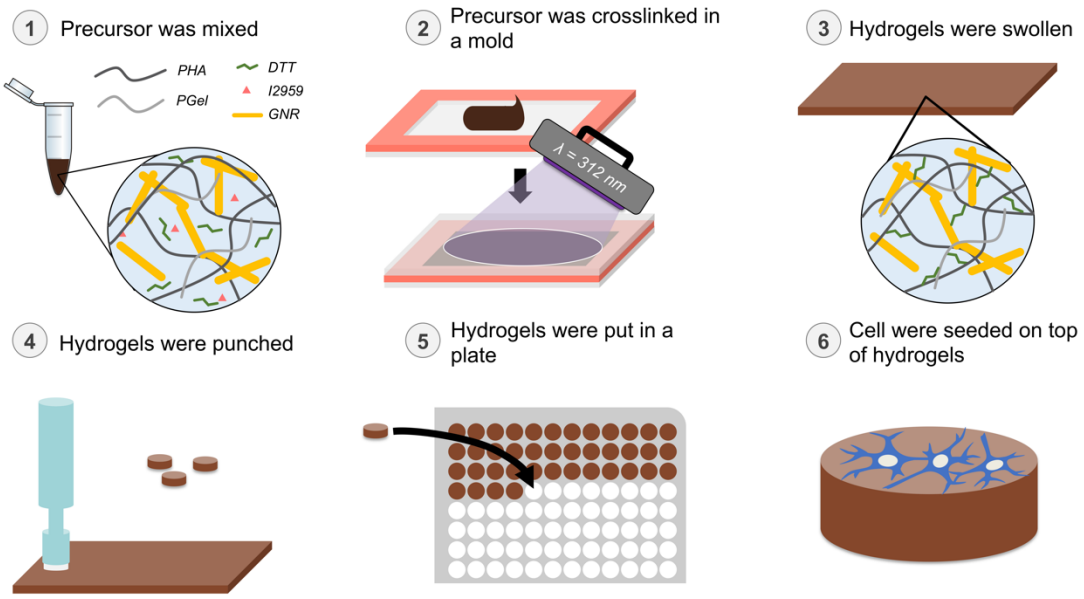

Figure 5.2: Aim 3 Illustration of GNR Hydrogel Formation

Graphic depicting GNR hydrogel formation for *in vitro* studies. **1)** Hydrogel precursor was mixed and contained pentenoate-functionalized hyaluronic acid (PHA), pentenoate-functionalized gelatin (PGel), crosslinker dithiothreitol (DTT), photoinitiator Irgacure 2959 (I2959), and citrate-GNRs. **2)** The hydrogel precursor was placed in a rubber gasket mold between two glass slides, followed by UV crosslinking at 312 nm for 2 minutes on each side. **3)** Hydrogels were removed from the molds and swollen in nanopure water overnight at 37°C. **4)** Cylindrical hydrogels were punched using a 6-mm biopsy punch. **5)** Hydrogels were placed in a 96-well plate. **6)** Rat neural stem cells (rNSCs) were seeded on top of hydrogels and cultured for 7 days.

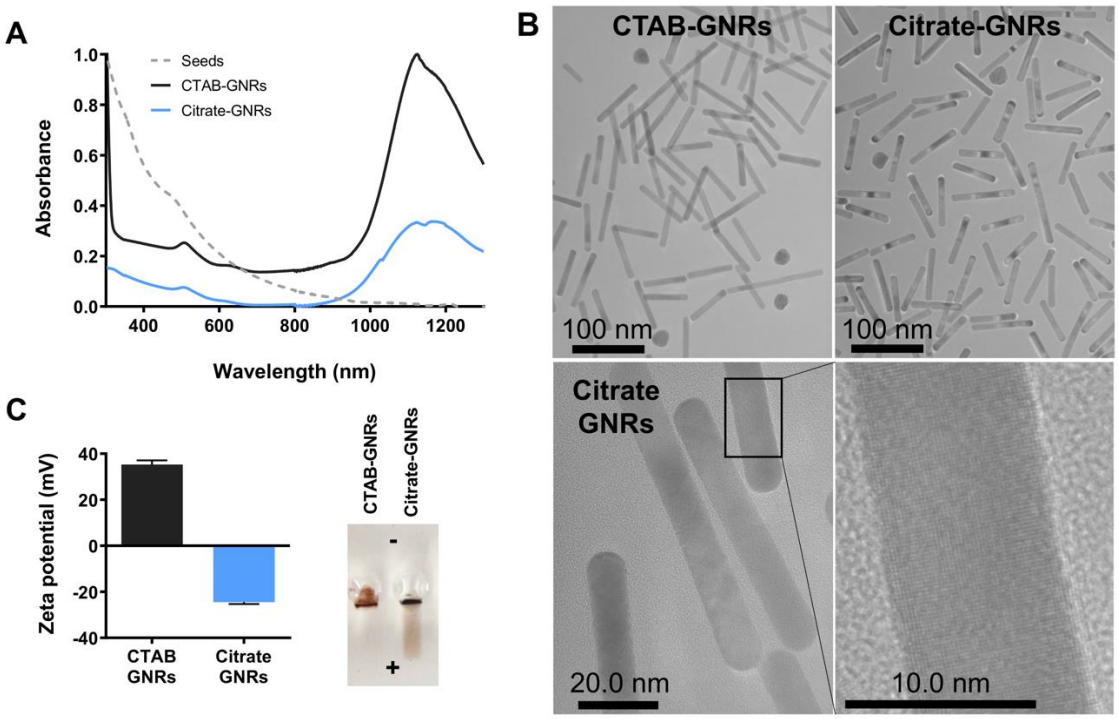

Figure 5.3: Aim 3 GNRs UV-Vis, TEM, and Zeta Potential

The GNRs were characterized to confirm that rods were synthesized and that the CTAB was replaced with citrate on the GNRs during the indirect ligand exchange. **A)** The UV-Vis-NIR spectra of the CTAB-GNRs (solid black line), citrate-GNRs (solid lighter blue line), and seed solution (dashed grey line) are shown. The seed solution absorbance was typical of 1-2 nm seeds, and the CTAB- and citrate-GNRs both had typical longitudinal (LSPR) and transverse surface plasmon resonance (TSPR) peaks at 1125 nm and 507 nm, respectively. **B)** The transmission electron microscopy (TEM) images confirmed that GNRs were formed from the synthesis (CTAB-GNRs, upper left panel) with minimal sphere contamination and that the GNRs were retained after the indirect ligand exchange process (citrate-GNRs, upper right panel). Higher magnification of the citrate-GNRs (bottom panels) show a regular rod shape (e.g., no dog-bone shape, or flat caps on the ends) and the atomic lattice structure of gold. **C)** The zeta potential (left half) of the CTAB-GNRs was positively charged from the CTAB and the ligand exchange with citrate was confirmed by the change to a negative zeta potential. Additionally, the ligand exchange was confirmed via gel electrophoresis (right half) where the citrate-GNRs migrated toward the cathode and the CTAB-GNRs aggregated and stayed within the well.

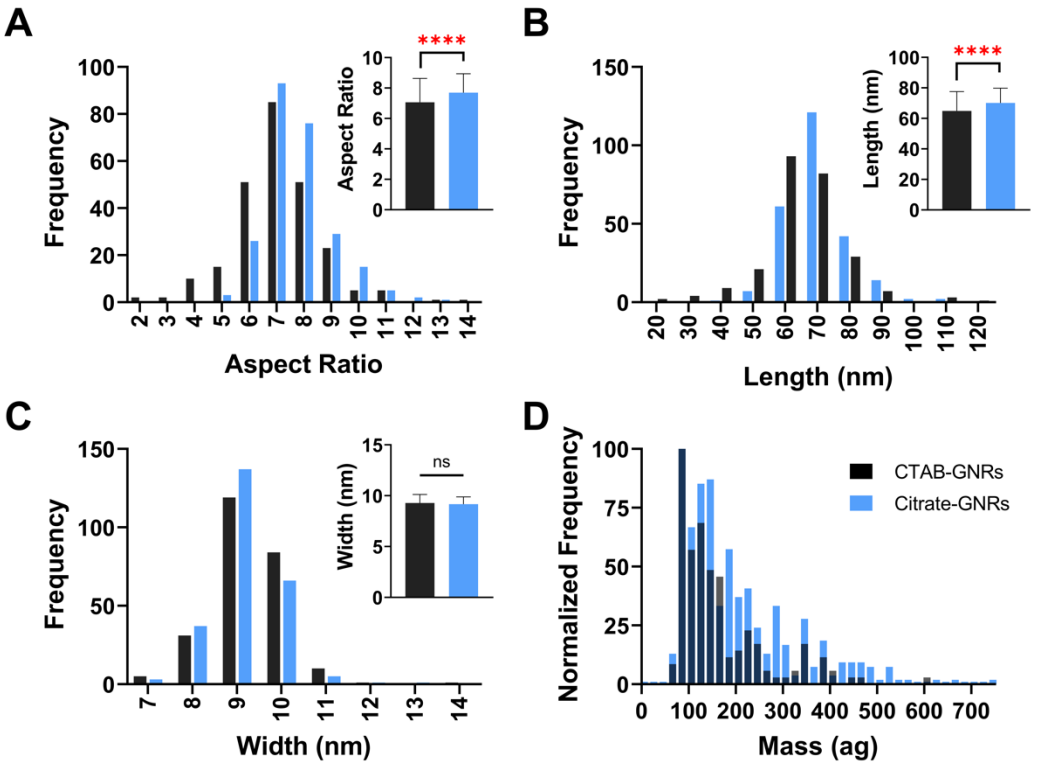

Figure 5.4: Aim 3 GNRs Aspect Ratio, Length, Width, and Mass Distributions

The citrate-GNRs (shown in blue) had high aspect ratios of ~7-8 and lengths of ~70 nm, which were greater than those of the CTAB-GNRs (shown in black). **A)** The histogram of the aspect ratio showed similar distributions between the citrate- and CTAB-GNRs, but the average aspect ratio (shown in the inset) of citrate-GNRs was ~6% higher than the CTAB-GNRs. **B)** The histogram of the lengths showed similar distributions between the citrate- and CTAB-GNRs, but the average length (shown in the inset) of citrate-GNRs was ~8% longer than the CTAB-GNRs. **C)** The histogram and the average widths (shown in the inset) showed similar distributions and widths between the citrate- and CTAB-GNRs. **D)** Single-particle ICP-MS showed similar and overlapping mass distributions between citrate- and CTAB-GNRs. **** $p < 0.0001$.

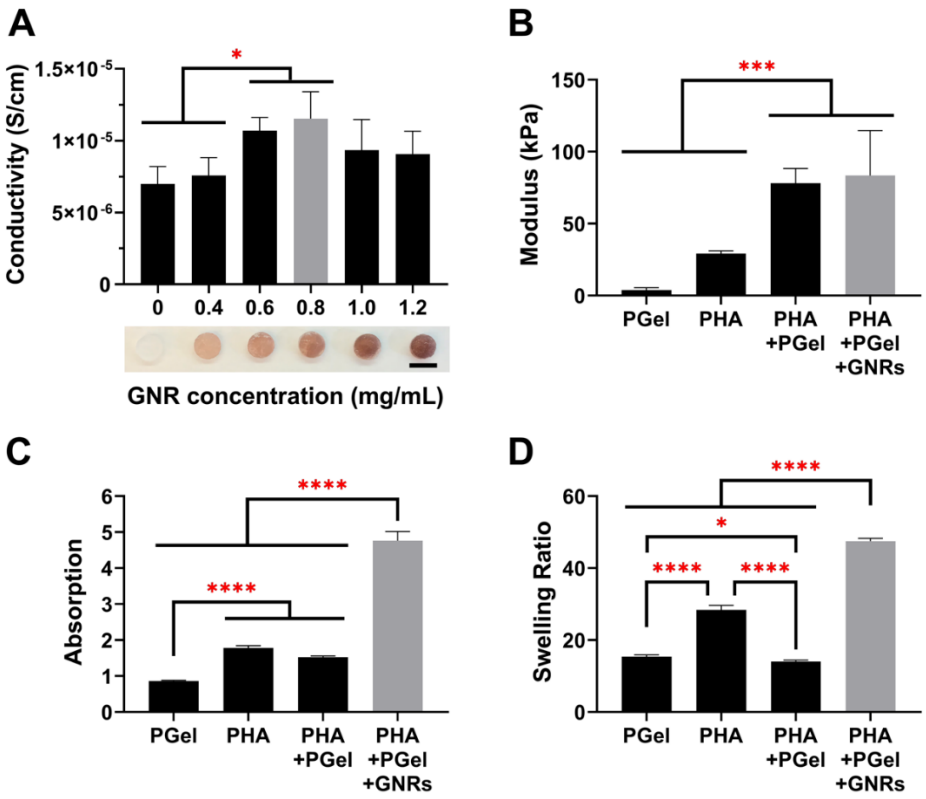

Figure 5.5: Aim 3 GNR Hydrogel Conductivity, Mechanical Performance, and Swelling

The conductivity of PHA/PGel hydrogels were increased with the addition of 0.6 or 0.8 mg/mL of citrate-GNRs. **A)** The conductivity of the GNR hydrogels was measured with citrate-GNR concentrations ranging from 0 to 1.2 mg/mL (n = 5 or 6), with the most conductive formulations containing 0.6 and 0.8 mg/mL GNRs. Coloration of the gels after swelling is shown the respective concentration on the plot. Scale bar: 6 mm. **B)** The compressive elastic modulus of the GNR hydrogels were not significantly different that of the PHA/PGel hydrogels (n = 5 or 6), but both were greater than the PHA and PGel hydrogels alone. **C)** The GNR hydrogels absorbed more water after fabrication than the PHA/PGel, PHA, and PGel hydrogels (n = 6). The PHA and PHA/PGel had similar absorption to each other and both absorbed more than PGel, which actually lost water after fabrication. **D)** The swelling ratio of the GNR hydrogels was greater than that of PHA/PGel, PHA, and PGel hydrogels (n = 6). The PHA had a greater swelling ratio than that of the PHA/PGel and gelatin hydrogels. The PHA/PGel had a greater swelling ratio than that of the PGel hydrogels. * $p < 0.05$, *** $p < 0.001$, **** $p < 0.0001$.

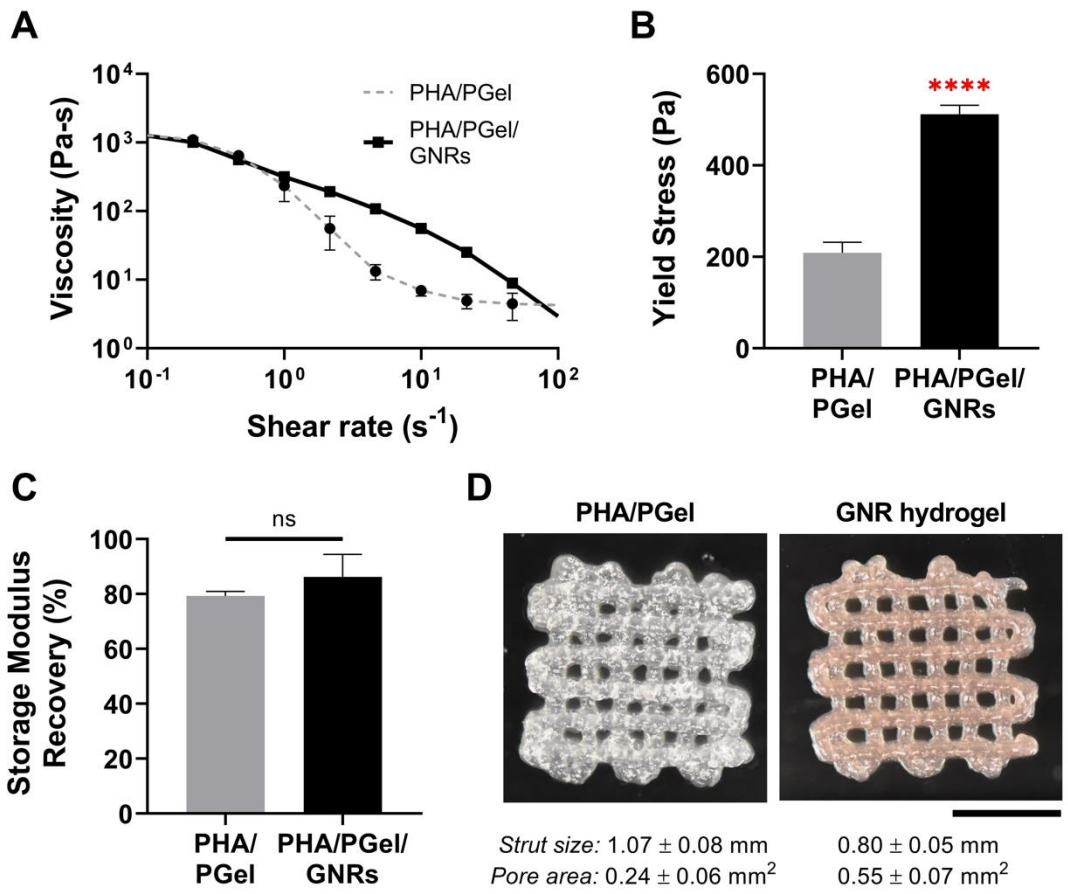

Figure 5.6: Aim 3 GNR Hydrogel Precursor Rheology and Printability

Rheological characterization of GNR hydrogel precursors showed similar shear thinning, higher yield stress, similar storage modulus recovery, and better printability than PHA/PGel alone. **A)** The viscosity curves of PHA/PGel/GNR (GNR hydrogel) precursors were not significantly different over different shear rates, and both were shear thinning (n = 3). **B)** The yield stress of GNR hydrogel precursors was 2.4 times higher than that of the PHA/PGel precursors (n = 3). **C)** The storage modulus recovery was not significantly different from that of the PHA/PGel precursors (n = 3). **D)** The bioprinted PHA/PGel precursors had had 34% greater printed strut sizes compared to GNR precursors ($p < 0.01$), which led to the GNR precursors having 2.3 times larger pore areas ($p < 0.01$), and overall better printability. **** $p < 0.0001$.

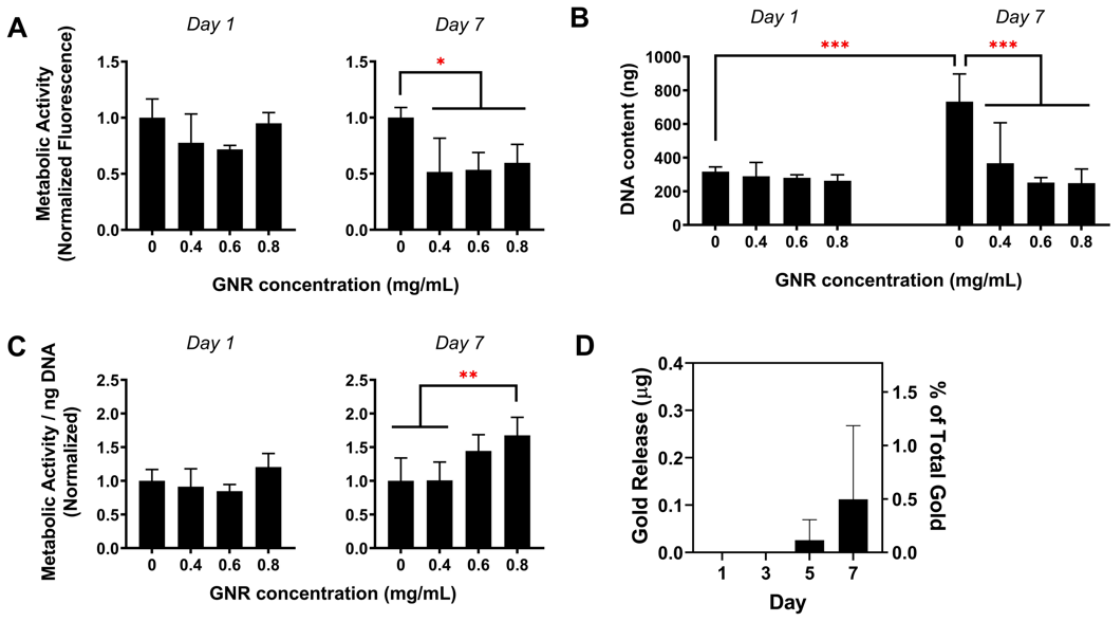

Figure 5.7: Aim 3 Cell Viability on GNR Hydrogels

In vitro assessment of seeded rNSCs on GNR hydrogels showed the hydrogels were not cytotoxic for rNSCs and < 1% of the total gold was released in the media samples during the 7 days of culture. **A)** The total metabolic activity of seeded rNSCs on day 1 was not significantly different between that of different PHA/PGel hydrogels, but was decreased after 7 days (n = 4 or 5). **B)** The total DNA content was not significantly different between any groups on day 1 but was higher in the hydrogels with no GNRs on day 7 compared to the hydrogels with 0.4 to 0.8 mg/mL of GNRs (n = 4 or 5). **C)** The normalized metabolic activity per nanogram of DNA and to the hydrogel with no GNRs was not significantly different between any of the groups on day 1; however, on Day 7, the hydrogels with 0.8 mg/mL of GNRs had 1.7 times greater metabolic activity than that of the hydrogels with 0 or 0.4 mg/mL GNRs. **D)** The media samples from the hydrogels with 0.8 mg/mL of GNRs and cells had 0.026 ± 0.043 µg of gold (or ~0.12% of the total gold in a hydrogel) in the day 5 media samples, and 0.11 ± 0.16 µg (~0.49% of the total gold) in the day 7 samples (n = 3). The medium samples from the hydrogels with no gold did not have an amount of gold that was above the background. * $p < 0.05$, ** $p < 0.01$, *** $p < 0.001$.

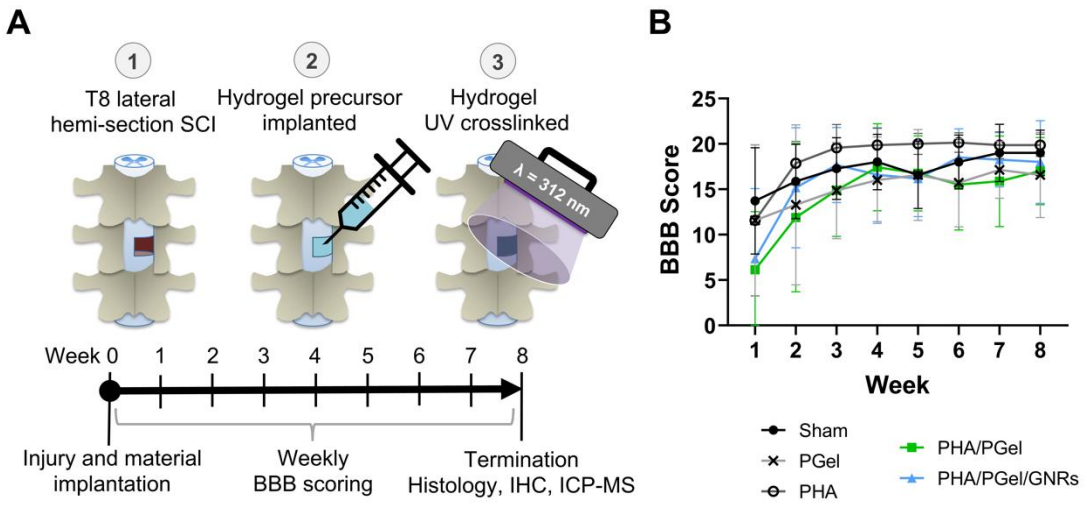

Figure 5.8: Aim 3 SCI Surgical Procedure and Functional Recovery in Rats

The injectable GNR hydrogel precursors were injected into a rat hemi-section model of SCI with no significant difference in functional recovery over 8 weeks. **A)** An illustration of the surgical procedures where a T8 lateral hemi-section was made in rats, followed by injection of a hydrogel into the injury, and subsequent exposure to UV-light for 2 minutes to crosslink the hydrogel precursor within the injury. **B)** The BBB scoring showed no significant difference in functional recovery across the GNR hydrogels (0.8 mg/mL GNRs), the other control materials of PGel, PHA, and PHA/PGel hydrogels, and the shams that received an injury and no treatment (n = 6-8).

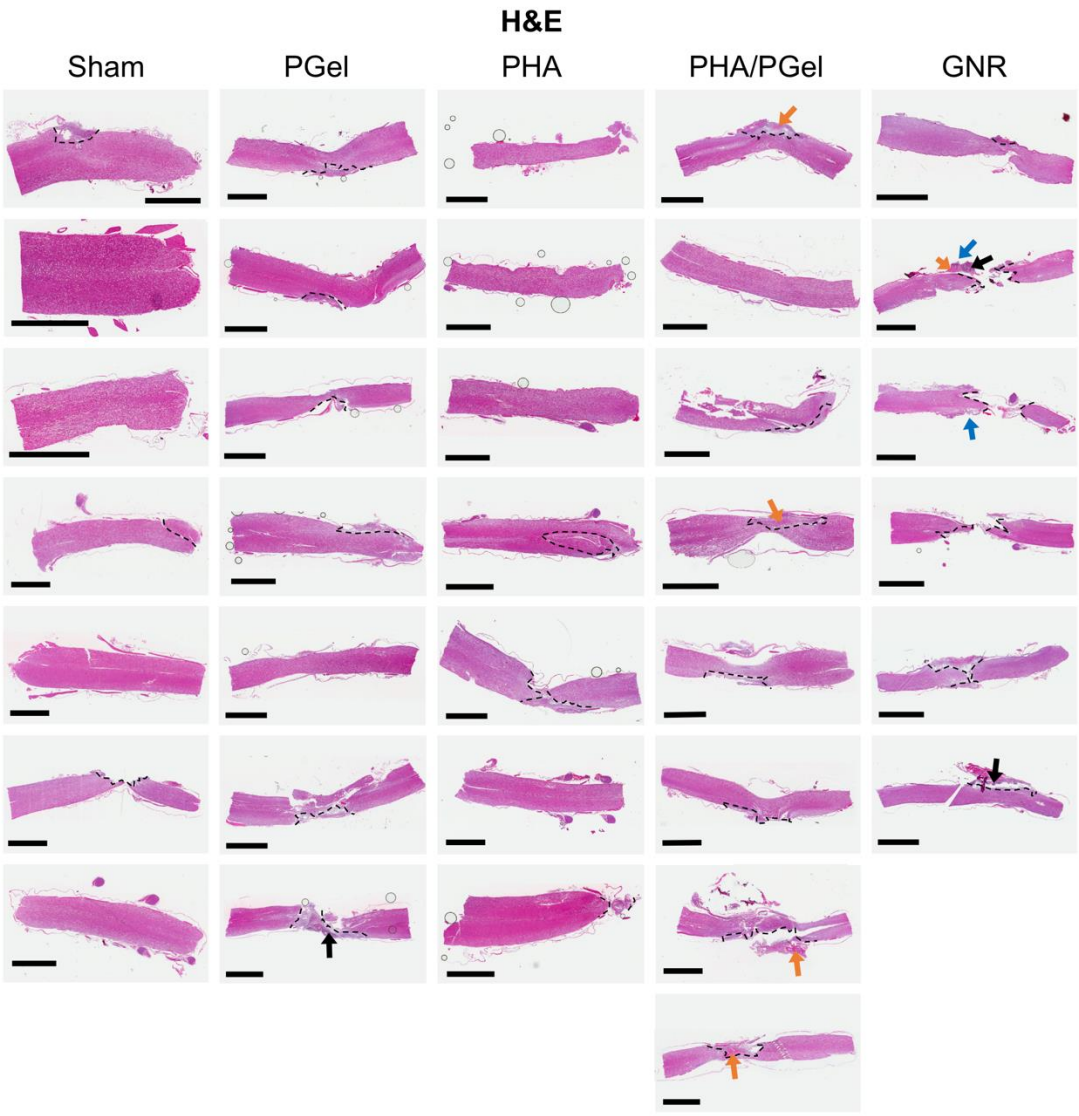

Figure 5.9: Aim 3 H&E on Spinal Cords

H&E staining on the spinal cords showed a high degree of variability in the injury after 8 weeks. The location of the injury was outlined by dashed lines, but the defect was not observed in several of the sections across all groups. Several spinal cords showed collagen (deep pink within the injury, indicated by orange arrows), which showed the fibrotic response within the injury. In the GNR hydrogel group, there was a foreign body response around a few small objects (smooth light purple area indicated by blue arrows), which may have been a small amount of leftover hydrogel. Some calcification was visible more laterally in some of the sections (dark purple spots, indicated by black arrows). Scale bars: 3 mm.

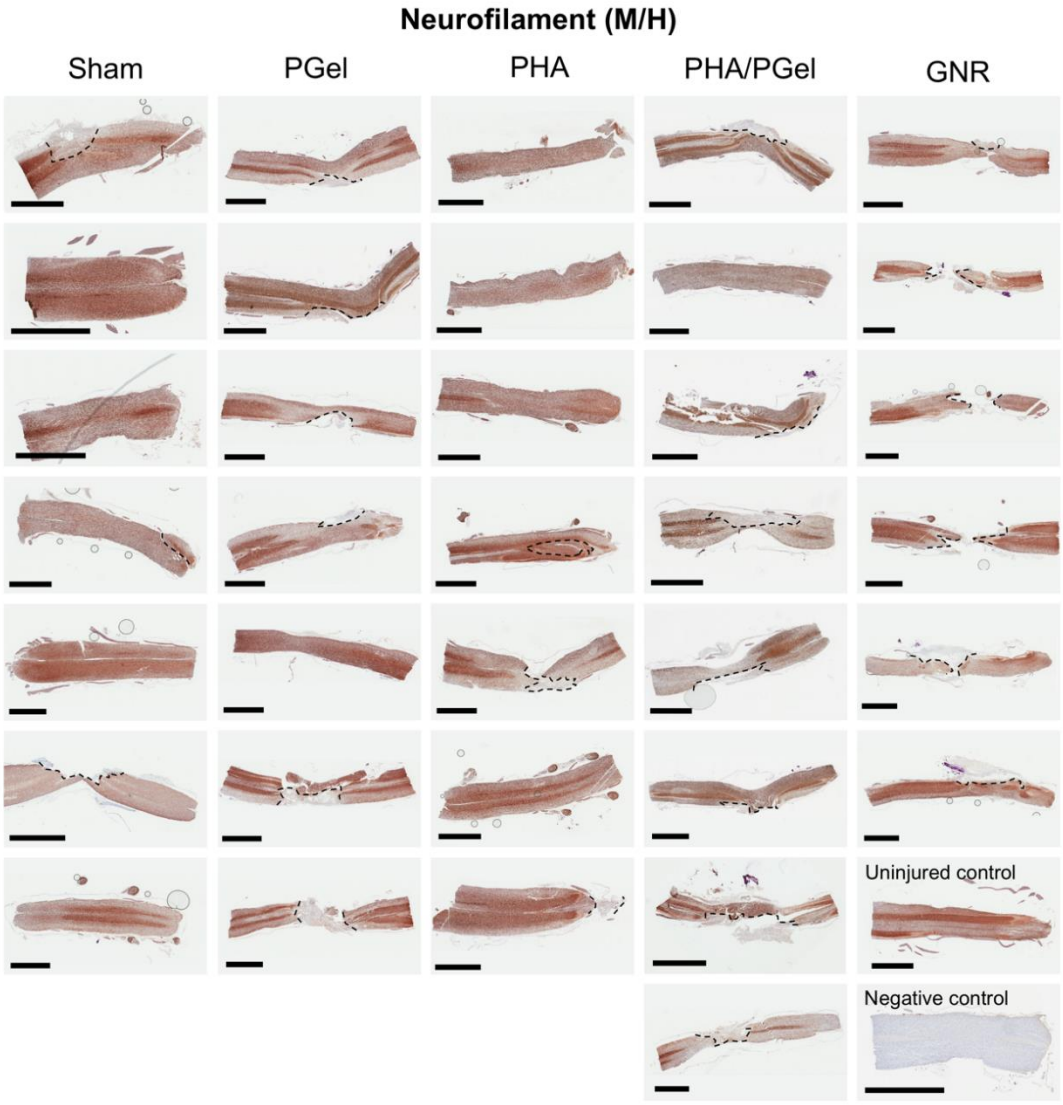

Figure 5.10: Aim 3 Neurofilament IHC on Spinal Cords

Neurons/axons were stained with a neurofilament (medium/heavy) antibody after 8 weeks post-injury showed darker staining of the neuron cell bodies (gray matter) compared to the axons (white matter), but the axonal pathways are visibly stained compared to the negative control. In the sections where an injury was visible, the location of the injury was outlined by dashed lines. The disruption of the axonal pathways within the injuries that could be seen were observed as a lack of stain in the injury. While no definitive conclusions can be drawn regarding differences among groups, there was not substantial evidence of any group showing any axon staining, and thus regeneration, in the injury. Scale bars: 3 mm.

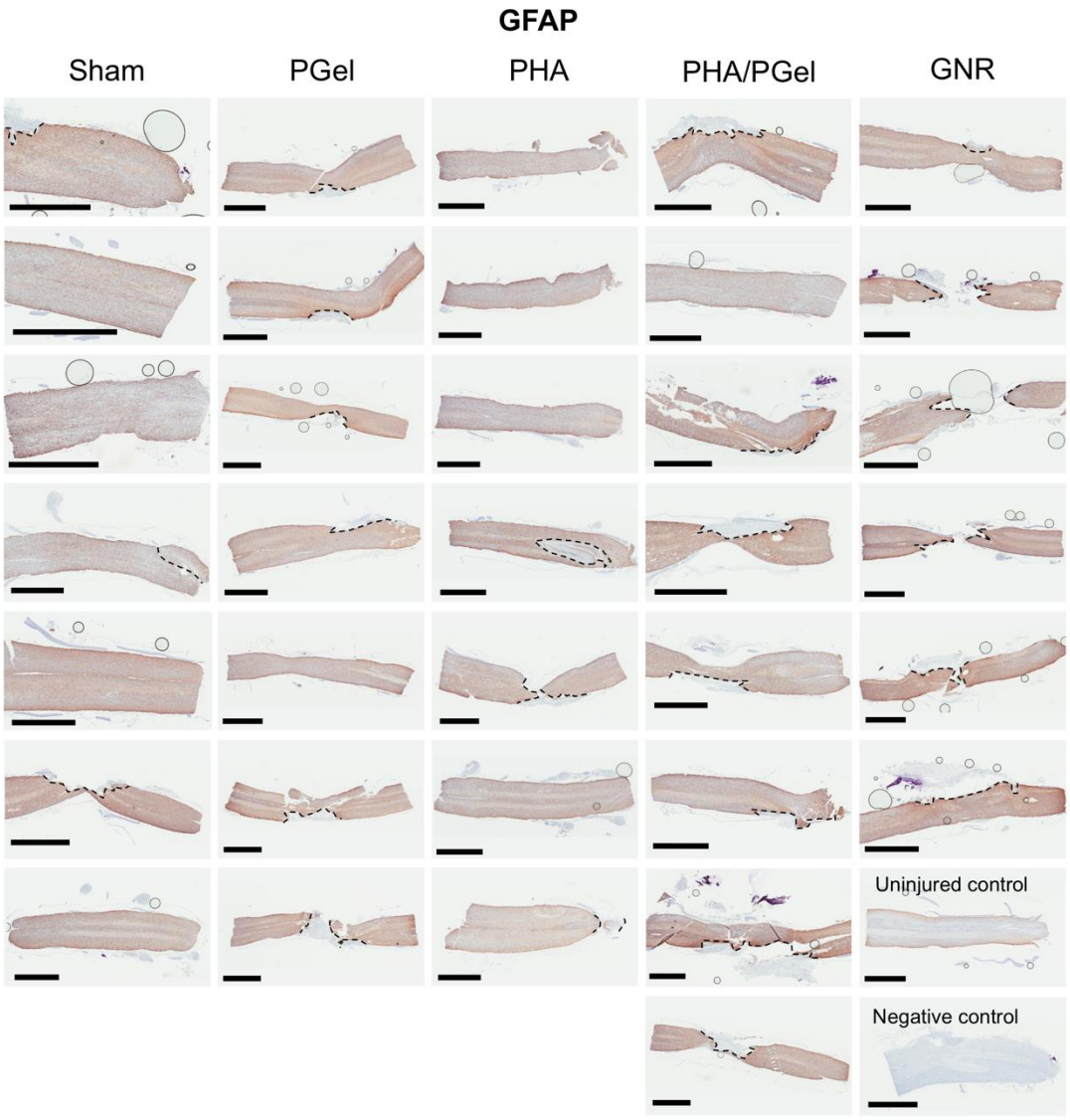

Figure 5.11: Aim 3 GFAP IHC on Spinal Cords

Astrocytes were stained with a GFAP antibody after 8 weeks post-injury. In the sections where an injury was visible, the location of the injury was outlined by dashed lines. The borders of the injury were distinguished by the lack of staining of the fibrotic tissue response within the injury. There were low levels of staining throughout the gray and white matter, but there was not substantial evidence of a reduction of activated astrocytes in the proximity of the injury in any of the groups. Scale bars: 3 mm.

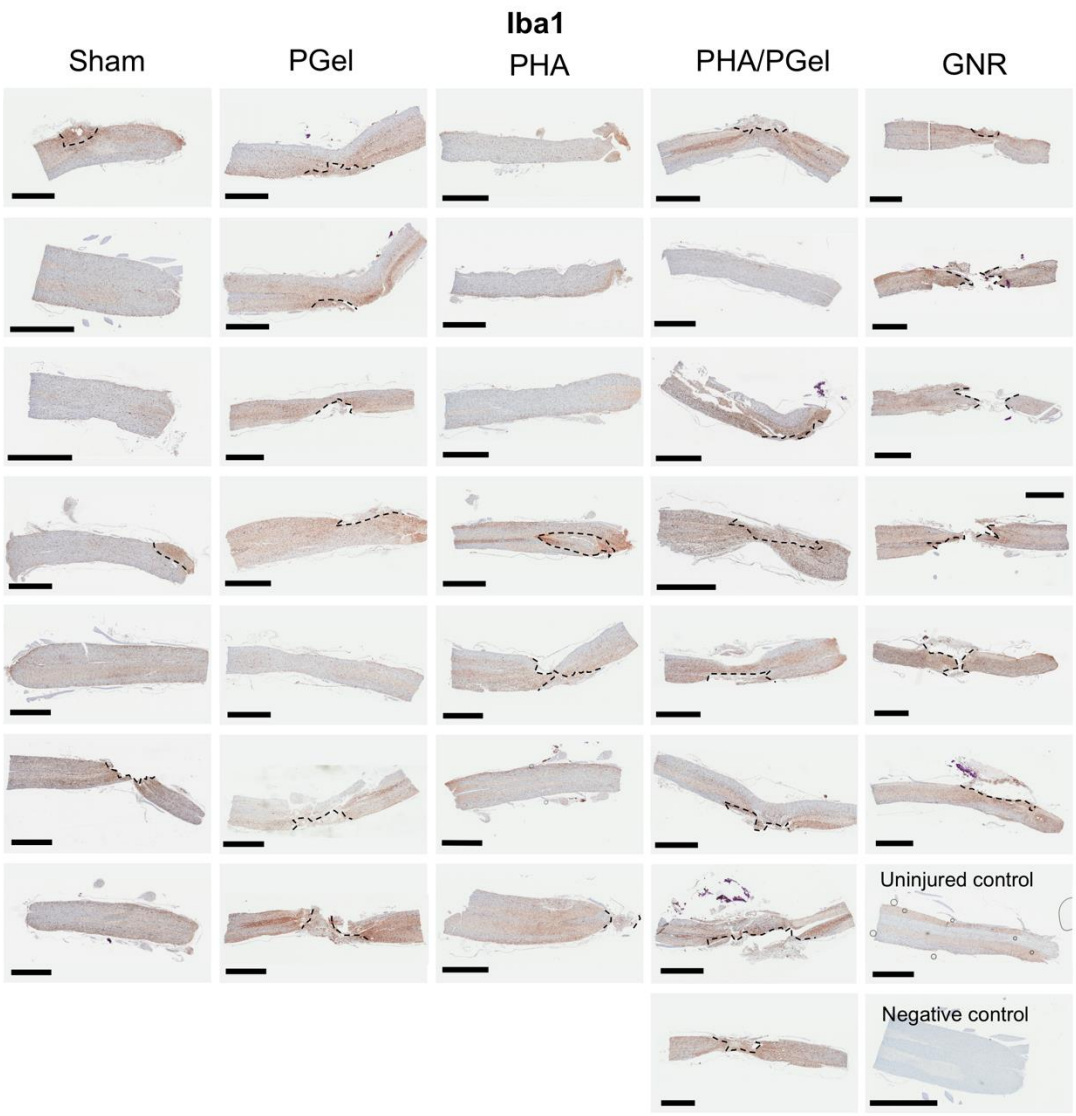

Figure 5.12: Aim 3 Iba1 IHC on Spinal Cords

Microglia and macrophages were stained with an Iba1 antibody after 8 weeks. In the sections where an injury was visible, the location of the injury was outlined by dashed lines. In all groups, there was staining of microglia throughout the gray and white matter of all injured spinal cords. Additionally, there were more macrophages in the vicinity of the injury (darker staining near the injuries) for most spinal cords, regardless of the group. There was not any significant reduction of macrophages and inflammation in the proximity or within the injury in any of the groups. Scale bars: 3 mm.

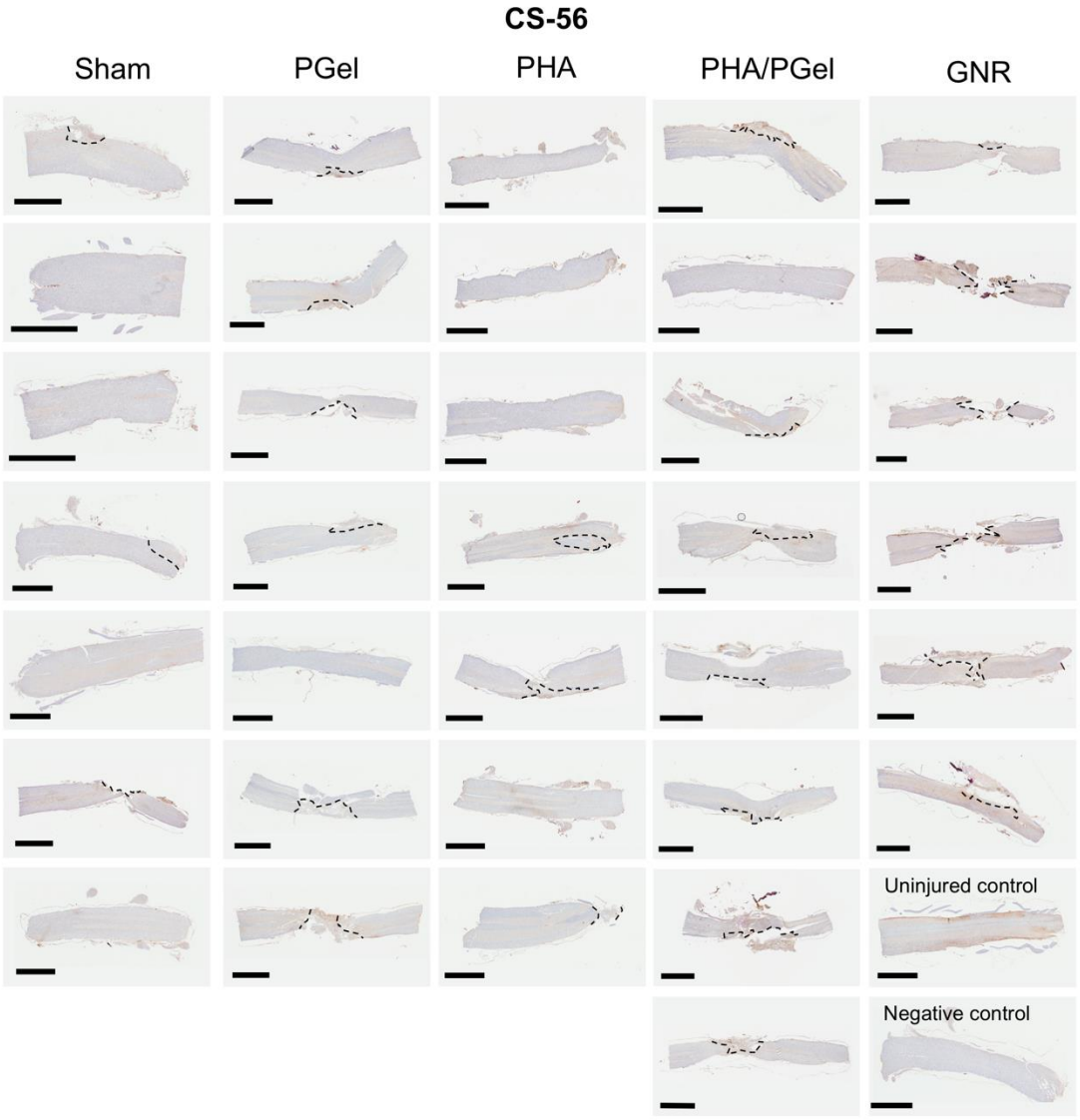

Figure 5.13: Aim 3 CS-56 IHC on Spinal Cords

CSPGs were stained with a CS-56 antibody after 8 weeks. In the sections where an injury was visible, the location of the injury was outlined by dashed lines. There was light staining of CSPGs within some of the injuries, where the location of the injury is outlined by dashed lines. There did not appear to be a significant reduction of CSPGs, and thus reduction of the axon-inhibiting environment, in any of the groups. Scale bars: 3 mm.

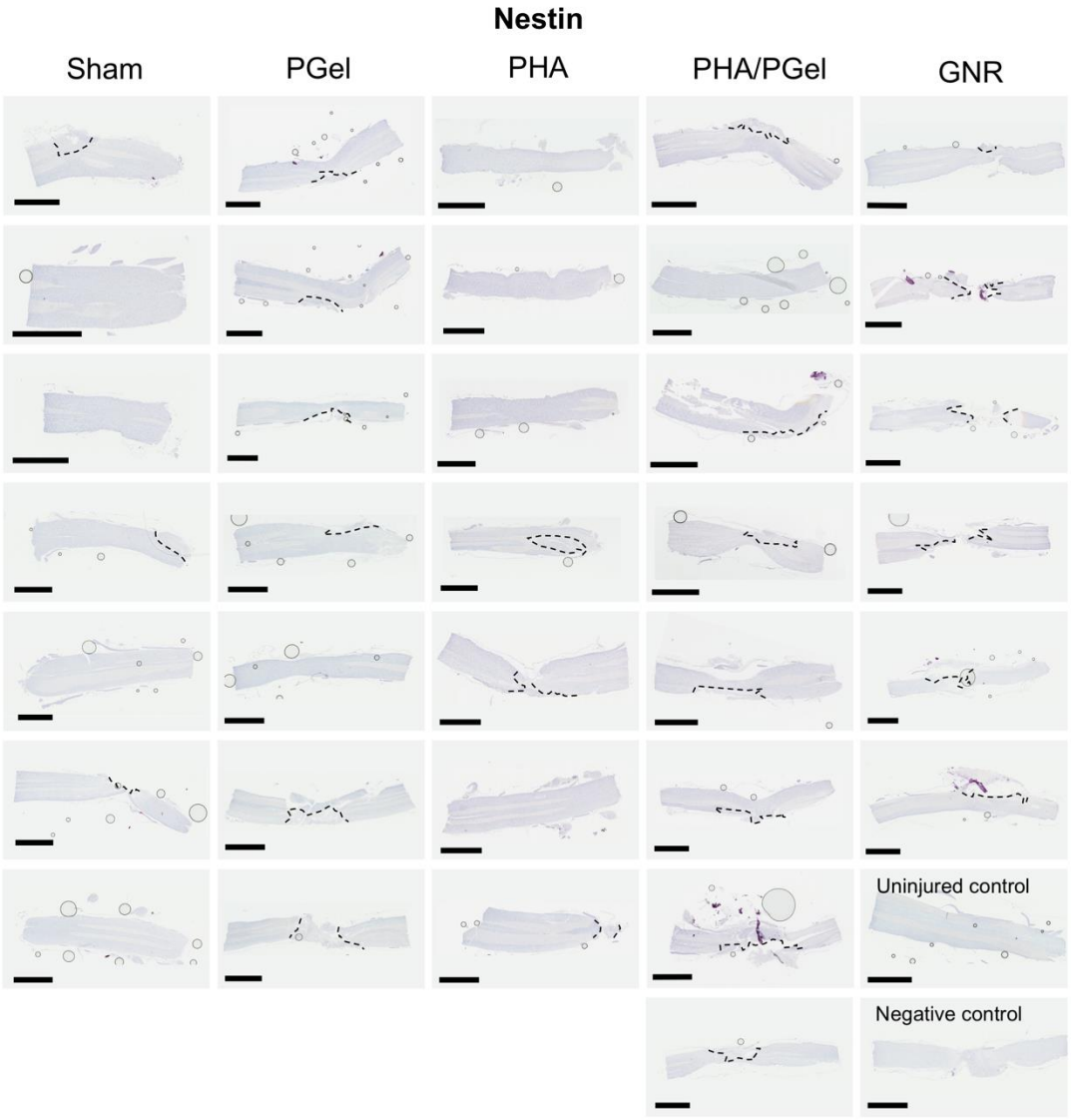

Figure 5.14: Aim 3 Nestin IHC on Spinal Cords

Nestin was stained with a nestin antibody after 8 weeks. In the sections where an injury was visible, the location of the injury was outlined by dashed lines. There was no visible staining of nestin in any of the spinal cords, which indicated that no NSCs were present in any of the groups. Scale bars: 3 mm.

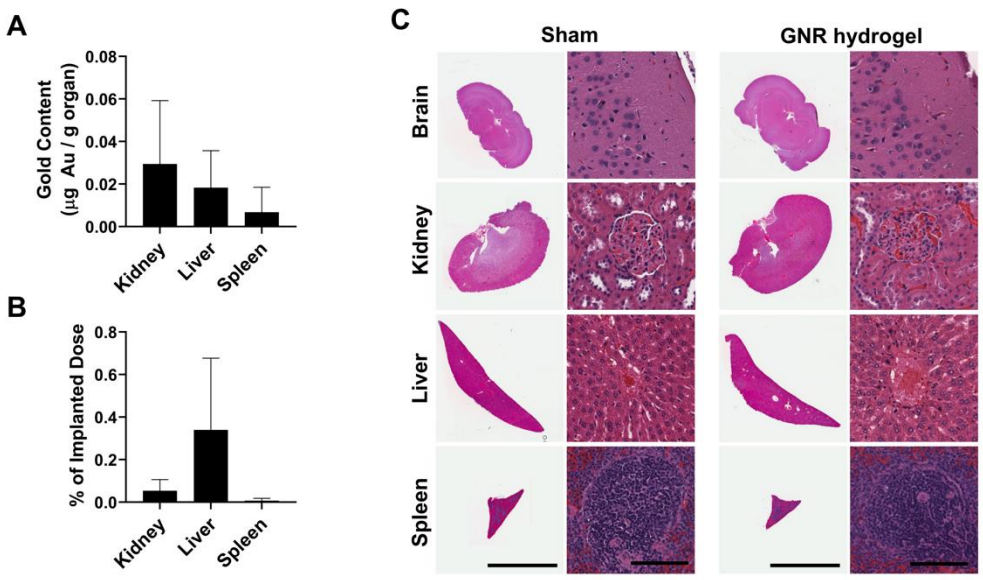

Figure 5.15: Aim 3 Gold Content in Rat Organs

After 8 weeks post-injury, there was <0.4% of the total estimated implanted gold detected in any one of the kidneys, livers, and spleens of rats treated with the GNR hydrogels. **A)** ICP-MS was used to detect the amount of total gold per mass of organ, and there was less than 0.03 µg of gold in the kidneys, livers, and spleens of the rats treated with GNR hydrogels, and no detected gold in the brain or blood (n = 3). The blood and organs of the rats in the sham group did not have amounts of gold above the background. **B)** As a percentage of the estimated total gold delivered, there was less than 0.4% of the total gold delivered that had accumulated in the kidneys, livers, and spleens, respectively (shown in blue markers, right axis). **C)** The histology, after 8 weeks, of the brain, kidney, liver, and spleen (top to bottom) of a rat treated with a GNR hydrogel are shown. Magnified images are to the right of the macroscopic image and show the outer layer of the cerebral cortex of the brain, the renal cortex with a glomerulus in the kidney, hepatocytes surrounding a blood vessel in the liver, and a lymphoid follicle of the spleen. The histology of the organs showed no pathological changes in the brain, kidney, liver, and spleen of the rats treated with GNR hydrogels versus the sham rats. There was no visible accumulation (e.g., in macrophages) or aggregation of GNRs in any of the organs. Scale bars: 3 mm.

Appendix B: Tables

Chapter 1: No Tables

Chapter 2: Tables 2.1-2.7

Chapter 3: Table 3.1

Chapter 4: Tables 4.1-4.4

Chapter 5: Table 5.1

Chapter 6: No Tables

Table 2.1: List of acronyms

List of acronyms

Acronym	Description
SCI	Spinal cord injury
ES	Electrical stimulation
ASIA	American Spinal Injury Association
AIS	ASIA Impairment Scale
MAP	Mean arterial pressure
MPSS	Methylprednisolone sodium succinate
GMP	Good manufacturing practice
ChABC	Chondroitinase ABC
ISP	Intracellular sigma peptide
CSPGs	Chondroitin sulfate proteoglycans
BDNF	Brain-derived growth factor
NGF	Nerve growth factor
NT-3	Neurotrophin-3
GDNF	glial-derived neurotrophic factor
IL-4	Interleukin 4
BSCB	Blood-spinal cord barrier
MAIs	Myelin-associated inhibitors
NgRs	Nogo receptors
PTPΩ	Protein tyrosine phosphatase sigma
NSCs	Neural stem cells
ESCs	Embryonic stem cells
iPSCs	Induced pluripotent stem cells
MSCs	Mesenchymal stem cells
OECs	Olfactory ensheathing cells
SCs	Schwann cells
Nogo-A	Neurite outgrowth inhibitor
RGMa	Repulsive Guidance Molecule A
CSF	Cerebral spinal fluid
PLGA	Poly(lactic-co-glycolic acid)
UC-MSCs	Umbilical cord-derived mesenchymal stem cells
CNTs	Carbon nanotubes
PEG	Polyethylene glycol
PEG-DA	Polyethylene glycol-diacrylate
EES	Electrical epidural stimulation
TBI	Traumatic brain injury
5-HTP	5-hydroxytryptophan
L-DOPA	Levodopa

PCLEEP	Poly(ε-caprolactone-co-ethyl ethylene phosphate)
IPN	Interpenetrating network
OLEDs	Organic light emitting diodes
PPy	Polypyrrole
PANI	Polyaniline
PT	Polythiophene
PEDOT	Poly(3,4-ethylenedioxythiophene)
PPV	Poly(p-phenylene vinylene)
PSS	Poly(4-styrenesulfonate)
GelMA	Methacrylated gelatin
SLA	Stereolithography
MEH-PPV	Poly[2-methoxy-5-(2-ethyl-hexyloxy)1,4-phenylene vinylene]
PCL	Polycaprolactone
GO	Graphene oxide
CNS	Central nervous system
rGO	Reduced graphene oxide
SWCNTs	Single-walled carbon nanotubes
MWCNTs	Multi-walled carbon nanotubes
PEG-SH	Thiolated PEG
AuNPs	Gold nanoparticles
IONPs	Iron oxide nanoparticles
AgNPs	Silver nanoparticles
FGF	Fibroblast growth factor
PNIPAM	Poly(N-isopropylacrylamide)
GNRs	Gold nanorods
CTAB	Hexadecyltrimethylammonium bromide
MRI	Magnetic resonance imaging
PLLA	Poly (L-lactic acid)

Table 2.2: Cell-based Clinical Trials

Current cell-based clinical trials that are active, recruiting, or not yet recruiting

Title abbv., Sponsor, NCT Identifier	Intervention	Phase	Patient population	Delivery	Placebo control?	Dates/Results
Neuralstem Inc. NCT01772810	"HSSC" or "NSI-566" Allogenic fetal spinal cord-derived NSC line	Phase I	Chronic (1-2y)	1 delivery of 6 injections into the cord around the lesion with a total of $0.6x10^6$ or $1.2x10^6$ cells	No	Aug 2014 – Dec 2022 (300)
SSCiSCI Neuroplast NCT04205019 NCT03935724	"Neuro-Cells" Autologous BMSCs	Phase I	Chronic	1 intrathecal transplant	No	April 2020 – May 2022
		Phase II/III	Subacute (6-8w)		Yes	June 2020 – June 2022
Da Nang Hospital NCT02923817	Autologous BM-mononuclear cells	Phase II	Not listed	1 lumbar injection	No	Sept 2016 – June 2019
Hospital Sao Rafael NCT02574572 NCT02574585	Autologous BM-MSCs	Phase I	Chronic	1 intralesional injection	No	Sept 2017 – June 2020
		Phase II		2 percutaneous injections, 3 months apart	Yes	Dec 2019 – Jan 2022
Cellgram-spine Pharmicell Co., Ltd. NCT01676441	Autologous BM-MSCs	Phase II/III	Chronic	1 injection intramedullary ($16x10^6$ cells) and intrathecal space ($32x10^6$ cells)	No	Aug 2008 – Mar 2020
Stem cells Arabia	Autologous BM or leukapheresis-	Phase II	Chronic	1 injection	No	Jan 2016 – Dec 2021

NCT02687672	derived stem cells (CD34+ and CD133+ stem cells)					
Univ. of Jordan NCT04288934	Autologous BM-MSCs and WJ-MSCs	Phase I	Chronic and subacute (>12w)	1 injection into spinal medulla	No	Aug 2017 – Sept 2020
Third Affiliated Hospital NCT03505034 NCT03521336 NCT03521323	Allogeneic UC-MSCs	Phase II	Sub-acute (2w-2m)	4 intrathecal monthly transplants	Yes	Sept 2019 – Dec 2021
			Early chronic (2m-12m)			
			Chronic (>12m)			
The First Affiliated Hospital of Dalian Medical University NCT04213131	Allogeneic UCB-MSCs and UC-MSCs	N/A	Chronic	1 injection of either UCB-MSCs or UC-MSCs via: Intravenous Lumbar Spinal cord	Yes	Jan 2018 – Jan 2021
CELLTOP Allan Dietz NCT03308565	Autologous adipose-derived MSCs	Phase I	Chronic (2w-1y)	1 intrathecal injection of $100x10^6$ expanded cells	No	Dec 2017 – Nov 2023
SPINE	“FAB117-HC”	Phase I/II	Acute (72-120h)	1 intramedullary injection of 20 or $40x10^6$ cells	Yes	Dec 2016 – Mar 2022

Ferrer Internacional S.A. NCT02917291	Allogenic adipose-derived MSCs, expanded and pulsed with H_2O_2					
StemCyte, Inc. NCT03979742	HLA-matched UCB-mononuclear stem cells + locomotor training	Phase II	Chronic (>12m)	1 transplant of $6.4x10^6$ cells into dorsal root zone with 6 weeks oral lithium carbonate and locomotor training for 6h/day, 6d/w, for 3-6m	Yes	July 2020 – Sept 2021
SciExVR Study MD Stem Cells NCT03225625	Autologous BMSCs + exoskeleton or virtual reality	N/A	Not listed	1 transplant of Bilateral paraspinal injection, with IV injection, with Intranasal injection	No	July 2017 – July 2022

Abbreviations: BMSCs, bone marrow-derived stem cells; NSCs, neural stem cells; BM, bone marrow-derived; MSCs, mesenchymal stem cells; WJ-MSCs, Wharton Jelly-derived MSCs; UC-MSCs, umbilical cord-derived MSCs; UCB-MSCs, umbilical cord blood-derived MSCs; HLA, human leucocyte antigen

Table 2.3: Drugs and Biologics in Clinical Trials

Current drugs and biologics in clinical trials that are active, recruiting, or not yet recruiting

Title abbv., Sponsor, NCT Identifier	Intervention	Phase	Patient population	Delivery	Placebo control?	Dates
NISCI University of Zurich NCT03935321	"NG-101" Antibody that binds Nogo-A	Phase II	Acute (4-28d)	6 intrathecal injections	Yes	May 2019 – Sept 2023
RESET ReNetX Bio, Inc. NCT03989440	"AXER-204" Human fusion protein that binds Nogo-A, MAI, OMgp	Phase I	Chronic (>1y)	1 dose, lumbar puncture	No	July 2019 – Dec 2021
		Phase II		Repeated doses in lumbar puncture	Yes	
ELASCI AbbVie NCT04295538	Elezanumab Monoclonal antibody that binds and inhibits RGMa to be neuroprotective, promote neuron regeneration, reduce inflammation	Phase II	Acute (<1d)	13 intravenous doses every 4 weeks	Yes	Jun 2020 – Dec 2022

Mitsubishi Tanabe Pharma Development America, Inc. NCT04096950	“MT-3921” Antibody to bind and inhibit RGMa	Phase I	Acute	1 low or high intravenous dose	No	Mar 2020 – Dec 2020
RISCIS AOSpine North America Research Network NCT01597518	“Riluzole” Sodium channel blocking drug	Phase II/III	Acute (<12 h)	2x/day doses for first 14 days after injury	Yes	Oct 2013 – May 2025
SCING Ohio State University NCT02524379	“Glyburide” Cation channel blocking drug	Phase I/II	Acute (<8h)	3 oral daily doses	No	Feb 2017 – Mar 2022
Coordinación de Investigación en Salud, Mexico NCT03899584	“4-aminopyridine” Potassium channel blocking drug	Phase III	Chronic (>2y)	Increasing oral doses every 2-4 weeks until max dose	Yes	July 2019 – May 2021
MASC Rick Hansen Institute NCT01828203	“Minocycline” Antibiotic that reduces oligodendrocyte and astrocyte apoptosis	Phase III	Acute (<12h)	7 days of 2x/day IV tapered doses	Yes	June 2013 – June 2018

Mikael Svensson NCT02363361	“Imatinib” Inhibition of PDGFR to restrict BSCB leakage and prevent neural and glial cell apoptosis	Phase II	Acute	14 days of 2x/day doses via gastric feeding tube	No	Apr 2018 – Dec 2021
Pharmazz, Inc. NCT04054414	“PMZ-1620 (Sovateltide)” Endothelin B receptor agonist that augments activity of neural progenitor cells in spinal cord to form new neurons and blood vessels	Phase II	Acute	3 doses via IV/day on day 1, 3, and 6	Yes	Jan 2019 – Oct 2020
Eusol Biotech Co., Ltd. NCT03229031	“ES135” Recombinant human acidic fibroblast growth factor (aFGF) with fibrin glue + rehabilitation	Subacute or chronic (>10w)	1 intrathecal surgical delivery, 2 lumbar puncture boosters	Phase III	No	Dec 2022 – Dec 2024
Kringle Pharma NCT02193334	“KP-100IT” Recombinant human HGF	Acute (>72h)	1x/week intrathecal injections starting at 3dpi for 6 weeks	Phase I/II	Yes	June 2014 – July 2018
Tehran University of Medical Sciences IRCT20110829744 1N1	“Filgrastim” Man-made version of G-CSF	Chronic (>6m)	1x/day for 7 days subcutaneous injection	Phase III	Yes	June 2013 – June 2016

Shirley Ryan AbilityLab NCT01753882	"Lexapro" Serotonin reuptake inhibitor + gait training	Subacute (2-7m)	4 weeks of doses + gait training	Phase I	No	Feb 2012 – July 2020
Shirley Ryan AbilityLab NCT02635893	"D-Cycloserine + training + stimulation" NMDA receptor agonist to improve corticospinal plasticity, with training and stimulation to enhance synaptic efficacy	Subacute (>1m)	1 dose before stimulation/training	Phase IV	Yes	Dec 2020 – Oct 2021
University of Louisville NCT04105114	Buspirone + transcutaneous ES + some form of locomotor activity A serotonin agonist with stimulation and gravity-neutral apparatus, treadmill training, Ekso Bionics Exoskeleton, or rolling walker	Chronic (>1y)	2x/day oral doses during treatment phase	Early Phase I	Yes	Sept 2019 – Mar 2020

Abbreviations: Nogo-A, Neurite outgrowth inhibitor-A; MAI, myelin-associated inhibitors; OMgp, oligodendrocyte-myelin glycoprotein; RGMa, Repulsive Guidance Molecule A; PDGFR, platelet-derived growth factor receptors; BSCB, blood-spinal cord barrier; HGF, hepatocyte growth factor; G-CSF, granulocyte colony-stimulating factor; NMDA, N-methyl-D-aspartate

Table 2.4: Biomaterials in Clinical Trials

Current biomaterials in clinical trials that are active, recruiting, or not yet recruiting

Title abbv., Sponsor, NCT Identifier	Intervention	Phase	Patient population	Delivery	Placebo control?	Dates	Outcomes
INSPIRE, INSPIRE 2 InVivo Therapeutics, NCT02138110 NCT03762655	"Neuro-Spinal Scaffold" PLGA-PLL scaffold	N/A	Acute (<7 dpi)	Implanted into lesion	No	Oct 2014 – Aug 2024	-
					Yes	May 2019 – July 2028	
Nicholls Spinal Injury Foundation NCT03933072	"OECs + Nerve Grafts" Autologous OECs and olfactory nerve fibroblasts from the olfactory bulb embedded in a collagen scaffold (Glial Neuropatch) with autologous sural nerve graft	Phase I/II	Chronic	Scar removal OEC and ONFs from 1 olfactory bulb (12 days in culture) were injected proximal	No	Mar 2016 – Mar 2022	-

				and distal to lesion 1 sural nerve implanted into the lesion			
Chinese Academy of Sciences NCT02352077	"NeuroRegen Scaffold+BMMCs or UC-MSCs" Collagen scaffold to promote axonal growth along fibers, with UC-MSCs or BMMCs to modulate inflammation	Phase I	Chronic	1 scaffold with $1x10^9$ BMMCs 1 scaffold with $4x10^7$ UC-MSCs	No	Jan 2015 – Dec 2020	Some patients had improved autonomic functions and SSEPs (301) Half of the patients had increased sensation, finger flexibility, trunk stability Majority had increased autonomic functions and MEPs(62)
Chinese Academy of Sciences NCT02510365	"NeuroRegen scaffold+UC-MSCs" Collagen scaffold to promote axonal growth along fibers, with UC-MSCs to modulate inflammation	Phase I	Acute (<21d)	Implanted into lesion	No	April 2015 – Dec 2020	1 thoracic SCI patient voluntary walking with brace and 1 cervical SCI patient voluntarily lifting legs and moving toes

Chinese Academy of Sciences NCT02688049	"NeuroRegen scaffold+ MSCs or NSCs" Collagen scaffold to promote axonal growth along fibers, with UC-MSCs or NSCs	Phase I	Chronic	1 scaffold with 10^7 MSCs	No	Jan 2016 – Dec 2020	-
		Phase II		1 scaffold with 10^7 NSCs			
Chinese Academy of Sciences NCT02688062	"NeuroRegen scaffold+BMMCs" Collagen scaffold to promote axonal growth along fibers, with BMMCs	Phase I/II	Chronic	1 implant	No	Jan 2016 – Dec 2020	-
BioArtic AB NCT02490501	"SC0806" A biodegradable device with fibroblast growth factor 1 and nerve implants + rehabilitation	Phase I/II	Subacute (>4m)	1 implant	Yes	June 2015 – Dec 2020	None of the initial 9 patients showed MEPs, and the study was terminated in Nov 2019
Chinese Academy of Sciences NCT03966794	"Collagen scaffold + EES" Functional neural regenerative collagen scaffold transplant + epidural ES	Phase I/II	Acute (<14d) Chronic (>6m)	1 implant	No	Aug 2019 – Dec 2021	-

Abbreviations: dpi, days post injury; PLGA poly(lactic-co-glycolic acid); PLL, poly-L-lysine; OECs, olfactory ensheathing cells; ONFs, olfactory nerve fibroblasts; BMMCs, Bone Marrow Mononuclear Cells; UC-MSCs, umbilical cord-derived MSCs; NSCs, neural stem cells; ES, electrical stimulation; EES, epidural ES

Table 2.5: Conductive Polymer Composites

Composites with conductive polymers and translational advantages and disadvantages

Conductive component	Methods	Material Combinations	Translational Advantages	Translational Disadvantages
Polypyrrole (PPy)	• In situ polymerization(112-116) • Coating(117, 121) • Blended polymer nanoparticles into films(118-120) or scaffolds(121, 122) • Hydrogel(106, 107, 123, 124)	• PCL(112, 121) • PDLLA(117) • PEG(113) • PLA(118, 119) • PLCL/silk fibroin(116) • PLGA(114) • PLLA(115, 121) • PVA(120) • Collagen(107, 122) • Hyaluronic acid(124) • Sodium alginate(106) • Tannic acid (dopant and crosslinker)(123)	• High conductivity • Good biocompatibility/ cell adhesion • One-step hydrogels or nanoparticles blended into other materials could fill a cyst-like injury	• Susceptible to • irreversible oxidation that may reduce conductivity over time • Insoluble monomer and polymer in water
Polyaniline (PANI) (emeraldine form)	• In situ polymerization(125-127) • Coating(134, 135) • Blend polymer nanoparticles into	• PEGDA(125) • PCL(129) • PVA(126, 127) • Alginate(132) • Agarose(132, 133) • Cellulose(135) • Chitosan(130)	• High conductivity • High stability • Polymer-grafted oligomers or nanoparticles blended into other	• Moderate biocompatibility • Insoluble monomer and polymer in water

	films(128, 129) or scaffolds(130) • Hydrogel(105) • Oligomers grafted to biomolecules(131-133)	• Collagen(145) • Gelatin(131) • Silk fibroin(128) • Zein(134) • Phytic acid (dopant and crosslinker)(105)	materials could fill a cyst-like injury	
Poly (3,4-ethylene dioxythiophene) (PEDOT)	• In situ polymerization(140) • Coating(11, 147) • Conductive scaffold formed followed by polymerization of non-conductive polymer(146, 148, 149) • Blend into films(142) or scaffolds(141-143, 145)	• PLLA(142) • Agarose(147) • Alginate(141) • Chitosan(140, 142) • Collagen(145) • Gelatin(140, 142) • GelMA(143) • PEGDA(148, 149) • Dopants: • PSS(143, 146) • Hyaluronic acid(142)	• High conductivity when doped • Good biocompatibility/ cell adhesion • High stability when doped with PSS • Water soluble monomers • Colloidal aqueous suspension of polymer	• Additives or post-processing needed for stability and conductivity
Poly(p-phenylene vinylene) (PPV)	• Blending into films(12)	• MEH-PPV/PCL(12) • PAA(151)	• Water soluble monomers • High stability	• Low conductivity • Insoluble polymer in water

Abbreviations: PCL, polycaprolactone; PDLLA, poly-d,l-lactic acid; PEG, polyethylene glycol; PEGDA, PEG-diacrylate; PLA, polylactic acid; PLCL, poly(L-lactide-co-ε-caprolactone); PLGA, poly(lactic-co-glycolic acid); PLLA, poly (L-lactic acid); PVA, poly(vinyl alcohol); GelMA, methacrylated gelatin; PSS, poly(styrenesulfonate); MEH-PPV, Poly[2-methoxy-5-(2'-ethylhexyloxy)-1,4-phenylene vinylene; PAA, polyacrylamide

Table 2.6: Carbon-based Material Composites

Composites with carbon-based materials and translational advantages and disadvantages

Conductive component	Methods	Material Combinations	Translational Advantages	Translational Disadvantages
Graphene oxide (GO)	Blended into films(172) or scaffolds(173) Coated(170, 171) Freeze-dried foams(166, 167, 169) Thermal crosslinking(168)	PCL(171) PLGA(172) PLLA(170) Gelatin(173)	Moderate biocompatibility Large surface area, easy functionalization Good hydrophilicity	Low to moderate conductivity, dependent on oxidation Toxicity not well-known, but dependent on method of synthesis, size, and dose Reduced form is less hydrophilic, can aggregate
Carbon nanotubes (CNTs) (single-walled or multi-walled)	Suspension(175, 176) Blended into films(15, 120, 180-182) or scaffolds(13, 14, 16, 183-190) Coated(178, 179) Nanofiber scaffold(177)	PLA(185) PLGA(15, 180) PCL(16, 181) PDMS(178) PEG(14, 176, 177, 179, 189) Polyurethane(182) PVA(120, 179) Chitin(184) Chitosan(187, 188) Chondroitin sulfate(186, 187) Collagen I(13) Gelatin(13, 181, 185, 187) Silk(181-183)	High conductivity Good stability Large surface area and easy to functionalize Functionalized CNTs are easy to blend with other materials Can cross the BBB	High hydrophobicity causes aggregation, inflammation, and toxicity

Abbreviations: PCL, polycaprolactone; PLGA, poly(lactic-co-glycolic acid); PLLA, poly (L-lactic acid); PLA, polylactic acid; PDMS, polydimethylsiloxane; PEG, polyethylene glycol; PVA, poly(vinyl alcohol)

Table 2.7: Metal Particle Composites

Composites with metallic particles and translational advantages and disadvantages

Conductive component	Methods	Forms	Material Combinations	Translational Advantages	Translational Disadvantages
Gold nanoparticles (AuNPs)	• *In situ* formation(102, 104) • Blended for films(204) or scaffolds(103, 199, 202-208, 210, 212) • Coated(200, 201)	• Nanoparticles(102, 104, 199-201, 204, 205) • Nanorods(203, 206, 207, 210, 212) • Nanowires(202)	• Chitosan(103, 104) • Alginate(202) • ECM(201, 205) • Gelatin(203, 206, 207, 210) • Agarose/PNIPAM(199) • PLLA(204) • PCL/Gelatin(200) • HEMA(102) • Silk fibroin(212)	• High stability • Low initial cytotoxicity • Easy to scale up • Ease of surface functionalization • Versatile shape and size	• Long-term cytotoxicity
Iron oxide nanoparticles (IONPs)	• Cell labeling(217, 218) • Blended for scaffolds(217, 219-223)	• Nanoparticles(217-223)	• Agarose(219) • Collagen I(217) • Fibrin(221, 223) • HA/collagen I(220) • Matrigel/fibrin or Matrigel/collagen I(222)	• Magnetic • Imaging capabilities • Low cytotoxicity	• Low stability

Abbreviations: ECM, extracellular matrix; PNIPAM, poly(N-isopropylacrylamide); PLLA, poly (L-lactic acid); PCL, polycaprolactone; HEMA, hydroxyethyl methacrylate; HA, hyaluronic acid

Table 3.1: Printable Bioink Yield Stresses

Yield stresses of different printable bioinks

Material	Nozzle diameter (mm)	Yield stress (Pa)	Notes	Author/Year
Pluronic F127/diacrylated Pluronic F127 (PF17/AC3)	0.3	151	No other printable or non-printable formulations.	Muller *et al.* (240)
25 wt% poloxamer 407	0.25	227	15, 20, and 30 wt% formulations were not printable.	Paxton *et al.* (244)
8% alginate/1% $CaCl_2$	0.25	166	No other alginate/$CaCl_2$ formulations were tested.	Paxton *et al.* (244)

Table 4.1: Hyaluronic Acid ^{1}H NMR Assignments

HA ^{1}H NMR peak assignments of the disaccharide repeat unit as determined from the TOCSY spectrum

Functional Group	**Resonances (ppm)**
*D-glucuronic acid**	(1')-CH: 4.33 (2')-CH: 3.25 (3',4',5')-CH: 3.0 – 4.0
*N-acetyl-D-glucosamine**	(1)-CH: 4.50 (2)-CH: 3.70 (3,4,5)-CH, (6)-CH_2: 3.0 – 4.0 (7)-CH_3: 1.90

Numbers in parentheses refer to carbon numbering in **Fig. 4.1A*

Table 4.2: PHA ^{1}H NMR Assignments

PHA ^{1}H NMR peak assignments of the disaccharide repeat unit and the pentenoate groups as determined from the TOCSY spectrum

Functional Group	Resonances (ppm)
Pentenoate group	α-CH_2 (8): 2.46 β-CH_2 (9): 2.27 γ-CH (10): 5.82 δ-CH_2 (11): 5.00
*D-glucuronic acid***	(1')-CH: 4.36 (2')-CH: 3.27 (3',4',5')-CH: 3.0 – 4.0
*N-acetyl-D-glucosamine***	(1)-CH: 4.50 (2)-CH: 3.72 (3,4,5)-CH, (6)-CH_2: 3.0 – 4.0 (7)-CH_3: 1.93

Numbers in parentheses refer to carbon numbering in **Fig. 4.2E*

Table 4.3: Gelatin ^{1}H NMR Assignments

Gelatin ^{1}H NMR peak assignments of the amino acids as determined from the TOCSY spectrum

Functional Group	**Resonances (ppm)**
Arginine	α-CH: 4.35 β-CH2: 1.78 β-CH2: 1.91 γ-CH2: 1.67 δ-CH2: 3.21
Lysine	α-CH: 4.33 β-CH2: 1.78 β-CH2: 1.87 γ-CH2: 1.45 δ-CH2: 1.68 ε-CH2: 3.00
Proline	α-CH: 4.43 β-CH2: 1.94 β-CH2: 2.29 γ-CH2: 2.02 δ-CH2: 3.64
Hydroxyproline	α-CH: 4.57 β-CH2: 2.08 β-CH2: 2.36 γ-CH2: 4.62 δ-CH2: 3.86
Alanine	α-CH: 1.40 β-CH2: 4.33
Glycine	α-CH: 3.97
Glutamic Acid	α-CH: 4.32 β-CH2: 1.96 β-CH2: 2.06 γ-CH2: 2.26
Aspartic Acid	α-CH: 4.60 β-CH2: 2.69 β-CH2: *not detected*
Serine	α-CH: 4.46 β-CH2: 3.89

Table 4.4: PGel ^{1}H NMR Assignments

PGel ^{1}H NMR peak assignments of the amino acids and pentenoate group as determined from the TOCSY spectrum

Functional Group	**Resonances (ppm)**
Pentenoate Group	α-CH_2: 2.27 β-CH_2: 2.49 γ-CH: 5.82 δ-CH_2: 5.05
Arginine	α-CH: 4.35 β-CH_2: 1.78 β-CH_2: 1.91 γ-CH_2: 1.67 δ-CH_2: 3.21
Lysine	*not detected*
Modified Lysine	α-CH: 4.34 β-CH2: 1.77 β-CH2: 1.83 γ-CH2: 1.50 δ-CH2: 1.40 ε-CH2: 3.16
Proline	α-CH: 4.43 β-CH_2: 1.95 β-CH_2: 2.29 γ-CH_2: 2.02 δ-CH_2: 3.61
Hydroxyproline	α-CH: 4.61 β-CH_2: 2.10 β-CH_2: 2.34 γ-CH_2: 4.62 δ-CH_2: 3.84
Alanine	α-CH: 1.40 β-CH_2: 4.30
Glycine	α-CH: 3.97
Glutamic Acid	α-CH: 4.32 β-CH_2: 1.96 β-CH_2: 2.06 γ-CH_2: 2.26
Aspartic Acid	α-CH: 4.60 β-CH_2: 2.71 β-CH_2: *not detected*
Serine	*not detected*

Table 5.1: Single Particle ICP-MS Conditions

Conditions for Single Particle Inductively Coupled Plasma Mass Spectrometer (SP-ICP-MS)

Parameter	Setting
RF Power [W]	1600
Nebulizer Gas Flow [mL min^{-1}]	0.4
Make up Gas Flow [mL min^{-1}]	0.7
Sample Flow Rate [mL min^{-1}]	0.010
Sample Volume [µL]	150
Dwell Time [µs]	50
Scan time [s]	60
Transport Efficiency [%], Mean ± StD	58.5 ± 3.9